6th BSME International Conference on Thermal Engineering (ICTE 2014)

Design and Fabrication of a Proposed Ocean Wave Energy Conversion System with the Analysis of Structural Stability

Md. Arefin Kowser*[a], Md. Tarequl Islam[a], Tapan Bihari Chakma[a], Md. Giyas Uddin[a]

*[a] *Department of Mechanical Engineering, Dhaka University of Engineering & Technology (DUET), Gazipur-1700, Bangladesh*

Abstract

In this paper, the design of a newly proposed ocean wave energy conversion system as well as the fabrication of experimental set-up of proposed system has been presented. This design is focused on the velocity of wave which will be able to capture energy from wave as a thrust force and this force will be used to the conversion of electrical energy as per design presented. Velocity, Frequency, intensity of wave has been varied so the intensity of force also varied that make a bad effect in the structure of the system. A simulation based structural analysis and determination of factor of safety also presented.

Keywords: Renewable Energ; Ocean Wave; Stability of structural; Energy Conversion;

1. Introduction

In the scientific community the energy conversion is a leading interest in the present situation. The conventional energy sources that have been leading the economics of the world, results the global warming. In the circumstances research on renewable energy is very important to mitigate the increasing power demand and a contribution to reduce global warming. Renewable energy source is one of the vital sources to reduce global warming that can achieve a green world. The ocean holds a tremendous amount of untapped energy. Ocean energy comes in a variety of forms such as geothermal vents, and ocean currents and waves. The most commercially viable resources studied so far are ocean currents and waves which have both undergone limited commercial development. Estimates conclude that marine and tidal currents combined contain about 5 TW [1] of energy, on the scale of the world's total power consumption. There is approximately 8,000-80,000 TWh/yr or 1-10 TW of wave energy in the entire ocean [1] and wave energy provides "15-20 times more available energy per square meter than either wind or solar" [2]. There is large number of concepts for wave energy conversion; over 1000 wave energy conversion techniques have been patented in Japan, North America, and Europe [3-7]. The ocean captures energy from sun to wind that produce wave continuously. These waves traveled along the coastal area with variable characteristics. The velocity and time period also varied that the variations of energy captured from different magnitude of wave are different. A curved plate is placed against the wave where the wave traveled towards the coastal area. When the wave strikes the curved plate it develops a linear motion on the energy collector. This energy will convert into electricity through some mechanism. A feasibility study of ocean wave energy conversion of Bay of Bengal has been studied also the power provided by the wave. A variable force is not accepted for a metal structure that reduces the life of the metal structure. The analysis of structure gives a proper solution for design of the system.

2. Feasibility Study of ocean wave of Bay of Bengal

The significant wave height of Bay of Bengal is measured at different year at the Longitude 92 East and Latitude at 21 North. The data collection time starts from 717 points which is gradually increases by adding one minute after every point. This Significant Wave height Map - Based on NRT merged data [8, 9].

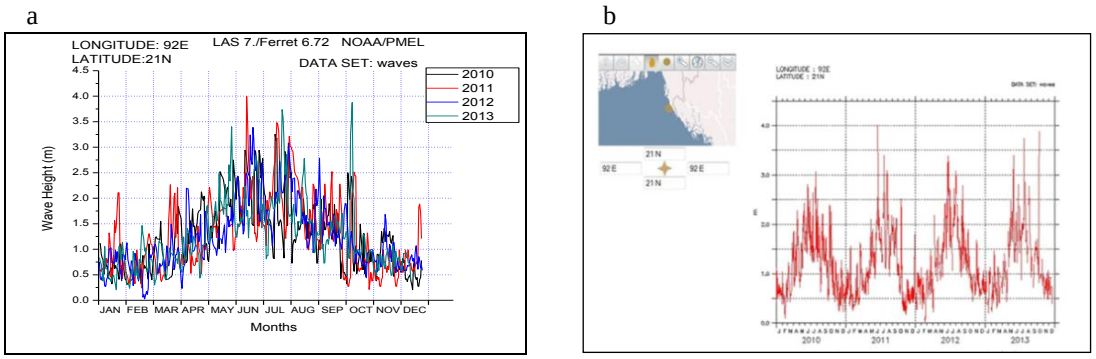

Fig. 1. (a) Significant wave height merged Horizontal in the year of 2010, 2011, 2012 and 2013; (b) Comparison of wave power at different months among the year of 2011, 2012 and 2013.

Fig. 1. (a) shows the significant wave height (m) in the year of 2010-2013 which overlapped each other. It also shows that the first three months i.e. January to March have the same trend which is varied between 0.4m to 1.2m but shows the upward tendency. The next six months that is April to October shows upward and downward tendency but it varies between 0.75m to 3.0m. The last three months shows the same trend of first three months. Fig. 1. (b) gives comparative information about the average energy of wave of the Bay of Bengal over the year 2011, 2012 &2013 are provided. During the first four months means January to April there is no considerable change of wave energy. From May to August significant change of wave energy is observed, whereas at the month of July of these years showing good average wave energy. The wave energy of September and October of presented years is too much better than November and December. It is also seen that the wave energy level are almost same for every year.

3. Method of Ocean Wave Energy conversion

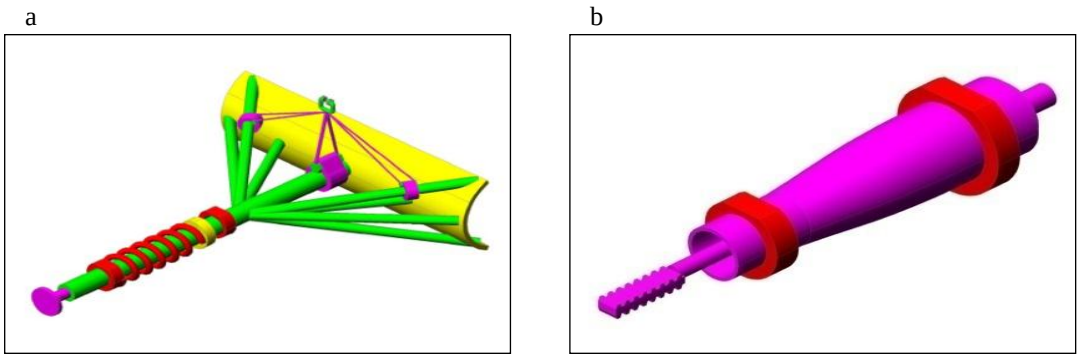

Fig. 2. (a) Wave Power Collector; (b) Power Transmission Line.

A curved plate is placed against the wave where the wave travelled towards the coastal area. When the wave strikes the curved plate it develops a linear motion on the energy collector. It moves along the rail in reverse direction. The spring stored energy equal to energy required to move the collector simultaneously, which is used to back the plate to its initial position when the effect of the wave is disappeared. The plate is flexible to move within a limit which is sensed by spring. The plate is always placed at its initial position by the action of spring. An energy transmission line is constructed to transmit produced energy. The motion conversion system is constructed with a few components are coupling on a shaft and the Flywheel is coupled with a ratchet mechanism. The wave energy is converted from linear to rotary motion. Flywheel is used to store energy. An

alternator is connected with the Flywheel. The rotation of Flywheel is transmitted to the alternator through a shaft which will generate electricity.

4. Fabrication of Experimental Setup

a b

Fig. 3. (a) Gear Mechanism; (b) Experimental Setup.

The Fabricated experimental setup is shown in Fig. 3 (b). Each component are indicated in the schematic diagram i.e. Collector, Flywheel, Generator, Rail with Bearing, Pinion with Shaft and Pillow Block, Ratchet mechanism, Chain, Rack and Pinion. The collector and Rack gear are fixed which can reciprocate on the rail. The other parts remain stationary but they can rotate about their axis. At the time of force applied to the collector it will move to back result the Flywheel start its rotation. The energy transmits from collector to flywheel by chain and sprocket. The collector move backward when force is disappeared due to spring action. The force is applied after a certain time and the speed of flywheel increases and this happened according to the time period. The generator receives energy as rotation from flywheel hence generates electricity [10].

5. Structural Stability

The structural stability of the experimental setup is analyzed in the Simulation environment of SolidWorks 2013. The various condition and element considered during simulation are described in the following table.

Table 1. Study Properties and Description of Simulation.

Study Properties	Description	Study Properties	Description
Unit system	SI (MKS)	Metal	Alloy steel
Analysis type	Static	Model type	Linear Elastic Isotropic
Incompatible bonding options	Automatic	Yield Strength	620.422 N/mm^2
Thermal Effect	on	Tensile strength	723.826 N/mm^2
Zero strain temperature	298 Kelvin	Elastic modulus	210000 N/mm^2
Mesh type	Solid Mesh	Poisson's ratio	0.28
Total Nodes	17865	Mass density	7700 g/cm^3
Total Elements	8113	Thermal expansion	1.3e-005 /Kelvin
Force	10000 N	Force Type	Normal Force

a b

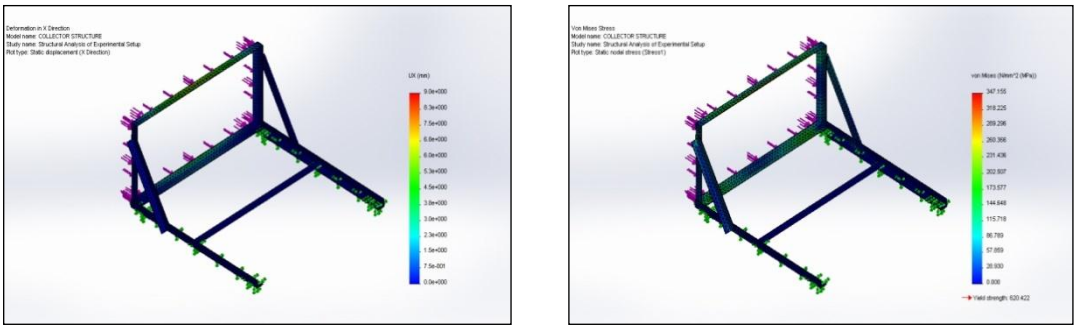

Fig. 4. (a) Deformation analysis of the structure; (b) Von Mises Stress analysis of the structure.

In Fig. 4 (a), it is shown that different colors are represents the intensity of deformation in X direction. The color red shows the maximum deformation and blue shows minimum deformation. The amount of deformation also represent in Fig. 4 (a). The Fig. 4 (b) represents the stress analysis. The maximum and minimum stress developed in the structure is characterized by the color where the red is maximum and blue is minimum. The yield strength does not exceed its limit so the structure will stable in that limit.

a b

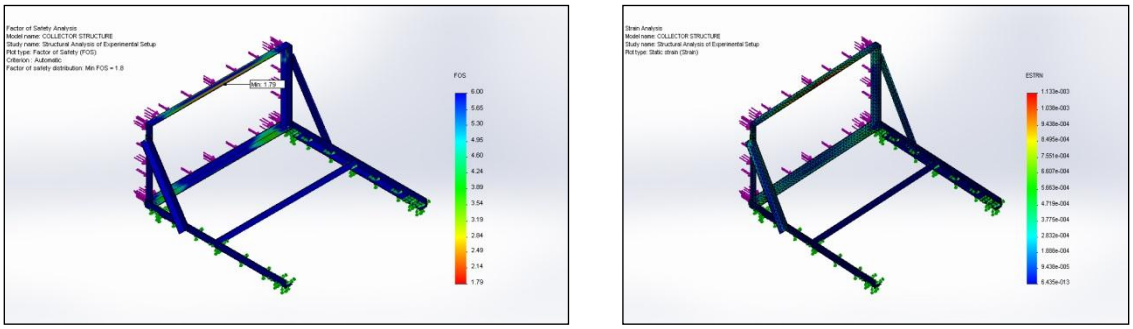

Fig. 5. (a) Static displacement of structure; (b) Strain analysis of the structure.

The contour plot of factor of safety represents in Fig. 5 (a). The amount of factor of safety shows by different color of which Red and blue showing minimum and maximum value respectively. The contour plot of strain analysis is shown in the Fig. 5 (b) it represent the intensity of stress in the structures which is shown by different color.

Acknowledgements

Authors are gratefully acknowledged for the financial support from the University Grants Commission (UGC), Bangladesh.

Conclusion

An experimental setup has been designed and fabricated for the conversion of ocean wave energy into electrical energy as a newly proposed wave energy conversion system. It is observed that the fabricated system is capable to convert energy from thrust force into electrical energy as per design. The power obtained from ocean wave of the Bay of Bengal has been studied in the feasibility study. The structural stability of the experimental setup has been analyzed under maximum loading condition and gives a factor of safety which is almost six times of required value that ensures the stability of the structure at adverse condition.

References

[1] Richard Boud. Status and Research and Development Priorities, Wave and Marine Accessed Energy, UK Dept. of Trade and Industry (DTI), FES-R-132, AEAT/ENV/1054, United Kingdom. 2003.
[2] Electric Power from Ocean Waves, Wavemill Energy Corp., http://www.wavemill.com, 2005.
[3] Clément, A., McCullen, P., Falc˜ao, A., Fiorentino, A., Gardner, F., Hammarlund, K., Lemonis, G., Lewis, T., Nielsen, K., Petroncini, S., Pontes, M.-T., Schild, B.-O., Sjöström, P., Søresen, H. C., and Thorpe,T. Wave energy in Europe: current status and perspectives. Renew. Sust. Energy Rev., pp. 405–431. 2002.
[4] Goswami, D. Y., & Kreith, F. (Eds.). Energy conversion. CRC press. 2007.
[5] Pelc, R., & Fujita, R. M. Renewable energy from the ocean. Marine Policy, 26(6), 471-479. 2002.
[6] Clarke, A. W., & Trinnaman, J. A. (Eds.). Survey of Energy Resources: 2004. Elsevier Science Limited. 2004.
[7] Drew, B., Plummer, A. R., & Sahinkaya, M. N. A review of wave energy converter technology. Proceedings of the Institution of Mechanical Engineers, Part A: Journal of Power and Energy, Vol. 223, No.8, pp. 887-902. 2009.
[8] http://atollaviso.vlandata.cls.fr:41080/thredds/dodsC/
[9] Md. Arefin Kowser, Md. Tarequl Islam, Md. Giyas Uddin, Tapan Bihari Chakma, Mohammad Zahedur Rahman Chowdhury. Feasibility Study of Ocean Wave of the Bay of Bengal to Generate Electricity as a Renewable Energy with a Proposed Design of Energy Conversion System, International Journal of Renewable Energy Research (IJRER) Vol.4, No.2, pp. 445-452. 2014.
[10] Tapan Bihari Chakma, Md. Tarequl Islam, Md. Giyas Uddin. Electrical power generation system by using ocean wave. B.Sc. thesis, Department of Mechanical Engineering, Dhaka University of Engineering & Technology, Bangladesh. pp. 70-82. 2014.

6th BSME International Conference on Thermal Engineering (ICTE 2014)

Performance analysis of a solar flat plate collector used for winter air conditioning by Computational Fluid Dynamics (CFD) simulation

Adib Bin Rashid[a]

[a]*Department of Mechanical and Chemical Engineering*
Islamic University of Technology (IUT), Dhaka, Bangladesh

Abstract

Simulation is an important tool for design and operation control. For the designer of a solar heating system, simulation makes it possible to find the optimum design and operating parameters. Solar flat plate collectors are commonly used for domestic and industrial purposes and have the largest commercial application amongst the various solar collectors. This is mainly due to simple design as well as low maintenance cost. Here the computational fluid dynamics (CFD) tool has been used to simulate the solar collector for better understanding of the heat transfer capability of solar air heater. 3D model of the collector involving air inlet, absorber plate, and glass cover plate is modelled and assembled by Solidworks and the unstructured grid was created in ANSYS Workbench meshing tool. The results were obtained by using ANSYS FLUENT software. The objective of this work is to compare experimentally measured work done with the work done by using computational fluid dynamics (CFD) tool with respect to flow and temperature distribution inside the solar collector. It's found a good similarity between the measured results.

Keywords: Solar air heater, flat plate collector, Computational Fluid Dynamics (CFD), ANSYS FLUENT

1.Introduction

Solar collectors are the key component of active solar- heating systems. They gather the sun's energy, transform its radiation into heat, and then transfer that heat to a fluid (usually water or air). The solar thermal energy can be used in solar water-heating systems, solar pool heaters, and solar space- heating systems. A typical flat-plate collector is an insulated metal box with a glass or plastic cover (called the glazing) and a dark-colored absorber plate. These collectors heat liquid or air at temperatures less than 80°C.

* Corresponding author. Tel.: +8801917188192;
E-mail address:adib@iut-dhaka.edu

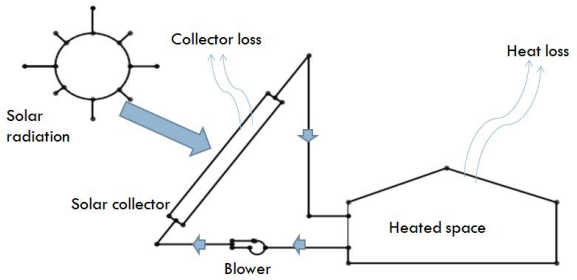

Fig.1. System diagram of air heater

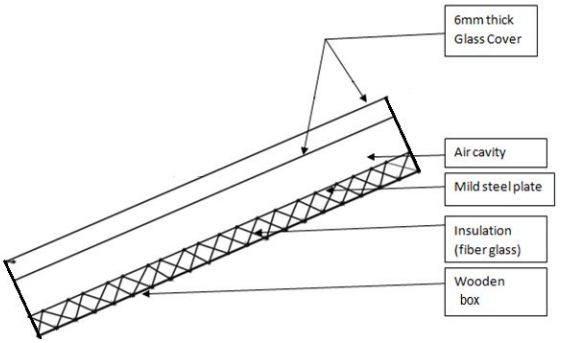

Fig.2. Design concept of solar air heater

In solar energy applications that require high temperatures, such as thermal power generations, solar energy can be optically concentrated before being transferred into heat, thereby increasing the thermal effect of the device. The reflected radiation is concentrated in a local zone, thus increasing the energy flux in the receiving target .

Two types of reflecting surfaces can be used: concave or flat surfaces. The concave ones are more complex in nature as it becomes essential to maintain a normal angle to the sun. Such collectors result in much higher capital costs and, therefore, the more common method for collecting solar thermal energy is a flat surface reflector.

Many theoretical and experimental studies have been done to investigate the effect of reflections on SAHs. The parametric study has been made by Tyagi et al. (2007) for different mass flow rates and concentration ratios using hourly solar radiation. Most of the performance parameters, such as, output energy, the inlet temperature, ambient temperature etc. increase as the solar intensity increases. The performance parameters, mentioned above, are found to be the increasing functions of the concentration ratio. [1]

An indirect forced convection with desiccant integrated solar dryer has been built and tested by Shanmugam and Natarajan (2007). The effect of reflective mirror on the drying potential of desiccant unit was also investigated. With the inclusion of a reflective mirror, the drying potential of the desiccant material is increased by 20% and the drying time is reduced. The temperature rise was about 10 ^{O}C by using the mirror. [2]

Major heat losses from flat- plate solar collectors are found to be through the top cover; heat losses from the bottom and the sides of the collector are low as they are adequately insulated. In order to minimize the heat losses and improve the efficiency, double glazing was recommended by several researchers, Martin, SRL.and Fjeld, GJ. (1975), Prasad et al. (2009). The best results were obtained by Parasad et al. (2009) who reported that the maximum efficiency which could be obtained by this improvement and using the porous media was 68.5% for the design and working parameters that mentioned in the previous section. Some others suggested to insert the absorber plate into the middle of the SAH channel, so that the air will pass above the absorber plate then directed to pass below it (Sopian et al., 1999; Sopian et al. 2009) or vice versa or to flow above and below the absorber at the same time (Yeh et al., 2002; Ozgen et al 2009). The best obtained efficiency (60%-70%) was by Sopian when he used double path collector with porous media in the second channel. [3, 4, 5]

As it is mentioned before, the absorber plate is one of the important parameters that affect the SAH performance. As a result of this, several configurations of absorber plates have been designed by different researchers to improve the heat transfer coefficient. Artificial roughness, obstacles and baffles in different shapes and arrangements were employed to increase the area of the absorber plate. As a result of this, the heat transfer coefficient between the absorber plate and the air path will be improved .[6, 7]

Literature review shows that (Suleyman Karsli,2007) the efficiency of the solar air collectors depends significantly on the solar radiation and surface geometry of the collectors.[8]

Turgut et. al. conducted an experimental and three dimensional numerical work to determine the average heat transfer coefficients for forced convection air flow over a rectangular flat plate. [9] Selmi et al. performed a CFD simulation of flat plate solar energy collector with water flow. [10] The CFD model was validated with experimental results. Janjai et al. developed a mathematical model for simulating the performance of a large area plastic solar Collector. [11] Lecoeuche and Lalot applied neural network technique to predict the thermal performance of a solar flat plate collector. [12]

The objective of present study is to perform CFD simulation of flat plate collector with air flow. The CFD model was validated with experimental results. Based on the results of the experiments CFD analysis of air on solar flat plate collector is carried out. There are certain limitations for experimental results thus data at each and every point cannot be obtained, hence CFD is the tool which handles complex situations where experimental is not applicable because of limitations and cost effectiveness problem. The overall aim of this work is to understand the flow and temperature distribution of air through solar flat plate collector.

Nomenclature

I	Irradiance (W m−2)
T	temperature (°C)
u, v, w	x, y, z velocity components (ms−1)
x, y, z	Cartesian coordinates
k	Turbulence kinetic energy
Cp	Specific heat (J kg-1 K-1)
α	Absorptance
τ	Transmittance
r	Reflectance
$\propto$	dynamic viscosity (Pa s)
$\lambda\rho$	thermal conductivity

2. Experimental details

The overall dimension for solar air collector is 1550X1050X300 mm^3 with 6 mm thick glass plate which is placed at around 126 mm from the top side of the collector. The black painted absorber plate of 1500 mm length, 1000 mm wide and 2 mm in thickness. Inlet and outlets of solar air collector is of circular cross section with diameter of 130 mm.

For the distribution of air in the conditioned space a blower of Pressure 55mm (water), 1400 RPM, Frequency 50Hz, air velocity of 12 m/s and air capacity of .4 m^3/s is used. A double glazing system is used to minimize the heat losses from the collector plate, which occur due to convection and radiation. The experimental work was performed beside the middle workshop, Mechanical & Chemical Engineering Department, Islamic University of Technology under Gazipur prevailing weather conditions during the summer months August and September. Data were collected on an hour interval from 9.00 am to 5.00 pm. Generally, the sky in Gazipur was clear all through the month of May to August with cloudy or partially cloudy from time to time. To observe an accurate reflection of the SAH performance, the data which was collected during more consistent weather condition was studied and considered. However some days were ignored in the analysis because of the weather conditions. The instantaneous values i.e. average mean value of the wind speed and relative humidity ratio were taken from the city office was hourly recorded

The outlet, T_{out}, and the inlet, T_{in}, temperatures were measured by using T- type thermocouples and the global solar radiation incident on an inclined surface was measured by using a Pyranometer.

Fig.3. Experimental set up of solar air heater

3. Domain description

3.1. Geometric modeling

In the present analysis, the geometry is considered to be oriented along the z-axis, with positive Z denoting the south direction while the positive X denotes the east direction. At first different components like wooden box, glass sheet, metal sheet, insulator, air domain etc were created by solidworks2010 with the dimension showed in Table.1 and then assembled according to the fig. 4

Table. 1 Geometrical parameters of SAH system.

Parameter	Dimension
Length	1550mm
Width	1050mm
Height	300mm
Inlet &Outlet Diameter	130mm
Glass plate thickness	6mm
Metal sheet thickness	2mm
Insulator Thickness	2″
Timber Thickness	2″

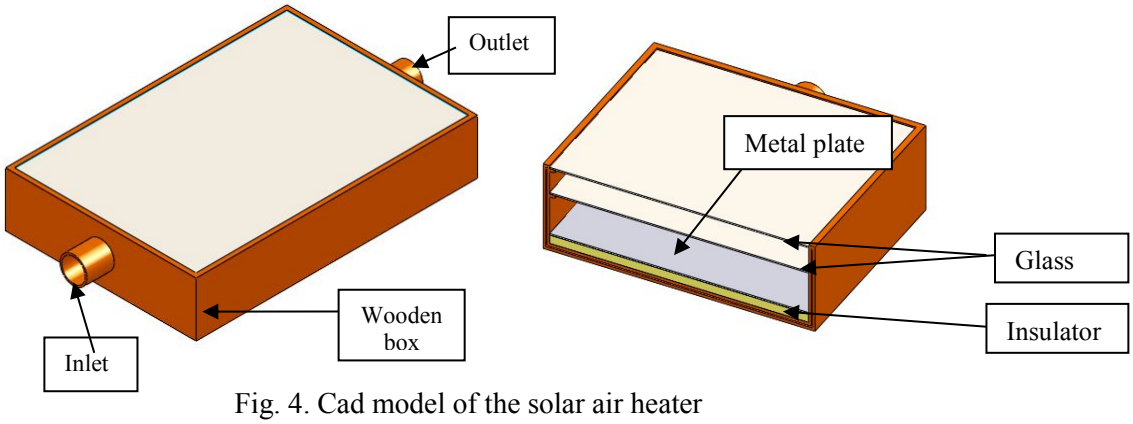

Fig. 4. Cad model of the solar air heater

3.2. Solar Load Model

ANSYS FLUENT provides a model that can be used to calculate radiation effects from the sun's rays that enter a computational domain. It includes a solar calculator utility that can be used to construct the sun's location in the sky for a given time-of-day, date, and position and can be used to model steady and unsteady flows. It allows simulating solar loading effects and determining the solar transmission through all glazed surfaces over the course of a day. The typical inputs needed are the global position (latitude, longitude and time-zone), starting date and time, grid orientation, solar irradiation method and the sunshine factor. The grid orientation is specified in the North (negative Z axis, in the present case) and East (positive X axis, in the present case) direction vector in the CFD grid with the default solar irradiation method as fair weather conditions. The values computed are the sun direction vector, direct normal solar irradiation at earth's surface, diffuse solar irradiation both for vertical and horizontal surface and ground reflected (diffuse) solar irradiation for vertical surface [14].

The solar loads calculated by ANSYS FLUENT are based on the published data from ASHRAE Handbook of Fundamentals [15]. The direct normal solar irradiation shows a typical bell-shaped curve.

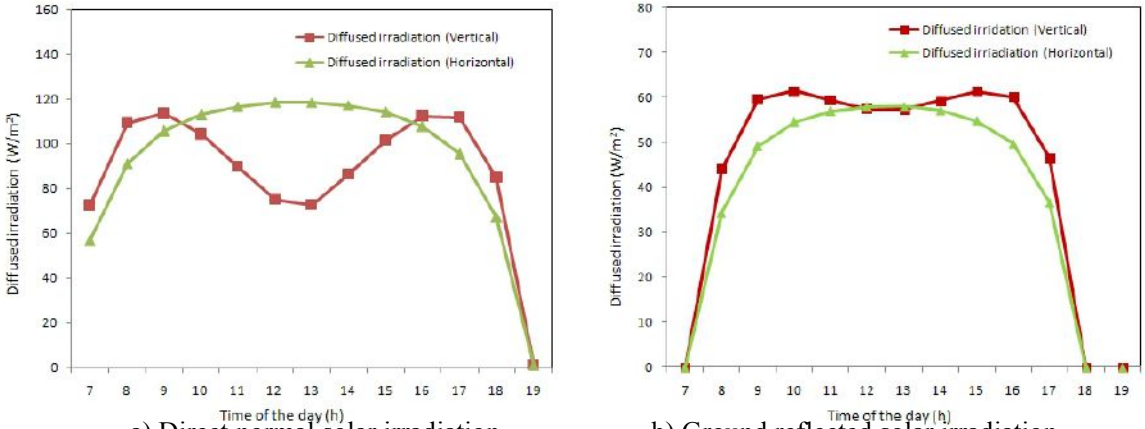

a) Direct normal solar irradiation b) Ground reflected solar irradiation

Fig. 5. Diurnal and seasonal variation of direct normal and ground reflected solar irradiation

The summer curve is more uniform while the winter curve has a higher gradient for diurnal variation. The ground reflected solar irradiation (Fig. 5, (b)) on the other hand, shows similar slope for summer and winter conditions although the summer values are higher due to higher incident solar flux on the ground surface. The diffused solar irradiation is different for vertical and horizontal surfaces (Fig. 6). Horizontal diffuse solar flux variations are the typical bell-shaped curves while the vertical surfaces receive a low diffused solar flux at around the noon time as the sun is in overhead position. The curve therefore has two maxima with minima at the noon time of the day.

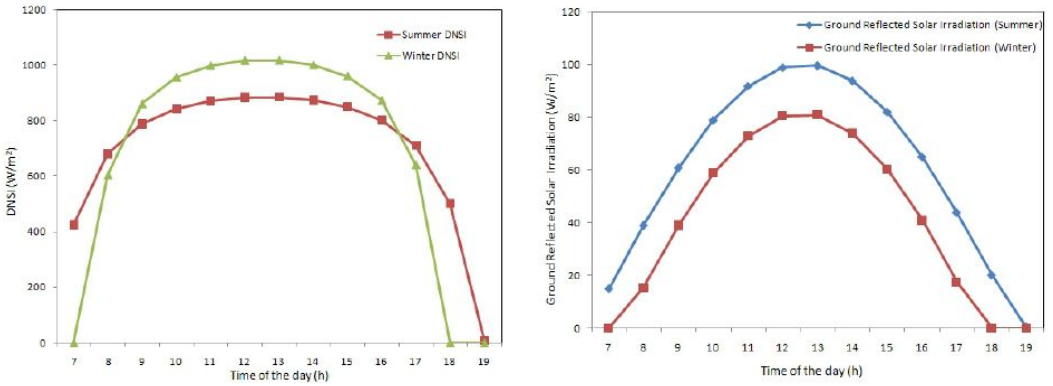

a) Summer b) Winter

Fig. 6. Diurnal and seasonal variation of diffuse solar irradiation

3.3. Radiation Model

The surface-to-surface radiation model makes it possible to simulate thermal radiation exchange between diffuse surfaces forming a closed set. The medium that fills the space between the surfaces is non-participating, i.e., it does not absorb, emit, or scatter any radiation. Therefore, the amount of radiation received and emitted by each surface is uniquely defined by the surface's optical properties and the thermal boundary conditions imposed on it.

3.4. Standard k-ω SST model with low-Re corrections

The SST k-ω turbulence model is a popular two-equation eddy-viscosity model in which the shear stress transport (SST) formulation combines the best of two worlds. The use of a k-ω formulation in the inner parts of the boundary layer makes the model directly usable all the way down to the wall through the viscous sub-layer. Hence the SST k-ω model can be used as a low-Re turbulence model without any extra damping functions. The SST formulation also switches to a standard k-ε behavior in the free-stream and thereby avoids the common k-ω problem that the model is too sensitive to the inlet free-stream turbulence properties. The model shows good behavior in adverse pressure gradients and separating flow although it does produce a bit too large turbulence levels in regions with large normal strain, but is much less pronounced than with a normal k-ε model.

4. Boundary conditions

4.1. *Flow conditions:*

The flow at the inlet was maintained as uniform mass flow at ambient temperature conditions. Flow is assumed to be turbulent. Turbulence specification method of turbulent intensity and viscosity ratio with 5 % and 10 respectively. By default these values are can be taken 3 % and 3 respectively or calculated as per model. Here it is been assumed that turbulence will be more so approximately value has been taken by doing trial and error for convergence of model results[5]. The outlet is maintained to at ambient pressure. The walls are said to have no-slip boundary conditions. Due to the highly

asymmetric nature of the physics and geometry, the full three dimensional domain has been considered for analysis with no symmetric boundaries.

4.2. *Thermal conditions*

The air entering under ambient conditions is considered to undergo a thermally developing flow due to the concentration of heat in the panel.

4.3. *Radiation boundary conditions*

The S2S radiation model requires the calculation of the view-factors which has been done using the ray-tracing method. As the surface to surface radiation is prominent in the vacuum region, the participating zones considered are only the glass-shield and surface of the flat plate. The solar ray tracing algorithm requires the description of the surfaces involved in the ray-tracing to be defined as either semi-transparent or opaque for accurate shadowing effect calculations. In the present analysis, the metallic plate is considered as an opaque surface while the outer glass-shield has been considered to be semi-transparent with optical properties as tabulated below.

Table 2. Optical properties of glass

	Spectrum type	Incident	Diffused
Absorptance, *(α)*	Visible	0.09	0.1
	Infrared	*0.09*	
Transmittance, *(τ)*	Visible	0.83	0.75
	Infrared	0.83	
Reflectance, *(r)*	Visible	0.08	0.84
	Infrared	0.08	

4.4. *Material properties*

As per the construction the property of the different materials should be set. The input material parameters used in the analysis are as shown in Table 3.

Table 3. Properties of Different material

Property	Value for Air	Value for Fibre glass	Value for Wood Block	Value for Glass
Mass flow rate of air	0.4 m^3/s			
Density	1.165 kg/m^3	0.025*(10^3 kg/m^3)*	1350 Kg/m^3	1000 Kg/m^3
Thermal Conductivity	100 W/m K	0.04W/m K	100 W/m K	1.75 W/m K
Specific Heat	1005 J/kg K	0.67 *(kJ/kg K)*	300-600 J/kg K	910 J/kg K

5. Numerical methodology

Tetrahedral mesh elements were generated using Ansys workbench meshing tool software through geometry decomposition. First the CAD model was imported in suitable file format. Then several parts of the model such as inlet, outlet, wall etc ere defined. Then mesh elements were generated of suitable size at different parts within the model. Fig.7 shows a sample of tetrahedral mesh and here the complete geometry was divided into around half-a-million cells for performing the coupled flow and thermal analysis. The picture of the model after meshing is given in Fig 7.

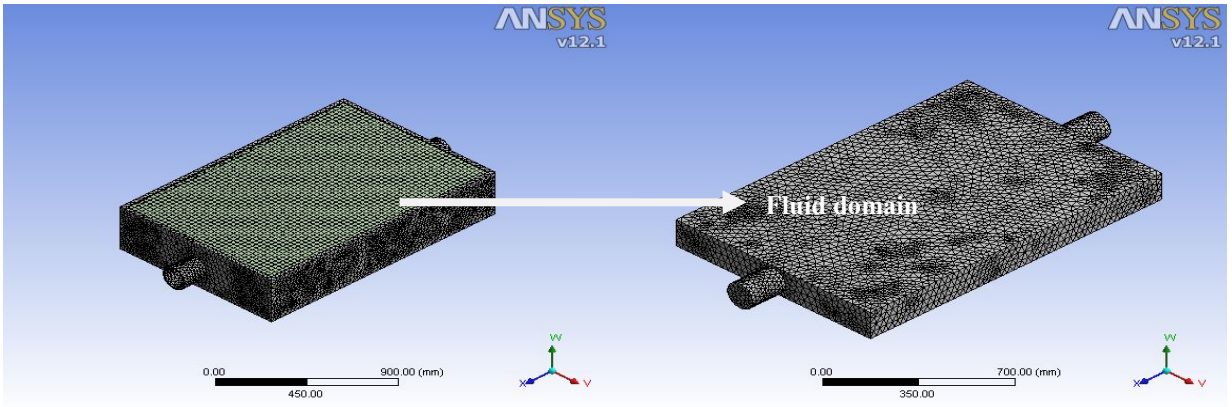

Fig.7. Structured Tetrahedral mesh

The governing equations were solved using the finite volume method by the pressure- based segregated spatially implicit solver available with ANSYS FLUENT 12.1. The 3-D steady state conservations equations are thereby, solved independently with the coupling between the momentum and the continuity equations being achieved using the pressure- correction equation approach Semi-Implicit Method for Pressure Linked Equations, as proposed by Spalding and Patankar[16]. The first order upwind differencing scheme is implemented for the momentum and energy equations.

A typical solution required around 4500 iterations to converge and this meant a simulation time of around 10 hours on a 2.60 GHz Intel micro-processor with 4 GB RAM. All simulations were performed with ANSYS FLUENT module considered in a stand-alone mode. The input parameters were defined for different cases and the corresponding output parameters were obtained with the parameterization feature available with ANSYS FLUENT.

6. Results and Discussion

The analyses of the simulations were done using the key features of ANSYS FLUENT and ANSYS CFD Post for efficient and good quality post-processing. The commercial software packages used are from the ANSYS suite of Fluid Dynamics products which has great potential for doing parametric analysis.

The results obtained from the CFD analysis of solar flat plate Collector are presented in this section. The simulation is carried out for different times of the day i.e. 9 am to 5 pm. Then the results obtained by this simulation compared with the experimental results as shown in Table 4. The curves are plotted to indicate experimental and simulated outlet temperatures versus time. From Table 4 it seems that the difference between experimental and simulated outlet temperature for different times is almost 2˚C.

The results obtained from the CFD analysis of solar flat plate Collector are presented in this section. The simulation is carried out for different times of the day i.e. 9 am to 5 pm. Then the results obtained by this simulation compared with the experimental results as shown in Table 4. The curves are plotted to indicate experimental and simulated outlet temperatures versus time. From Table 4 it seems that the difference between experimental and simulated outlet temperature for different times is almost 2˚C.

Table.4 Comparison of experimental and CFD results

Time Hrs	Solar Intensity (W/m^2)	Ambient Temperature (˚C) obtained by Experiment	Outlet Temperature (˚C) obtained by Experiment	Outlet Temperature (˚C) obtained by CFD analysis
9 am	621.7	32.5	41.3	40.7
10 am	750.5	34.7	43.6	42.5
11 am	879.5	35	46.1	44.4
12	909	35.9	48	46.5
1 pm	948	36.5	49.8	48.1
2 pm	909.5	36.3	48.7	47.2
3 pm	790	34	47.2	43.8
4 pm	597.5	32	45.3	42.3
5 pm	357	30	43.1	41.2

6.1. Temperature variation

Fig. 6 shows the plot of temperature variation of SAH along the length of the system at different times of the day. It can be seen that the temperature rise at noon for a day in August is about maximum. These findings are in accordance with the expected results due to the cold conditions in winter.

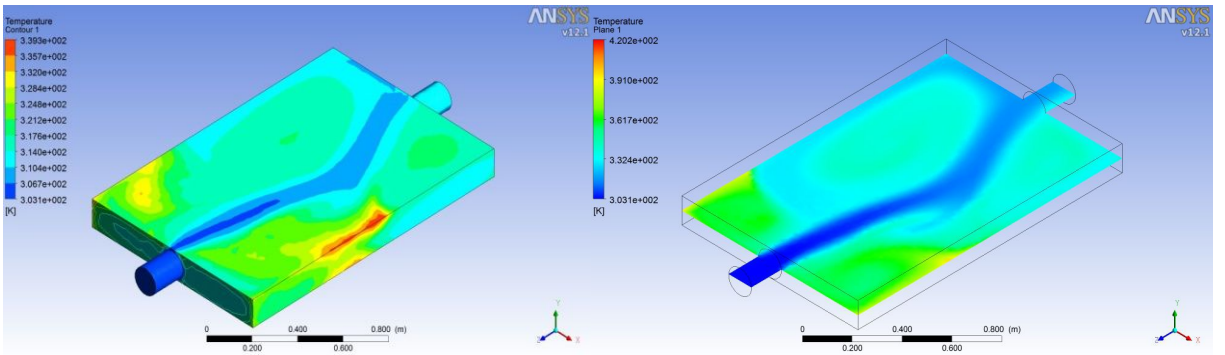

a) Contour b) Plane

Fig.8. Variation of temperature along the length of the Flat plate at 5 pm

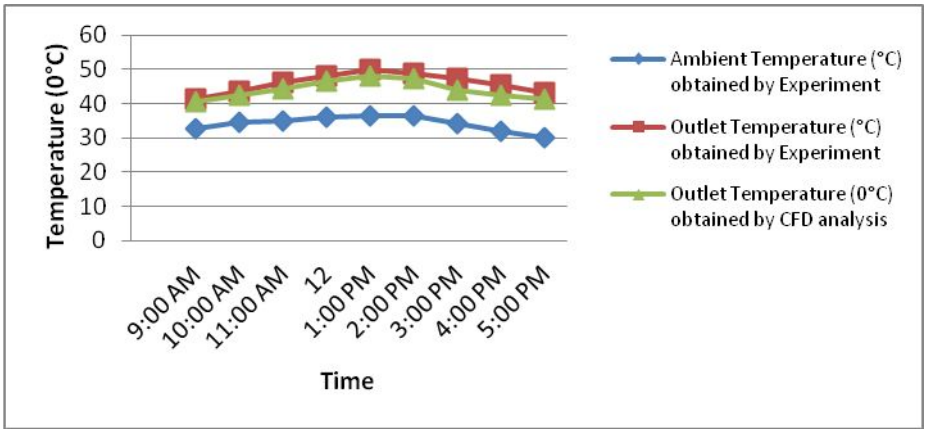

Fig .9. Comparison of Experimental T_{out} vs. Simulated T_{out}

6.2. Flow behavior

The flow phenomenon displays a highly three dimensional swirling pattern especially due to the asymmetric heating of the SAH Plate transferring energy to the air with highly temperature dependent properties.

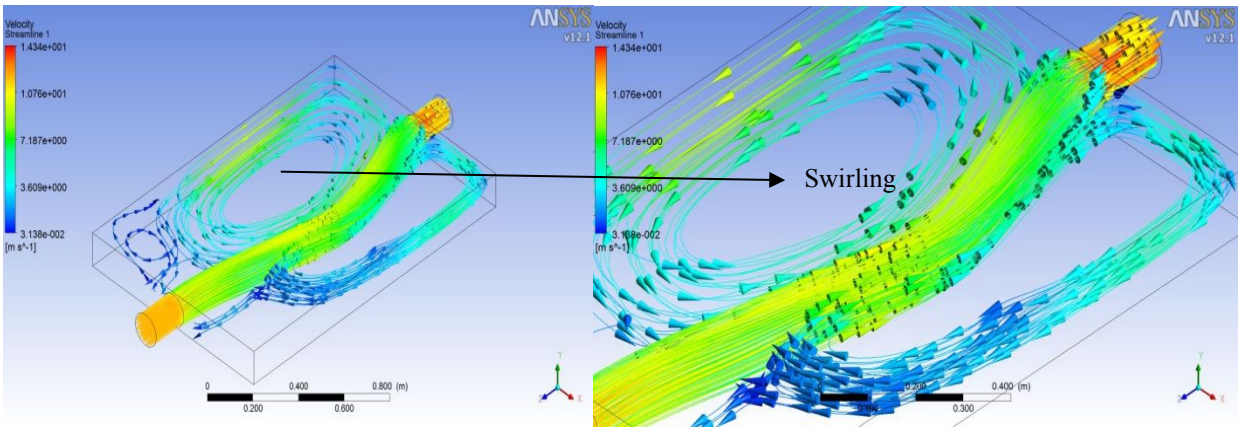

Fig.10. Flow streamlines under steady flow showing the highly swirling phenomenon

The highly turbulent eddies ensure a high residence time of the fluid inside the SAH system thereby allowing it efficiently absorb heat and transfer it across the SAH Panel. The load on the Blower maintaining a constant mass flow rate thereby increase but can be justified by the high amount of thermal energy that the air carries. The density being a function of temperature causes enhanced turbulence under the downward gravity.

7. Conclusion

This study analyzed the 3-D conjugate heat transfer mechanism involved in the receiver element of a Flat plate Solar Collector. There is a good agreement between the experimental and simulated results for outlet air temperatures. Although there are some small discrepancies due to some experimental imperfectness matters, we still have a good confidence in the CFD simulation program that can be used in the future for more complex solar collector problem. It is found from the CFD analysis that the flow of air in the solar flat plate collector is not properly distributed. In order to overcome this issue we can introduce baffles at the inlet of collector which improves the efficiency of solar flat plate collector.

8. References

[1] Tyagi, S.K., Shengwei Wang , M.K. Singhal, Kaushik S.C, Parkd, S.R. 2007. Exergy analysis and parametric study of concentrating type solar collectors. International Journal of Thermal Sciences. 46, 1304-1310.

[2] Shanmugam, V. and Natarajan, E. 2007. Experimental study of regenerative desiccant integrated solar dryer with and without reflective mirror. Applied Thermal Engineering 27,1543-1551.

[3] Prasad,S.B., Saini, J. S., Singh Krishna, M., 2009. Investigation of heat transfer and friction characteristics of packed bed solar air heater using wire mesh as packing material. Solar Energy 83, 773-783.

[4] . Sopian, Supranto, M.Y. Othman, W.R.W. Daud, B.Yatim. 2007, Double-pass solar collectors with porous media sutable for higher-temperature solar- Assisted Drying systems; Jurnal of energy Engineering 13, 9402 133 -1 13.

[5] Yeh,H.M.,Ho,C.D. 2009. Solar air heaters with external recycle. Applied Thermal Engineering 29, 1694-1701

[6] Romdhane, ben salma, 2007.The air solar collectors: Comparative study, Introduction of baffles to favor the heat transfer. Solar Energy, 139-149.

[7] Garg,H.P. and Adhikari R.S., 1999. Performance Evaluation of a single solar air heater with N-Subcollectors Connected in Different combination. Int. J. Energy Res., 23, 403-414

[8] Suleyman Karsli, 2006. Performance analysis of new-design solar air collectors for drying applications. Renewable Energy 32 , 1645-1660.

[9] Turgut, O. and Onur, N, "Three dimensional numerical and experimental study of forced convection heat transfer on solar collector surface", *International Communications in Heat and Mass Transfer*, vol. 36, 2009, pp. 274-279.

[10] Selmi, M., Al-Khawaja, M. J., and Marafia, A., "Validation of CFD simulation for flat plate solar energy collector", *Renewable Energy*,vol.33, 2008, pp. 383-387.

[11] Janjai, S., Esper, A., Muhlbauer, W., "Modelling the performance of a large area plastic solar collector", Renewable energy, vol. 21, 2000, pp. 363-376.

[12] Lecoeuche, S. and Lalot, T. S., "Prediction of the daily performance of solar collectors", *International Communications in Heat and Mass Transfer,*vol.32, 2005, pp. 603-611.

[13] Mohamed Selmi, Mohammed J. Al-Khawaja and Abdulhamid Marafia, "Validation of CFD simulation for flat plate solar energy collector," *Renewable Energy 33 (2008) 383-387*

[14] Romdhane, ben salma, 2007.The air solar collectors: Comparative study, Introduction of baffles to favor the heat transfer. Solar Energy, 139-149.

[15] ANSYS Inc., ANSYS Fluent 12.1, User's Guide, 2009.

[16] D.B. Spalding and S.V. Patankar (1980). Numerical Heat Transfer and Fluid Flow. Taylor & Francis. ISBN 978-0891165224.

6th BSME International Conference on Thermal Engineering (ICTE 2014)

Automatic prevention model for vehicle fuel theft

Rubayat Islam[a], Muntasir Alam[a], Irfan Ahmed[a] and A.K. Azad[b]

[a]*Department of Mechanical Engineering, Bangladesh University of Engineering and Technology, Dhaka 100, Bangladesh*
[b]*School of Engineering and Technology, Central Queensland University, Rockhampton, QLD 4702, Australia*

Abstract

The discovery of automobile vehicles is the blessing to human being from engineering and science. The uses of automobile are increasing day-by-day as a transport vehicle. The majority of the transport vehicles are powered by traditional petroleum fuel such as gasoline, octane, diesel etc. The price of these transport fuels are also increasing worldwide and the high oil price becomes a factor of concern for civilization. From this point of view, advanced security system should be ensured for the fuel safety. The objective of this article is to describe the automatic prevention of fuel theft. An experimental study has been made by suing ultrasonic sensor to measure the fuel flow rate by measuring the distance of fuel level with respect to time. When the fuel flow rate or fuel consumption rate becomes more than usual rate or fuel level falls drastically then the sensor is activated and sends a signal. After receiving the signal the GSM module sends a message to a specific number instantly by indicating that something is unusual so that one can immediately go into inspection. It has been found that it is a very low cost technology and it can also be implemented not only for vehicles but also in those sectors where liquid petroleum fuels are used such as power plant industries.

Keywords: Ultrasonic sensor; transport vehicle; transport fuel; fuel theft; GSM module.

1. Introduction

The developments of automobiles have a significant role in modern civilization over the past few decades. Most of these vehicles are cars, motorcycles, buses, trucks etc. runs by traditional transport fuels such as gasoline, octane, diesel etc. The problems associated with these vehicles are to use this fuel effectively and ensure the safety, security and benefits of the users. Now-a-days security is one of the key issues in modern society. With fleeting time crime rates is also increase in time beings [1]. Furthermore, the fuel price over the past few years is increasing which may effect on the modern life. The vehicle may lose fuel in many ways such as leakage, cracking of fuel tank and fuel theft. It may hamper both safety of life and economic loss. So, the fuel loss or theft from the vehicle is an important issue in many countries in the world. Although there are many alarming issues, in this work preference is given to the unanticipated issue of fuel theft from the transport vehicles. Most of the transport users are counting a loss of a lot of currencies because of this unusual fuel loss. This unexpected fuel loss has a great impact on the economy of a country. It is very alarming and undesirable issue for developing countries like Bangladesh, India and China etc. Petrol and diesel theft is an international problem [2]. In the developing countries the fuel theft rate is incredibly high. So, the issue of fuel theft has become a major annoyance for the users which may one of the causes to derive

increasing fuel price. For instance, since 2003, fuel prices has been doubled in Canada and nearly tripled in USA [3]. To detect the fuel theft problem as well as suddenly decrease the fuel level different sensors have been invented such as pressure sensor, capacitive sensor [4-6], ultrasonic sensor etc. All of these sensors have some advantages and disadvantages such as pressure sensor is suitable for large size of fuel tank. It is not suitable for small range.

In this work, ultrasonic sensor is used. Ultrasonic sensor is really helpful to prevent fuel theft rate as it is very accurate with respect to other sensors. This paper explains an effective and advanced system implementations for fuel level monitoring and ensures maximum security using GSM module. The proposed system has been designed to work with GSM technology which will send a message to a specific number when fuel level falls drastically. GSM is the mature technology and at present there is no area where GSM network is not available. Mobile communication makes this technology viable and unique in such a way that many of the system or applications designed can be made to work with GSM. GSM technology is a worldwide used, wide covering area, implemented and following standards [7]. So the main objective of this work paper is to detect abnormal fuel flow rate of transport vehicle with the help of ultrasonic sensor and by the basic program of microcontroller it will send a signal to GSM module. Then the GSM module will notify the users by sending message of the drastic fuel falling. Practically this technology is used not only for the vehicles but also it can be used in the fuel storage tanks in industries. So this can be a better choice for industrial applications. In a word, the main perspective of this work is to sense the abnormal fuel flow rate of transport vehicle and prevent this unusual fuel theft. The installation of this set up is not time consuming. It has been found that this is a very cost efficient and effective technology and can ensure advanced security. By applying this technology, unexpected economical losses can be avoided.

Nomenclature

S	Distance of the fuel surface from the ultrasonic sensor, m
v	Velocity of sound in air, m/sec
t_1	Time for transmitted sound wave, sec
t_2	Time for reflected sound wave, sec
t	Average time for sound propagation , sec

2. Device Construction

2.1. Sensor section

Ultrasonic sensors are characterized by a low-cost and by the possibility of being used in environments and situations where it is not possible to use more complex sensors. In this work, TS601-01 ultrasonic sensor is used. Ultrasonic electric telemeter modules were employed as ultrasonic transmitter and receiver [8, 9]. This sensor can measure the distance within 0.3~3m effectively.

2.2. Microcontroller section

This section consists of AVR Microcontroller (ATMEGA32) embedded in PCB and some other parts. The Atmel AVR ATmega32 is a low power CMOS 8-bit microcontroller based on the AVR enhanced RISC architecture. By executing powerful instructions in a single clock cycle, ATmega achieves throughputs approaching 1 MIPS per MHz allowing the system designed to optimize power consumption versus processing speed [10].

2.3. Signal processing section

The main purpose of this section is to receive signal from ultrasonic sensor and bypass it to communication section or GSM module whenever it is needed. So, in this section whenever a signal is fetched from the ultrasonic sensor, signal processing section starts to work. Signal is processed by the basic program of microcontroller and bypass it to the communication section so that communication section can send the message to the owner if needed. Actually this section is the controlling part of the entire work.

2.4. Communication section

This section contains a GSM module SIM 300cz with breakout board. The GSM modem can accept any GSM network operator SIM card and act just like a mobile phone with its own unique phone number. In GSM the serial communication is followed. Serial communication is the most simplistic form of communication between two devices. RS-232 is a standard by which two serial devices communicate [11-13]. Whenever it gets any signal from microcontroller it instantly sends a message to a specific number so that one can go into inspection as soon as possible. GSM can send message to any part of the world where GSM network is available. The breakout board should be properly interfaced with the GSM SIM otherwise it will not work properly.

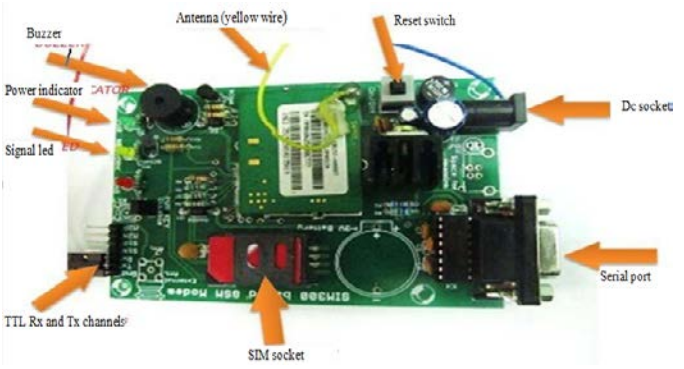

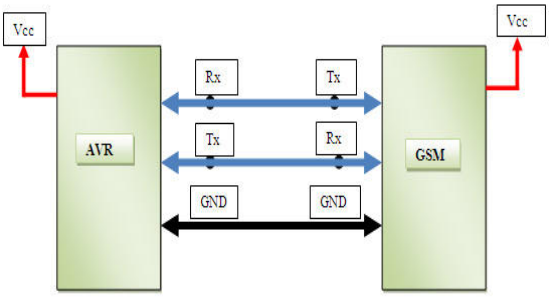

Fig. 1. GSM module (SIM 300cz) with breakout board. Fig. 2. Interfacing of AVR microcontroller with GSM.

3. Methodology and working principle

The aim of this work is to sense the abnormal fuel flow rate. This is sensed by ultrasonic sensor (Model no: TS 601-01). If the vehicle is in running condition, the fuel flow is very slow. The distance measured by the sensor will be changed (in this case distance will be always increased) very slowly. But when the fuel is theft, the distance will be changed more rapidly. As soon as it occurs, ultrasonic sensor senses this condition and sends a signal to the microcontroller. With the help of basic program of microcontroller, the microcontroller sends a signal which is interfaced by the GSM module. The GSM module then sends a warning message to a specific number so that one can go into inspection as soon as possible. The schematic diagram of this work is presented in Figure 3.

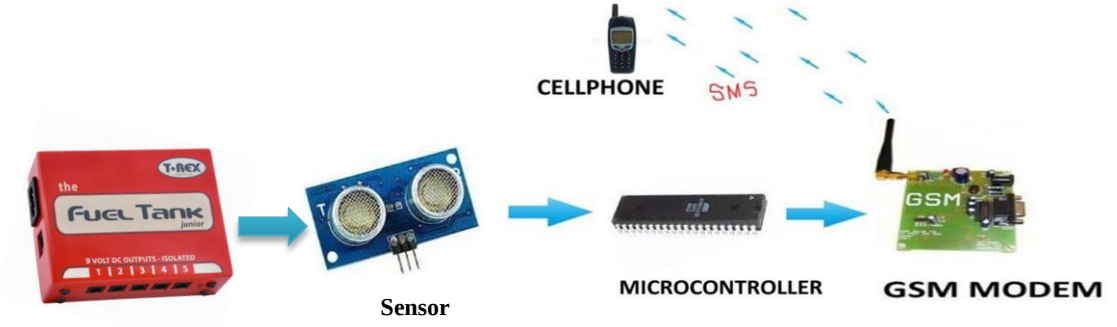

Fig. 3. Overall system design for drastically fuel loss of the vehicle.

4. Flow chart and controlling

The flow chart of this work is presented in Figure 4. The key feature of this work depends on signal receiving by ultrasonic sensor, signal processing with the AVR microcontroller ATMEGA 32 and interfacing of the microcontroller with the GSM module.

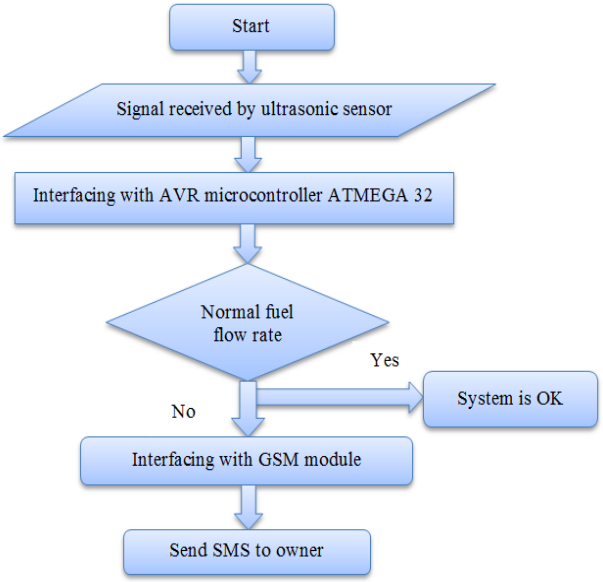

Fig. 4. Flowchart of the working principle of the proposed system.

5. Interfacing

The first part of this work is the operation of ultrasonic sensor. Ultrasonic sensors are categorized as non-intrusive sensors. Ultrasonic sensors generate high frequency sound waves and evaluate the echo which is received back by the sensor. Sensors calculate the time interval between sending the signal and receiving the echo to determine the distance of the fuel surface from the sensor. Sensing and controlling is the most vital part of this work. At first a square pulse is triggered and the ultrasonic transmitter sends out a signal at an angle of 45 degree. Fuel level within this range is detected and the signal is sent back to the ultrasonic receiver. The square impulse is given to the SIG pin of the sensor. The electrical level of the SIG line rises as shown by T1. This triggers a range of 40 KHz signals. The receiving pulse will come back to the output pin after 200us [14]. When the fuel level is detected, the sensor will send back the signal that is indicated by the T3. Thus ultrasonic sensor determines the fuel level in a fuel tank. Controller is basically the electronics part which controls the entire feature of the work. In real case the fuel in the fuel tank will always be decreased when the vehicle is in running condition. When the vehicle is in running condition, the fuel flow is very low or its decrease rate with respect to time will not differ so much. The distance measured by the ultrasonic sensor will be changed very rapidly with respect to previous time. When this abnormal fuel flow rate happens, the sensor will sense the condition and send a signal to the microcontroller. Then by the basic program of microcontroller the microcontroller sends a signal to the GSM module for sending the warning message to the owner.

The final part of this work is GSM module section. GSM stands for Global System for Mobile Communication. GSM offers wide range of services like voice, data and internet access. The low cost mobile communication is used in GSM using mobile communication the user can activate ON/OFF control remotely. A GSM modem is a specialized type of modem which accepts a SIM card, and operates over a subscription to a mobile operator, just like a mobile phone [15, 16]. In this work, SIM 300cz GSM module is used. SIM 300cz is a powerful tool which can work on frequencies EGSM 900 MHz, DCS 1800 and PCS 1900 MHz's. It is a tri-band GMS/GPRS device. It can also support GPRS coding schemes like CS-1, CS-2, CS-3 and CS-4 [17]. In this work used AVR microcontroller ATmega 32. The system is interfaced with the GSM modem. The GSM modem is connected to the microcontroller through a level shifter MAX232 and an RS232 cable. The GSM modem is a highly flexible plug and play quad band GSM modem for direct and easy integration to RS232 applications. The communication between the user and GSM modem is maintained by SMS (Short Message Service) protocol [18]. MAX232 is an integrated circuit that

converts signals from an RS232 serial port to signals suitable for use in TTL compatible digital logic circuits. MAX232 is a dual driver/receiver which typically converts the R_X, T_X, CTS and RTS signals. Here in the device, MAX232 is expected to serially interface the GSM module with the microcontroller [19].

SIM abbreviates as Subscriber Identity Module. It is a chip on small card consisting of user's information as well as phone book. User can alter the operator on the same handset as per convenience. The SIM is inserted in a slot available on the GSM modem. The breakout board operates within an input voltage range of 3.4 to 4.5V. All communication between the module takes place between the serial transmit and receive lines marked Tx and Rx on the board. These pins are provided along with the power pins- +V and Gnd. The Tx line of the breakout board is connected to the Rx line of the microcontroller and the Rx line is connected to the Tx line of the microcontroller [20]. When the GSM modem receives an SMS command from any cell phone, it will communicate that information to the microcontroller through the level shifter IC (MAX232). MAX232 will convert the signal into appropriate form that can be understood by the microcontroller. The microcontroller will process the command and sends signal to GSM modem and the GSM sends message to the number of the owner. AT commands are instructions used to control the GSM modem. AT is the abbreviation of Attention. Every command line starts with "AT" or "at". That's why modem commands are called AT commands. Many of the commands that are used to control wired dialed-up modems. Besides this common AT command set, GSM/GPRS modems and mobile phones support an AT command set that is specific to the GSM technology [21].

Table 1. Commands implemented using the system

Command	Description	Command	Description
AT	Check the serial interface with GSM modem	AT+CMGF	SMS string format , how they are compressed
ATEO	Turn echo off, less traffic on serial line	AT+CMGR	Read new message from a given location
AT+CNMI	Display of new incoming SMS	AT+CMGS	Send message to a given recipient
AT+CPMS	Selection of SMS memory	AT+CMGD	Delete message

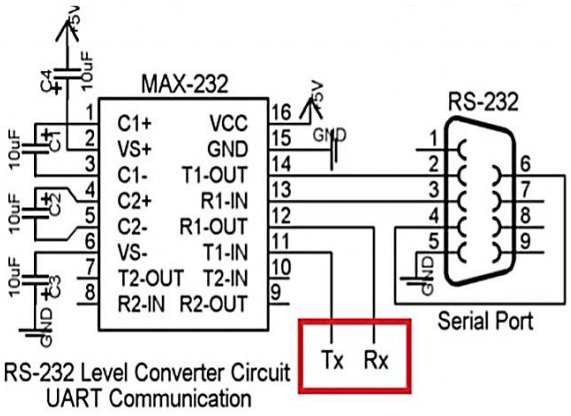

Fig. 5. Interfacing of RS232 with MAX232.

6. Results and solution validation

In this case t_1 is considered as the time taken for transmission of sound wave and t_2 as the time taken for reflection of sound wave. So the average time taken as, $t = (t_1 + t_2)/2$. The velocity of sound in air is considered constant and that is taken approximately 332 m/s. The distance of the fuel surface from the ultrasonic sensor is calculated as, S= v*t. Ultrasonic sensor responses effectively within the range of 0.3~3m effectively. As some ripple occurs in liquid, the value given by the sensor fluctuates a little. So, one of the limitations of this approach is that this can not be used for fuel reservoir fully filled with fuel. At least there should be some gap or level difference so

that ultrasonic sensor can not touch the liquid as the sensor is non-contact type. Proper calibration is needed to get reliable value from ultrasonic sensor.

7. Conclusion

In this work, an advanced and cost effective approach for vehicle fuel security has been proposed. It can be installed in vehicle at some hidden place so that it cannot be approached by any thief. We used ultrasonic sensor which gives a very good response in measurement of distance of fuel level. Infect this sensor is very cost efficient and easy to install. GSM technology is used for ensuring advanced security to the user. This low cost system has achievability and good usability. With the development of technology, GSM technology provides us outstanding services. In future GPS technology can be added to this work so that one can also track the vehicle fuel thief's position as well as get noticed.

References

[1] V. Hachenburg, B. D. Holm, and J. I. Smith, "Data signaling functions for a cellular mobile telephone system," *Vehicular Technology, IEEE Transactions on*, vol. 26, pp. 82-88, 1977.

[2] *Stop Diesel Theft: 6 Ways to Prevent Diesel Fuel Thieves. 2014; [cited on 19 July 2014]; Available from: <http://pro-vigil.com/2008/06/stop-diesel-theft-6-ways-to-prevent-diesel-fuel-thieves/>*.

[3] G. D. Obikoya, "Design, construction, and implementation of a remote fuel-level monitoring system," *EURASIP Journal on Wireless Communications and Networking*, vol. 76, pp. 1-10, 2014.

[4] G. Lu, H. Hu, B. He, and S. Chen, "A new-type sensor for monitoring oil-water interface level and oil level," in *Electronic Measurement & Instruments, 2009. ICEMI'09. 9th International Conference on*, 2009, pp. 981-983.

[5] E. Terzic, J. Terzic, R. Nagarajah, and M. Alamgir, "Capacitive Sensing Technology," in *A Neural Network Approach to Fluid Quantity Measurement in Dynamic Environments*, ed: Springer, 2012, pp. 11-37.

[6] N. I. Giannoccaro and L. Spedicato, "Ultrasonic Sensors for Measurements of Liquid Level, Volume and Volumetric Flow in a Tank," *Precision Instrument and Mechanology*, vol. 1, pp. 1-6.

[7] H. Huang, S. Xiao, X. Meng, and Y. Xiong, "A remote home security system based on wireless sensor network and GSM technology," in *Networks Security Wireless Communications and Trusted Computing (NSWCTC), 2010 Second International Conference on*, 2010, pp. 535-538.

[8] G. Bucci and C. Landi, "Numerical method for transit time measurement in ultrasonic sensor applications," *Instrumentation and Measurement, IEEE Transactions on*, vol. 46, pp. 1241-1246, 1997.

[9] S. Oh, L. Schenato, P. Chen, and S. Sastry, "Tracking and coordination of multiple agents using sensor networks: system design, algorithms and experiments," *Proceedings of the IEEE*, vol. 95, pp. 234-254, 2007.

[10] M. A. Mazidi, J. G. Mazidi, and R. D. McKinlay, *The 8051 microcontroller and embedded systems* vol. 1: Prentice hall Upper Saddle River, NJ, USA:, 2000.

[11] N. Nithya and M. Hemalatha, "GSM based cost effective street lighting application," *Procedia Engineering*, vol. 30, pp. 737-741, 2012.

[12] P. U. Ketkar, K. P. Tayade, A. P. Kulkarni, and R. M. Tugnayat, "GSM Mobile Phone Based LED Scrolling Message Display System," *International Journal of Scientific Engineering and Technology*, vol. 2, pp. 149-55, 2013.

[13] K. Foram, M. Anubbhav, and M. Pritish, "Display Message on Notice Board using GSM," *Advance in Electronic and Electric Engineering*, vol. 3, pp. 827-832, 2013.

[14] S. R. Khan, A. Ferdousi, and S. R. Khan, "Real Time Generator Fuel level Measurement Meter Embedded with Ultrasound Sensor and Data Acquisition System," *Journal of Automation and Control Engineering Vol*, vol. 1, 2013.

[15] S. Sharieh, A. Ferworn, and V. Toronov, "A GSM mobile system to monitor brain function using a near-infrared light sensor," in *Electrical and Computer Engineering, 2008. CCECE 2008. Canadian Conference on*, 2008, pp. 000665-000668.

[16] B. Nagaraja, R. Rayappa, M. Mahesh, C. M. Patil, and T. Manjunath, "Design & Development of a GSM Based Vehicle Theft Control System," in *Advanced Computer Control, 2009. ICACC'09. International Conference on*, 2009, pp. 148-152.

[17] V. Pandya and D. Shukla, "GSM Modem Based Data Acquisition System," *International Journal of Computational Engineering Research*, vol. 2, p. 1663, 2013.

[18] B. Yuksekkaya, A. A. Kayalar, M. B. Tosun, M. K. Ozcan, and A. Z. Alkar, "A GSM, internet and speech controlled wireless interactive home automation system," *Consumer Electronics, IEEE Transactions on*, vol. 52, pp. 837-843, 2006.

[19] Y. Zhao and Z. Ye, "A low cost GSM/GPRS based wireless home security system," *Consumer Electronics, IEEE Transactions on*, vol. 54, pp. 567-572, 2008.

[20] I. Lita, I. B. Cioc, and D. A. Visan, "A new approach of automobile localization system using GPS and GSM/GPRS transmission," in *Electronics Technology, 2006. ISSE'06. 29th International Spring Seminar on*, 2006, pp. 115-119.

[21] p. Priya, s. Singh, a. Mhalan, and g. s. Yadav, "Vehicle theft alert system using GSM," *International Journal of Engineering Science & Technology*, vol. 5, pp. 1070-1075, 2013.

6th BSME International Conference on Thermal Engineering (ICTE 2014)

Effect of Temperature on Torsional Modulus of Rigidity of Neoprene Rubber by Means of a Torsion Tester

Tawsif Ahmed, Dr. Md. Abdus Salam Akanda

Department of Mechanical Engineering, Bangladesh University of Engineering and Technology (BUET), Dhaka, Bangladesh.

Abstract

In today's world of modern science and technology, there has been an enormous global interest on developing scientific methods to unveil the properties associated with various rubber materials that can be easily found around us. The main objective has been to accomplish substantial expertise in accessing these materials with a view to understanding their practical usability as engineering materials in various purposes. This paper, however, illustrates various findings obtained while pursuing a strong study on neoprene rubber. Neoprene rubber was taken as a strip and considered as a wire with two ends fixed on support was allowed to twist under torsion. Thereby, apparent modulus of rigidity was obtained by mathematical manipulation. However, the same procedure was followed for different neoprene rubber with different ash content. For different ash content similar graphs were drawn which clearly demonstrates the variation of torsional rigidity with temperature. Furthermore calculation of apparent modulus of rigidity of neoprene rubber with different ash content led to some concrete findings regarding the behavior of neoprene rubber under different temperature.
(ICTE 2014).

Keywords: Neoprene rubber; torsion tester; modulus of elasticity; ASTM;

1 Introduction

Here the main focus is to comprehend the temperature-rigidity behaviour of neoprene rubber which might be of great help to consider as neoprene is a widely used engineering material. Though there has been available information of neoprene rubber, however it is necessary to determine the torsional rigidity for the temperature range of Bangladesh. Neoprene rubber bearing pad are widely used in bridge and flyovers. Elastomeric bearings are placed between the bridge girders and their supports have two main functions: support the gravity loads (dead load and live loads) and accommodate the changes in the length of the bridge resulting from temperature variations and rotations caused by bending and twisting load. So it is very much necessary to determine whether a specific neoprene rubber bearing pad would able to sustain the twisting load over the whole temperature range of Bangladesh as the rigidity of rubber widely changes with the temperature. Determination of torsional rigidity of rubber will help us to predict that if an specific rubber bearing pad will work properly throughout the whole year or not. This kind of tests are necessary for determining the perfect bearing for a specific purpose.

2 Experimental methodology

In this experiment ASTM standards D1043-02 test method for stiffness properties of plastics as a function of temperature by means of a torsion test has been used. So all mathematical expressions described under ASTM D1043-02 test method, have been used in this thesis. The equation used here for calculation is:

$$G = 72522.848 \times T(N.m)/(\theta(deg)), MPa$$

This equation is basically a reformed shape of the given equation in the standard. Keeping all the constants according to our experimental setup we have got this simple form. In this test, the prime intension was to apply axial load on the neoprene sample and let the sample to twist. The deflection was calculated by the angle measuring scale attached on the top of the torque pulley. This is the value of twist, θ, in degree. The electronic balance is quite sensitive and the disk has to be set perfectly horizontal before placing the weight over it. After measuring the value of the weight attached with the load cord of the torsion tester the amount of torque, T, can be easily found in (N.m). Now by putting the value of T and θ in the equation the value of rigidity, G, in calculated.

3 Test utensils and consideration used in the study

3.1 Experimental setup

The CAD design of the torsion tester was done using SolidWorks. All parts were drawn in separate part file then all the parts were assembled in an assemble file. Fabrication of torsion tester was done by using mild steel. After making all individual parts they were welded together to make the torsion tester.

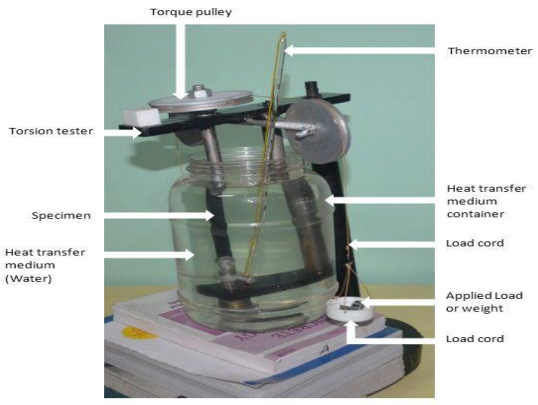

Fig.1. Experimental setup.

Fig.2. Torsion tester.

3.2 Test specimens

The torsion test were conducted at different temperature to study the effect of temperature on modulus of rigidity. All specimens were tested for the temperature range of -15^{0}C to 45^{0}C. The test was conducted for different specimen having different elastomer content and ash content. The list of specimens are as follows.

Table 1. Properties of test specimens

Test Specimen	Elastomer Content (%)	Ash Content (%)
S1	71	2.3
S2	73	4.2
S3	80	2.5
S4	78	3.4
S5	75	2.9

Higher temperatures were gained by heating water and using it as a heat transfer media. Lower temperature were gained by cooling water. For the lower temperature below zero degree Celsius 25% brine solution was used.

4 Experimental results and discussions

4.1 Effect of temperature on rigidity for specimen S1

The effect of temperature on modulus of rigidity individually for specimen S1 has been given in Fig.1. This is basically a rigidity vs. temperature curve. Figure shows the rigidity-temperature curve is a logarithmic decay curve. It means that as temperature rises the modulus of rigidity of neoprene rubber decreases logarithmically and after a certain temperature neoprene loses it rigidity. Fig.1 is also a representation of rigidity-temperature curve. This graph is drawn by plotting log(G) in ordinate and temperature in abscissa. As log(G) has been kept in ordinate, the curve shows a linear decay characteristic which again means that rigidity-temperature relation is logarithmic.

4.2 Effect of temperature on rigidity for specimen S2

Fig.3 and Fig.4 show the effect of temperature on rigidity in two different form for specimen S2. The properties of these two graphs are same as the properties of graphs of specimen S1 described above.

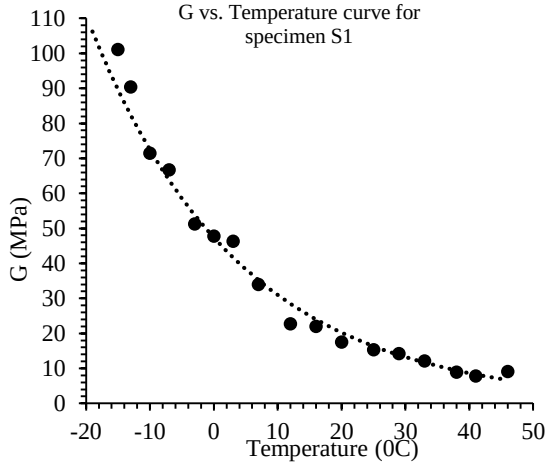

Fig.3. G vs. Temperature curve for specimen S1

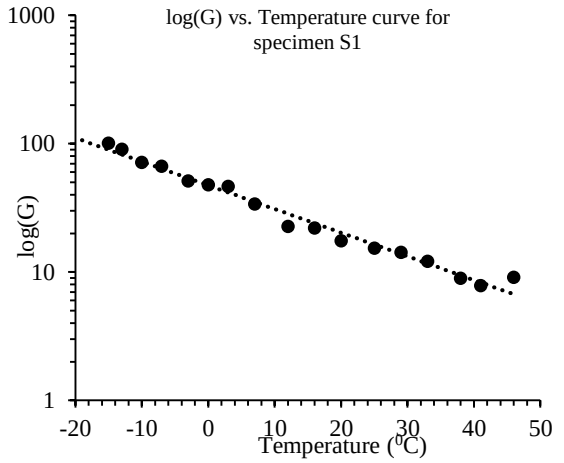

Fig.4. log(G) vs. Temperature curve for specimen S1

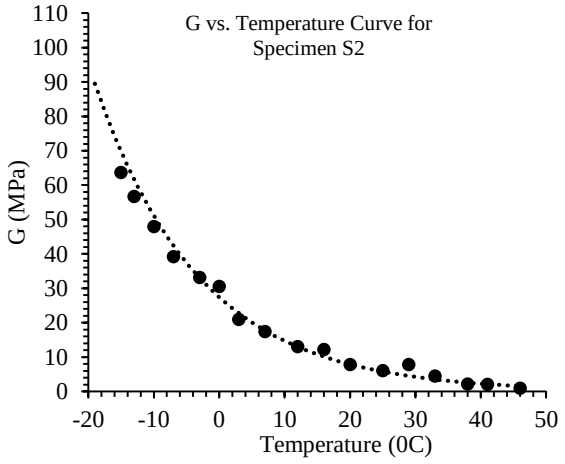

Fig.5. G vs. Temperature Curve for Specimen S2

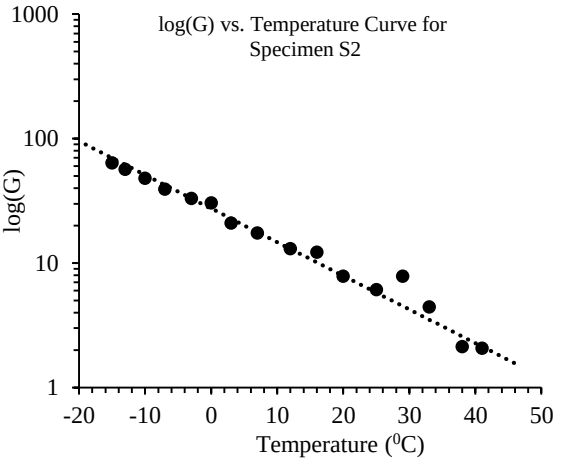

Fig.6. log(G) vs. Temperature Curve for Specimen S2

4.3 Effect of temperature on rigidity for specimen S3

Fig.5 and Fig.6 also show the effect of temperature on rigidity in two different form for specimen S3. The properties of these two graphs are same as the properties of graphs of specimen S1 described above.

4.4 Effect of temperature on rigidity for specimen S4

Fig.7 and Fig.8 also show the effect of temperature on rigidity in two different form for specimen S4. The properties of these two graphs are same as the properties of graphs of specimen S1 described above.

4.5 Effect of temperature on rigidity for specimen S5

Fig.9 and Fig.10 also show the effect of temperature on rigidity in two different form for specimen S5. The properties of these two graphs are same as the properties of graphs of specimen S1 described above.

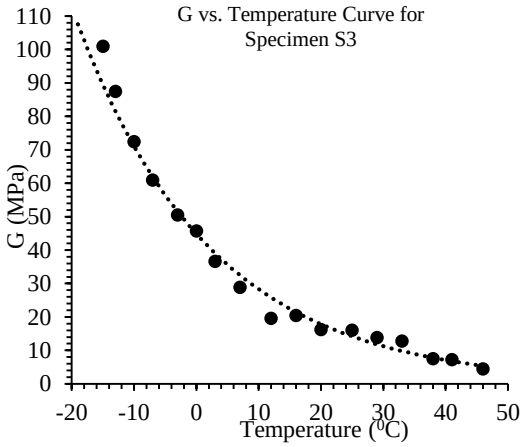

Fig.7. G vs. Temperature Curve for Specimen S3

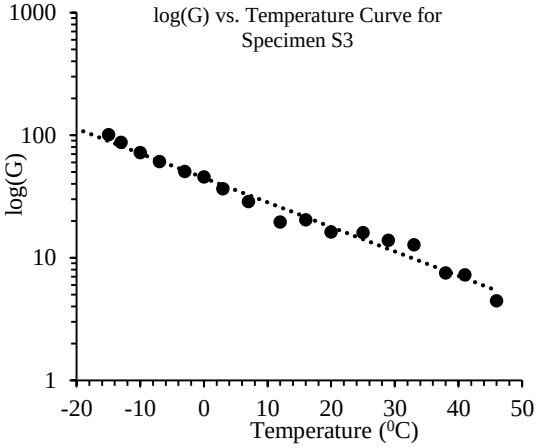

Fig.8. log(G) vs. Temperature Curve for Specimen S3

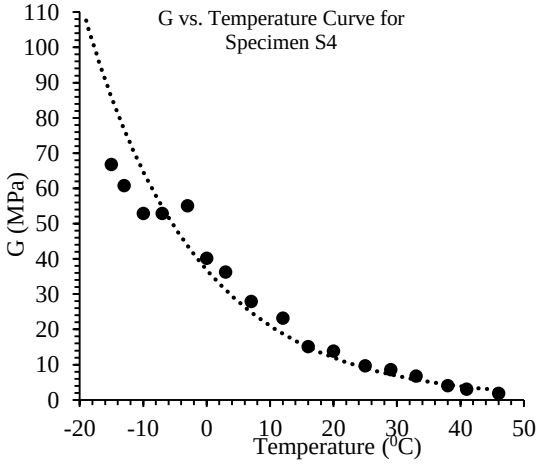

Fig.9. G vs. Temperature Curve for Specimen S4

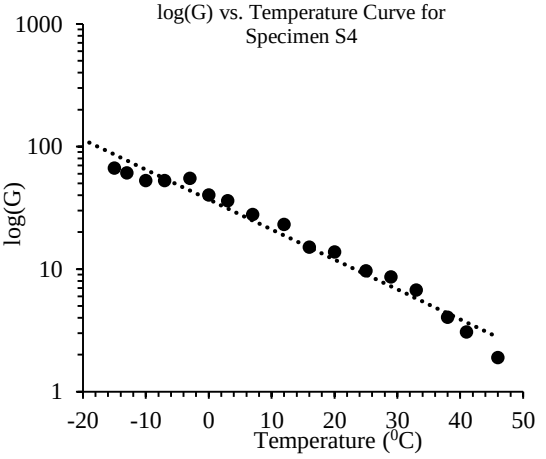

Fig.10. log(G) vs. Temperature Curve for Specimen S4

5 Basic findings

This thesis on effect of temperature on neoprene rubber finally gives us the following graphs as shows in figure Fig.11 and Fig.12. Both the graph tell us how the modulus of rigidity changes with temperature and what is the effect of ash content on the rigidity-temperature relation. These graphs show that as the ash content of the neoprene increases the rigidity-temperature curves shifts downward respectively. It means that with the increase of ash content the rigidity of neoprene decreases considerably.

This kind of graphs are more important for the tropical countries like Bangladesh. That is because of the temperature range of those countries are 15 to 45 ^{0}C. At this temperature range the modulus of rigidity is generally very low so ash content of the rubber can play an important role in this case. The rigidity of the neoprene rubber can be significantly increased by decreasing the ash content. Which means that during choosing of rubber bearing pad for any application in country like Bangladesh one should chose a bearing pad with the lowest ash content otherwise the neoprene rubber of the bearing pad will lose its rigidity at higher temperature and the rubber will flow like a fluid under pressure causing failure of the total structure. So rubber bearing pad made of neoprene rubber having lower ash content is always safer to use in tropical countries.

On the other hand in the continental countries like Canada or central and eastern Europe the temperature generally remains in the region of -20 to 20 ^{0}C. In this temperature region the value of rigidity is generally high. So no extra attention is needed to pay on ash content in these countries while choosing rubber bearing pad.

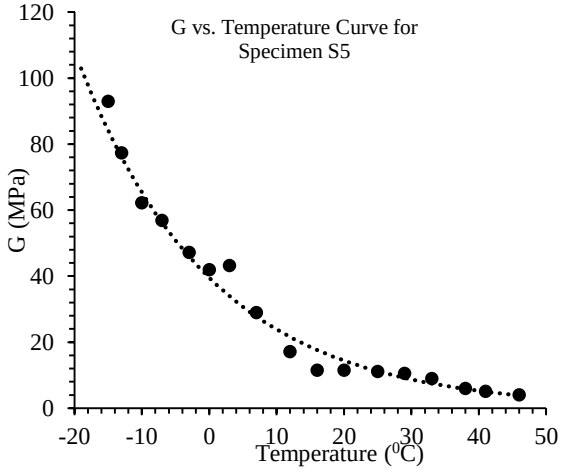

Fig.11. G vs. Temperature Curve for Specimen S5

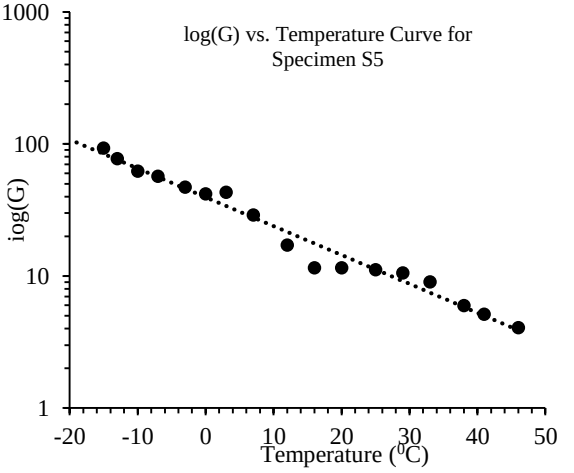

Fig.12. log(G) vs. Temperature Curve for Specimen S5

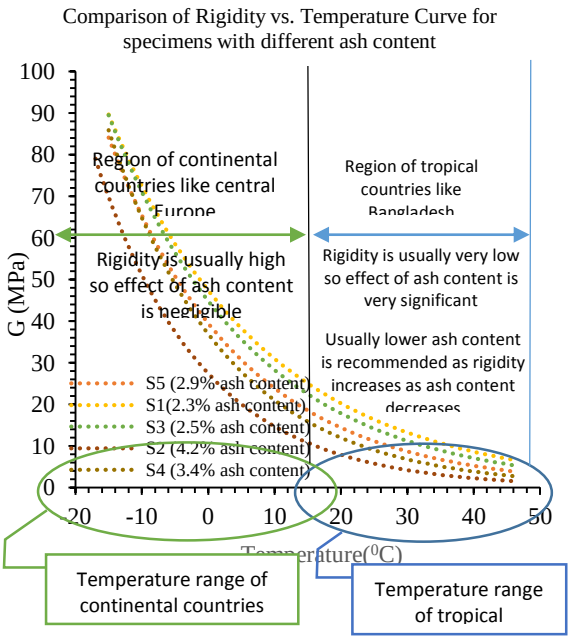

Fig.13. Significance of G vs. temperature in selecting neoprene rubber bearing pad in tropical and continental countries

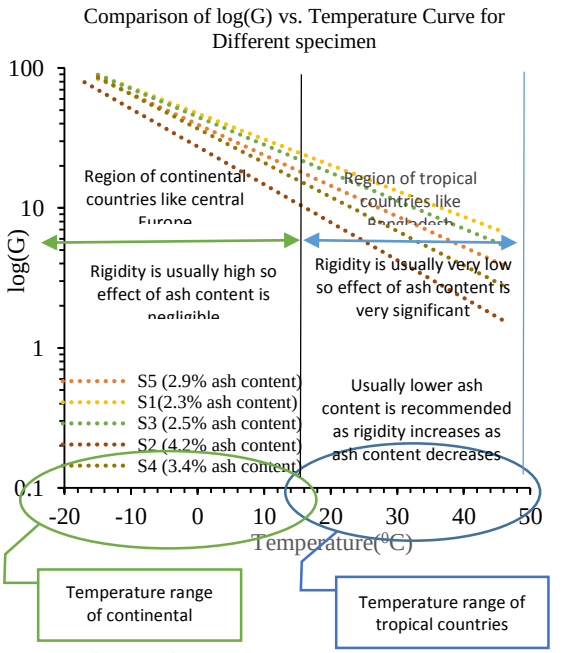

Fig.14. Significance of log(G) vs. temperature in selecting neoprene rubber bearing pad in tropical and continental countries

6 Conclusion

The vigorous study under the periphery of this thesis yielded significantly appropriate information not only for the field of mechanical engineering but also this can be highly applicable for the civil engineers associated with the construction of bridge and flyover. This experiment gives us information about the most perfect working temperature range of neoprene rubber. Again as the ash content of neoprene increases this temperature range increases. Thus this thesis will further help the engineers to determine the perfect neoprene rubber for any specific work. Though the process of experiment, we observed various sources of error. Due to various constrains, it was unavoidable on our part to modulate the experimental procedure to accomplish higher accuracy. In spite of that we obtained remarkable impact of temperature and ash content on modulus of rigidity of neoprene rubber.

References

[1] Goran Spetz; "Review of Test Methods for Determination of Low-Temperature Properties of Elastomers"; Elsevier Science Publishers Ltd, England; Received 23 December 1988; revised version received 1 April 1989; accepted 22 May 1989.

[2] "Standard Test Method for Stiffness Properties of Plastics as a Function of Temperature by Means of a Torsion Test"; American Society for Testing and Materials (ASTM); Designation D1043-02.

[3] Brown, R. P.; "Physical Testing of Rubber"; Elsevier Applied Science Publishers, New York; 1986.

[4] Lehman DE, Roeder CW, Larson R, Curtin K; "Cotton Duck Bearing Pad: Engineering Evaluation and Design Recommendations"; Department of Civil and Environmental Engineering"; University of Washington; 2003.

[5] Yura J, Kumar A, Topkaya C, Becker E, Collingwood J; "Elastomeric Bridge Bearings: Recommended Test Methods"; National Cooperative Highway research Program (NCHRP); Report 449; 2001.

6th BSME International Conference on Thermal Engineering (ICTE 2014)

Study on MHD Free Convection and Mass Transfer Flow past a Vertical Flat Plate

S. Mondal[1], M. Z. Islam[2], S. F Ahmmed[3]

1,3 Mathematics Discipline, Khulna University, Khulna-9208, Bangladesh
2 Mathematics and Statistics Dept., Jessore University of Science and Technology, Jessore, Bangladesh

Abstract

In this paper, we discuss two dimension free convection and mass transfer flow of an incompressible, viscous and electrically conducting fluid past a continuously moving vertical flat plate in the presence of heat source, thermal diffusion, large suction and under the influence of uniform magnetic field applied normal to the flow is studied numerically and analytically. In this study we make the governing equations dimensionless by appropriate co-ordinate transformation. We also consider the effect of heat source parameter and soret number for the above mentioned problem. Then these dimensionless momentum, energy and concentration equations are solved numerically by using explicit finite difference technique with the help of a computer programming language Compaq Visual FORTRAN 6.6. The obtained results of this study have been discussed for the different values of the well know parameter with different time step. Also the steady case of these problems has been solved analytically. The usual similarity transformations are introduced to solve the steady momentum, energy and concentration equations. To obtain the solutions of the problem, the ordinary differential equations are solved using perturbation technique. The expressions for velocity field, temperature distribution, concentration field, skin friction, rate of heat and mass transfer have been obtained by using Mathematical programming. The results are discussed in detailed with the help of graphs and tables to observe the effect of different parameters.
(ICTE 2014).

Keywords: MHD, Free Convection, Mass Transfer, Thermal Diffusion.

Introduction

MHD is the branch of continuum mechanics which deals with the flow of electrically conducting fluids in electric and magnetic fields. Probably the largest advances towards an understanding of such phenomena have come from the field of astrophysics. It has long been suspected that most of the matter in the universe is in the plasma or highly ionized gaseous state and much of the basic knowledge in the area of electromagnetic fluid dynamics evolved from these studies. As a branch of plasma physics the field of Magneto hydrodynamics consists of the study of a continuous, electrically conducting fluid under the influence of electromagnetic fields. Originally, MHD included only the study of strictly incompressible fluid but today the terminology is applied to studies of partially ionized gases as well. Other names have been suggested such as magneto fluid-mechanics or Magneto hydrodynamics but

original nomenclature has persisted. The essential requirement for problems to be analyzed under the laws of MHD is that the continuum approach be applicable. The principal MHD effects were first demonstrated in the experiments of Faraday and Ritchie. Faraday [1] carried out experiments with the flow of mercury in glass tubes placed between poles of a magnet and discovered that a voltage was induced across the tube due to the motion of the mercury across the magnetic fields, perpendicular to the direction of flow and to the magnetic field. These waves are produced by disturbances which propagate simultaneously in the conducting fluid and the magnetic field.

Workers likes Hossain and Mandal [2] have investigated the effects of magnetic field on natural convection flow past a vertical surface. Free convection flows are of great interest in a number of industrial applications such as fiber and granular insulation, geothermal systems etc. Buoyancy is also of importance in an environment where differences between land and air temperatures can give rise to complicated flow patterns. Convection in porous media has applications in geothermal energy recovery, oil extraction, thermal energy storage and flow through filtering devices. The phenomena of mass transfer are also very common in theory of stellar structure and observable effects are detectable at least on the solar surface. The study of effects of magnetic field on free convection flow is important in liquid-metal, electrolytes and ionized gases. The thermal physics of hydro-magnetic problems with mass transfer is of interest in power engineering and metallurgy. The study of flows through porous media became of great interest due to its wide application in many scientific and engineering problems. Such type of flows can be observed in the movement of underground water resources for filtration and water purification processes, the motion of natural gases and oil through oil reservoirs in petroleum engineering and so on. The porous medium is in fact a non-homogeneous medium. The velocity is usually so small and the flow passages are so narrow that laminar flow may be assumed without hesitation. Rigorous analysis of the flow is not possible because the shape of the individual flow passages is so varied and so complex. Poonia and Chaudhary [3] studied about the flows through porous media. Recently researchers like Alam and Rahman [4], Sharma and Singh [5] Chaudhary and Arpita [6] studied about MHD free convection heat and mass transfer in a vertical plate or sometimes oscillating plate. An analysis is performed to study the effect of thermal diffusing fluid past an infinite vertical porous plate with Ohmic dissipation by Reddy and Rao [7]. The combined effect of viscous dissipation, Joule heating, transpiration, heat source, thermal diffusion and Hall current on the hydro-Magnetic free convection and mass transfer flow of an electrically conducting, viscous, homogeneous, incompressible fluid past an infinite vertical porous plate are discussed by Singh *et. al*. [8]. Singh [9] has also studied the effects of mass transfer on MHD free convection flow of a viscous fluid through a vertical channel walls.

The problem of convective heat transfer in a porous media is a topic of rapidly growing interest due to its applications to geophysics, geothermal reservoirs, thermal insulation engineering, exploration of petroleum and gas fields, water movements in geothermal reservoirs etc. Soundalgekar [10] obtained approximate solutions for the two-dimensional flow of an incompressible, viscous fluid past an infinite vertical porous plate with constant suction normal to the plate. Raptis [11] considered mathematically the case of time-varying two-dimensional natural convection flow of an incompressible, electrically conducting fluid along an infinite vertical porous plate through a porous medium. Chen [12] analyzed about heat and mass transfer in MHD free convection from a vertical surface with Ohmic heating and viscous dissipation. Cookey *et al.* [13] extend this with the influence of viscous dissipation and radiation. Also Helmy [14] add the porous plate with this. Kim [15] investigated unsteady MHD convective heat transfer past a semi-infinite vertical porous moving plate with variable suction by assuming that the free stream velocity follows the exponentially increasing small perturbation law. Hossain and Mandal [16] presented effects of mass transfer and free convection on the unsteady MHD flow past a vertical porous plate with constant suction. Chaudhary and Jain [17], studied about Combined heat and mass transfer effects on MHD free convection flow past an oscillating plate embedded in porous medium.

A numerical solution of unsteady free convection and mass transfer flow is presented by Alam and Rahman [18] when a viscous, incompressible fluid flows along an infinite vertical porous plate embedded in a porous medium is considered. In view of the application of heat source and thermal diffusion effect, the study of two dimensional MHD free convection and mass transfer flow past an infinite vertical porous plate taking into account the combined effect of heat source and thermal diffusion with a great agreement was conducted by Singh *et. al.* [19]. Also Nasrin and Alim [20] investigated about MHD free convection flow along a vertical flat plate with thermal conductivity and viscosity depending on temperature.

In our present work, we have studied about MHD free convection and mass transfer flow past a vertical flat plate. The governing equations for unsteady case are studied. Then these dimensionless momentum, energy and concentration equations are solved numerically by using explicit finite difference technique with the help of a computer programming language Compaq visual Fortran 6.6. The obtained results of this problem have been discussed for the different values of the well known parameters with different time step.

Governing Equations

Introducing a Cartesian co-ordinate system, *x*-axis is chosen along the plate in the direction of flow and *y*-axis normal to it. A uniform magnetic field is applied normally to the flow region. The plate is maintained at a constant temperature T_w and the concentration is maintained at a constant value C_w. The temperature of ambient fluid is T_∞ and the concentration of uniform fluid is $C_{\infty,.}$

Within the frame work of delete such assumptions the equations of continuity, momentum, energy and concentration are follows.

$$\frac{\partial u}{\partial x}+\frac{\partial v}{\partial y}=0 \tag{1}$$

$$\frac{\partial u}{\partial t}+u\frac{\partial u}{\partial x}+v\frac{\partial v}{\partial y}=\vartheta\frac{\partial^2 u}{\partial y^2}+g\beta(T-T_\infty)+g\beta^*(C-C_\infty)-\frac{\sigma' {B_0}^2(x)}{\rho}u \tag{2}$$

$$\frac{\partial T}{\partial t}+u\frac{\partial T}{\partial x}+v\frac{\partial T}{\partial y}=\frac{K}{\rho C_p}\frac{\partial^2 T}{\partial y^2} \tag{3}$$

$$\frac{\partial C}{\partial t}+u\frac{\partial C}{\partial x}+v\frac{\partial C}{\partial y}=D_M\frac{\partial^2 C}{\partial y^2} \tag{4}$$

The boundary conditions relevant to the problem are

$$\begin{aligned} &u=U_0, \quad v=v_0(x), \quad T=T_{w,} \quad C=C_w \qquad \text{at} \quad y=0 \\ &u=0, \quad v=0, \qquad T=T_{\infty,} \quad C=C_\infty \qquad \text{as} \quad y\to\infty \end{aligned} \tag{5}$$

where *u* and *v* are velocity components along *x*-axis and *y*-axis respectively, *g* is acceleration due to gravity, *T* is the temperature. T_w is the wall temperature, T_∞ is the temperature of the uniform flow, *K* is thermal conductivity, σ' is the electrical conductivity, D_M is the molecular diffusivity, U_0 is the uniform velocity, *C* is the concentration of species, C_∞ is the concentration of species for uniform flow, $B_0(x)$ is the uniform applied magnetic field, C_p is the specific at constant pressure, C_w is the mean concentration, $C(x)$ is variable concentration at the plate, $v_0(x)$ is the suction velocity, ρ is the density, ϑ is the kinematic viscosity, β is the volumetric coefficient of thermal expansion and β^* is the volumetric coefficient of thermal expansion with concentration and the other symbols have their usual meaning.

Calculation Technique

Many physical phenomena in applied science and engineering when formulated into mathematical models fall into a category of systems known as non-linear coupled partial differential equations. Most of these problems can be formulated as second order partial differential equations. A system of non-linear coupled partial differential equations with the boundary conditions is very difficult to solve analytically. For obtaining the solution of such problems we adopt advanced numerical methods. The governing equations of our problem contain a system of partial differential equations which are transformed by usual transformations into a non-dimensional system of non-linear coupled partial differential equations with initial and boundary conditions. Hence the solution of my problem

would be based on advanced numerical methods. The Explicit Finite Difference Method will be used for solving my obtained non-similar coupled partial differential equations.

Mathematical Formulation

Since the solutions of the governing equations from (1) to (4) under the initial conditions (5) will be based on the finite difference method, it is required to make the said equations dimensionless. For this purpose we now introduce the following dimensionless quantities.

$$X = x\frac{U_0}{\upsilon}, Y = y\frac{U_0}{\upsilon}, U = \frac{u}{U_0}, V = \frac{\upsilon}{U_0}, \tau = t\frac{U_0^2}{\upsilon}, T = T_\infty + (T_w - T_\infty)\theta, C = C_\infty + (C_w - C_\infty)\phi \quad (6)$$

We can rewrite the above dimensionless quantities as follows

$$u = UU_0, \ \upsilon = VU_0 \quad (7)$$

Now using these relations we have substituted the values of the derivatives in to the equations (1) to (4) and after simplifications we obtain the following non-linear coupled of partial differential equation in terms of dimensionless variables,

$$\frac{\partial U}{\partial X} + \frac{\partial V}{\partial Y} = 0 \quad (8)$$

$$\frac{\partial U}{\partial \tau} + U\frac{\partial U}{\partial X} + V\frac{\partial U}{\partial Y} = \frac{\partial^2 U}{\partial Y^2} + Gr\,\theta + Gm\,\phi - MU \quad (9)$$

$$\frac{\partial \theta}{\partial \tau} + U\frac{\partial \theta}{\partial X} + V\frac{\partial \theta}{\partial Y} = \frac{1}{\Pr}\frac{\partial^2 \theta}{\partial Y^2} \quad (10)$$

$$\frac{\partial \phi}{\partial \tau} + U\frac{\partial \phi}{\partial X} + V\frac{\partial \phi}{\partial Y} = \frac{1}{Sc}\frac{\partial^2 \phi}{\partial Y^2} \quad (11)$$

The boundary conditions of the equation (5) are reduced in the following form

$$U = 1, \ V = \frac{V_0}{v_0}, \ \theta = 1 \ \phi = 1 \text{ at } Y = 0 \quad (12)$$

$$U = 0, \ V = 0, \ \theta = 0, \ \phi = 0 \ \text{ at } Y \to \infty$$

Numerical Solutions

In this section, we attempt to solve the governing second order nonlinear coupled dimensionless partial differential equations with the associated initial and boundary conditions. For solving a transient free convection flow with mass transfer past a semi-infinite plate, Callahan and Marner(1976) used the explicit finite difference method which is conditionally stable. On the contrary, the same problem was studied by Soundalgekar and Ganesan(1980) by an implicit finite difference method which is unconditionally stable. The only difference method between the two methods is that the implicit method being unconditionally stable is less expansive from the point of view of computer time. However, these two methods respectively employed by Callahan and Marner(1976) and Soundalgekar and Ganesan(1980) produced the same results. From the concept of the above discussion, for

simplicity the explicit finite difference method has been used to solve equations from (1) to (4) subject to the conditions given by (5).To obtain the difference equations the region of the flow is divided into a grid or mesh of lines parallel to *X* and *Y* axis is taken along the plate and *Y*-axis is normal to the plate. Here we consider that the plate of height $X_{\max} = 100$ i.e. *X* varies from 0 to 100 and regard $Y_{\max} = 60$ as corresponding to $Y \to \infty$ i.e. *Y* varies from 0 to 60. There are *m*=100 and *n*=100 grid spacing in the *X* and *Y* directions respectively. It is assumed that ΔX and ΔY are constant mesh sizes along *X* and *Y* directions respectively and taken as follows,

$$\Delta X = 1.0(0 \le x \le 100)$$

$$\Delta Y = 0.60(0 \le y \le 60)$$

with the smaller time-step, $\Delta\tau = 0.05$ Now, U', V', θ' and ϕ' denote the values of U, V, θ and ϕ at the end of time step respectively . Using the explicit finite difference approximation.
We have

$$\left(\frac{\partial U}{\partial \tau}\right)_{i,j} = \frac{U'_{i,j} - U_{i,j}}{\Delta\tau}, \qquad \left(\frac{\partial U}{\partial X}\right)_{i,j} = \frac{U_{i,j} - U_{i-1,j}}{\Delta X}, \qquad \left(\frac{\partial U}{\partial Y}\right)_{i,j} = \frac{U_{i,j+1} - U_{i,j}}{\Delta Y},$$

$$\left(\frac{\partial V}{\partial Y}\right)_{i,j} = \frac{V_{i,j} - V_{i,j-1}}{\Delta Y}, \qquad \left(\frac{\partial \theta}{\partial \tau}\right)_{i,j} = \frac{\theta'_{i,j} - \theta_{i,j}}{\Delta\tau}, \qquad \left(\frac{\partial \theta}{\partial X}\right)_{i,j} = \frac{\theta_{i,j} - \theta_{i-1,j}}{\Delta X},$$

$$\left(\frac{\partial \theta}{\partial Y}\right)_{i,j} = \frac{\theta_{i,j+1} - \theta_{i,j}}{\Delta Y}, \qquad \left(\frac{\partial \phi}{\partial \tau}\right)_{i,j} = \frac{\phi'_{i,j} - \phi_{i,j}}{\Delta\tau}, \qquad \left(\frac{\partial \phi}{\partial X}\right)_{i,j} = \frac{\phi_{i,j} - \phi_{i-1,j}}{\Delta X},$$

$$\left(\frac{\partial \phi}{\partial Y}\right)_{i,j} = \frac{\phi_{i,j+1} - \phi_{i,j}}{\Delta Y}, \qquad \left(\frac{\partial^2 U}{\partial Y^2}\right)_{i,j} = \frac{U_{i,j+1} - 2U_{i,j} + U_{i,j-1}}{(\Delta Y)^2}, \qquad \left(\frac{\partial^2 \theta}{\partial Y^2}\right)_{i,j} = \frac{\theta_{i,j+1} - 2\theta_{i,j} + \theta_{i,j-1}}{(\Delta Y)^2},$$

$$\left(\frac{\partial^2 \phi}{\partial Y^2}\right)_{i,j} = \frac{\phi_{i,j+1} - 2\phi_{i,j} + \phi_{i,j-1}}{(\Delta Y)^2}$$

In the system of partial differential equations (1) to (4), we substitute and obtain an appropriate set of following finite differential equations.

$$\frac{U_{i,j} - U_{i-1,j}}{\Delta X} + \frac{V_{i,j} - V_{i,j-1}}{\Delta Y} = 0 \tag{13}$$

$$\frac{U'_{i,j} - U_{i,j}}{\Delta\tau} + U_{i,j}\frac{U_{i,j} - U_{i-1,j}}{\Delta X} + V_{i,j}\frac{U_{i,j} - U_{i,j-1}}{\Delta Y} = \frac{U_{i,j+1} - 2U_{i,j} + U_{i,j-1}}{(\Delta Y)^2} + Gr\theta_{i,j} + Gm\phi_{i,j} - MU_{i,j} \tag{14}$$

$$\frac{\theta'_{i,j} - \theta_{i,j}}{\Delta\tau} + U_{i,j}\frac{\theta_{i,j} - \theta_{i-1,j}}{\Delta X} + V_{i,j}\frac{\theta_{i,j+1} - \theta_{i,j}}{\Delta Y} = \frac{1}{\Pr}\frac{\theta_{i,j+1} - 2\theta_{i,j} + \theta_{i,j-1}}{(\Delta Y)^2} \tag{15}$$

$$\frac{\phi'_{i,j}-\phi_{i,j}}{\Delta\tau}+U_{i,j}\frac{\phi_{i,j}-\phi_{i-1,j}}{\Delta X}+V_{i,j}\frac{\phi_{i,j+1}-\phi_{i,j}}{\Delta Y}=\frac{1}{Sc}\frac{\phi_{i,j+1}-2\phi_{i,j}+\phi_{i,j-1}}{(\Delta Y)^2} \tag{16}$$

And the initial and boundary conditions with the finite difference scheme are

$$\begin{aligned} &U^0{}_{i,j}=1,\ V^0{}_{i,j}=\frac{V_0}{v_0},\ \theta^0{}_{i,j}=1,\ \phi^0{}_{i,j}=1 \quad \text{at } y=0 \\ &U^n{}_{i,j}=0,\ V^n{}_{i,j}=0,\ \theta^n{}_{i,j}=0,\ \phi^n{}_{i,j}=0 \quad \text{at } y\to\infty \end{aligned} \tag{17}$$

Here the subscripts *i* and *j* designate the grid points with *x* and *y* coordinates respectively and the superscript n represents a value of time, $\tau = n\Delta\tau$ where n= 0, 1, 2, 3… from the initial condition (5), the values of *U*, θ and ϕ are known at $\tau = 0$. During any one time-step, the coefficients $U_{i,j}$ and $V_{i,j}$ appearing in equations (2) to (4) are treated as constants. Then the end of anytime step $\Delta\tau$, the new velocity U', the new temperature θ', the new concentration ϕ' and V' at all interior nodal points may be obtainedby successive applications of equations (2), (3), (4) and (1) respectively. This process is repeated in time and provided the time-step is sufficiently small, *U*, *V*, θ and ϕ should eventually converge to values which approximate the steady state solution of equations from (1) to (4). These converged solutions are shown graphically in Figs. We also calculate the Skin-friction as $C_f = -u'(0)\frac{Gr^{\frac{3}{4}}}{\sqrt{2}}$. The Nusselt Number is obtained from the relation $Nu = \theta'(0)\frac{Gr^{\frac{1}{4}}}{\sqrt{2}}$ and the Sherwood Number is obtained from the relation $Sh = \phi'(0)\frac{Gr^{\frac{1}{4}}}{\sqrt{2}}$.

Results and Discussions

To observe the physical situation of the problem of our study, the velocity field, temperature field and concentration field are discussed by assigning numerical values to the parameters encountered into the corresponding equations.
The velocity profiles *U* for different values of the above parameters are illustrated in Fig.1 to Fig.5, the temperature profiles for different values of the Prandtl number *Pr* parameters are described in Fig.6 and the concentration profiles for different values of the Schmidt number *Sc* are expressed in Fig.7. Also the skin-friction is sown in Fig.8 and Fig.9, the rate of heat transfer or Nusselt number are in Fig.10 and the rate of mass transfer or Sherwood number is presented in Fig.11 and Fig.12. All the velocity, temperature and concentration profiles are given against the co-ordinate variable (*Y*) and the skin-friction, the rate of heat transfer or Nusselt number and the rate of mass transfer or Sherwood number is presented against the non-dimensional time step.
The Fig.1 depicts the velocity distributions *U* for different values of magnetic parameter *M* for time step (τ) 70. In this figure it is observed that the velocity decreases with the increases of magnetic parameter. In Fig.1 the pick points of the curves for *M*=1.0, 3.0 and 5.0 are obtained for *Y*=1.80, *Y*=1.20 and *Y*=0.6 respectively and after arriving the pick point it decrease smoothly. For our interest, we calculate the decreasing rate of the velocity at the corresponding point *Y*=10.20 of the curve form *M*=1.0 to *M*=3.0 is 30.78% and from *M*=3.0 to *M*=5.0 is 6.55%. The Fig.2 demonstrates the velocity distributions for different values of Prandtl number (*Pr*). In this figure we have noticed that the velocity decreases with the increases of Prandtl number. Physically this is true because the increase in the Prandtl number due to increasing the viscosity of the fluid which makes the fluid thick and hence a decrease in the

velocity of fluid. The Fig.3 represents the velocity distributions for different values of Schmidt number (*Sc*). After analysis the figure it is noticed that the velocity decreases with the increases of Schmidt number.The velocity distributions for different values of Grashof number *Gr* are shown in the Fig.4. Through this figure it is marked that the velocity increased with the increases of Grashof number. The Fig.5 described the velocity distributions for different values of modified Grashof number *Gm*. From this figure it is observed that the velocity increases with the increases of modified Grashof number *Gm.* In the temperature profile of the Fig.6 we see that the temperature decreases with the increases of different values Prandtl number *Pr*. Through the Fig.7 it is observed that the concentration profiles are decreases with the increases of different values of Schmidt number *Sc.*

The graph of skin-friction, rate of heat transfer and rate of mass transfer are drawn against τ for different values of the well known parameters. Fig.8 explains that the skin-friction increase with the increase of Grashof number *Gr*. Fig.9 elaborates that the skin-friction increases with the increase of values of Schmidt number *Sc.* The Nusselt Number is decreasing with the increasing value of magnetic parameter which is depicted in Fig.10. Fig.11 describes that the rate of mass transfer (Sherwood Number) decrease with increase of Grashof number *Gr*. The Sherwood Number decrease with increase of Schmidt number that is described in the Fig.12

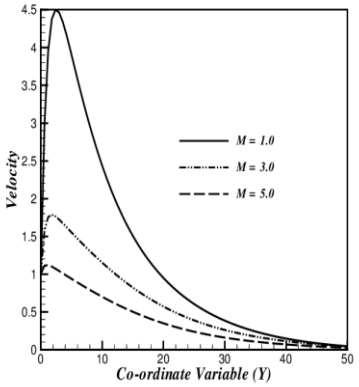

Fig.1 Variation of velocity *U* for different values of magnetic parameter *M* where τ=70, *Gr*=3.0, *Gm*=3.0, *Sc*=0.22 and *Pr*=0.71

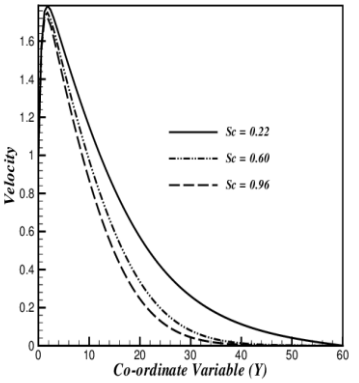

Fig. 3 Variation of velocity *U* for different values of Schmidt number *Sc* where τ=70, *Gr*= 3.0, *Gm*= 3.0, *M*=3.0 and *Pr*=0.71

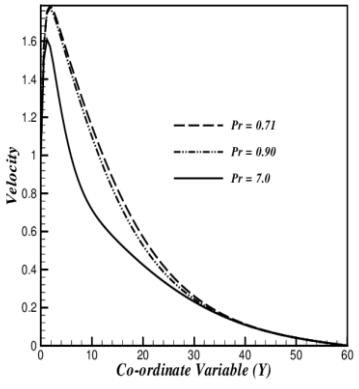

Fig. 2 Variation of velocity *U* for different values of Prandtl number *Pr* where τ=70, *Gr*= 3.0, *Gm*= 3.0, *M*=3.0 and *Sc* =0.22

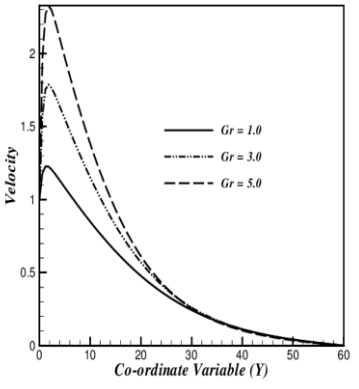

Fig. 4 Variation of velocity *U* for different values of Grashof number *Gr* where τ=70, *Gm*= 3.0, *M*=3.0, *Pr*=0.71 and *Sc*=0.22

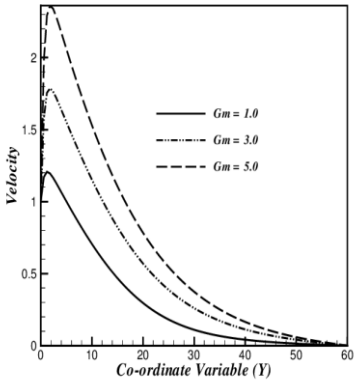

Fig. 5 Variation of velocity for different values of Modified Grashof number where τ=70, *Gr*= 3.0, *M*=3.0, *Pr*=0.71 and *Sc*=0.22

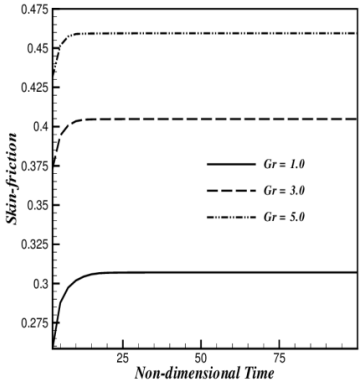

Fig. 8 Variation of Skin-friction for different values of Grashof number *Gr* where *Gm*= 3.0, *M*=3.0, *Pr*=0.71 and *Sc* =0.22

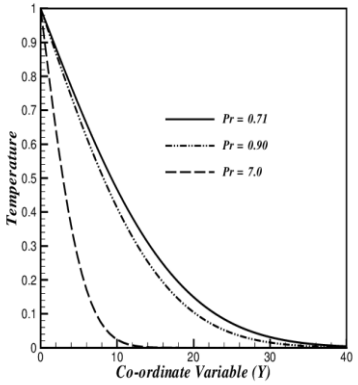

Fig. 6 Variation of temperature θ for different values of Prandtl number where τ=70, *Gr*= 3.0, *Gm*= 3.0, *M*=3.0 and *Sc* =0.22

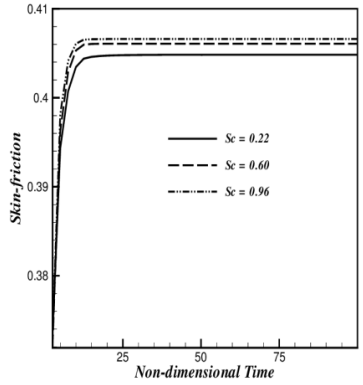

Fig. 9 Variation of Skin-friction for different values of Schmidt number *Sc* where *Gr*= 3.0, *Gm*= 3.0, *M*=3.0 and *Pr*=0.71

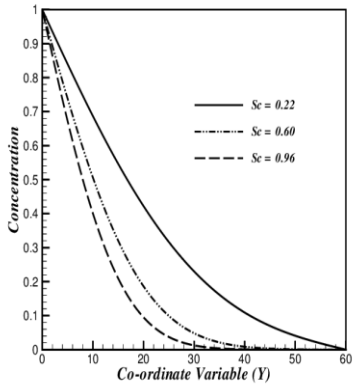

Fig. 7 Variation of concentration ϕ for different values of Schmidt number *Sc* where τ=70, *Gr*= 3.0, *Gm*= 3.0, *M*=3.0 and *Pr*=0.71

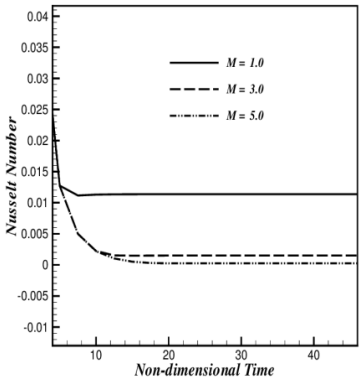

Fig. 10 Variation of rate of heat transfer (*Nu*) for different values of magnetic parameter *M* where *Gr*=3.0, *Gm*=3.0, *Sc*=0.22 and *Pr*=0.71

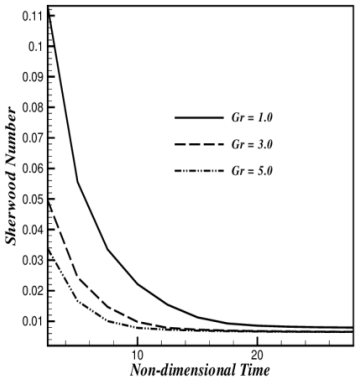

Fig. 11 Variation of rate of mass transfer (*Sh*) for different values of Grashof number *Gr* where *Gm*= 3.0, *M*=3.0, *Pr*=0.71, *Sc* =0.22 and *S*=1.0

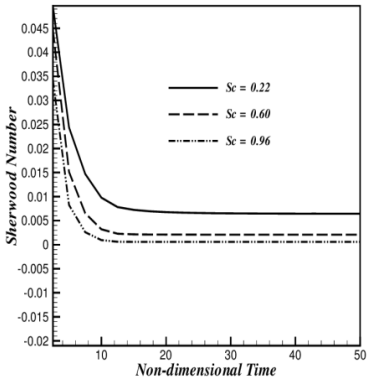

Fig. 12 Variation of rate of mass transfer (*Sh*) for different values of Schmidt number *Sc* where *Gr*= 3.0, *Gm*= 3.0, *M*=3.0 and *Pr*=0.71

References

[1] M. Faraday, *Experimental researches in electrically philosophical transaction*, Vol-15, page 175

[2] M. A. Hossain and A. C. Mandal, 'Mass transfer effects on the unsteady hydro-magnetic free convection flow past accelerated vertical porous plates.' *Journal of Physics D:Applied Physics*, Volume 18, pp. 163-9, 1985

[3] H. Poonia and R. C. Chaudhary, 'MHD free convection and mass transfer Flow over an infinite vertical porous plate with viscous dissipation.' *Theoret. Applied Mechanics*, Vol.37, No.4, pp. 263-287, Belgrade 2010

[4] M. S. Alam and M. M. Rahaman, 'MHD free Convective Heat and Mass Transfer flow Past an Inclined Surface with Heat Generation Thammasat.' *Int. J. of Science and Technology*, Volume II. No.4. October-December 2006

[5] P.R. Sharma and G. Singh, 'Unsteady MHD free convective flow and heat transfer along a vertical porous plate with variable suction and internal heat.' *Int. J. of Appl*. Math and Mech. 4(5): 1-8, 2008

[6] R. C. Chaudhary and J. Arpita, 'Combined heat and mass transfer effects on MHD free convection flow past an oscillating plate embedded in porous medium.' *Roman J. Phy.*, Volume 52, Nos. 5-7, P. 505-524, Bucharest, 2007

[7] B. P. Reddy and J. A. Rao, 'Numerical solution of thermal diffusion effect on an unsteady MHD free convective mass transfer flow past a vertical porous plate with ohmic dissipation.' *Int. J. of Applied Math and Mech.* 7(8): 78-97, 2011

[8] A. K. Singh, A. K. Singh and N.P. Singh, 'Hydro-magnetic free convection and mass transfer flow with joule heating, thermal diffusion, heat source and hall current.' *Bulletin of the institute of mathematics academia since*, Volume 33, number 3, September 2005

[9] A. K. Singh, 'Effect of Mass Transfer on MHD Free Convection Flow of a Viscous Fluid Through a Vertical Channel.' *J. Energy Heat Mass Transfer,* pp. 41-46, 22, 2000

[10] V.M Soundalgekar, 'Free convection effects on the oscillatory flow past an infinite vertical porous plate with constant suction.' *Proc. Royal. Soc. London*, 333(A), pp. 25 – 36, 1973.

[11] A Raptis, 'Flow through a porous medium in the presence of magnetic field.' *Int. J. Energy Research*, 10, pp.97 – 101, 1986.

[12] C.H Chen, 'Combined heat and mass transfer in MHD free convection from a vertical surface with Ohmic heating and viscous dissipation.' *Int. J. Eng. Sci*, 42, pp.699 – 713, 2004.

[13] C.I. Cookey, A. Ogulu and V.B. Omubo-Pepple, 'Influence of viscous dissipation and radiation on unsteady MHD free convection flow past an infinite heated vertical plate in a porous medium with time dependent suction.' *Int. J. Heat and Mass Transfer*, 46, pp. 2305 – 2311, 2003.

[14] K.A. Helmy, 'MHD unsteady free convection flow past a vertical porous plate.' ZAAM, 78, pp. 255 – 270, 1998.

[15] Y.J. Kim, 'Unsteady MHD convective heat transfer past semi-infinite vertical porous moving plate with variable suction.' *Int. J. Eng. Sci*, 38, pp. 833 – 845, 2000.

[16] M.A. Hossain and A.C. Mandal, 'Effects of mass transfer and free convection on the unsteady MHD flow past a vertical porous plate with constant suction.' *Int. J. Energy Research*, 10, pp. 409 – 416, 2007.

[17] R. C. Chaudhary, Arpita jain, 'Combined heat and mass transfer effects on MHD free convection flow past an oscillating plate embedded in porous medium.' *Rom. Journ. Phys.*, Vol. 52, Nos. 5–7, P. 505–524, Bucharest, 2007

[18] M. S. Alam and M. M. Rahman, 'Free convection and mass transfer flow past an infinite vertical porous plate with dufour and soret effects in a porous medium.' *BRACK University J.*, Volume II, No.1, pp.111-115, 2005

[19] N. P. Shingh, A. K. Shingh and A. K. Shingh, 'MHD free convection and mass transfer flow past a flat plate.' *The Arabian J. for Science and Engineering*, Volume 32, Number 1A January 2007

[20] Rehena Nasrin and M. A. Alim, 'MHD free convection flow along a vertical flat plate with thermal conductivity and viscosity depending on temperature.' *J. of Naval Architecture and Marine Engineering.* V6i2.4994, PP.72-83

6th BSME International Conference on Thermal Engineering (ICTE 2014)

Electricity Generation Based On Biomass Residue: Scope, Relevance And Applications

Imrul Reza Shishir[a], Abul Kalam Azad[b], Tanjim Ahmed[c]

[a]*Department of Mechanical Engineering, Bangladesh University of Engineering & Technology*
[b]*School of Engineering and Technology, Central Queensland University*
[c]*Department of Civil Engineering, Bangladesh University of Engineering & Technology.*

Abstract

Biomass is one of the prospective sources of renewable energy to produce electricity in different countries in the world. Bangladesh has more potential for biomass resources for electricity generation. For this reason, it can be considered as one of the prospective country for bio-energy generation. The objective of this work is to analyze the feasibility of recovering energy from the major sources of biomass residue in Bangladesh. The agricultural crop residues, industrial crop wastes and city green wastes etc. is investigated and discussed in this paper. The concept will be contributed substantially to harness solid waste management system. The review found that the technique can give a new pathway for waste management and reduce the major disposal problem of biomass residue. The productive use of the waste can supply the required energy to meet the growing energy demand in Bangladesh.
(ICTE 2014).

Keywords: Biomass; waste management; electricity generation; Bio-energy

Introduction:

Bangladesh is a country with huge demand of energy. In recent years, the demand has overtaken the present consumption of 321 KWH [1]. At present the country is capable of producing 10,416 MW (June 2014) [1]. But the production is still too poor to meet the total demand. As, Bangladesh depends mostly on fossil fuel for energy production, scarcity of fossil fuel and expensive procedures are causing difficulties in increasing production of energy. So, non-conventional and renewable energy sources are becoming popular every day. As a promising source of energy, biomass has a great potential to play in context of Bangladesh. It can become the real weapon to fight against energy crisis in developing country like Bangladesh.

* Corresponding author. Tel.: +8801723104361
E-mail address: imrul.reza.shishir@gmail.com

Bangladesh Energy Scenario:

Bangladesh is basically a gas dependent country in energy production sector. A recent study shows the distribution of resource in energy production as below;

Table 1: Resource Distribution [2]

Source	Percentage of Usage (%)
Gas	81%
HSD	8%
Coal	3%
HFO	3%
Hydro	3%
Fossil oil	2%

This shows a huge dependency on fossil fuel with a least chance of sustainability. Fossil fuels are limited and their conversion into energy is expensive. So, for country like Bangladesh, Biomass may be a perfect solution for energy crisis.

Main Biomass Resources in Bangladesh:

Being an agricultural country, Bangladesh has a huge opportunity in using Biomass as a source of energy. The main resources from plantation residues are abundantly wasted in Bangladesh. These residues can produce a huge amount of energy in a cost effective process. Main resources can be rice straws. Sugarcane bagasse and other agricultural residues can be productive in terms of converting into energy. In last 35 years, dependency on biomass fuels has increased. In 1980, 236.08 PJ energy was produced from biomass which increased by 1.73% in next 20 years reaching 356.66 PJ [3]. The distribution of traditional biomass usage in recent years can be shown as;

Table 2: Distribution of Biomasses in accordance to usage [3]

Source	Percentage of Usage (%)
Cow dung	20.4
Jute stick	7.5
Rice straw	11.6
Rice husk	23.3
Bagasse	3.2
Fire wood	10.4
Twig and leaves	12.5
Other wastes	11.1

Rice husk has shown a great potential by serving 76.35PJ energy in 1991 which increased to 106.1 in 2004 [3]. As South and Southeast Asia produces 90% of the total rice produced on earth [4], rice husk will remain first choice as a biomass for converting into energy in this region.

Technology:

Major technologies involved in conversion of biomass into energy can be specified as,

Gasification: Gasification can be defined as a process of converting carbonaceous materials into carbon monoxide, hydrogen and carbon dioxide. It is done by reacting biomass or fossil fuel at a high temperature (>700^{o}C). Combustion is not occurred here and a controlled amount of oxygen sometimes with stream produces syngas or producer gas as a fuel [5][6]

A flow chart can represent gasification as;

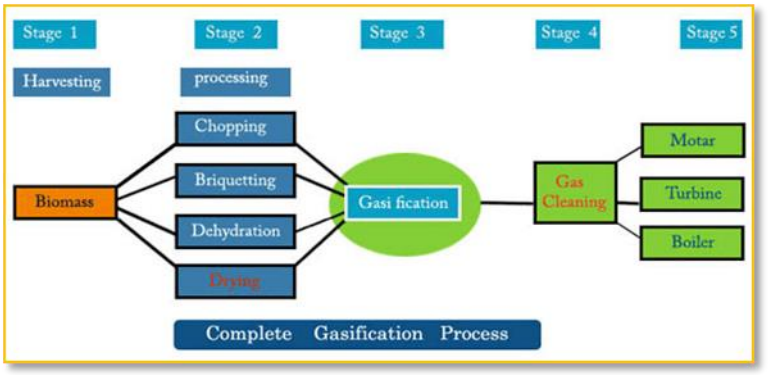

Figure 1: Gasification Procedure

Combustion: Combustion means the burning of fuel which is a chain of exothermic chemical reactions involving a fuel and an oxidant producing heat and glowing flame. Common formula can be stated as,

Fuel + Oxidizer → Combustion products + Heat energy

Oxygen must be present in case of combustion. In Bangladesh, most of the biomass in rural are go through combustion process to produce energy but in a very inefficient way [7].

The process progresses as follows;

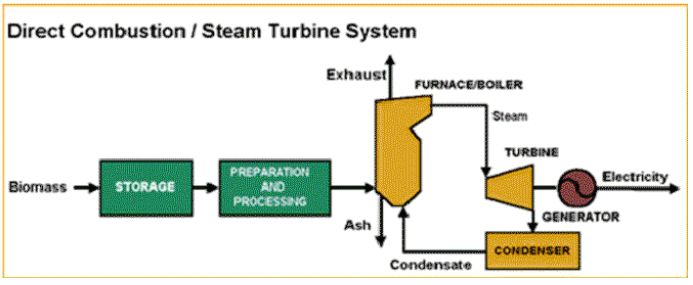

Figure 2: Combustion Procedure

Pyrolysis: Pyrolysis involves chemical decomposition and physical change of state at an elevated temperature in absence of oxygen or halogen. This process is endothermic [8], irreversible and a type of thermolysis. This process helps to turn biomass into syngas and biochar [9]. It also decomposes complex oils into lighter compositions.

The process can be operated as the flow diagram below;

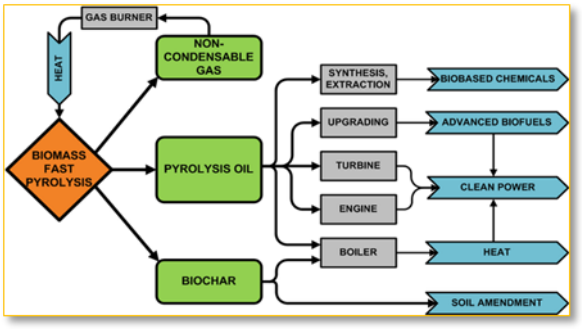

Figure 3: Pyrolysis Procedure

Economic and environmental analysis and energy efficiency of electricity generation from biomass resources:

Biomass is always cost effective in terms of energy conversion. Most importantly, resources, most of the times, are wastes. So, using biomass for energy conversion does not need any extra attention for resources. These resources also emit less carbon and sulphates in comparison to fossil fuel. As, such, these are environment friendly sustainable source of energy. [10][11]

In some cases, bio fuel crops compete with food crops. But, biomasses are part of food corps. So, competition will never arise here. Biomass also absorbs carbon during its growth. So, carbon emission during energy conversion can be sum up as zero. [10]

Result of a study is shown below figuring a comparison between different source of energies in terms of cost and carbon emission. This can also show the eligibility of biomass to be a sustainable energy source. [11]

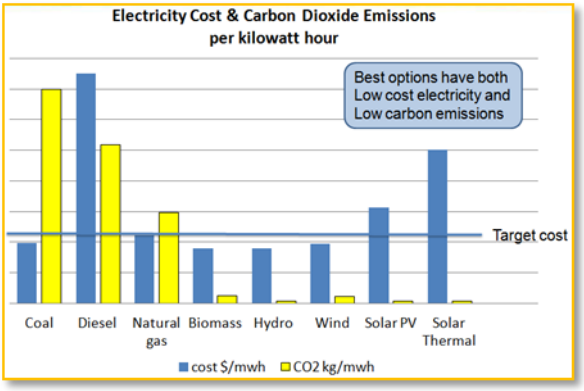

Figure 4: Comparison of efficient energy sources

Challenges for biomass based power generation:

There are few challenges in using biomass as a mainstream resource of energy as; this technology is still a developing one. Especially in Bangladesh, finance in this sector is very poor. Also, the supply chain is a big issue for getting residues at proper time. There is no straight government policy in this sector to motivate private investment either. Technical support is also rare in Bangladesh. So, organizations willing to take such projects as being demoralized by the reluctance and lack of knowledge of proper authority and common mass. As a result, putting on a power plant on commercial basis is quite a challenge here. [12][113][14]

Case study of biomass based power plant:

In Bangladesh, two power plants under finance of Infrastructure Development Company Limited (IDCOL) are in production. One of them is at Kapashia, Gazipur, another at Chilarong, Thakurgaon. Their specifications are shown below;

Table 3: Salient Features of Two Biomass Based Power Plants

Feature	Kapashia	Chilarong
Capacity	250MW	400MW
Project cost	BDT 25 million	BDT 64.25 million
Authority	Dreams Power Private Limited (DPPL)	Sustainable Energy & Agro-resource Limited (SEAL)
Major Fuel	Rice Husk	Rice Husk
Conversion Method	Gasification	Gasification
Beneficiaries	Sorrounding 300 households	A silica factory, irrigation pumps and numerous rice mills

Figure 5: Biomass based power plant at Kapashia, Gazipur, Bangladesh

Conclusion:

As, fossil fuel is turning out to be a non-sustainable energy solution, present world needs a sustainable, cost effective and environment friendly energy solution. In this context, Biomass can play a vital role in solving energy problem all through the globe. Biomass, also being waste itself, biomass based power plant can also be a good solution for waste management. So, for a better and greener earth encouragement with logical and financial support should be provided to biomass based power plants. With less carbon emission and greater efficiency, no doubt, biomass is going to be one of the best choices for energy production in future world.

References:

[1] Official website of power division of Bangladesh, http://www.powerdivision.gov.bd/user/brec1/30/1

[2] A study of green infra bangla, http://greeninfrabangla.com/593/

[3] M. Ahiduzzaman. “Rice Husk Energy Technologies in Bangladesh” Agricultural Engineering International: the CIGR Ejournal. Invited Overview No. 1. Vol. IX. January, 2007.

[4] T.B. Reed, Biomass Gasification Principles and Technology, Noyes Data, Park Ridge, NJ, 1981

[5] Clean Renewable Fuel from the Plasma Gasification of Waste, www.waste-management-world.com

[6] S. K. Patra and P.P. Datta, Technical Digest, Insights into Biomass Gasification Technology

[7] M. Rofiqul Islam, M. Rabiul Islam and M. Rafiqul Alam Beg, "Renewable energy resources and technologies practice in Bangladesh", Renewable and Sustainable Energy Reviews (2006), doi:10.1016/j.rser. 2006.07.003

[8] He, Fang; Weiming Yi; Xueyuan Bai (September 2006). "Investigation on caloric requirement of biomass pyrolysis using TG–DSC analyzer". Energy Conversion and Management 47 (15–16): 2461–2469. doi:10.1016/j.enconman.2005.11.011

[9] Lehmann, Johannes. "Biochar: the new frontier". Archived from the original on 2008-06-18. Retrieved 2008-07-10

[10] Biomass energy and its benefits, The public utilities commission of Ohio, http://www.puco.ohio.gov/puco/index.cfm/industry-information/industry-topics/biomass-energy-and-its-benefits/

[11] Biomass vs. Other Alternative Energy: High Reliability, Low Cost, http://www.viaspace.com/biomass_versus_alternatives.php

[12] Renewable Energy World, Wednesday, August 6, 2014; http://www.renewableenergyworld.com/rea/news/article/2010/02/biomass-an-emerging-fuel-for-power-generation

[13] Potentiality of Biomass Energy for Electricity Generation in Bangladesh, M. S. Islam & T. Mondal, Department of Electrical & Electronic Engineering, Rajshahi University of Engineering and Technology, Rajshahi, Bangladesh

[14] Mafakheri, F.; Nasiri, F. (2014). "Modeling of biomass-to-energy supply chain operations: Applications, challenges and research directions". Energy Policy 67: 116. doi:10.1016/j.enpol.2013.11.071

6th BSME International Conference on Thermal Engineering (ICTE 2014)

Investigation of Stress State near The Crack Tip of Central Cracks of Copper by Numerical Analysis

Md. Mahiuddin[a], Md. Arefin Kowser[a*]

[a]*Assistant Professor, Dhaka University of Engineering & Technology, Gazipur – 1700, Bangladesh*
[a*]*Associate Professor, Dhaka University of Engineering & Technology, Gazipur – 1700, Bangladesh*

Abstract

This paper based on fracture problem which is solved by Computer-aided engineering (CAE) system. Main objective of the numerical simulation is to investigate the stress fields near the crack tip of copper material through determination of stress intensity factors for different crack lengths. The existence of cracks and defects inside the material of the structural members is necessary to calculate, since they can lead to an undesired formation of macroscopic cracks. The danger of macroscopic cracks in terms of the brittle fracture is the possibility of their instability. Thus may occur a sudden and uncontrollable particle separation of the material through a fracture with the speed nearly propagation of the elastic waves in the material without need to supply an energy to the process from the outside. The geometrical model is thick plate (plane strain condition) with symmetric central crack. To compare the results obtained by numerical method have been calculated by analytical approach also. The results were made the same calculations for the plane stress conditions of this problem to compare with that of the plane strain condition. This condition simulates same problem but the plate in this case is taken as thin. Results pattern of the stress intensity factors were identical as results obtained for plane strain conditions. But the critical value of stress intensity factor is for the plane stress conditions greater than the value of plain strain condition. If critical value of the stress intensity factor is known for the used material and the calculated stress intensity factors then can be said whether the crack will be grow or not. This approach can lead to design very quality, safety and reliable products for end users. From the obtained results, it can be observed that the numerical results give very close data with the analytical results. Thus the numerical approach can be used for the solving of a global crack problem with very high accuracy of results. The deviation of numerical results with the analytical results is obtained within the range of ±3.78%.

Keywords: ANSYS; CAE; crack; stress intensity factor; fracture mechanics.

Nomenclature

K	stress intensity factor
a	half crack length
K_{IC}	fracture toughness
σ	applied stress
T_σ	stress tensor
t	crack thickness
ρ	crack tip radius
r, φ	coordinates

* Corresponding author. Tel.: +88-920-4710; fax: +88-02-920-4710.
E-mail address: nadimduet@yahoo.com

b	width of plate
c	height of plate
$f_{ij}(\varphi)$	function depends on crack opening mode
$f_k(a,b)$	function depends on boundary conditions

Introduction

The numerical methods are used as a leading computational utility for many years. The finite element method (FEM) has today become one of the main computing resources in the engineering field. The main advantage of FEM is graphic interpretation often very abstract phenomena in which classical method of solutions introduces considerable simplification at the expense of accuracy.

The mankind has begun to deal with causes of a components fracture in the second half of the 19th century. However to date comprehensive theory explaining the brittle failure still not exist in its complexities and all contexts. With the existence of cracks and defects in the material of the structural members is necessary to calculate, since they can lead to an undesired formation of macroscopic cracks. The danger of macroscopic cracks in terms of the brittle fracture is the possibility of their instability. Thus may occur a sudden and uncontrollable particle separation of the material through a fracture with the speed nearly propagation of the elastic waves in the material without need to supply an energy to the process from the outside [1,3,11].

Theory

A crack is the most important case of a failure of the body stability in terms of strength. A surface violation of stability with the zero thickness and thus with the zero radius of the curvature on the crack tip is the most preferable calculation model of a crack. Fig.1. shows this case. The crack tip is in this case the singular point in which are obtained infinite mechanical stresses. Therefore the state of stress near the crack tip is very inhomogeneous. Thus the plastic deformation in the crack tip will be occurred also at very small loading [1,4,5].

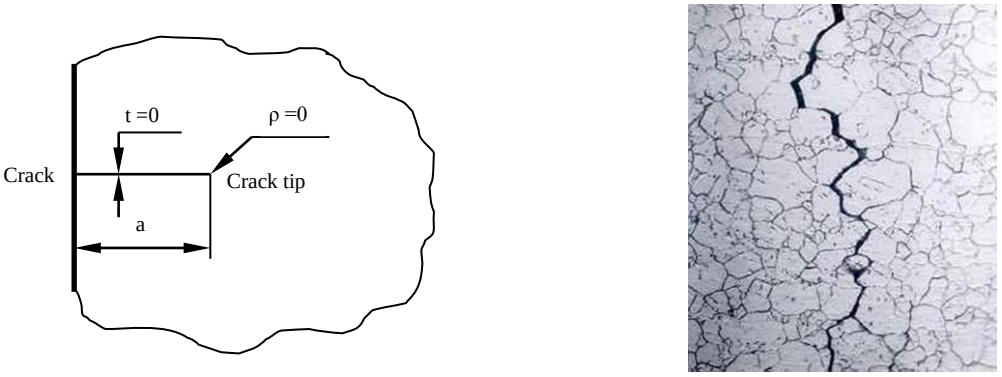

Fig.1. Ideal computational model of a crack and the real crack in the material

For a classification of a stress state around a crack is considered an infinite plate with a central crack (Fig.2.). In the point P of the object which has coordinates with regard to the crack tip is the stress state given to the stress tensor T_σ .

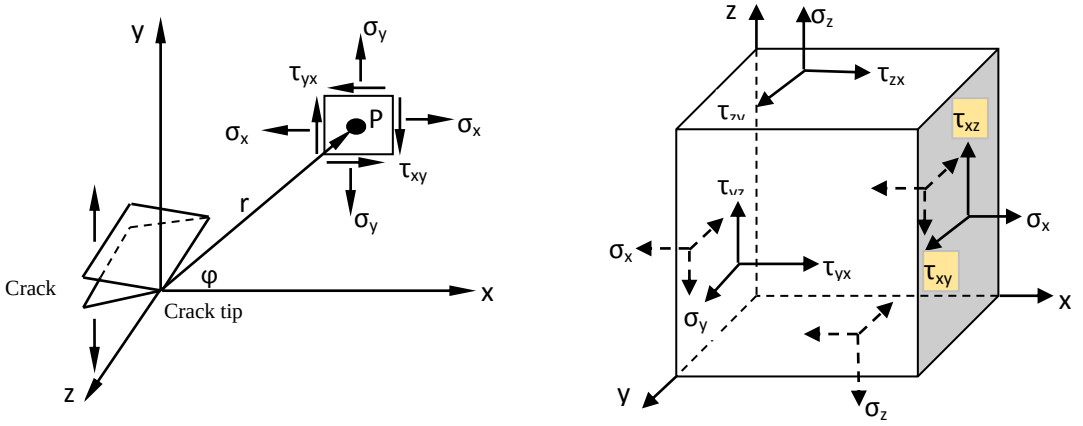

Fig.2. Infinite plate with a central crack and the Cauchy stress tensor

The individual components of the stress tensor can be expressed by the formula

$$\sigma_{ij} = \frac{K}{\sqrt{2\pi r}} f_{ij}(\varphi) \tag{1}$$

Where $f_{ij}(\varphi)$ is function which depends only on a type of a crack opening mode. The parameter K depends on the geometry of the crack, geometry of the part itself and from the nominal stress in the sufficient distance from the crack tip. Irwin named this parameter as a stress intensity factor. For the objects of finite dimensions with variously situated cracks loaded with different modes can be expressed this coefficient in the form

$$K = \sigma\sqrt{\pi a}\, f_k(a,b) \tag{2}$$

Where b is the dimension of the part in the crack seam direction and the function $f_k(a,b)$ depends on the boundary conditions of given configuration of the object with a crack.

There are three types of crack opening, termed modes I, II, and III which are shown in Fig.3. Mode I is a normal opening mode while modes II and III are shear sliding modes [1,3,6].

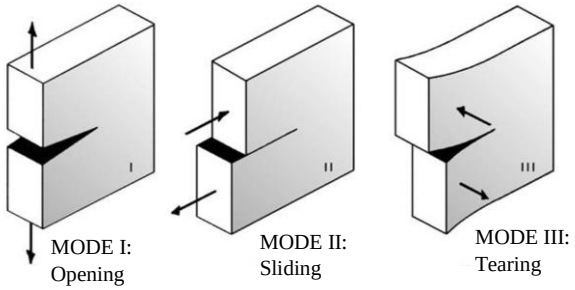

Fig.3. Three modes of the crack deformation

If stress intensity factors K_I, K_{II}, K_{III} are known for all these modes, the stress state near the tip of the crack for linear elastic material is described by the equation (the principle of superposition).

$$\sigma_{ij} = \frac{1}{\sqrt{2\pi r}} \sum_{n=I}^{III} K_n \; f_{ij,n}(\varphi) \tag{3}$$

The stress intensity near a crack tip characterizes the stress intensity factor by the theory K-conception. If critical value of the stress intensity factor is known for the used material and the calculated stress intensity factors then can be said whether the crack will be grow or not. The critical stress intensity factor for mode I obtained by experimental test of the material K_{IC} is called as the plane strain fracture toughness [1,7,8].

Problem definition

A thick plate with the dimensions $(2b \times 2c)$ made from the copper is loading with different pressures on its ends. The plate contains a central crack which is symmetric. The crack length a can be different which is shown in Table.1.

Table 1. Problem definition and applied load.

Assumption	Plate Dimension	Crack Length (m)	Applied Load (MPa)
Plane Strain	0.2m×1m	a ϵ {0.01; 0.09}	σ ϵ {100, 130, 180}
Plane Stress	0.2m×1m	a ϵ {0.01; 0.09}	σ ϵ {100, 130, 180}

It is needed to determine a state of safety for this type of the crack which can be created on this plate as we can see in Fig.4. In linear elastic problems, the stress intensity factor is the very important parameter of fracture mechanics from which a singular stress and strain around the crack tip can be obtained [2,9,10].

Thus for determining a state of operation safety of the plate have to be known the stress intensity factor at crack tip. Then the calculated stress intensity factor can be compared with the material parameter K_{IC}. For the copper the fracture toughness is $K_{IC} = 105\,\mathrm{MPa}.\mathrm{m}^{1/2}$ [12]. If the calculated stress intensity factor is smaller as the fracture toughness of used material then the crack will not be grown (stable state). This loading state will be therefore safe for plate with that crack. The numerical approach will be used for the investigating of stress intensity factors values.

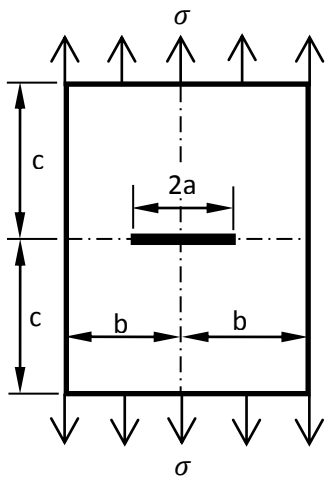

Fig.4. Plate with central crack together with defined parameters

Analytical calculation

The analytical method of fracture mechanics is conservative approach to solution of cracks in the material. Stress intensity factors can be calculated analytically for a central crack by equation

$$K_I = \sigma\sqrt{\pi a}\left(\frac{1-0.5q+0.37q^2-0.044q^3}{\sqrt{(1-q)}}\right),\ K_{II} = K_{III} = 0 \tag{4}$$

Where parameter $q = a/b$ and the condition $c/b \geq 3$ have to be satisfied for obtaining precise results. The calculated results through the analytical approach will serve only for the investigation whether the results obtained by the numeric method will be calculated enough exactly [1].

Numerical approach

The numerical calculations was realized with CAE software ANSYS. The goal of the numerical simulation is to calculate the stress intensity factors. The geometry of the problem is shown in Fig. 4. The geometry represents a thick cracked plate. The plate is made from the copper which has Young's modulus $E = 130\,\text{GPa}$ and Poisson's ratio $\upsilon = 0.34$. The task was idealized into the simple symmetrical 2D model as illustrated in Fig.5.

The crack seam in 2D idealized model is localized bottom left. The top left edge of the model is not being able to move in the X direction and bottom edge in the Y direction. Other degrees of freedom for other nodes were defined default as free. The part was loaded by the pressures $100\,\text{MPa}, 130\,\text{MPa}$, and $180\,\text{MPa}$ on the right edge of the model in the negative orientation respectively.

In the study of fracture mechanics interest is often focused on the singularity point where quantities such as stress become (theoretically, but not practically) infinite. Near such singularities normal, polynomial-based finite element approximations perform badly.

To determine the singularity in strain, the crack faces should be coincident, and the elements around the crack tip should be quadratic, with the middle side nodes placed at the quarter points. Such elements are called singular elements and should be used around the singularity point (crack tips) [2]. Fig.6. shows 2D singular elements PLANE183 (plane strain) placed around the crack tip (node 2).

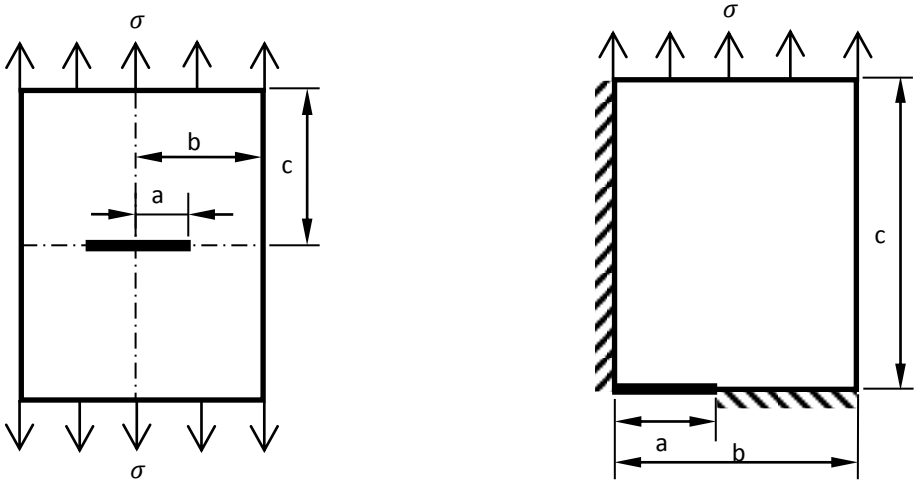

Fig.5. 2D idealization of the geometrical model along symmetry planes with schematic boundary conditions and the loading

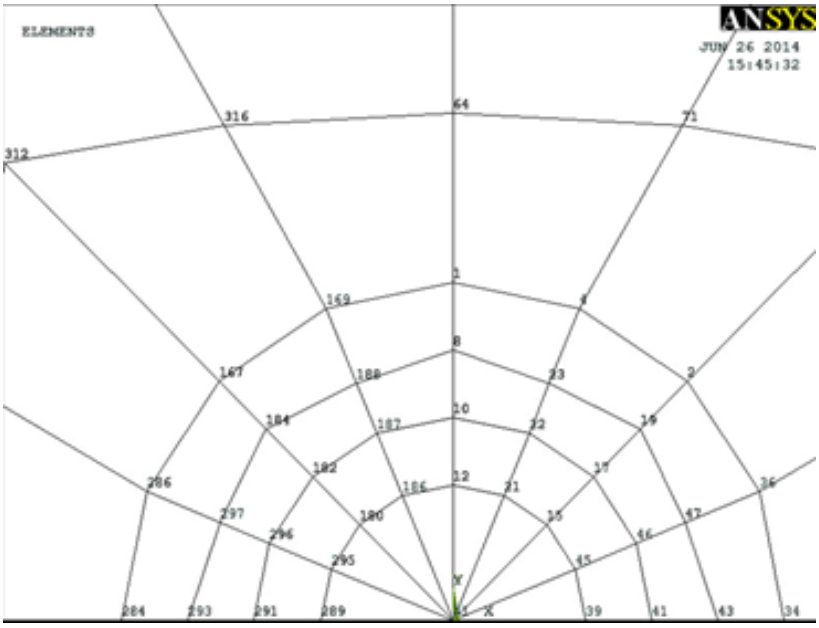

Fig.6. Mesh around the crack tip with 2D singular elements PLANE183

Obtained results and discussion

Fig.7. is illustrated the output format of the results of the stress intensity factors for given crack seam obtained by numerical approach (ANSYS). Here is described that solved problem was defined as the plane strain condition, simplified by the symmetry boundary condition, made from the material with described material properties and assigned node of the crack tip. The last row of this output shows the stress intensity factors for all three modes of the crack deformation. This type of the loading generates only first mode (opening) thus the stress intensity factors K_{II} and K_{III} had zero value.

**** CALCULATE MIXED-MODE STRESS INTENSITY FACTORS ****

ASSUME PLANE STRAIN CONDITIONS

ASSUME A HALF-CRACK MODEL WITH SYMMETRY BOUNDARY CONDITIONS (USE 3 NODES)

EXTRAPOLATION PATH IS DEFINED BY NODES: 2 11 10
WITH NODE 2 AS THE CRACK-TIP NODE

USE MATERIAL PROPERTIES FOR MATERIAL NUMBER 1
EX = 0.13000E+06 NUXY = 0.34000 AT TEMP = 0.0000

**** KI = 17.733 , KII = 0.0000 , KIII = 0.0000 ****

Fig.7. Sample output of stress intensity factors obtained from ANSYS

Fig.8., Fig.9., Fig.10. and Fig.11. shows the curve of the stress intensity factor K_I which was obtained by the numerical analysis of the solved problem in the range of the crack length from 0.01 m to 0.09 m.

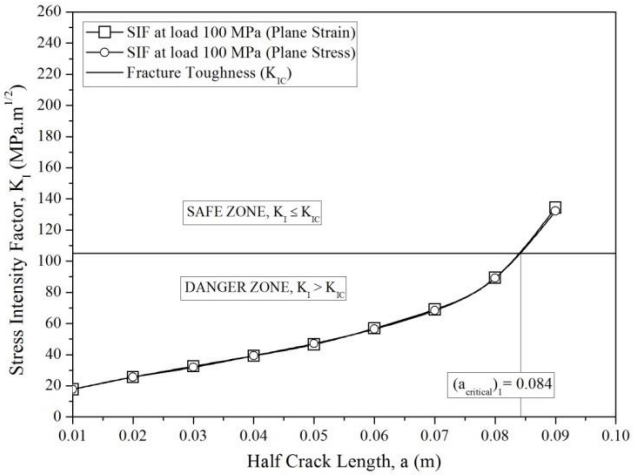

Fig.8. Stress intensity factor versus half crack length of Copper at load 100 MPa

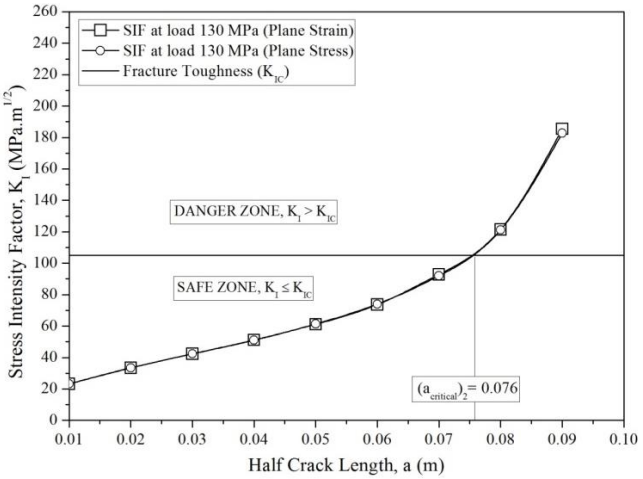

Fig.9. Stress intensity factor versus half crack length of Copper at load 130 MPa

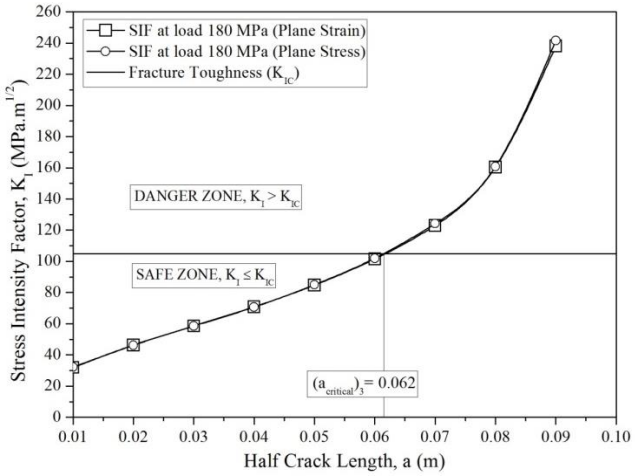

Fig.10. Stress intensity factor versus half crack length of Copper at load 180 MPa

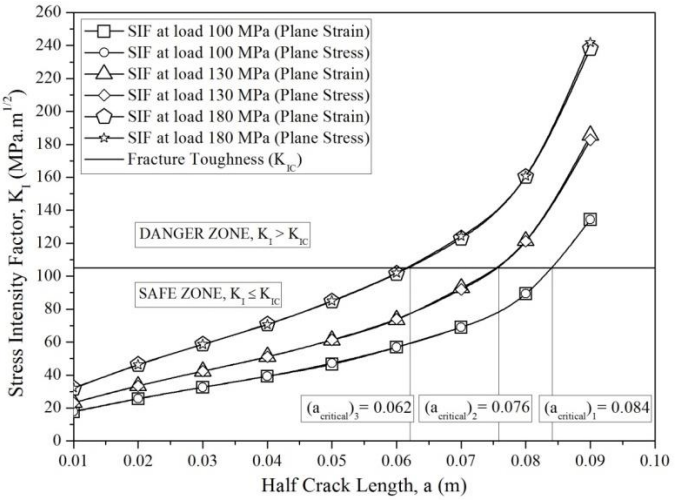

Fig.11. Combined curve of Stress intensity factor versus half crack length of Copper

The material properties called as the plane strain fracture toughness divides the graph on a safe zone and a danger zone. All values of the stress intensity factors, which are above the value of material toughness, are in the danger zone because the crack will be grown if it is exceeded this value of the material properties at the plane strain conditions. The values below are in the safe zone which represents a region where is the crack in stabile state thus the crack will not be grown. The fracture toughness K_{IC} is determined in terms of the plane strain conditions (thick parts) at the crack tip thus the results obtained from the numerical analysis for the plain strain conditions can be compared directly with the fracture toughness of the material.

For the plane strain conditions has been obtained minimal value of the stress intensity factor of copper is 17.73 MPa.m$^{1/2}$, 23.27 MPa.m$^{1/2}$ and 31.92 MPa.m$^{1/2}$ when the length of the crack had the value 10 mm and the maximum value 134.39 MPa.m$^{1/2}$, 185.47 MPa.m$^{1/2}$ and 238.13 MPa.m$^{1/2}$ was calculated when the length of the crack had the value 90 mm. The value of the half crack length a = 84 mm, 76 mm and 62 mm is critical from the safety point of view at load range 100 MPa, 130 MPa and 180 MPa respectively.

Table 2. Stress intensity factors obtained by numerical approach for Copper.

Half Crack Length, a m	Numerical value of SIF MPa.m$^{1/2}$					
	100 MPa		130 MPa		180 MPa	
	Plane Strain	Plane Stress	Plane Strain	Plane Stress	Plane Strain	Plane Stress
0.01	17.73	17.90	23.27	23.27	31.92	32.22
0.02	25.61	25.67	33.47	33.37	46.34	46.20
0.03	32.56	32.56	42.33	42.33	58.62	58.61
0.04	39.27	39.27	51.17	51.05	70.86	70.68
0.05	46.60	47.22	61.21	61.38	84.75	84.99
0.06	56.89	56.89	73.65	73.96	101.58	101.97
0.07	69.01	69.01	92.88	91.98	122.97	124.21
0.08	89.36	89.34	121.48	121.19	160.41	160.80
0.09	134.39	134.36	185.47	182.79	238.13	241.60

Fig.12. Shows the contour plot for the applied load 130MPa and the crack length 0.02m.

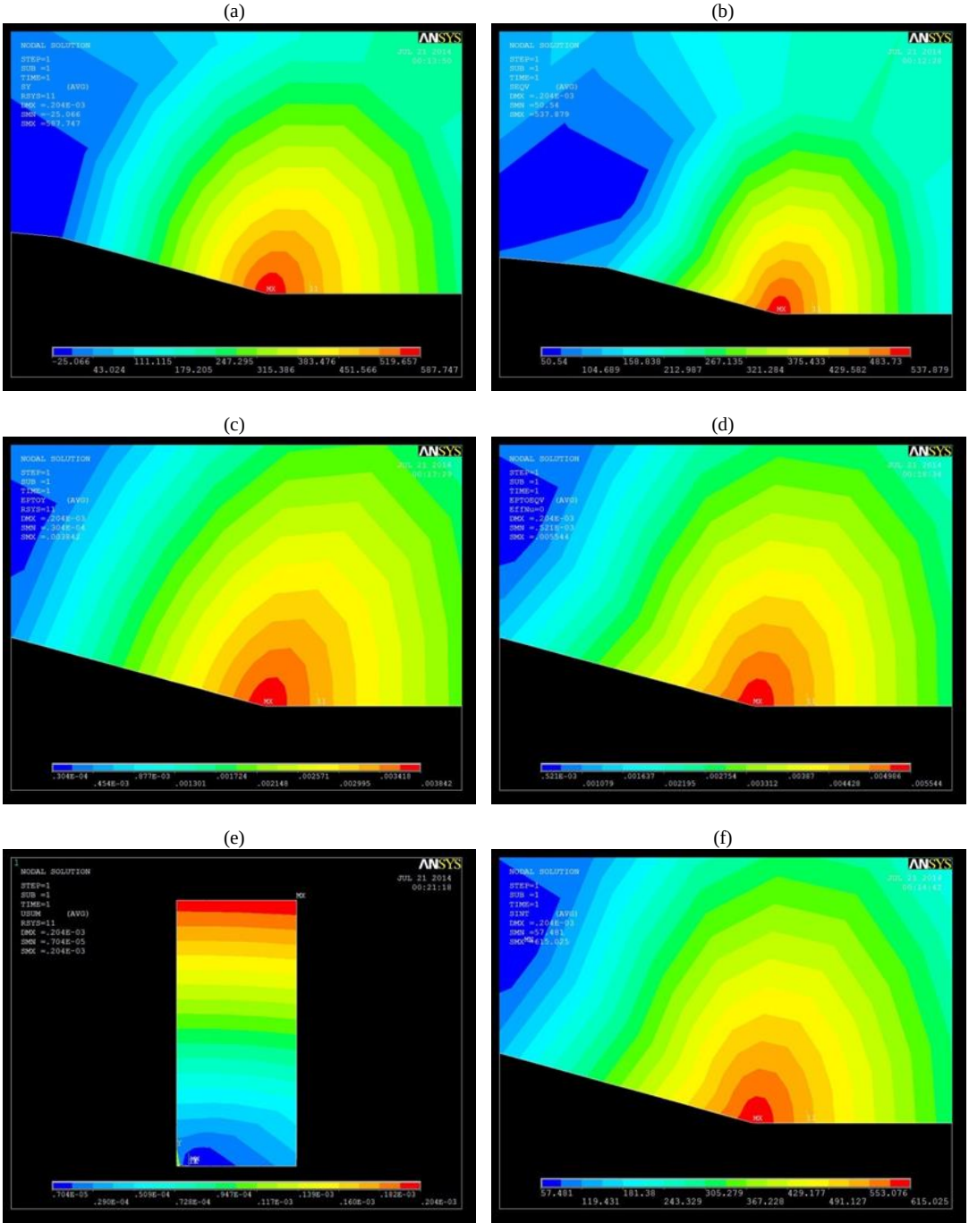

Fig.12. Contour plot of (a) Y Component of stress, (b) Von mises stress, (c) Y component of total mechanical strain, (d) Von mises total mechanical strain, (e) Displacement vector sum and (f) Stress intensity factor

As the copper material is considered isotropic, the Fig.13. shows that the stress intensity factor in wide range of crack length is linear over the applied load.

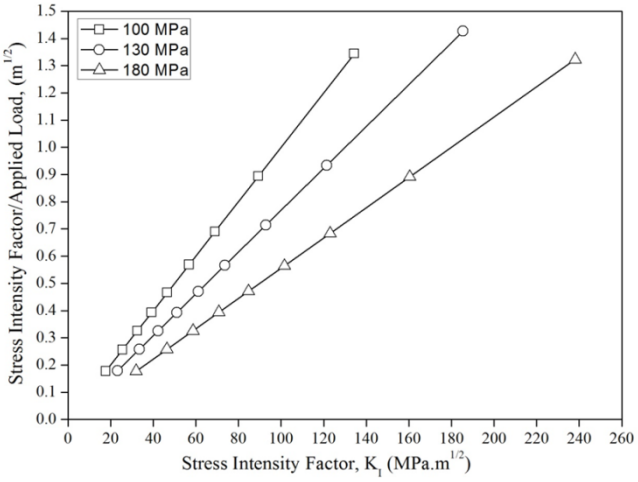

Fig.13. Linearity of stress intensity factor against SIF/applied load for Copper

Conclusion

When machine parts are dimensioned, the design engineer should always keep in the mind that materials can contain cracks which are very large concentrators of mechanical stresses. The cracks can cause the state of disrepair even though the components will be designed very well in terms of the carrying capacity. Thus the components can be destroyed by brittle fracture even before some signs of plastic deformation will be able to visible. By the analytical method of the calculation of cracks parameters may be solved very exactly but only for simple models with simple crack seams. Therefore main advantage of the numerical approach to the calculation of the stress intensity factors in the crack tip is that a shape and position of cracks in a model are not limited. Thus in other words, solving of complicated cracks in a complex shaped model through the analytical approach is almost impossible or very inefficient in the terms of the time. From the obtained results can be seen that the numerical results give very exactly data if their compare with the analytically obtained results. Thus the numerical approach can be used for the solving of a global crack problem with very well accuracy of results. The numerical results had the deviate from the analytics results in the range only ±3.78%. To ensure this very good accuracy should be defined around the crack tip the singular elements otherwise obtained results will be incorrect. From the analysis it is seen that the stress intensity factor in wide range of crack length for the isotropic material is linear with the applied load. By solving the defined problem with the thick plate was determined the critical value of crack length. If the value of the crack length a=84mm or greater (at load 100MPa), a=76mm or greater (at load 130MPa) and a=62mm or greater (at load 180MPa) will be achieved then part will be broken by brittle fracture because the critical value of the stress intensity factor of the material toughness for the plane strain conditions K_{IC} on the crack tip which will not be able to carry the loading without damage. This approach can lead to design very quality, safety and reliable products for end users.

References

[1] F. Trebuna, F. Simcak, Elasticity, strength and plasticity in engineering, printed by Emilena Kosice, 2005, ISBN 80-8073-276-0.

[2] J. Ju, Calculation and Comparison of Fracture Parameter of 3-D Thin-walled Structure in ANSYS, National University of Ireland, 2004.

[3] M. D. Olson, M. R. Hill, Determination of residual stress intensity factor in the compact tension coupon, in: Engineering Fracture Mechanics, Volume 88, July 2012, Pages 28-34.

[4] Z. Zhou, X. Xu, A. Y.T. Leung, Y. Huang, Stress intensity factors and T-stress for an edge interface crack by symplectic expansion, in: Engineering Fracture Mechanics, Volume 102, April 2013, Pages 334-347.

[5] T. Fett, H. A. Bahr, Mode I stress intensity factors and weight functions for short plates under different boundary conditions, in: Engineering Fracture Mechanics, Volume 62, Issue 6, April 1999, Pages 593-606.
[6] X. Yan, Stress intensity factors for cracks emanating from a triangular or square hole in an infinite plate by boundary elements, in: Engineering Failure Analysis, Volume 12, Issue 3, June 2005, Pages 362-375.
[7] C. E. Freese, F. I. Baratt, Single edge-crack stress intensity factor solutions, in: Engineering Fracture Mechanics, Volume 73, Issue 5, March 2006, Pages 616-625.
[8] Y. Zhang, N. A. Noda, K. T. Takaishi, X. Lan, Stress intensity factors of a central interface crack in a bonded finite plate and periodic interface cracks under arbitrary material combinations, in: Engineering Fracture Mechanics, Volume 78, Issue 6, 2011, Pages 1218-1232.
[9] A. O. Ayhan, Three-dimensional mixed-mode stress intensity factors for cracks in functionally graded materials using enriched finite elements, in: International Journal of Solids and Structures, Volume 46, Issues 3-4, February 2009, Pages 796-810.
[10] Ch. Hwu,T. L. Kuo, A unified definition for stress intensity factors of interface corners and cracks, in: International Journal of Solids and Structures, Volume 44, Issues 18-19, September 2007, Pages 6340-6359.
[11] M. Kadlec, P.Hausild, J. Siegl, A. Materna, J. Bystriansky, Thermal fatigue crack growth in stainless steel, in: International Journal of Pressure Vessels and Piping, Volume 98, October 2012, Pages 89-94.
[12] Michael F. Ashby, Materials selection in mechanical design, third ed., Elsevier publishing, Page 59.

6th BSME International Conference on Thermal Engineering (ICTE 2014)

Finite Difference Solution of Chemically Reacting Unsteady MHD Boundary Layer Flow having Soret and Dufour Effect

Bibhuti Roy, Ariful Islam*1

**Mathematics Discipline, Science, Engineering and Technology School, Khulna University, Khulna-9208, Bangladesh*

Abstract

An electrically conducting, viscous, incompressible boundary layer flow of a continuously moving vertical plate in a chemically reactive medium has been investigated in the presence of transverse magnetic field, chemical reaction, thermal radiation and Dufour and Soret effect with suction. The governing equations have been non-dimensionalzed by using usual transformations and obtained coupled non-linear partial differential equations have been solved by explicit finite difference technique. The effcts of various parameters on the flow and heat transfer is analyzed and discussed through graph in detail. The values of local Skin friction, average Skin friction, local Nusselt number, average Nusselt number and the Sherwood number for different parameters are also elucidated in the form of graph.

Keywords: MHD Flow; Thermal Radiation; Soret and Dufour effect; Chemical Reaction; Explicit Finite Difference Method; Explicit finite difference technique.

1. Introduction

The study of MHD flow field near a boundary layer with the effect of chemical reaction and thermal radiation has been achieved a myriad of emphasize by the scientists and researchers during the last few decades because of its considerable application in chemical and hydrometallurgical industrial industries. Processes such as nuclear reactor safety and combustion systems, solar collectors, extrusion of plastic and rubber sheets, polymer processing, packed-bed catalytic reactor's efficacy demand more and more scientific research on the study of heat and mass transfer

* Corresponding author. Tel.: +8801921649393;
*E-mail address:*plato.roy@gmail.com

with chemical reaction . The first research regarding the boundary-layer behaviour in moving surfaces was undertaken by Sakaidis[1]. Makinde[2] investigated free convection flow with thermal radiation and mass transfer past a moving vertical porus plate. The effect of chemical reaction of an unsteady flow past a vertical plate with constant heat and mass transfer was observed by Das et al[3].the problem of magneto-hydrodynamics natural convection about a vertical impermeable flat plate can be found in Sparrow and Cess[4]. Olanrewaju[5] examined Dufour and Soret Effects of a Transient Free Convective Flow with Radiative Heat Transfer Past a Flat Plate Moving through a Binary Mixture.

Motivated by all these studies, we have had our research on the result of chemical reaction, thermal radiation on unsteady MHD boundary layer flow with soret and dufour effect. To solve the problem numerically, governing partial differential equation has been transformed into non-similar coupled partial differential equation by usual transformation. These equations has been solved numerically by FORTRAN-95 and effects of parameters such as dufour number, soret number, radiation parameter and chemical reaction parameter on velocity, temperature and concentration profile along with local sheer stress, nusselt number and sherwood number have been illustrated by graphs.

2. Mathematical formulation

An unsteady, Two dimensional, laminar MHD boundary layer flow of an incompressible, viscous, radiating Boussinesq fluid near impermeable vertical plate stretching with velocity U, temperature distribution T_w and concentration distribution C_w is considered, in the presence of thermal diffusion (Soret) and diffusion-thermo (Dufour) effects. The positive X coordinate is measured along the plate in the direction of fluid motion and the positive Y coordinate is measured normal to the plate. A uniform magnetic fluid is applied in the direction perpendicular to be stretching surface. The transverse applied magnetic field and magnetic Reynolds number are assumed to be very small, so that the induced magnetic field is negligible. The schematic diagram of the problem is shown below.

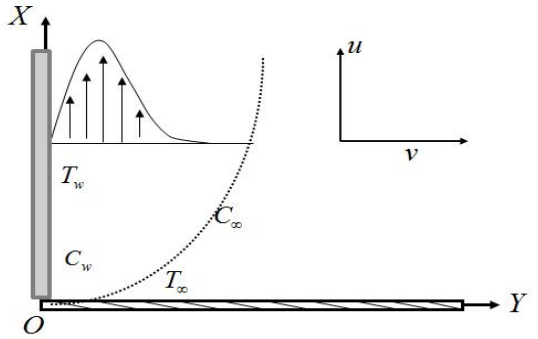

Fig.1. Physical configuration

Now, under the usual Boussinesq's and boundary layer approximations, the governing equations for the flow field under consideration are

Continuity equation

$$\frac{\partial u}{\partial v}+\frac{\partial v}{\partial y}=0 \tag{1}$$

Momentum equation in X-direction

$$\frac{\partial u}{\partial t}+u\frac{\partial u}{\partial x}+v\frac{\partial u}{\partial y}=\upsilon\frac{\partial^2 u}{\partial y^2}+g\beta\left(T-T_\infty\right)+g\beta^*\left(C-C_\infty\right)-\frac{\sigma {B_0}^2 u}{\rho} \tag{2}$$

Energy equation (neglecting viscous dissipation and Joule heating term)

$$\frac{\partial T}{\partial t}+u\frac{\partial T}{\partial x}+v\frac{\partial T}{\partial y}=\frac{\kappa}{\rho C_p}\frac{\partial^2 T}{\partial y^2}+\frac{Dk_t}{C_s C_p}\frac{\partial^2 C}{\partial y^2}-\frac{1}{\rho C_p}\frac{\partial q_r}{\partial y}+\frac{Q}{\rho C_p}\left(T-T_\infty\right)^p \tag{3}$$

Concentration equation

$$\frac{\partial C}{\partial t}+u\frac{\partial C}{\partial x}+v\frac{\partial C}{\partial y}=D\frac{\partial^2 C}{\partial y^2}+\frac{Dk_t}{T_m}\frac{\partial^2 T}{\partial y^2}-k_0\left(C-C_\infty\right)^q \tag{4}$$

With corresponding boundary conditions

$$u=U\left(X\right),v=V,T=T_w,C=C_w \text{ at } y=0 \tag{5}$$

$$u=0,v=0,T=T_\infty,C=C_\infty \qquad \text{at } y=\infty \tag{6}$$

where u and v are the x and y components of velocity vector, υ is the kinematic coefficient viscosity, ρ is the density of the fluid, κ is the thermal conductivity, c_p is the specific heat at the constant pressure, k_0 is the rate of chemical reaction and D is the coefficient of mass diffusivity, k_t is the thermal diffusion ratio, c_s is the concentration susceptibility, respectively. Here p and q are considered as positive constant.

By employing Rosseland approximation the radiative heat flux q_r is given by

$q_r=\frac{-4\sigma^*}{3k^*}\frac{\partial T^4}{\partial y}$, where σ^* is the Stefan-Boltzmann constant and k^* is the mean absorption coefficient.

It should be noted that by using the Rosseland approximation, the present analysis is limited to optically thick fluids. If the temperature differences within the flow field are sufficiently small, then it can be linearized by expanding T^4 into the Taylor series about T_∞, which after neglecting higher-order terms takes the form

$$T^4\approx 4T_\infty\bar{T}-3{T_\infty}^4$$

To obtain the governing equations and the boundary condition in dimension less form, the following non-dimensional quantities are introduced as;

$$X=\frac{xU_\infty}{\upsilon},Y=\frac{yU_\infty}{\upsilon},U=\frac{u}{U_\infty},V=\frac{v}{U_\infty},\tau=\frac{t{U_\infty}^2}{\upsilon},\bar{T}=\frac{T-T_\infty}{T_w-T_\infty},\bar{C}=\frac{C-C_\infty}{C_w-C_\infty}$$

Substituting the above relations in equations (1)-(4) and corresponding boundary conditions (5) and (6) are;

Momentum equation

$$\frac{\partial U}{\partial \tau}+U\frac{\partial U}{\partial X}+V\frac{\partial U}{\partial Y}=\frac{\partial^2 U}{\partial Y^2}+G_r\bar{T}+G_m\bar{C}-MU \tag{7}$$

Energy equation

$$\frac{\partial \bar{T}}{\partial \tau}+U\frac{\partial \bar{T}}{\partial X}+V\frac{\partial \bar{T}}{\partial Y}=\left(\frac{1+R}{P_r}\right)\frac{\partial^2 \bar{T}}{\partial Y^2}+D_u\frac{\partial^2 \bar{C}}{\partial Y^2}+\beta\bar{T}^p \tag{8}$$

Concentration equation

$$\frac{\partial \bar{C}}{\partial \tau}+U\frac{\partial \bar{C}}{\partial X}+V\frac{\partial \bar{C}}{\partial Y}=\frac{1}{S_c}\frac{\partial^2 \bar{C}}{\partial Y^2}+S_r\frac{\partial^2 \bar{T}}{\partial Y^2}-\gamma \bar{C}^q \tag{9}$$

Boundary conditions are

$$U=1,V=1,\bar{T}=1,\bar{C}=1 \quad \text{at } y=0 \tag{10}$$

$$U=0,V=0,\bar{T}=0,\bar{C}=0 \text{ at } y=\infty \tag{11}$$

where τ represents the dimensionless time, Y is the dimensionless Cartesian coordinate, U and V are the dimensionless velocity component in X and Y direction, T is the dimensionless temperature, C is the dimensionless concentration, $G_r=\frac{g\beta(T-T_\infty)\upsilon}{U_\infty{}^3}$ (Grashoff Number), $G_m=\frac{g\beta^*(C-C_\infty)\upsilon}{U_\infty{}^3}$ (Modified Grashoff Number), $M=\frac{\sigma B_0{}^2\upsilon}{\rho U_\infty{}^2}$ (Magnetic Parameter), $R=\frac{16\sigma^* T_\infty{}^3}{3k^*\kappa}$ (Radiation Parameter), $P_r=\frac{\rho c_p\upsilon}{\kappa}$ (Prandlt Number), $D_u=\frac{Dk_t}{\upsilon c_s c_p}\frac{(C_w-C_\infty)}{(T_w-T_\infty)}$ (Dufour Number), $E_c=\frac{U_\infty{}^2}{c_p(T_w-T_\infty)}$ (Eckert Number), $\beta=\frac{Q\upsilon(T_w-T_\infty)^{p-1}}{\rho c_p U_\infty{}^2}$ (Heat Generation or Absorption Parameter), $S_c=\frac{\upsilon}{D}$ (Schimidt Number), $S_r=\frac{Dk_t(T_w-T_\infty)}{\upsilon T_m(C-C_\infty)}$ (Soret Number) and $\gamma=\frac{k_0\upsilon(C-C_\infty)^{q-1}}{U_\infty{}^2}$ (Chemical Reaction Parameter).

3. Shear Stress and Nusselt Number

From the The skin friction at the plate with effect of different parameter on it has been obtained according to the formula $\tau_x=\mu_0\left(\frac{\partial U}{\partial Y}\right)_{Y=0}$. From temperature profile various effect of different parameters have been calculated and Nusselt number $N_u=-\mu_0\left(\frac{\partial \bar{T}}{\partial Y}\right)_{Y=0}$ is also found. Similarly from concentration profile Sherwood number have been analyzed and the Sherwood number is $S_h=-\mu_0\left(\frac{\partial \bar{C}}{\partial Y}\right)_{Y=0}$.

4. Numerical Solutions

Explicit finite difference technique has been imposed to solve the equations numerically. In this section, the region of flow is divided into a grid of lines parallel to X and Y axis. It has been considered that $X_{\max}=100$ and the number of grid spacing in X direction is 40 with constant mesh size $\Delta X=2.5$. in Y direction $Y_{max}=10$ corresponding to $Y\to\infty$, i.e. varies from 0 to 10 with number of grid spacing 40 and constant mesh size is $\Delta Y=0.25$. Time step $\Delta\tau=0.001$.

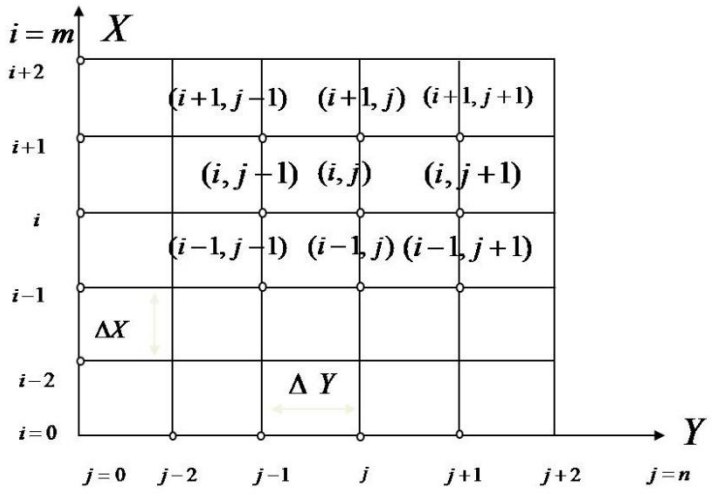

Fig.2: Finite Difference System

Let $U^n, \bar{T}^n$ and $\bar{C}^n$ denote the values of $U, \bar{T}$ and $\bar{C}$ at the end of a time-step respectively. Then the equations from previous section become as following:

$$\frac{U_{i,j} - U_{i-1,j}}{\Delta X} + \frac{V_{i,j+1} - V_{i,j}}{\Delta Y} = 0 \tag{12}$$

$$\frac{U^n{}_{i,j} - U_{i,j}}{\Delta \tau} + U_{i,j}\frac{U_{i,j} - U_{i-1,j}}{\Delta X} + V_{i,j}\frac{U_{i,j+1} - U_{i,j}}{\Delta Y} = \frac{U_{i,j+1} - 2U_{i,j} + U_{i,j-1}}{(\Delta Y)^2} + G_r\bar{T}_{i,j} + G_m\bar{C}_{i,j} - MU_{i,j} \tag{13}$$

$$\frac{\bar{T}^n_{i,j} - \bar{T}_{i,j}}{\Delta \tau} + U_{i,j}\frac{\bar{T}_{i,j} - \bar{T}_{i-1,j}}{\Delta X} + V_{i,j}\frac{\bar{T}_{i,j+1} - \bar{T}_{i,j}}{\Delta Y} = \left(\frac{1+R}{P_r}\right)\frac{\bar{T}_{i,j+1} - 2\bar{T}_{i,j} + \bar{T}_{i,j-1}}{(\Delta Y)^2} + D_u\frac{\bar{C}_{i,j+1} - 2\bar{C}_{i,j} + \bar{C}_{i,j-1}}{(\Delta Y)^2} + \beta\left(\bar{T}_{i,j}\right)^p \tag{14}$$

$$\frac{\bar{C}^n_{i,j} - \bar{C}_{i,j}}{\Delta \tau} + U_{i,j}\frac{\bar{C}_{i,j} - \bar{C}_{i-1,j}}{\Delta X} + V_{i,j}\frac{\bar{C}_{i,j+1} - \bar{C}_{i,j}}{\Delta Y} = \frac{1}{S_c}\frac{\bar{C}_{i,j+1} - 2\bar{C}_{i,j} + \bar{C}_{i,j-1}}{(\Delta Y)^2} + S_r\frac{\bar{T}_{i,j+1} - 2\bar{T}_{i,j} + \bar{T}_{i,j-1}}{(\Delta Y)^2} - \gamma\left(\bar{C}_{i,j}\right)^q \tag{15}$$

With boundary conditions

$$U_0^n = 1, \bar{T}_0^n = 1, \bar{C}_0^n = 1 \text{ at } L = 0 \tag{16}$$

$$U_0^n = 0, \bar{T}_0^n = 0, \bar{C}_0^n = 0 \text{ at } L = \infty \tag{17}$$

Where subscripts i and j denotes X and Y respectively and the superscript n represents a value of time, $\tau = n\Delta\tau$. Where $n = 0,1,2, \ldots \ldots$ The primary velocity U, temperature $\bar{T}$and concentration $\bar{C}$ distributions at all interior nodal points may be computed by successive applications of the above finite difference equations. The numerical values of the local shear stresses, local Nusselt number and local Sherwood are evaluated by Fivepoint approximate formula and the average shear stresses, average Nusselt number and average Sherwood number are calculated by the Simpson's $1/3$ integration rule.

5. Result and discussion

In order to get a physical insight into the problem, a representative set of numerical results is shown graphically in Figs.3-6(b) when $p = 0.9$ and $q = 0.9$. For different values of γ velocity, concentration and temperature profile have been illustrated. With the increase of the values of γ velocity and concentration increases and temperature decreases. From Fig 5(a)-6(b) effect of Dufour number on Nusselt Number, Skin friction and Sherwood number has been explained. At last from fig illustrates the effect of soret number on Nusselt Number, Skin friction and Sherwood number.

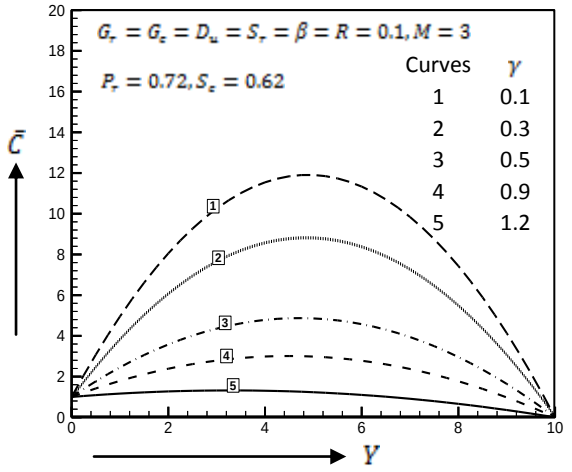

Fig: 3 Concentration profile for various values of γ

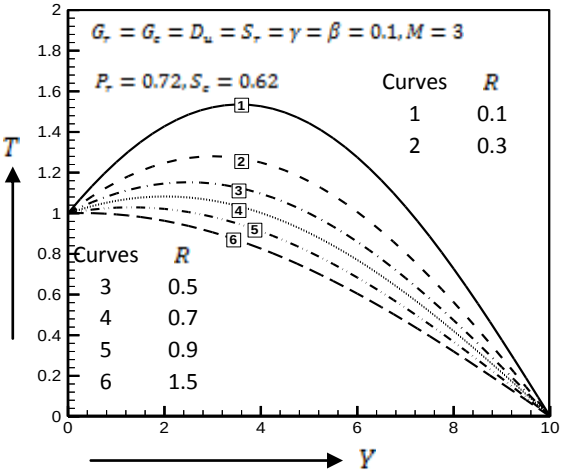

Fig: 4 Temperature profile for various values of R

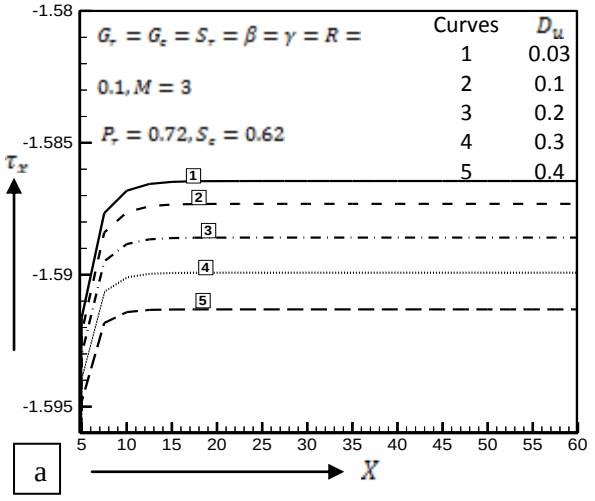

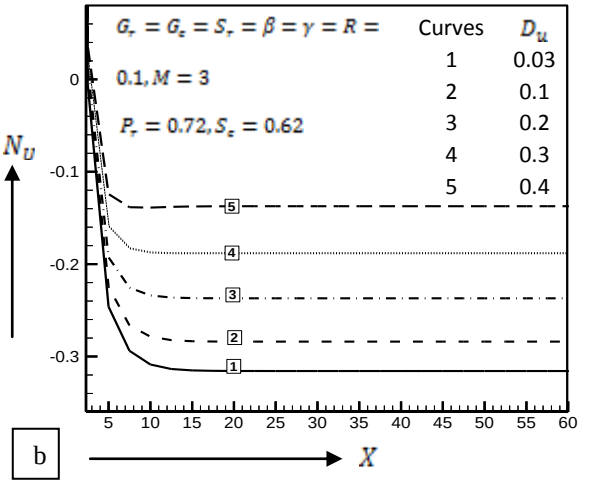

Fig: 5 Illustration of (a) Local Shear Stress (b) Nusselt Number for different values of D_u

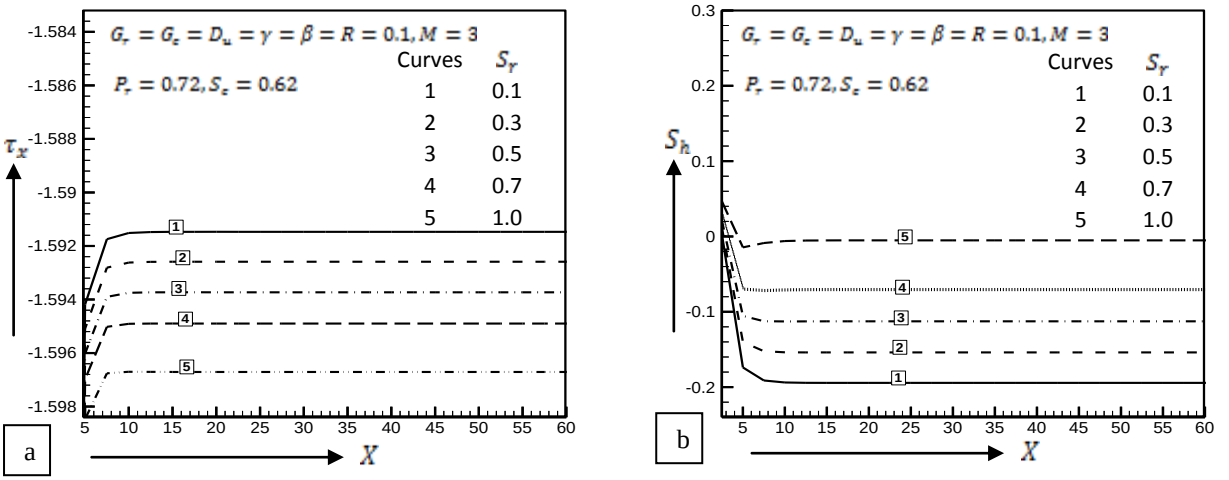

Fig: 6 Illustration of (a) Local Shear Stress (b) Sherwood Number for different values of S_r

6. Conclusions

In this research, the explicit finite difference solution of unsteady viscous, incompressible boundary layer flow of a fluid has been investigated. The physical properties are illustrated graphically for different values of corresponding parameters. Among them some important findings of this investigation are mentioned here;

1. The Shear stress at stationary wall and moving wall decreases with the increase of D_u
2. The Nusselt number and Sherwood number increases with the increase of D_u.
3. The Shear stress at stationary wall and moving wall decreases with the increase of S_r.
4. The Nusselt number and Sherwood number increases with the increase of S_r.

References

[1] Sakiadis BC., Boundary layer behaviour on continuous solid surfaces: I boundary layer equations for two dimensional andaxisymmetric flow, AIChE J (1961); 7:26–8.

[2] O.D. Makinde, Free-convection flow with thermal radiation and mass transfer past a moving vertical porous plate. International communications in heat and mass transfer 32 (2005) 1411-1419.

[3] Das, U. N., Dekha, R., Soungalgekar, V. M., Effects on mass transfer on flow past an impulsively started infinite vertical plate with constant heat flux and chemical reaction, Forschungim Ingenieurwesen 60(1994) 284-287.

[4] Sparrow E.M., Cess R.D., The effect of a magnetic field on free convection heat transfer. Int. J. Heat Mass Transfer, Vol.4, pp. 267-274, 1961.

[5] Olanrewaju P. O., Dufour and Soret Effects of a Transient Free Convective Flow with Radiative Heat Transfer Past a Flat Plate Moving Through a Binary Mixture. Pacific Journal of Science and Technology, Vol. 11. No. 1, 2010.

6th BSME International Conference on Thermal Engineering (ICTE 2014)

Numerical Investigation on MHD Fluid Flow in the Presence of Chemical Reaction with Soret and Dofour Effects over a Vertical Plate in a Rotating System

Md. Mizanur Rahman[1*], Md. Shakhaoath Khan[2] and Md Rafiqul Islam[3]

[1]Department of Mathematics, Faculty of Applied Science and Technology, Islamic University, Kushtia-7003, Bangladesh
Email[*]: mizan_iu@yahoo.com
[2] Department of Chemical Engineering, School of Engineering, University of Newcastle, Callaghan, NSW 2308, AUSTRALIA
Email: mdshakhaoath.khan@uon.edu.au
[3] Mathematics Discipline, Khulna University, Khulna-9208, Bangladesh
Email[3]: mrislam_66@yahoo.com

Abstract

The MHD free convection fluid flow over a vertical porous flat plate in a rotating system is investigated numerically in the presence of radiation, chemical reaction, heat generation with Soret and Dofour effect. The governing equations of the problem contain a system of partial differential equations. An explicit finite difference technique is used to solve the obtained non-similar, coupled, non-linear partial differential non-dimensional equations. Numerical results are performed to examine the various physical parameters on the velocities, temperature and concentration within the boundary layer and shown graphically. Finally, a qualitative comparison with previous published work is shown in tabular form.

*Keywords:*Rotating System; Chemical Reaction; Soret and Dofour Effect; Heat generation; Finite Difference Method

1. Introduction

The phenomenon of MHD free concentration flow is not often caused entirely by the effect of temperature profiles but also by difference in concentrations of dissimilar chemical reaction species. The Chemical Reaction with Soret and Dofour effect of heat transfer and thermal radiation on MHD boundary layer flow has become important in several industrial, scientific and engineering fields. Flows arising from differences in convections or material construction alone and in conjunction with temperature differences have great significance not only of their own interest but also for the application to the geophysics, aeronautics, astrophysics and Bio-engineering. Condensing and boiling are characteristic for many separation processes in chemical engineering as drying, evaporation, distillation, condensation, rectification and absorption of a fluid.MHD heat and mass transfer has great importance in the liquid metal flows, ionized gas flow in a nuclear reactor and electrolytes. The heat radiation and chemical reaction with or without magnetic field, suction or injection, has been analyzed by several characters. There are many engineering aspect of such flows, so the recent year's analytical solution of such problems of flow have been presented by many researchers. The Rotation and Radiation Effects on MHD Flow Past an Impulsively Started Vertical Plate with Variable Temperature have been investigated by Rajput and Kumar [1]. Agarwal et al. [2] studied the effects of Hall Current on the hydro-magnetic free convection with mass transfer in a rotating fluid. Seth et al. [3] studied Effect of Rotation on Unsteady Hydromagnetic Natural Convection Flow Past an Impulsively

* Corresponding author. Cell Phone: +88-01717252603;
*E-mail address:*mizan_iu@yahoo.com; mmrahman@math.iu.ac.bd

Moving Vertical Plate with Ramped Temperature in a Porous Medium with Thermal Diffusion and Heat Absorption.

Bestman and Adjepong [4] investigated the unsteady hydro-magnetic free convection flow with radiative heat transfer in rotating fluid. Bhupendra et al. [5] investigated the Hall effects on MHD mixed convective flow of a viscous incompressible fluid past a vertical porous plate immersed in porous medium. Dufour And Soret Effects On Steady MHD Free Convection And Mass Transfer Fluid Flow Through A Porous Medium In A Rotating System have been investigated by Nazmul and Alam [6]. Aiyesimi et al. [7] have investigated the hydro-magnetic free convection of heat and mass transfer flow over a stretching vertical plate with suction. Dileep and Priyanka [8] studied the effects on heat transfer of rotating couette flow in a channel partially filled by a porous medium with hall current. Garg [9] studied combined effects of thermal radiations and hall current on moving vertical porous plate in a rotating system with variable temperature. Sahin et al. [10] established a mathematical model on magneto-hydrodynamic transient free and forced convective flow with induced magnetic field effects. Sivaiah [11] studied the MHD flow of a rotating fluid past a vertical porous flat plate in the presence of chemical reaction and radiation. Lavanya and Leela [12] studied Dufour and soret effects on steady MHD free convective flow past a vertical porous plate embedded in a porous medium with chemical reaction, radiation, heat generation and viscous dissipation. Effects of thermal radiation on hydro-magnetic flow due to a porous rotating disk with Hall Effect have been studied by Anjali and Uma [13]. Guchhait et al. [14] studied combined Effects of hall currents and Rotation on MHD Mixed Convection Oscillating Flow in a Rotating Vertical Channel.

The main objective of the present investigation is to study the MHD Free Convection fluid flow over a Vertical Porous Plate in a Rotating System in the presence chemical reaction, Soret and Dofour effect, Heat generation and radiation. Also our principle aim of this paper is to extend the work of Ismail et al. [15] for the case where we consider the fluid in presence of Heat generation and Soret effect Flow in a Porous Medium with with Ramped Wall Temperature. The problem is solved by explicit finite difference method. The proposed model has been transformed into non-similar coupled partial differential equation by usual transformations. Finally, the comparison of the present results with the results of Ismail et al. [15] has been shown.

2. Mathematical Formulation

Consider an unsteady MHD free convection and mass transfer flow of an electrically conducting viscous fluid through a porous medium along an infinite vertical porous plate $y = 0$ in a rotating system. The flow is also assumed to be in the x-direction which is taken along the plate in the upward direction and y-axis is normal to it. Initially the fluid as well as the plate is at rest, after that the whole system is allowed to rotate with a constant angular velocity Ω about the y-axis. Since the system rotates about $y-axis$, so we can take $\mathbf{\Omega} = (0,-\Omega,0)$. A uniform transverse magnetic field of magnitude B_0 is applied in the direction of $y-$axis. Initially; it is considered that the plate as well as the fluid is at the same temperature $T(=T_\infty)$ and concentration level $C(=C_\infty)$. Also it is assumed that the temperature of the plate and concentration are raised to $T_w(>T_\infty)$ and $C_w(>C_\infty)$ respectively, which are there after maintained constant, where T_w, C_w are temperature and concentration at the wall and T_∞, C_∞ are the temperature and concentration of the species outside the boundary layer respectively. The physical configuration of the problem is furnished in Figure 1.Within the framework of the above-stated assumptions the generalized equations relevant to the unsteady problem are governed by the following system of coupled partial differential equations as;

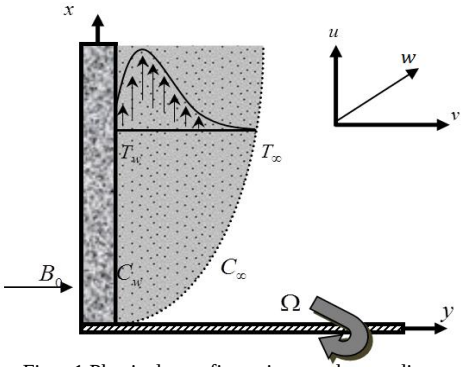

Fig. 1.Physical configuration and coordinate system.

The Continuity equation;

$$\frac{\partial u}{\partial x}+\frac{\partial v}{\partial y}=0. \quad (1)$$

The Momentum equation in $x-$axis ;

$$\frac{\partial u}{\partial t}+u\frac{\partial u}{\partial x}+v\frac{\partial u}{\partial y}=\upsilon\frac{\partial^2 u}{\partial y^2}+gB_T\left(T-T_\infty\right)+gB_C\left(C-C_\infty\right)-\frac{\sigma B_0^2 u}{\rho}+2\Omega w-\frac{\upsilon}{\kappa'}u \tag{2}$$

The Momentum equation in $z-$axis ;

$$\frac{\partial w}{\partial t}+u\frac{\partial w}{\partial x}+v\frac{\partial w}{\partial y}=\upsilon\frac{\partial^2 w}{\partial y^2}+\frac{\sigma B_0^2 u}{\rho}-2\Omega u-\frac{\upsilon}{\kappa'}u \tag{3}$$

The Energy equation;

$$\frac{\partial T}{\partial t}+u\frac{\partial T}{\partial x}+v\frac{\partial T}{\partial y}=\frac{\kappa}{\rho c_p}\frac{\partial^2 T}{\partial y^2}-\frac{1}{\rho c_p}\frac{\partial q_r}{\partial y}+\frac{D_m K_t}{c_s c_p}\frac{\partial^2 C}{\partial y^2}+\frac{Q}{\rho c_p}\left(T-T_\infty\right) \tag{4}$$

The Concentration equation;

$$\frac{\partial C}{\partial t}+u\frac{\partial C}{\partial x}+v\frac{\partial C}{\partial y}=D_m\frac{\partial^2 C}{\partial y^2}+\frac{D_m K_t}{T_m}\frac{\partial^2 T}{\partial y^2}-K_r\left(C-C_\alpha\right)^n \tag{5}$$

The corresponding boundary conditions are;

$$\begin{aligned}&u=0,\ v=0,\ w=0,\ T=T_w,\ C=C_w \quad \text{at } y=0,\\ &u=0,\ v=0,\ w=0,\ T\to T_\infty,\ C\to C_\infty \quad \text{as } y\to\infty\end{aligned} \tag{6}$$

where u,v and w are the x,y and z components of velocity vector, σ is the electric conductivity, υ are the kinematic coefficient viscosity, ρ is the density of the fluid, κ is the thermal conductivity, c_p is the specific heat at the constant pressure , D_m is the coefficient of mass diffusivity, k_t is the thermal diffusion ratio, T_m is the mean fluid temperature, Q is the heat absorption coefficient, β_T is the co-efficient of volumetric expansion for heat transfer, β_C is the co-efficient of volumetric expansion for mass transfer. The radiative heat flux q_r is described by the Rosselandapproximation (Brewster [16]) such that, $q_r=-\left(4\sigma^*/3\mathrm{k}^*\right)\left(\partial T^4/\partial y\right)$ where σ^* and k^* are the Stefan-Boltzman constant and the mean absorption coefficient, respectively. If the temperature difference within the flow are sufficiently small so that T^4 can be expressed as a linear function after using Taylor series to expand T^4 about the free stream temperature T_∞ and neglecting higher-order terms. This result in the following approximation: $T^4\approx 4\mathrm{T}_\infty^3 T-3\mathrm{T}_\infty^4$.

To obtain the governing equations and the boundary condition in dimension less form, the following non-dimensional quantities are introduced as; $X=xU_0/\upsilon$, $Y=yU_0/\upsilon$, $U=u/U_0$, $V=v/U_0$, The magnetic Reynolds number of the flow is taken to be very small and the induced magnetic field is negligible in comparison with applied magnetic field and the magnetic lines are fixed relative to the fluid. Using the relation $\nabla\cdot\mathbf{J}=0$ for the current density $\mathbf{J}=\left(J_x,J_y,J_z\right)$ where $J_y=\text{constant}$. Since the plate is non-conducting, $J_y=0$ at the plate and hence zero everywhere. $W=w/U_0$, $\tau=tU_0^2/\upsilon$, $\bar{T}=\left(T-T_\infty\right)/\left(T_w-T_\infty\right)$ and $\bar{C}=\left(C-C_\infty\right)/\left(C_w-C_\infty\right)$ .Substituting the above dimensionless variables in equations (1)-(5) and corresponding boundary conditions (6), the obtained dimensionless coupled non-linear partial differential equations are;

$$\frac{\partial U}{\partial X}+\frac{\partial V}{\partial Y}=0 \tag{7}$$

$$\frac{\partial U}{\partial \tau}+U\frac{\partial U}{\partial X}+V\frac{\partial U}{\partial Y}=\frac{\partial^2 U}{\partial Y^2}+G_r\bar{T}+G_m\bar{C}-\left(M+K\right)U+R'W \tag{8}$$

$$\frac{\partial W}{\partial \tau}+U\frac{\partial W}{\partial X}+V\frac{\partial W}{\partial Y}=\frac{\partial^2 W}{\partial Y^2}+\left(M-K\right)W-R'U \tag{9}$$

$$\frac{\partial \bar{T}}{\partial \tau}+U\frac{\partial \bar{T}}{\partial X}+V\frac{\partial \bar{T}}{\partial Y}=\left(\frac{1-R}{P_r}\right)\frac{\partial^2 \bar{T}}{\partial Y^2}+D_u\frac{\partial^2 \bar{C}}{\partial Y^2}+\beta\bar{T} \tag{10}$$

$$\frac{\partial \bar{C}}{\partial \tau}+U\frac{\partial \bar{C}}{\partial X}+V\frac{\partial \bar{C}}{\partial Y}=\frac{1}{S_c}\frac{\partial^2 \bar{C}}{\partial Y^2}+S_0\frac{\partial^2 \bar{T}}{\partial Y^2}-\gamma\bar{C}^n \tag{11}$$

and boundary conditions are;

$$U=0,\ W=0,\ \bar{T}=1,\ \bar{C}=1 \text{ at } Y=0 \tag{12}$$

$U = 0, W = 0,\ \overline{T} = 0,\ \overline{C} = 0 \text{ as } Y \to \infty$.

Where τ represents the dimensionless time, U, V and W are the X, Y and Z components of dimensionless velocity vector, X and Y are the dimensionless Cartesian coordinates, $\overline{T}$ is the dimensionless temperature, $\overline{C}$ is the dimensionless concentration, and the parameters are given such as $G_r = \left(gB_T\left(T_w - T_\infty\right)\upsilon\right)/U_0^3$ (Grashof Number), $G_m = \left(gB_C\left(C_w - C_\infty\right)\upsilon\right)/U_0^3$ (Modified Grashof Number), $M = \left(\sigma B_0^2 \upsilon/\rho U_0^2\right)$ (Magnetic Parameter), $R' = 2\Omega\upsilon/U_0^2$ (Rational Parameter), $K = \mu\upsilon/\rho\kappa' U_0^2$ (Permeability of the porous medium), $R = \left(16\sigma^* T_\infty{}^3/3\kappa^*\kappa\right)$ (Radiation parameter) $P_r = \left(\rho c_p \upsilon/\kappa\right)$ (Prandtl Number), $\beta = \left(Q\upsilon/\rho c_p U_0^2\right)$ (Heat generation/ Absorption parameter), $S_c = \left(\upsilon/D\right)$ (Schmidt Number) and $S_0 = \left(D_m k_t\left(T_w - T_\infty\right)/\upsilon T_m\left(C_w - C_\infty\right)\right)$ (Soret Number), $D_u = \left(D_m k_t\left(C_w - C_\infty\right)/\upsilon c_s c_p\left(T_w - T_\infty\right)\right)$ (Dufour Number), $\gamma = \left(D_m k_r \upsilon\left(C_w - C_\infty\right)^{n-1}/U_0^2\right)$(Chemical Reaction Parameter).

3. Numerical Solutions

The system of non-dimensional, nonlinear, coupled partial differential equations (7)-(11) with boundary condition (12) are solved numerically using explicit finite difference method. To obtain the difference equations, the region of the flow is divided into a grid or mesh of lines parallel to X and Y axes, where X -axis is taken along the plate and Y -axis is normal to the plate.Here the plate of height $X_{\max}\left(=100\right)$ is considered i.e. X varies from 0 to 100 and assumed $Y_{\max}\left(=30\right)$ as corresponding to $Y \to \infty$ i.e. Y varies from 0 to 30 . There are $m\left(=180\right)$ and $n\left(=180\right)$ grid spacing in the X and Y directions respectively as shown in Figure 2 It is assumed that ΔX , ΔY are content mesh size along X and Y directions respectively and taken as follows, $\Delta X = 0.50\left(0 \le X \le 100\right)$ and $\Delta Y = 0.15\left(0 \le Y \le 30\right)$ with the smaller time-step, $\Delta\tau = 0.005$ .Let $U', W', \overline{T}'$ and $\overline{C}'$ denote the values of U, W, $\overline{T}$ and $\overline{C}$ are the end of a time-step respectively. Using the explicit finite difference approximation, the following appropriate set of finite difference equations are obtained as;

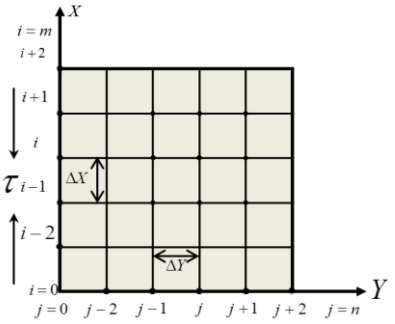

Fig. 2.Explicit finite difference system grid.

$$\frac{U'_{i,j} - U'_{i-1,j}}{\Delta X} + \frac{V_{i,j} - V_{i,j-1}}{\Delta Y} = 0 \tag{13}$$

$$\frac{U'_{i,j} - U_{i,j}}{\Delta\tau} + U_{i,j}\frac{U_{i,j} - U_{i-1,j}}{\Delta X} + V_{i,j}\frac{U_{i,j+1} - U_{i,j}}{\Delta Y} = \frac{U_{i,j+1} - 2U_{i,j} + U_{i,j-1}}{\left(\Delta Y\right)^2} + G_r\overline{T}'_{i,j} + G_m\overline{C}'_{i,j} \tag{14}$$

$$\frac{W'_{i,j} - W_{i,j}}{\Delta\tau} + U_{i,j}\frac{W_{i,j} - W_{i-1,j}}{\Delta X} + V_{i,j}\frac{W_{i,j+1} - W_{i,j}}{\Delta Y} = \frac{W_{i,j+1} - 2W_{i,j} + W_{i,j-1}}{\left(\Delta Y\right)^2} + \left(M - K\right)W_{i,j} - R'U_{i,j} \tag{15}$$

$$\frac{\overline{T}'i,j - \overline{T}i,j}{\Delta\tau} + U_{i,j}\frac{\overline{T}i,j - \overline{T}i{-}1,j}{\Delta X} + V_{i,j}\frac{\overline{T}i,j{+}1 - \overline{T}i,j}{\Delta Y} = \left(\frac{1-R}{P_r}\right)\frac{\overline{T}i,j{+}1 - 2\overline{T}i,j + \overline{T}i,j{-}1}{\left(\Delta Y\right)^2} + D_u\frac{\overline{C}i,j{+}1 - 2\overline{C}i,j + \overline{C}i,j{-}1}{\left(\Delta Y\right)^2} + \beta\overline{T} \tag{16}$$

$$\frac{\overline{C}'_{i,j} - \overline{C}_{i-1,j}}{\Delta\tau} + U_{i,j}\frac{\overline{C}_{i,j} - \overline{C}_{i-1,j}}{\Delta X} + V_{i,j}\frac{\overline{C}_{i,j+1} - \overline{C}_{i,j}}{\Delta Y} = \frac{1}{S_c}\frac{\overline{C}_{i,j+1} - 2\overline{C}_{i,j} + \overline{C}_{i,j-1}}{\left(\Delta Y\right)^2} + S_0\frac{\overline{T}_{i,j+1} - 2\overline{T}_{i,j} + \overline{T}_{i,j-1}}{\left(\Delta Y\right)^2} - \gamma\overline{C}^n{}_{i,j} \tag{17}$$

with the boundary condition;

$$U^n_{i,0} = 0,\ W^n_{i,0} = 0,\ \overline{T}^n_{i,0} = 1,\ \overline{C}^n_{i,0} = 1, \tag{18}$$

$$U^n_{i,L} = 0,\ W^n_{i,L} = 0, \overline{T}^n_{i,L} = 0,\ \overline{C}^n_{i,L} = 0 \text{ where } \mathrm{L} \to \infty.$$

Here the subscript i and j designates the grid points with X and Y coordinates respectively and the superscript n represents a value of time, $\tau = n\Delta\tau$ where $n = 0,1,2,\ldots\ldots$. The velocity $\left(U,W\right)$, temperature $(\overline{T})$ and concentration

$(\overline{C})$ distributions at all interior nodal points have been computed by successive applications of the above finite difference equations.

4. Results and Discussion

For investigating the physical situation of the problem, the numerical values and graphs of velocities (U) and (W), temperature $(\overline{T})$ and concentration $(\overline{C})$ distributions within the boundary layer have been computed for different values of Magnetic parameter (M), Rational Parameter (R'),Permeability of the porous medium (K) ,Heat generation (β),Dufour Number (D_u), Radiation parameter (R), Prandtl number (P_r), Schmidt number (S_c), Soret number (S_0) and Chemical Reaction Parameter (γ) with the help of a computer programming language Compaq Visual Fortran 6.6a and Tecplot 7. These computed numerical results have been shown graphically. To obtain the steady-state solutions, the computation has been carried out up to $\tau = 80$. It is observed that the numerical values of U, W, $\overline{T}$ and $\overline{C}$ however, show little changes after $\tau = 45$. Hence at $\tau = 45$ for all variables are steady-state solutions. The importance of cooling problem in nuclear engineering in connection with the cooling of reactors, the value of the Grashof number for heat transfer is taken to be positive $(G_r > 0)$ and the present analysis has considered $G_r = 3.00$. Since the most important fluids are atmospheric air, water and methanol, so that the results are limited to $P_r = 0.71$ (Prandtl number for air at $20^\circ C$), $P_r = 1.00$ (Prandtl number for or salt water)and $P_r = 7.00$ (Prandtl number for water at $20^\circ C$) and $P_r = 11.62$ (Prandtl number for methanol at $20^\circ C$). However the values of other parameters are chosen arbitrarily and also the modified Grashof number $G_m = 3.00$ for mass transfer are considered as a fixed value.Moreover for the accuracy of the present results a qualitative comparison with the published results of Ismail et al. [15] presented in table 1. It was found that the accuracy of the present results is qualitatively as well as quantitatively good in case of all the flow parameters.

To investigate the physical situation of the problem, the solutions have been illustrated in Fig. 3-8. The primary velocity and secondary velocity profiles have been displayed for various values of Permeability parameter (K) in Fig. 3(a) and 3(b) respectively. These results show that the primary velocity increases and secondary velocity decreases with the increase of Permeability parameter (K). The effect of Magnetic parameter (M) and rational parameter (R') are illustrated in fig. 4(a) and 4(b) respectively. It is observed that the temperature profiles increases with increases Magnetic parameter and Secondary velocity decreases with increases rational parameter.

Table 1: Comparison of the prediction of primary as well as velocity profiles, temperature profiles and concentration profiles for several physical parameters.

Increased	Ismail et al. [15]		Present result					
Parameter	u	w	T	C	U	W	$\overline{T}$	$\overline{C}$
Sc				Dec.				Dec.
β			Inc.				Inc.	Inc.
R'	Inc.	Dec.				Dec.		
Pr			Dec.				Dec.	
Du							Inc.	
K					Inc.	Dec.		
R								Inc.
So								Dec.
M							Inc.	

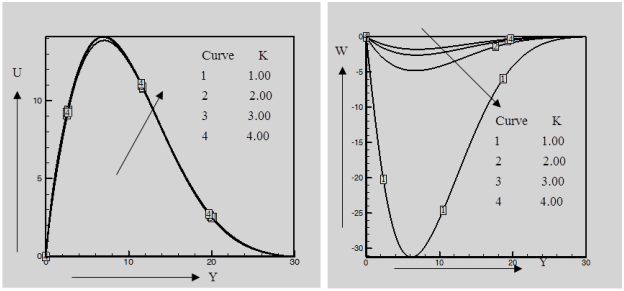

Fig.3. (a) Primary velocity profiles and (b) Secondary velocity profiles for different values of K when $G_r = 3.00, G_m = 3.00,$ $\beta = 0.20,\ M = 1.00, R' = 0.4, D_u = 0.20,\ R = 0.30, P_r = 0.71,$ $\gamma = 1.00, S_c = 0.60,\ S_0 = 0.30$.

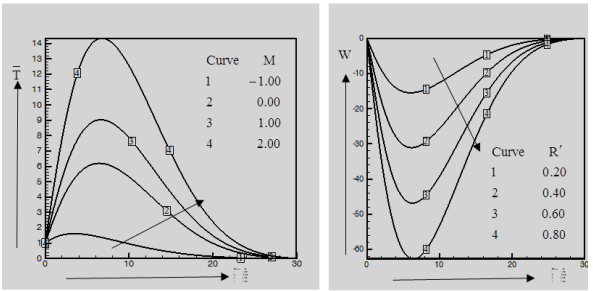

Fig. 4. (a) Temperature profiles for different values of M and (b) Secondary velocity profiles for different values of R' when $G_r = 3.00, G_m = 3.00, \beta = 0.20,\ K = 1.00, M = 1.00, R' = 0.4,$ $D_u = 0.20,\ R = 0.30, P_r = 0.71, \gamma = 1.00, S_c = 0.60,\ S_0 = 0.30$.

The temperature profiles and fluid concentration profiles have been displayed for various values of Prandtl number (P_r) and Radiation parameter (R) in Fig. 5(a) and 5(b) respectively. It is noted that the temperature profiles decreases with the increasesPrandtl number and the fluid concentration profiles have initially increases but a few time the fluid concentration decreases with the increases Radiation parameter.The temperature profiles and fluid concentration profiles have been illustrated for several values of heat generation or absorption parameter (β) in Fig. 6(a) and 6(b) respectively.

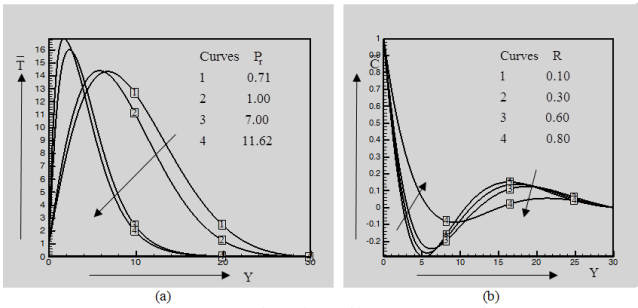

Fig. 5. (a) Temperature profiles for different values of P_r and (b) Concentration profiles for different values of R when. $G_r = 3.00, G_m = 3.00, \beta = 0.20,\ K = 1.00, M = 1.00,$ $R' = 0.4, D_u = 0.20,\ R = 0.30, P_r = 0.71, \gamma = 1.00, S_c = 0.60,\ S_0 = 0.30$

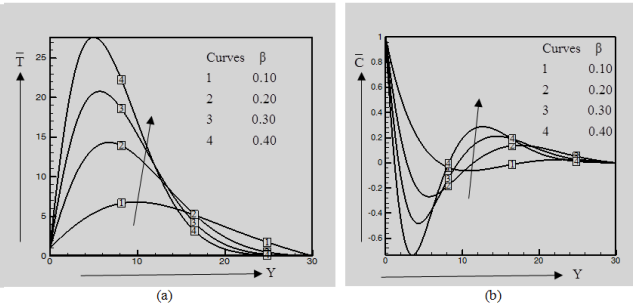

Fig.6. (a) Temperature profiles and (b) Concentration profiles for different values of β when $G_r = 3.00, G_m = 3.00,\ K = 1.00,$ $M = 1.00, R' = 0.4, D_u = 0.20,\ R = 0.30, P_r = 0.71, \gamma = 1.00, S_c = 0.60,\ S_0 = 0.30$

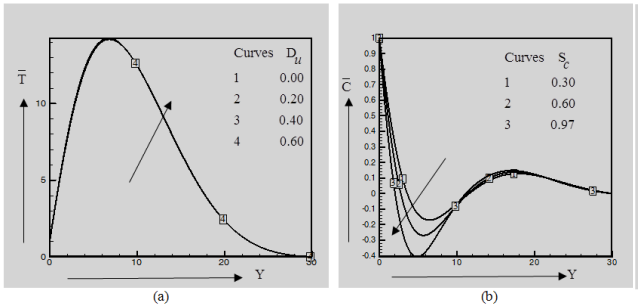

Fig. 7. (a) Temperature profiles for different values of D_u and (b) Concentration profiles for different values of S_o when $G_r = 3.00, G_m = 3.00, \beta = 0.20,\ K = 1.00, M = 1.00, R' = 0.4,$ $D_u = 0.20,\ R = 0.30, P_r = 0.71, \gamma = 1.00, S_c = 0.60,\ S_0 = 0.30$.

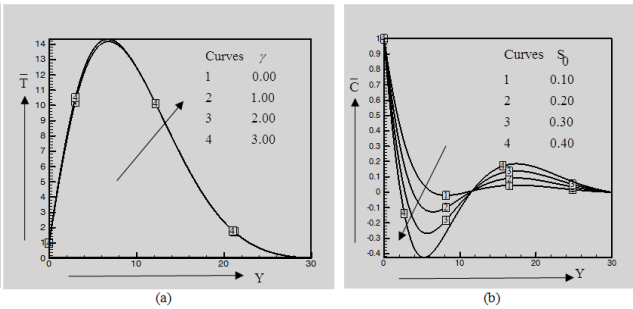

Fig. 8. (a) Temperature profiles for different values of γ and (b) Concentration profiles for different values of S_o when $G_r = 3.00, G_m = 3.00, \beta = 0.20,\ K = 1.00, M = 1.00, R' = 0.4,$ $D_u = 0.20,\ R = 0.30, P_r = 0.71, \gamma = 1.00, S_c = 0.60,\ S_0 = 0.30$.

These results show that the temperature and fluid concentration profiles increases with increase of are treated as heat absorption and generation respectively. The temperature profiles have been displayed for various values of Dofour number (D_u) and Chemical Reaction Parameter (γ) in fig. 7(a) and 8(a) respectively. These graph shows that the minor increasing effect on the temperature profiles with increases Dofour number and Chemical Reaction Parameter. The temperature profiles in the presence of different species with various Schimdt number (S_c), namely, helium $(S_c = 0.30)$, oxygen $(S_c = 0.60)$, and methanol $(S_c = 0.97)$, at $25^0 C$ temperature and 1 atmosphere pressure, are shown in Fig. 7(b). It is seen that the fluid concentration decreases with increases S_c. The fluid concentration profiles have been displayed for various values of Soret number (S_0) in Fig. 8(b). It is observed that the concentration profile has been fluctuated with increase Soret number.

5. Conclusion

In this study, the explicit finite difference solution of MHD Free Convection fluid flow over a Vertical Porous Plate in a Rotating System in the presence chemical reaction, Soret and Dofour effect, Heat generation and radiationis investigeted. The physical properties are discussed for different values of parameters and iimportant findings of this investigation are: (a) The primary velocity profiles increase with the increase of K. (b) The secondary velocity profiles decreses with the increase of β, K. (c) The temperature distributions increase with the increase of β, M, D_u and decreases with increases in P_r. (d) The concentration profiles inecrease with the increase of β, R and reverse effects with the increse S_0 and S_c .It is expected that the findings of this study may be useful for study of movement oil or gas and water through the reservoir of an oil or gas field, in the migration of underground water or oil as well as in the filtration and water purification processes.

6. Reference

[1]. U.S. Rajput, S. Kumar, Rotation and Radiation effects on MHD Flow Past an Impulsively Started Vertical Plate with Variable Temperature, Int. Journal of Math. Analysis, 5(24) (2011) 1155 – 1163.

[2]. H. L. Agarwal, P. C. Ram, V. Singh, Effects of Hall currents on the hydro-magnetic free convection with mass transfer in a rotating fluid, Astrophysics and Space Science, 100 (1984) 277-283.

[3]. G. S. Seth, R. Nandkeolyar, M. S. Ansari, Effect of Rotation On Unsteady Hydromagnetic Natural Convection Flow Past An Impulsively Moving Vertical Plate With Ramped Temperature in A Porous Medium With Thermal Diffusion And Heat Absorption, Int. J. of Appl. Math and Mech.,7(21) (2011) 52-69.

[4]. A. R. Bestman, S. K. Adjepong, Unsteady hydro-magnetic free convection flow with radiative heat transfer in a rotating fluid, Astrophysics and Space Science, 143 (1998) 217-224.

[5]. B. K. Sharma, A. K. Jha, R. C. Chaudhary, Hall effect on MHD mixed convective flow of a viscous incompressible fluid past a vertical porous plate immersed in porous medium with heat source/sink, Journal of Physics, 52 (5) (2007) 487-503.

[6]. N. Islam, M. M. Alam, Dufour Soret Effects On Steady Mhd Free Convection And Mass Transfer Fluid Flow Through A Porous Medium in A Rotating System, Journal of Naval Architecture and Marine Engineering, 4 (2007) 43-55.

[7]. Y. M. Aiyesimi, S. O. Abah, G. T. Okedaya, The analysis of hydro-magnetic free convection heat and mass transfer flow over a stretching vertical plate with suction, American Journal of computational and Applied Mathematics, 1(1) (2011) 20-26.

[8]. D. S. Chauhan, P.Rastogi, Heat transfer effects on rotating MHD Couette flow in a channel partially filled by a porous medium with Hall current, Joumal of Applied Science and Engineering, 15(3) (2012) 281-290.

[9]. B. P. Garg, Combined effects of thermal radiations and hall current on moving vertical porous plate in a rotating system with variable temperature, International Journal of Pure and Applied Mathematics, 81(2) (2012) 335-345.

[10]. S. Ahmed, O. A. Beg, S. Vedad, M. Zeinalkhani, A. Heidary, Mathematical modeling of Magneto-hydrodynamics transient free and forced convective flow with induced magnetic field effects, International Journal of Pure and Applied Sciences and Technology, 1(1) (2012) 109-125.

[11]. S. Sivaiah, MHD flow of a rotating fluid past a vertical porous flat plate in the presence of chemical reaction and radiation, Journal of Engineering Physics and Thermo-Physics, 86(6) (2013) 1328-1336.

[12]. B. Lavanya, A. L. Ratnam, Dufour and soret effects on steady MHD free convectin flow past a vertical porous plate embedded in a porous medium with chemical reaction, radiation, heat generation and viscous dissipation, Advances in Applied Science Research, 5(1) (2014) 127-142.

[13]. S.P. Anjali Devi, R. Uma Devi, Effects of Thermal Radiation on Hydromagnetic Flow due to a Porous Rotating Diskwith Hall Effect, Journal of Applied Fluid Mechanics, 5(2) (2012) 1-7.

[14]. S. K. Guchhait, S. Das, R.N. Jana, Combined Effects of Hall Currents and Rotation on MHD Mixed Convection Oscillating Flow in a Rotating Vertical Channel, International Journal of Computer Applications, 49 (13) (2012) 0975– 8887.

[15]. Z. Ismail, I. Khan, S. Shafie, Rotation and Heat Absorption Effects on Unsteady MHD Free Convection Flow in a Porous Medium past an Infinite Inclined Plate with Ramped Wall Temperature, Recent Advances in Mathematics, 1st International Conference on Mathematical, Computational and Statistical Sciences, (2013)161-167.

[16]. M. Q. Brewster, Thermal Radiative Transfer and Properties, John Wiley and Sons Inc., New York: USA, 1992.

6th BSME International Conference on Thermal Engineering (ICTE 2014)

Fabrication and Performance Test of Continuous Flow down Draught Gasifier for Wood Gasification System

Md. Arefin Kowser*[a], Md. Alim Badsha[a], Nayeem Md. Lutful Huq[a], Md. Khaled Khalil[a], Hasan Mohammad Mostofa Afroz[a], Zulfikar Hossain[a]

*[a] *Department of Mechanical Engineering, Dhaka University of Engineering & Technology (DUET), Gazipur-1700, Bangladesh*

Abstract

Saw dusts are used as fuel for cooking, electricity generation, and other purposes, but in most of these applications the maximum energy loss occurs due to inefficient burning process. To utilize maximum energy, saw dusts should be burned properly. Fluidized bed rice husk gasification is one of the systems where saw dusts are burned properly for the utilization of maximum energy. In the present work, a down draught rice husk gasifier is fabricated, where; the fluidized bed reactor is constructed to carry out a variety of multiphase chemical reaction. In fluidized bed reactor, gas is passed through a solid material at high velocity to suspend the solid and cause it to behave as though it were a fluid. Using the saw dust gasifier a continuous flow gas is produced which ensures a continuous supply of usable form of energy. In this method once the processes is started it can be kept running as long as needed. The burnt solid waste is removed automatically after a certain period. As it gives efficient energy conversion it leaves a less environmental impact. Thus the system has made the burning process a user and environment friendly one. Gasification tests were made with varying air flow rate and fuel feed rate. The typical wall temperature of gasification process was about 400-450°C. The average temperature of producer gas was about 600-800°C. The highest heating value of producer gas was 3.9MJ/m^3 to 4.5MJ/m^3 with the volume flow rate. The models of gasifier are based on the mass energy conservation equation and include the energy exchange between solid and gaseous phases. Different gasification sub processes are in corporate Drying, Pyrolysis, Combustion, Oxidation, reduction and hydrocarbon reforming the model was validated experimentally in a small scale gasifier by comparing the experimental temperature field, saw dust burning sates and fuel/air reaction with predicted results. A good agreement between experimental and estimated results was achieved. The maximum efficiency was obtained with the smaller particle size and lower air velocity. It was a consequence of the higher fuel/air ratio in the gasifier and so the production of a gas with a higher calorific value. The model can be used as a tool to study the influence of process parameter, air flow velocity, gasifier geometry, composition and inlet temperature of the gasifying agent propagation velocity (flame front velocity) and its efficiency.

Keywords: Biomass; Gasification; Down draught; Propagation velocity; Saw dust; fluidized bed reactor.

1. Introduction

Alternative energy sources, like biomass, have become the point of interest to the people around the world. This is because the supply of fossil fuel is becoming scarce, causing its price to be high enough for domestic as well as for industrial usage. In addition to this, emission of burnt gases, brought about by the production of these fossil fuels, create a lot of problems to the environment. An agricultural residue that could be utilized in a large number of countries for the recovery of energy because of its reasonably high energy content (12–18MJ/kg) is rice husk. Large quantity of rice husk is generated annually as the major by-product of rice milling industry. The total annual rice production worldwide is about 500 million tones [1]. Assuming 20% rice husk recovery rate from rice grains [2] the annual rice husk production of about 100 million tonnes. Kandpal TC et. al., 1996 carried out a work for testing the viability and estimated per unit electricity production cost to be 0.05-0.2 USD [3]. Near about 7 million tons of rice husk is produced in Bangladesh per year. Despite the increasing trend of the rice husk surplus, proper methods of its utilization are yet to be developed. Many countries have imposed

new regulations to restrict field burning of rice husks, primarily for environmental reasons. Consequently, this has increased the interest in the utilization of rice husk as a renewable source of energy [4]. Moreover converting rice husk into gaseous or liquid fuels will be beneficial to the countries who have no conventional energy resources and whose economies are tied to agriculture and local industries. Gasifying saw dust means, burning it with limited amount of air. Several studies in the past revealed that a bluish-flame gas can be generated from rice husk when gasified. Using the biomass as a source of energy was started in early 1980s [5]. At that time the EERC conducted a series of research projects involving the utilization of sunflower hulls, wood residue, and sewage sludge for power using both combustion and gasification technologies. In the year 1999 Ghaly AE et. al., 1999 [6] used a dual distributor type fluidized bed gasifier for producing fuel gas. The San San Rice husk Gasifier Stove developed in Myanmar, 2005, offers smokeless combustion of rice husk in an efficient manner [7]. Alexis TB et. al., in the year 2010 designed a continuous flow rice husk gasifier for thermal applications, such as, cooking, drying etc. [8].Gasification is not a newly discovered process. In the previous researches, huge amount of works have been presented about wood gasification system [9-17]. It was used in the past for heating, lighting and vehicle fuel. During world war two over a million gasifiers were in use In the early 1980s, the concept of Combined Heat and Power generation through wood gasification was one of many research programs. Renewable energy sources in Bangladesh can play a major role to meet electricity demands in the rural areas of the country. We employ a technology known as wood gasification to convert wood waste to alternative fuel (methane). It is a method of extracting clean energy from wood-based materials that produces electricity, heat and substitute natural gas emergency alternate of petrol and diesel fuel.Wood gasification is considered clean, efficient and economically viable. It leaves a small footprint and provides 20 times the heat transfer of traditional gasification systems, while offering greater fuel flexibility. Wood gasification is the process of turning wood into carbon monoxide and hydrogen by reacting the raw material (wood) at high temperatures with a controlled amount of oxygen. This is achieved by reacting the material at high temperatures (600°C-800°C), without combustion, with a controlled amount of oxygen. The resulting gas mixture is called syngas (from synthesis gas or synthetic gas) or producer gas and is itself a fuel. The power derived from gasification of wood residue and combustion of the resultant gas is considered to be a source of renewable energy. This gas can be used as fuel in an internal combustion engine. The gas, which is combustible, can be used in diesel engines to replace up to 80 percent of the fuel. Wood Gasification is also used industrially in the production of electricity, ammonia and liquid fuels (oil) using Integrated Gasification Combined Cycles (IGCC), with the possibility of producing methane and hydrogen for fuel cells. IGCC is also a more efficient method of CO_2 capture as compared to conventional technologies. Mechanical energy from the engines may be used for driving water pumps for irrigation or for coupling with an alternator. Gasifiers offer a flexible option for thermal applications, as they can be retrofitted into existing gas fueled devices such as ovens, furnaces, boilers, etc., where syngas may replace fossil fuels. Heating values of syngas are generally around 4-10 MJ/m3. In small business and building applications, where the wood source is sustainable, syngas from wood and burn it in reciprocating engines connected to a generator with heat recovery for electrical power generation.

Thus attempts have been made in several saw dust producing countries in Asia to develop continuous saw dust gasification plants. However, this technology is still not well proven till today and the problems are still arising even in the commercial systems. Further research and development work needs to be undertaken to improve this technology.

Nomenclature

IGCC	Integrated Gasification Combined Cycles
EERC	Energy and Environmental Research Center
DDGF	Down Draft Gasifier Fabrication
SGR	Specific Gasification Rate
SSR	Specific solid flow rate

2. The Gasifier Unit

Gasification is a process in which solid biomass fuels are broken down by the use of heat in an oxygen-starved environment, to produce a combustible gas. Biomass fuels that can be gasified include wood, charcoal, rice husks, coconut shells and a variety of other dry biomass materials. A biomass gasification system consists primarily of a reactor into which fuel is fed along with a limited (less than stoichiometric or that required for

complete combustion) supply of air. Heat for gasification is generated through partial combustion of the feed material. The resulting chemical breakdown of the fuel and internal reactions result in a combustible gas usually called "producer gas". The heating value of this gas varies between 4.0 and 6.0 MJ/m^3.

The gasifier was designed as shown in figure 1 and fabricated using the available materials in Bangladesh so that the system can be constructed at any corner of the country economically.

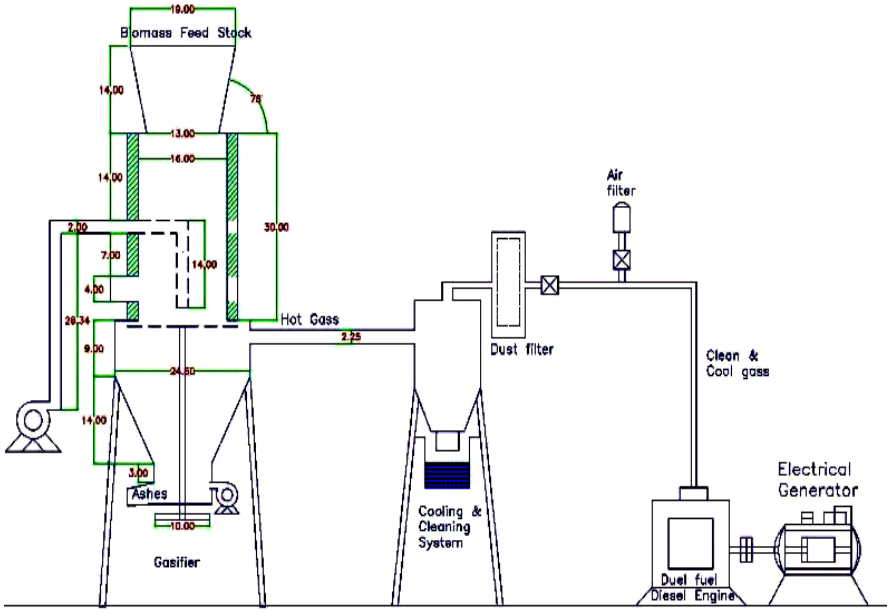

Fig.1. Design of the Down Draught Wood Gasification System

a)

b)

Fig. 2. (a) Scraper (b) Flame after Gasification

Gasification is a physicochemical process in which chemical transformations occur along with the conversion of energy. The chemical reactions and thermo chemical conversions, which occur inside a wood gas generator, are too long and too complicated to discuss here; however, a detailed knowledge on that is not necessary for constructing and operating a wood Gasifier. By weight, the gas (wood gas) produced in a gasifier unit contains approximately as follows:

- Carbon monoxide, CO – (15-27)%
- Hydrogen, H_2 – (10-22)%
- Methane, CH_4 – (1-3)%
- Carbon dioxide, CO_2 – (20.3)%
- Water vapor, H_2O – (2.50)%
- Nitrogen, N_2 – rest.

Only three first gases (marked with green color) are combustible. The rest is not combustible and may be considered as impurity, diluting the wood gas and decreasing its heating value. That is why it is good idea to

remove those gases. One cannot remove the nitrogen from the wood gas (it is the main component of air, which is used as "gasification agent"), removal of water vapor is rather easy (it condenses when gas is being cooled). The carbon dioxide content depends on the temperature side the gasifier (the higher the temperature, the lower the CO_2 content). Gasification is a way of manufacturing gaseous fuel from biomass like anaerobic digestion (which gives methane), but it is an instant thermochemical process in contrast to rather slow biological digestion.

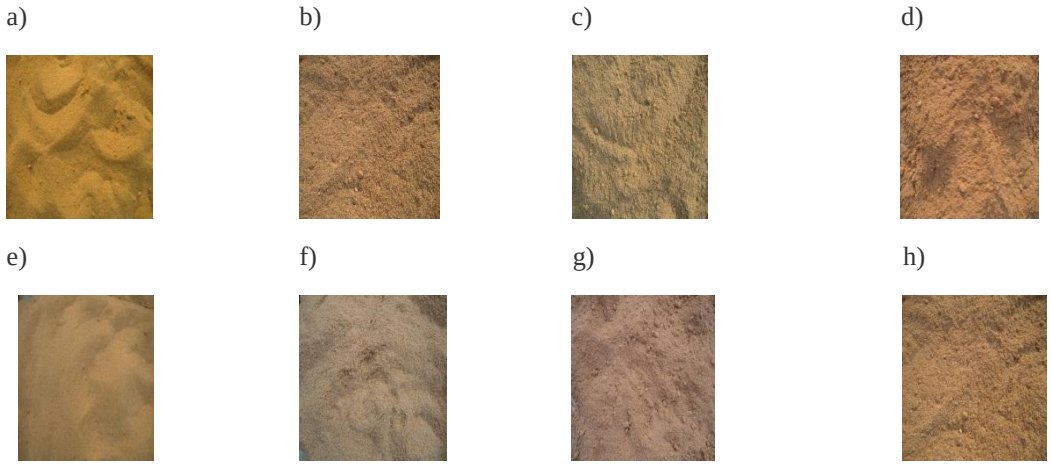

Fig. 3. Different sawdust (a) Jackfruit (b) Olive (c) Mango (d) Mahogany (e) Teak (f) Jumbline (g) Gamary (h) Rain tree

2.1. Main Components of Gasifier :

- Hopper
- Reactor (800^0C – 1400^0C)
- Scraper (10 microns)
- Blower (1 hp)
- Char chamber (150^0C – 250^0C)
- Thermocouple (K type)
- Gas analyzer (Digital)
- Air flow meter
- Radiator
- Dust filter
- Air filter
- Reservoir (Cylinder type)

2.2. Processes occurring in the down draught gasification:

In the downdraught gasifier, the fuel is introduced at the top, the air is normally introduced at some intermediate level and the gas is taken out at the bottom. It is possible to distinguish four separate zones in the gasifier, each of which is characterized by one important step in the process of converting the fuel to a combustible gas. The processes in these four zones are examined below and the design basis will be discussed in the following section.

2.2.1. Working zones of Gasification:

- Drying zone
- Pyrolysis Zone (250°C – 500°C)
- Oxidation Zone (800°C – 1400°C)
- Reduction zone (600°C – 700°C) endothermic.

3. Biomass characteristics related to gasification

Each type of biomass has its own specific properties, which determine its performances a fuel in gasification plants. The most important properties relating to gasification are:

- moisture content,
- ash content (6.25%),
- elemental composition (low nitrogen and sulphur)
- bulk density and morphology (4.1 kg /hr)
- volatile matter content (50- 80)%.

3.1. Mass balance:

The mass and energy balances were determined measuring the sawdust quantity, the gas flow, solid wastes (charcoal and ash), LPG quantity and secondary air. The total dry air is determined to close the mass balance and the sawdust, while the air moisture determines the water quantity Equivalence Ratio (ER). ER fixes the amount of air supplied for gasification and is defined as the ratio of oxygen supplied per kilogram of wood to the stoichiometric requirement. A value of 0.3 ER is the theoretical optimum.

3.1.1. Specific gasification rate (SGR)

SGR is the volumetric flow rate of gas per unit area based on Exhaust pipe diameter (the gas volume is measured at the standard conditions).

3.1.2. Specific solid flow rate (SSR):

SSR is the fuel mass flow measured at the throat and it is a derived parameter which can be obtained from SGR. As one kilogram of wood gives approximately 2.5 m^3 of the producer gas, SSR can be related to SGR as SGR/2.5

3.2. Chemical Reaction occur into Gasification system:

In the oxidation zone:

$$C + O_2 = CO_2 + 401.9 \text{ kJ/mol} \quad (1)$$

$$H + O_2 = H_2O + 241.1 \text{ kJ/mol} \quad (2)$$

In the reduction zone:

$$C + CO_2 + 164.9 \text{ kJ/mol} = 2CO \quad (3)$$

$$C + H_2O + 122.6 \text{ kJ/mol} = CO + H_2 \quad (4)$$

$$CO_2 + H_2 + 42.3 \text{ kJ/mol} = CO + H_2O \quad (5)$$

$$C + 2H_2 = CH_4 \quad (6)$$

$$CO + 3H_2 = CH_4 + H_2O + 205.9 \text{ kJ/mol} \quad (7)$$

Heating value of wood saw dust can be calculated as equation (8)

Heating value per one gm. of fuel= (Heat absorbed by calorimeter - heat released from fuse wire) (8)

=(1900+432)gm.×1 Cal/gm.× ΔT-2.3 Cal/cm×10 cm

ΔT=1.92℃

Unburned wire=1.5cm= 18.72 MJ/kg.

Excess air to be obtained from equation (9)

$$\% \text{ Excess Air} = \frac{\%O2\ measured}{(20.9 - \%O2\ measured)} \times 100 \quad (9)$$

Combustion Efficiency can be calculated using equation (10)

Although combustion efficiency cannot be measured directly, it can be calculated by

Identifying all of the losses that occur during combustion. It is important to consider all factors including sensible heat losses, unburned gases, radiation, and unburned particles. In most instances, the values of the skin losses and latent heat losses are not taken into account. The following equation can be used to calculate combustion efficiency,

$$\text{Efficiency (\%)} = 100\% - \left(\frac{\text{Total Heat losses}}{\text{Fuel heating value}}\right) \times 100 \quad (10)$$

After gasification process the burning wood dust (Ash) can be calculated from (11)

$$\text{Ash content} = \frac{Weight\ of\ burned\ dust}{Weight\ of\ saw\ dust} \times 100 \quad (11)$$

$= \frac{5}{80} \times 10 = 6.25\%$ (Experimental value).

4. Results and Discussion

Results obtained in this research work are presented in following figures. Figure 4 – 8 show the graphical representations of different characteristic parameters for the gasification system.

Fig. 4(a) shows the calorific value of different types of woods. Where jackfruit shows the highest energy content and teak is second in place. In figure 4(b) moisture and ash contents are portrayed for different woods. Moisture contents are almost same for all of them. However, ash content is maximum in olive, which has negative impact in performance as a fuel.

a) b)

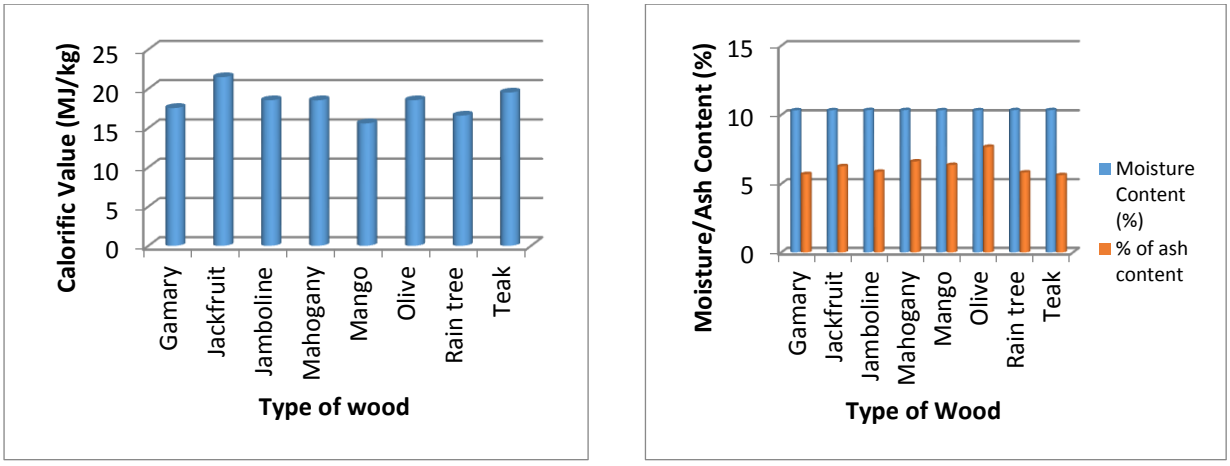

Fig. 4. (a) Calorific values and (b) Moisture and Ash contents of sawdusts

Teak has the lowest fuel consumption rate, while jackfruit and gamari are moving side by side with good potential as a fuel depicted in Figure 5(a). From fig. 5(b) to 7(a), different particle contents (CO, CH_4, SO_2, and NO_x), after gasification, are presented as function of inlet air velocity. All the woods show almost similar characteristics with change in inlet air velocity. Mango has the minimum CO and CH_4 content while the others change their positions at different temperatures. Among them jackfruit shows better position among them. On the other hand, rain tree has the highest SO_2 and NO_x at almost all temperature. Again, jackfruit gives better output with minimum SO_2 and gamari, jamboline, mango, jackfruit, and mahogany gives very low NO_x.

a) b)

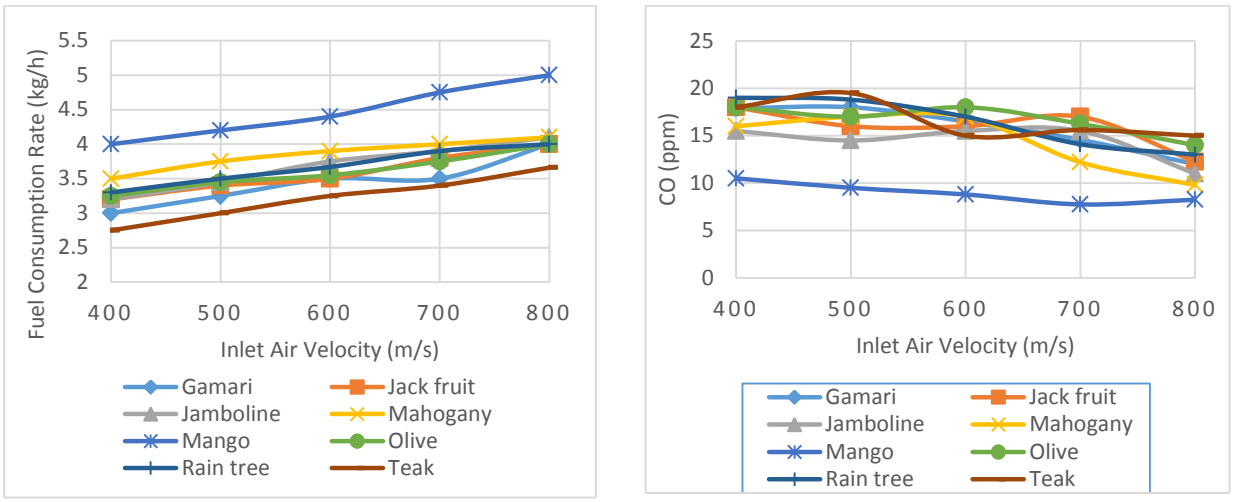

Fig. 5. (a) Fuel consumption characteristics and (b) CO content for different sawdusts

a) b)

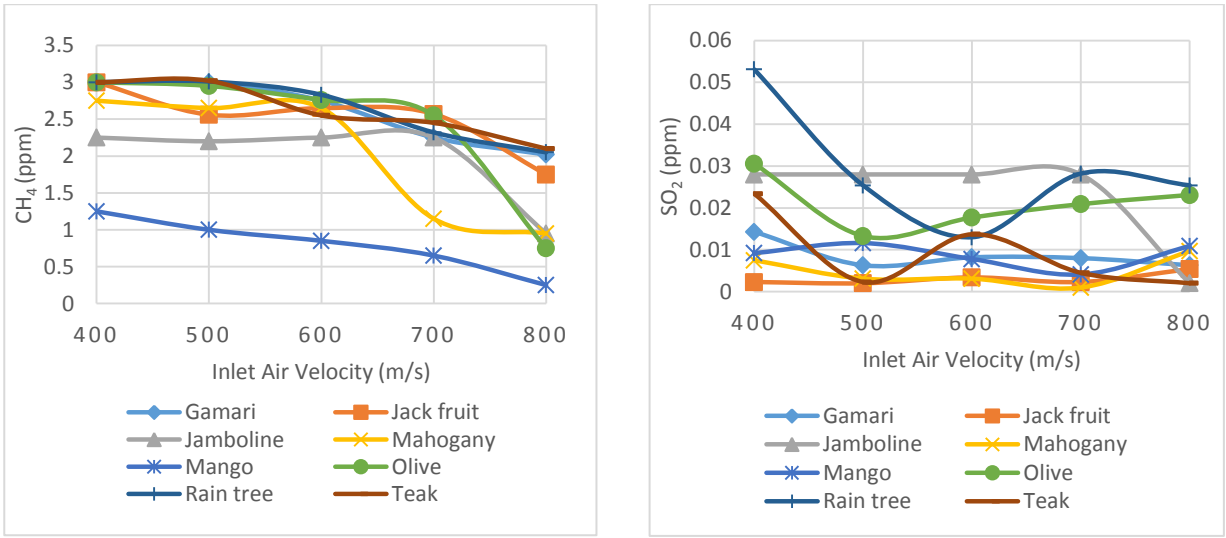

Fig. 6. (a) CH_4 content and (b) SO_2 content in diferent sawdusts

a) b)

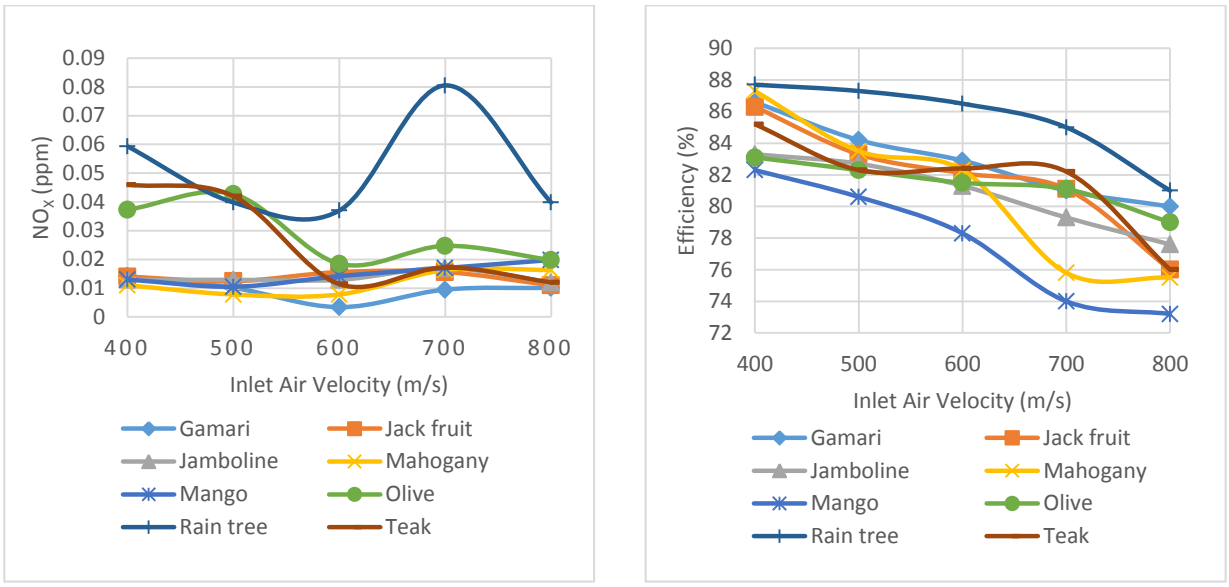

Fig. 7. (a) NO_x production with air inlet velocity and (b) Efficiency characteristics for different sawdusts

In efficiency trend lines in figure 7(b), mango gives lowest efficiency at all temperature and rain tree is just the opposite of mango. Gamari is the second in command. Figure 8(a) shows the temperature variation with the variation of inlet air velocity for saw dusts. The produced temperature with the time during gasification is also presented in figure 8(b) are obtained from bomb calorimeter.

a) b)

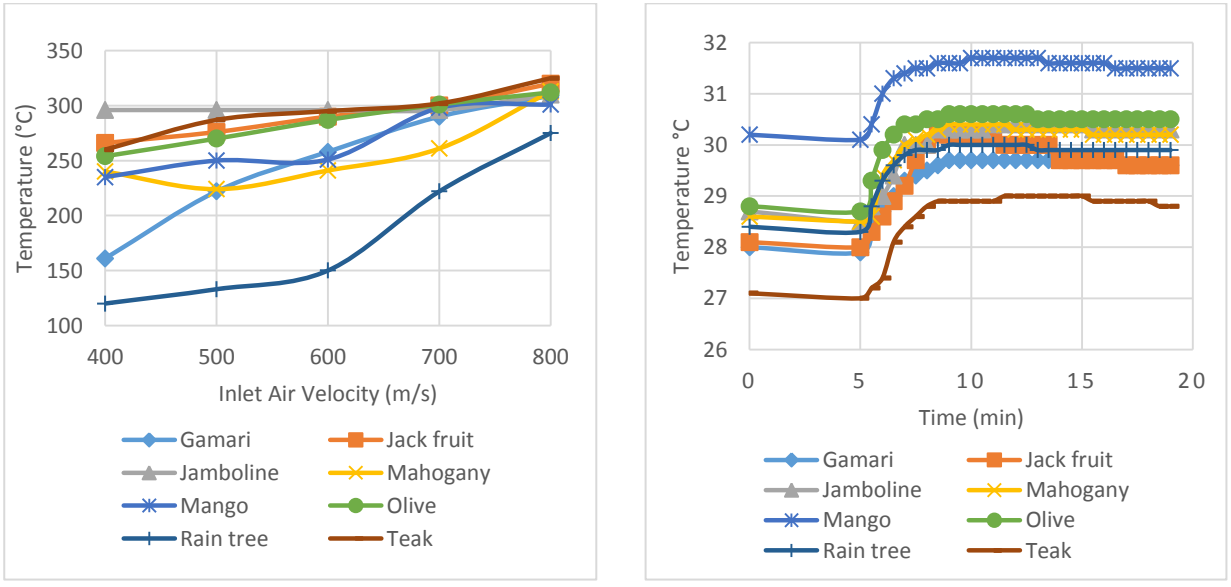

Fig. 8. (a) Temperature variation with change in inlet air velocity and (b) Time Temperature for different sawdusts

In summary, the mango wood should be rejected as a fuel on the contrary jackfruit and teak has a very good potential for future alternative bio-mass fuel. It is evident from the diagram that at lower air inlet speed the performance of the system is more effective.

5. Conclusions

Saw dust as solid biomass fuel suitable for gasification .In that case eight types of sawdust was used to determine the biomass characteristics of saw dust as solid biomass fuel, Saw dust are composed primarily of carbon with varying amounts of hydrogen, oxygen, and impurities, such as sulfur, nitrogen oxide, ash, and moisture. Thus, the aim of gasification is the almost complete transformation of these constituents into gaseous form so that only the ashes and inert materials remain. Temperature of the different zone of gasifier was determined by thermocouple .The temperature of the drying zone was (75 – 85) °C, at temperatures 250°C-500°C, pyrolysis of the biomass fuel starts. A burning (oxidation) zone is formed at the level where oxygen (air) is introduced. Reactions with oxygen are highly exothermic and result in a sharp rise of the temperature up to (800 – 1400) °C.

The reaction products of the oxidation zone (hot gases and glowing charcoal) move downward into the reduction zone. These reactions are endothermic – the reduction requires heat and so, the gas temperature decreases (app. 600 – 700 C). Temperature is maximum in the combustion chamber800℃-1400℃, outer shell temperature of the reactor is about 500℃-700℃. Flame temperature of the gas is450℃ – 620℃, Exhaust gas temperature was different with different inlet air velocity as shown in table. Heating value of different sawdust was different. Calorific value of all saw dust sample was determined by oxygen Bomb calorimeter. Heating value of mango wood is lower and higher is jack fruit tree, on the other hand heating value of another sample is slightly variation with each other .It was conclude that Heating value of hard wood is higher and soft wood is lower. Solid sawdust fuel is converted to gaseous fuel with different mass concentration and the emission of gas composition was determined using exhaust gas analyser. It was displayed in tabular form in the previous section. With the help of the chemical analysis, it was decided that combustible gas is produced by mango tree is small, and other sample is almost same with good percentage. Air velocity was determined by anemometer, when excess air is high and combustible gas composition is limited hence flame not be stable and on the other hand excess air is small amount then combustible gas composition is good with stable flame. Finally recommended that Small air velocity is required for achieve continuous flow of combustible gas production and higher efficiency of gasifier and lower fuel consumption.

There is little net production of carbon dioxide, the major greenhouse gas, from wood combustion. Because the carbon dioxide generated during combustion of wood equals the carbon dioxide consumed during the life cycle of the tree.

Wood fuel contains minimal heavy metals and extremely low levels of sulfur, hence wood fuel is no threat to acid rain pollution. Usually wood ash is less than 1% of the weight of the wood if moisture content possible to maintained 1 to 2 percent. Sometimes ash may be used in biomass fertilizer production. However, experimental value of ash content was different for sample of sawdust for the reason of moisture content and combustion efficiency of the gasifier and the ash content amount was near about 5.7% to 7.69 %. The principle economic advantage of wood burning systems is that wood fuel is usually less expensive than competing fossil fuels.

Advantages of sawdust as fuel:

- Renewable: Wood fuel has several environmental advantages compared with fossil fuels. Wood can be continually replenished, which leads to a sustainable and dependable supply. However, proper forest management must be practiced to ensure that growing conditions are not degraded during biomass production.
- Low carbon emission: There is little net production of carbon dioxide, the major greenhouse gas, from wood combustion. Because the carbon dioxide generated during combustion of wood equals the carbon dioxide consumed during the life cycle of the tree. Transporting the material using petroleum generates excess carbon dioxide.
- Minimal metal and sulphur: Wood fuel contains minimal heavy metals and extremely low levels of sulphur; wood fuel is no threat to acid rain pollution.
- Minimal Ash: Particulate emissions from wood are controllable through standard emission control devices such as bag houses, cyclone separators, and electronic precipitators. Bottom ash is minimal usually wood ash is less than 1% of the weight of the wood and sometimes ash may be used as a fertilizer biomass production.

The combustion process is extremely dependent on time, temperature, and turbulence. Time is important to combustion because if a fuel is not given a sufficient amount of time to burn, a significant amount of energy will

be left in the fuel Wood fuel has several environmental advantages compared with fossil fuels. Wood can be continually replenished, which leads to a sustainable and dependable supply.

References

[1] Food and Agriculture Organization. Yearbook Production 1995. Rome: FAO, 1996.
[2] Beagle E. Rice husk conversion to energy. In:Agricultural Services Bulletin, 31. Rome, Italy: FAO,1978.
[3] Kapur T, Kandpal TC and Garg HP. Electricity Generation from Rice Husk in Indian Rice Mills: Potential and Financial Viability. Biomass and Bioenergy 10(5/6), pp. 393-403, 1996.
[4] Boateng AA, Walawender WP, Fan LT, Chee CS. Fluidized bed steam gasification of rice hull. Bioresource Technology 1992;40(2):235-9.
[5] The Energy and Environmental Research Center. A History of Biomass Experience and Expertise. EDGE 2007; 18(1).
[6] Mansaray KG, Ghaly AE, Al-Taweel AM, Hamdullahpur F, Ugursal VI. Air gasification of rice husk in a dual distributor type fluidized bed gasifier. Elsevier Science Ltd. Biomass and Bioenergy 1999;17:315-32.
[7] SAN SAN INDUSTRIAL Cooperative., Ltd., Myanmar. Accessed 20 Feb 2005. http://www.benergyssic.com/sansanrice.htm
[8] Alexis TB, Daniel AHB, Lucio L. Continuous-flow rice husk gasifier for thermal applications. 10th PCIERD Regional S&T Fora and Competition February 26, 2010;
[9] Bhattacharya S.C., Attalage R.A., Augustus Leon, M., Thanawat. C, Potential of Biomass Fuel Conservation in Selected Asian Countries. Energy Conversion and Management, Volume 40, Issue 11, July 1999, Pages 1141-1162.
[10] IEA Bioenergy Agreement. Task 33: Thermal Gasification of Biomass; Technology Brief: Fixed Bed Gasification. http://www.gastechnology.org/webroot/downloads/en/IEA/FixedBedGasificationr.pdf (accessed 20 Feb 2005).
[11] Reed T. Ba., and Walt Rb, The "Turbo" Wood-Gas Stove. The Biomass Energy Foundation, 1810 Smith Rd., Golden, CO 80401; Community Power Corporation, Aurora, CO.1998.http://www.ikweb.com/enuff/public_html/Turbo/Turbo.htm.
[12] Anderson, Paul S., The Origins of the Juntos Gasifier Stoves.Dept of Geography-Geology, Illinois State Univ., Normal, IL 61790-4400, 2002.
[13] TERI, Gasifier for large-scale cooking applications. http://www.teriin.org/division/eetdiv/docs/products/cooking.htm (accessed on 20 Feb 2005).
[14] F. P. Zimmerman, Oak Ridge National Laboratory, Energy Division, FEMA Interagency Agreement Number: EMW-84-E-1737 Work Unit: 3521 D.Federal Emergency Management Agency, Washington, D.C. 20472
[15] Stassen, H.E.M.; UNDP/World Bank Small Scale Gasifier Monitoring Report, Volume1-Findings, Biomass Technology Group, The Netherlands (1993)
[16] Ministry of the Environment. Environmentally Related Energy Taxation in Finland.[Online] (Updated 8 July 2008) Available at: http://www.environment.fi/de- fault.asp? contentid=147208&lan=en [Accessed 21 April 2009
[17] Niessen, W.R.,. Combustion and Incineration Processes. Third Edition, Revised and Expanded. New York: Marcel Dekker, Inc. 698 p. ISBN 0-8247-0629-3, 2002.

6th BSME International Conference on Thermal Engineering (ICTE 2014)

Developing an Alternative Power Source for Hybrid Car

A.A. Safe[a], M. Moniruzzaman[b],M.R.C.Dipu[c] and M. T. Islam[d]
[a,b,c]*Student, Department of Mechanical Engineering, CUET, Chittagong-4349, Bangladesh*
[d]*Professor, Department of Mechanical Engineering, CUET, Chittagong-4349, Bangladesh*

Abstract

Abstract: This paper is focused on a hybrid vehicle technology that uses wind energy as an alternative source of power. There is described a process that can be used to extract energy from the wind and add to a vehicle for producing driving force. Usually a car moves through air which always is a disadvantage as it produces a drag force while moving forward which resist the driving force. In a research we used this air flow to generate electricity using a vertical axis wind turbine. This electricity can be used to charge a battery which would provide energy to drive a vehicle. We used a vertical axis wind turbine of Darrieus type to receive energy from the wind. If some VAWTs are placed at location that won't increase drag area of the vehicle a good amount of electricity will be generated without adding any significant resistive force.

Key words: Vehicle, Turbine, Wind, Power, RPM, Research, Battery, Electricity

1. Introduction

A hybrid electric vehicle (HEV) has two types of energy storage units, electricity and fuel. Electricity means that a battery (sometimes assisted by ultra-caps) is used to store the energy, and that an electromotor (from now on called motor) will be used as traction motor. Fuel means that a tank is required, and that an Internal Combustion Engine (ICE, from now on called engine) is used to generate mechanical power, or that a fuel cell will be used to convert fuel to electrical energy. In the latter case, traction will be performed by the electromotor only. In the first case, the vehicle will have both an engine and a motor.on this contrary we would like to introduce wind power to the hybrid car as solar power is introduced so far.To do so we designed a turbine and power generation system to develop an alternate power source for hybrid car**.** We would set up VAWT in front of radiator through some arrangements. Thus while vehicle will move on and it will cut though wind layer, VAWT will generate power for vehicle. Even while vehicle's engine on but it's not moving on but our system can produce power for vehicle through the help of radiator fan . In this qualitative research we fabricated a VAWT with smart blade and an alternator which consists a stator of armature and revolving magnetic field which is coupled with VAWT And also the total arrangement how it will be more efficient and it will work on while the vehicle is moving on or not.Through this arrangement we can get power from this system from while it will moving or stand by at any traffic.

2. TURBINE PARAMETER

2.1 Swept Area

$$S = 2\,R\,L \quad (1)\ [1]$$

where S is the swept area [m2], R is the rotor radius[m], and L is the blade length [m].

2.2POWER

$$Pw = \tfrac{1}{2}\,\rho\,s\,V_o^3 \quad (2)\ [1]$$

Peer-review under responsibility of organizing committee of the 6th BSME International Conference on Thermal Engineering (ICTE 2014).

where Vo is the velocity of the wind [m/s] and ρ is the air density [kg/m3], can be consulted.

2.3 Tip Speed Ratio.

$$TSR=R* \omega / V_o \quad (3)\ [1]$$

where ω is the angular speed [rad/s], R the rotor radius [m] and Vo the ambient wind speed [m/s]. Each rotor design has an optimal tip speed ratio at which the maximum power extraction is achieved.

2.4Blade Chord

The chord is the length between leading edge and trailing edge of the blade profile

2.5 Number of Blades

Blade No. has a direct effect in the smoothness of rotor operation and it compensates cycled aerodynamic loads.

2.6 Angle of Attack, Pitch Angle

Angle of attack which is a dynamic angle, depending on both the speed of the blade and the speed of the wind. The pitch angle is the angle between the chord line of the blade and the plane of rotation. Even the blades were twisted to improve the efficiency. When the blade is twisted, the pitch angle will change from hub to tip. [2]

Table1:VAWT parameter

Parameter	**Turbine**
Blade length(bl)	.48m
Chord length(cl)	.07m
Rotor radius	0.1m
Rotor height	.48m
Swept area	.096m^2
Angle of attack(degree)	50˚-80˚
Pitch angle(degree)	120˚
Blade number	3
Co efficient of lift(C_l)	0.75
Co efficient of drag(C_d)	1.7

3. WORKING PRINCIPLE OF TURBINE

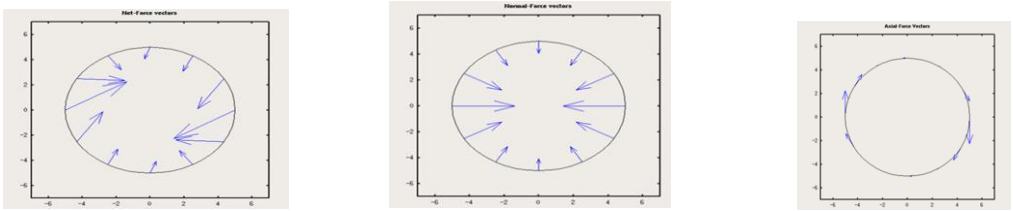

(a) (b) (c)

Fig.1: Force Diagram: a) Net force vectors; b) Normal force; c) Axial force

The action of this apparent flow on each foil section generates both a lift and drag force, the sum of which is shown in the Fig. 2(A). Each of these net force vectors can be split into two orthogonal vectors: a radial component and a tangential component, shown here as "Normal force" as in Fig. 2(B) and "Axial force" in Fig. 2(C) respectively. The normal forces are opposed by the rigidity of the turbine structure and do not impart any rotational force or energy to the turbine. The remaining force component propels the turbine in the clockwise direction, and it is from this torque that energy can be harvested [3].

3.1 Lift and Drag Force

The lift and drag forces can be calculated using the following equations, respectively [4].

$$F_l=.5* \rho*W*cl*bl* C_l \quad (4)$$

$$F_d=.5* \rho*W*cl*bl* C_d \quad (5)$$

Where

F_l: lift force (N)

F_d: drag force (N)

bl: blade length (m)

C_l: lift coefficient

C_d: drag coefficient

W: wind speed

The lift and drag forces were then resolved into components parallel and perpendicular to the blades path of rotation. The following four equations were used to resolve the lift and drag forces into parallel and perpendicular components [4].

$$F_{l,help} = F_l \cos\left[\left(\frac{90\pi}{180}\right) - \left(\frac{\alpha\pi}{180}\right)\right] \quad (6)$$

$$F_{l,circ} = F_l \sin\left[\left(\frac{90\pi}{180}\right) - \left(\frac{\alpha\pi}{180}\right)\right] \quad (7)$$

$$F_{d,hurt} = F_d \cos\left(\frac{\alpha\pi}{180}\right) \quad (8)$$

$$F_{d,circ} = F_d \sin\left(\frac{\alpha\pi}{180}\right) \quad (9)$$

Finally, parallel forces are added, and perpendicular forces are added to obtain expressions for F1 and F2, as given by equations [4]

$$F_1 = F_{l,help} - F_{d,hurt} \quad (10)$$

$$F_2 = F_{l,circ} + F_{d,circ} \quad (11)$$

Where

F_1: forces contributing to torque (N)

F_2: centrifugal forces (N)

The resulting forces, F1 and F2, are the forces experienced by a turbine with one blade rotating about a central axis. [1].

4. ALTERNATOR PARAMETER.

4.1Frequency:

The frequency of any ac generator in hertz (Hz), which is the number of cycles per second, is related to the number of poles and the speed of rotation, as expressed by the equation.[5]

$$F = N*P/120 \quad (12)$$

Where P is the number of poles, N is the speed of rotation in revolutions per minute (rpm), [5]

4.2Equation of Induced EMF:

Max $emf_{ind} = NAB\omega$ [6]

N=turn number

A=cross section area

B= magnetic flux density

ω= angular speed

$$B = emf_{ind}/(N*A*\omega) \quad (13)$$

$$\Phi = B*A \quad (14)$$

Φ= Flux pole in webers

Let,

Z= No. of conductors or coil sides in series/phase=2T

T= No. of coils or turns/phase (remember one turn or coil has two sides)

P= No. of poles

f= Frequency of induced emf in Hz

Φ= Flux pole in webers

N= rotor rpm

Average emf induced per conductor=2f Φ (15) [7]

If there are Z conductors in series/phase, then average emf/phase= 2fΦZ volt=4 fΦT volt (16)

RMS value of emf/phase =1.11×4 fΦT volt= 4.44fΦT (17)[7]

Table2: Alternator parameter

Parameter	**Alternator**
Number of poles	16
Spacing of pole	22.5degree
Armature wire diameter	28gage
Turn number of each Coil	200(min)
Coil Number	16
Coil shape	Oval shape

5. DESIGN AND FABRICATION

6.1Design:

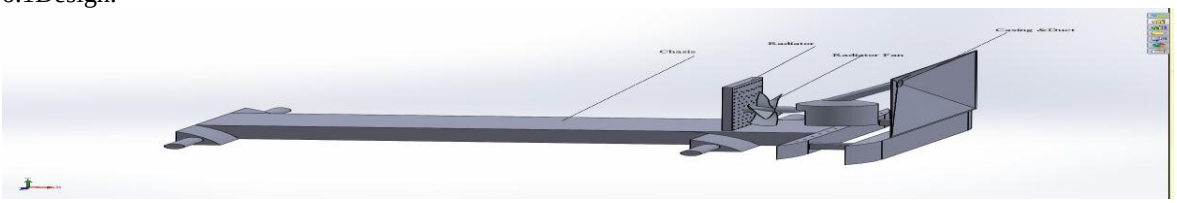

Fig2: Ideal set up for VAWT with Chassis

Our desired design is to install a VAWT in front of radiator which will be mounted on chassis. But due to unavailability of further assistance from all resources we managed to establish a scenario as much as possible to close to our design and also to increase its performance, we assembled a casing with it.as a raw concept we can show our imagination through this picture.

We are unable to manufacture this design. But we created the same scenario of the vehicle and other parts of VAWT. We introduced radiator fan, VAWT, casing, alternator etc.to manufacture the same scenario which is enough to establish the concept. the three different parts to complete this research are

1. VAWT
2. Alternator
3. Casing

Here we will demonstrate each part of this design and fabricated parts with description.

5.2 Fabrication

Fig.3: Flow chart of total procedure

5.2.1Turbine:

VAWT Materials: 1.Aluminum, 2.Stainless steel(ss), 3.Bearings 4. Bolts connections

According to the précised dimensions which we figured out earlier, we molded and casted the turbine's rotor and shaft by aluminum. The design of the blade is the complicated and smart so we molded it with ss with précised dimensions. The twisted blade got inclination of 54degree from horizontal axis. Then we assembled all the parts of the turbine, to form the turbine.

Blades are connected with rotor by screw joints. We used a holder to hold the turbine the turbine.

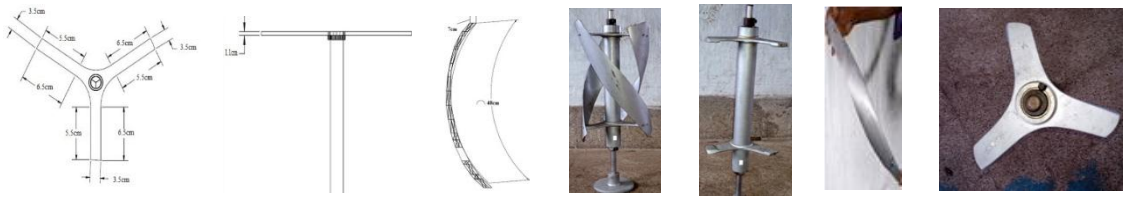

(a) (b) (c) (d) (e) (f) (g)

Fig4: Various components of Turbine Designed: a) Rotor B) Hub thickness C) blade. Fabricated:d) VAWT, e) Rotor &shaft F) Twisted blade,e)Hub.

5.2.2Alternator:

Materials: 1. Permanent magnet, 2.Copper wire, 3.Acrolyte plate, 4. Silicon glue, 5.Screw and nuts

Alternator got two parts 1.stator, 2.rotor.In rotor 16magnets is attached in circular disk, which equally spaced 22.5 degree from each other. Rotor's back part covered with the Teflon and hose pipes to increase reluctance of the magnate in that direction. Stator consists of 16 coils of 28gage copper enameled wire and each coil got

200 windings. We tried to set close the stator and rotor as close as possible but still about 1.5cm causes poor performance.

6. Experimental Setup

We positioned all components' as far demonstrated in figure. Then we used various wind sources to get various wind speed. The wind source is placed at the cone and tachometer meter is used to get rpm and anemometer to get wind speed, multimeter to get voltage, current and resistance. We also placed radiator cooling fan at various distance to see the impact.

(a) (b) (c) (d) (e) (f) (g)

Fig5:a)Rotor disk,b)stator disk,c)Radiator fan & casing,d)side view of total set up,e)Rear view ,f) VAWT attached with alternator,g)conical inlet.

7.Result

Table 2 : Vehicle Standby

Distance from Radiator Fan (inch)	RPM
2	136
3	110
4	87
5	66
6	34
7	12
8	0

Table 3: Turbine's Characteristics Using equations 1, 2 & 3,4,5,6,7,8,9,10,11. Radiator distance = 3inch,

Wind Speed (m/s)	RPM	TSR	Power in wind	lift force F_b(N)	drag force F_d,(N)	$F_{L\ help}$	$F_{L\ circ.}$	$F_{D\ hurt}$	$F_{D\ circ.}$	$F_1 = F_{L\ help} - F_{D\ hurt}$	$F_2 = F_{L\ circ.} - F_{D\ circ.}$
5.2	128	0.026	7.627	0.385	0.873	0.3489	0.1627	0.3688	0.7909	-0.0199	-0.6282
6.8	160	0.025	17.055	0.658	1.492	0.5967	0.2782	0.6307	1.3525	-0.0340	-1.0742
7.3	200	0.029	21.100	0.759	1.720	0.6877	0.3207	0.7268	1.5587	-0.0392	-1.2380
8.7	280	0.034	35.717	1.078	2.443	0.9767	0.4554	1.0323	2.2139	-0.0556	-1.7584
9.9	350	0.037	52.629	1.395	3.163	1.2647	0.5897	1.3368	2.8667	-0.0720	-2.2770
11.4	382	0.035	80.359	1.850	4.194	1.6770	0.7820	1.7725	3.8012	-0.0955	-3.0192
14.7	488	0.035	172.29	3.077	6.974	2.7884	1.3003	2.9473	6.3204	-0.1588	-5.0202
15.8	535	0.035	213.94	3.554	8.057	3.2214	1.5021	3.4049	7.3017	-0.1835	-5.7996

Table 4: Alternator's Output using equation 12,13,14,15,16,17

Wind Speed (m/s)	Voltage (with transformer)	Voltage (without transformer), V	Current, I	Power, P=VI	Frequency (Hz)	Average emf induced per conductor (volt)	Average emf/phase (volt)	RMS value of emf/phase (volt)
5.2	16.694	1.3845	0.027	0.0374	17.0622	0.0128	0.2048	0.2303
6.8	22.9084	1.8997	0.0366	0.0695	21.3278	0.0160	0.2560	0.2879
7.3	30.6764	2.5437	0.0486	0.1236	26.6598	0.0200	0.3200	0.3599
8.7	46.2124	3.8317	0.0726	0.2782	37.3238	0.0281	0.4480	0.5039
9.9	59.8064	4.9587	0.0936	0.4641	46.6548	0.0351	0.5600	0.6299
11.4	66.0208	5.4739	0.1032	0.5649	50.9204	0.0383	0.6112	0.6875
14.7	86.606	7.1805	0.135	0.9694	65.0502	0.0489	0.7808	0.8783
15.8	95.7334	7.9372	0.1491	1.1834	71.3153	0.0536	0.8560	0.9629

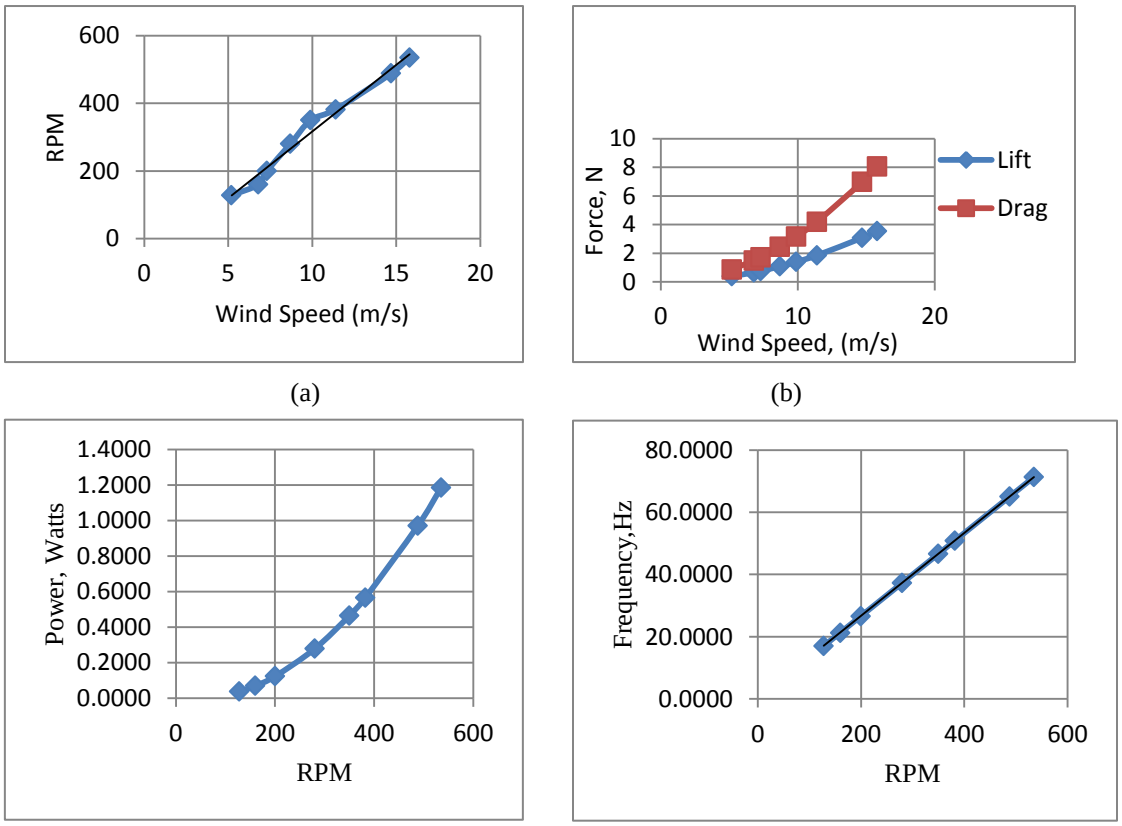

Fig6**:** Graphs a) wind speed vs. RPM , b)wind speed vs lift force & drag force ,c) RPM vs Power d) RPM vs frequency

8.Discussion & conclusion

If we manufacture better casing and make air flow one direction through structure we will be able make much better and perfect structure for the desired design. If we can introduce frictionless bearing we can produce more power from our generator. We had to design much more qualitative alternator to get more current through it. We will work on our casing a lot, because this structure is the least affirmative for our desired design. If we mount this turbine on vehicle we can get more pragmatic data. We are still working on it to improve it.so far we would like to add that if we able to make full structure more aerodynamic we must get most pragmatic result.

9.Acknowledgment

During this project we are highly helped and co-operated by a couple of teachers of the mechanical department and lab assistants. We like to especially grateful to Professor Dr. Sajal Chandra Banik. We are always ought to show proper respect to our department and Mr. Gaffar for engineering works..

References

[1]] J Castilo “Small scale vertical axis wind turbine Design upcommons.upc.edu/pfc/bitstream/2099.1/19136/4/memoria.pdf [2] W. Strunk Jr., E.B. White, The Elements of Style, third ed., Macmillan, New York, 1979.
[2] G. L. Johnson “Wind Energy Systems”
[3] www.wikepedia .com
[4] MECH 4010 Design Project
Vertical Axis Wind Turbine J D Coste, D McKay ,B Robinson, and S W, S
[5] Chapter 3Alternating Current Generators,14177_Ch3.Pdf
[6] http://newburyparkhighschool.net/wright/Physics/powerpoints/19_generators.pdf
[7]] B. L. Theraja, A. K. Theraja, “A Textbook of ELECTRICAL TECHNOLOGY in SI Units Volume II, AC & DC Machines”, S. Chand & Company Ltd

6th BSME International Conference on Thermal Engineering (ICTE 2014)

Study of 3D Heat Transfer through a Solar Collector: Effect of Solid Volume Fraction

Rehena Nasrin*, Salma Parvin and M.A. Alim

Department of Mathematics, Bangladesh University of Engineering and Technology, Dhaka - 1000, Bangladesh

*E-mail: raity11@gmail.com

Abstract

A three-dimensional heat transfer model is developed in which direct sunlight is incident on transparent glass cover of a flat plate solar collector (FPSC). Due to renewable and nonpolluting nature of solar energy it is often used in applications such as electricity generation, thermal heating and chemical processing. “Flat-plate” type solar collectors are the most cost effective. Water/copper nanofluid is used as the heat transfer medium. The governing partial differential equations are solved using finite element method with Galerkin’s weighted residual technique. In order to evaluate the fluid flow and temperature profiles within the collector, the mass, momentum and energy balance equations are solved numerically. Average Nusselt number (Nu), average temperature (θ_{av}), collector efficiency (η), outlet temperature (T) for both nanofluid and base fluid through the collector are presented as function of the parameter mentioned above. It is observed that the highest rates of heat transfer and thermal efficiency are obtained at 2% solid volume fraction of Cu nanoparticles. Heat transfer rate and collector efficiency using nanofluid become higher than that of using pure water.

Keywords: Flat plate solar collector, finite element method, nanofluid, collector efficiency and rate of heat transfer.

1. Introduction

Solar flat plate collectors are commonly used for domestic and industrial purposes and have the largest commercial application amongst the various solar collectors. This is mainly due to simple design as well as low

Peer-review under responsibility of organizing committee of the 6th BSME International Conference on Thermal Engineering (ICTE 2014).

maintenance cost. Solar radiation is radiant energy emitted by the sun. It is particularly electromagnetic energy. Solar irradiance (I) is the combination of bright light and radiant heat. Heat transfer due to emission of electromagnetic waves is known as thermal radiation. The heat transfer rate per unit area as thermal radiation is called radiative heat flux. Forced convection is a mechanism in which fluid motion is generated by an external source. Significant amounts of heat energy can be transported very efficiently by this system and it is found very commonly in everyday life, including central heating, air conditioning, steam turbines and in many other machines. The fluids with solid-sized nanoparticles suspended in them are called “nanofluids”. Applications of nanoparticles in thermal field are to augment warmth transport from solar collectors to luggage compartment tanks, to pick up proficiency of coolants in transformers.

Karanth et al. [1] numerically simulated a solar flat plate collector using Discrete Transfer Radiation Model. A 3D model of the collector involving the water pipe, absorber plate, the glass top and the air gap in-between the absorber plate and the glass top was modeled to provide for conduction, convection and radiation in their analysis. Bég et al. [2] performed non-similar mixed convection heat and species transfer along an inclined solar energy collector surface with cross diffusion effects, where the resulting governing equations were transformed and then solved numerically using the local nonsimilarity method and Runge-Kutta shooting quadrature. Manjunath et al. [3] analyzed three dimensional conjugate heat transfers through unglazed solar flat plate collector. They used finned tubes and the heat transfer simulation due to solar irradiation to the fluid medium, increased with an increase in the mass flow rate. Vestlund [4] studied gas-filled flat plate solar collector. The gases examined were argon, krypton and xenon in his thesis paper. Manjunath et al. [5] studied comparatively solar dimple plate collector with flat plate collector to augment the thermal performance. Their result described that the average exit water temperature showed a marked improvement of about 5.5^0C for a dimple solar collector as compared to that of a flat plate solar collector.

CFD analysis of solar flat plate collector was conducted by Ingle et al. [6]. His work attempted to present numerical simulation of solar collector developed exclusively for grape drying. CFD analysis of triangular absorber tube of a solar flat plate collector was performed by Basavanna and Shashishekar [7] where the numerical results obtained using the experimentally measured temperatures are compared to the temperatures determined by the CFD model. Tagliafico et al. [8] reviewed dynamic thermal models and CFD analysis for flat-plate thermal solar collectors. They presented an updated review of models for flat-plate thermal solar collectors, including a proper classification and a description of their main characteristics and performance. Very recently, Nasrin and Alim [9] developed a semi-empirical relation for forced convective analysis through a solar collector. A new correlation was derived from their obtained results and it was easy to use heat transfer purposes.

From the above literature review it is mentioned that some 2D numerical analyses have been done using nanofluids, some experimental works also have been conducted but a very few 3D numerical studies have been completed using traditional fluid that is water, gas, air etc.

Thus there is a large scope to work 3D numerical investigation of heat transfer through a flat plate solar collector using nanofluid. Necessary three dimensional numerical studies are very much required to monitor the variation of collector efficiency, heat transfer system with economic and environmental considerations due to using different nanofluids in assisted convection mode, which forms the basis of the motivation behind selecting the present work.

Nomenclatures

A	Surface area of solar flat plate collector (m^2)
C_p	Specific heat at constant pressure ($J\ kg^{-1}\ K^{-1}$)
I	Intensity of solar radiation ($W\ m^{-2}$)
k	Thermal conductivity ($W\ m^{-1}\ K^{-1}$)
L	Length of the solar collector (m)
m	Mass flow rate ($Kg\ s^{-1}$)

Nu Nusselt number,

Pr Prandtl number,

Re Reynolds number

T Dimensional temperature (K)

T_{in} Input temperature of nanofluid (K)

T_{out} Output temperature of fluid (K)

u, v, w Dimensional x, y and z components of velocity (m s^{-1})

U_l Local heat transfer coefficient (W m^{-2} K^{-1})

U_i Input velocity of fluid (ms^{-1})

U, V, W Non dimensional velocities

V Volume of the absorber tube (m^3)

X, Y, Z Non dimensional co-ordinates

x, y, z Dimensional co-ordinates (m)

Greek Symbols

α Fluid thermal diffusivity (m^2 s^{-1})

β Thermal expansion coefficient (K^{-1})

ϕ Nanoparticles volume fraction

v Kinematic viscosity (m^2 s^{-1})

η Collector efficiency,

θ Dimensionless temperature,

ρ Density (kg m^{-3})

μ Dynamic viscosity (N s m^{-2})

Subscripts

a absorber

av mean

f fluid

nf nanofluid

s solid particle

$usfl$ useful

2. Geometrical Modeling

A schematic diagram of the system in three dimensional as well as cross sectional view considered in the present study is shown in Fig. 1(i)-(ii). The system consists of a flat plate solar collector. This figure shows an absorber plate containing a riser pipe. The working fluid in the collector is water-based nanofluid containing Cu nanoparticles. The nanoparticles are generally spherical shaped and diameter is taken as 5 nm. The nanofluid is considered as single phase flow and surfactant analysis is neglected. The solar collector is a metal box with highly transparent and anti-reflected glass cover (called the glazing) on top and a dark colored copper absorber plate on the

bottom. There is an air gap of 0.01m between glass cover and absorber plate. The glass top surface is exposed to solar irradiation. The glass cover is made up of borosilicate which has a thermal conductivity of 1.14 W/mK and a refractive index of 1.47. The specific heat is taken as 750 J/kg-K and coefficient of sunlight transmission is 95%. The wavelength of visible light is roughly 0.7 μm. Thickness of glass cover is 0.004m. Length, width and thickness of the absorber plate are 1m, 0.15m and 0.0008m respectively. The riser pipe has inner diameter 0.01 m and thickness 0.0005m. Coefficients of heat absorption and emmision of copper absorber are 95% and 5% respectively. A trapezium shaped bonding conductance is located from middle one-third part of width of the absorber plate. It covers the three-fourth part of the riser pipe. It is as long as the absorber plate and tube. The bonding conductance is made of copper metal. The computation domain is the copper absorber plate containing a fluid passing copper riser pipe with bonding conductance. The riser pipe is generally ultrasonically welded to the absorber plate.

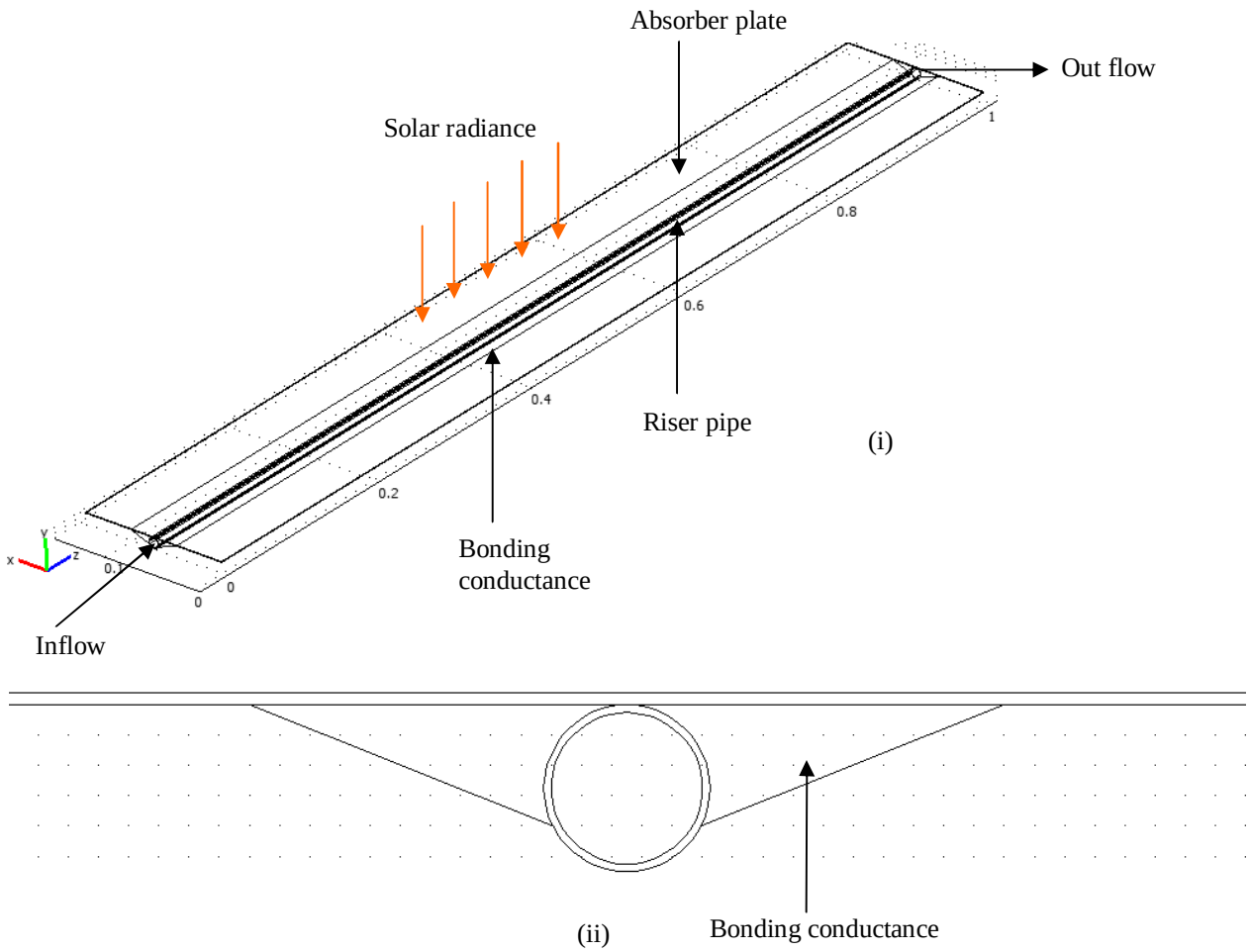

Fig. 1: Schematic diagram of the flat plate solar collector (i) 3D and (ii) cross sectional view

3. Mathematical Modeling

In the present problem, it can be considered that the flow is three-dimensional and there is no viscous dissipation. The nanofluid is assumed incompressible and the flow is considered to be laminar. It is taken that water and nanoparticles are in thermal equilibrium and no slip occurs between them. Only steady state case is considered. The 3D governing equations in dimensional form are as follows

$$\frac{\partial u}{\partial x}+\frac{\partial v}{\partial y}+\frac{\partial w}{\partial z}=0 \tag{1}$$

$$\rho_{nf}\left(u\frac{\partial u}{\partial x}+v\frac{\partial u}{\partial y}+w\frac{\partial u}{\partial z}\right)=-\frac{\partial p}{\partial x}+\mu_{nf}\left(\frac{\partial^2 u}{\partial x^2}+\frac{\partial^2 u}{\partial y^2}+\frac{\partial^2 u}{\partial z^2}\right) \tag{2}$$

$$\rho_{nf}\left(u\frac{\partial v}{\partial x}+v\frac{\partial v}{\partial y}+w\frac{\partial v}{\partial z}\right)=-\frac{\partial p}{\partial y}+\mu_{nf}\left(\frac{\partial^2 v}{\partial x^2}+\frac{\partial^2 v}{\partial y^2}+\frac{\partial^2 v}{\partial z^2}\right) \tag{3}$$

$$\rho_{nf}\left(u\frac{\partial w}{\partial x}+v\frac{\partial w}{\partial y}+w\frac{\partial w}{\partial z}\right)=-\frac{\partial p}{\partial z}+\mu_{nf}\left(\frac{\partial^2 w}{\partial x^2}+\frac{\partial^2 w}{\partial y^2}+\frac{\partial^2 w}{\partial z^2}\right) \tag{4}$$

$$u\frac{\partial T}{\partial x}+v\frac{\partial T}{\partial y}+w\frac{\partial T}{\partial z}=\alpha_{nf}\left(\frac{\partial^2 T}{\partial x^2}+\frac{\partial^2 T}{\partial y^2}+\frac{\partial^2 T}{\partial z^2}\right) \tag{5}$$

$$\frac{k_a}{\rho C_p}\left(\frac{\partial^2 T_a}{\partial x^2}+\frac{\partial^2 T_a}{\partial y^2}+\frac{\partial^2 T_a}{\partial z^2}\right)=0 \tag{6}$$

where, $\alpha_{nf}=k_{nf}/\left(\rho C_p\right)_{nf}$ is the thermal diffusivity,

$\rho_{nf}=\left(1-\phi\right)\rho_f+\phi\rho_s$ is the density

$\left(\rho C_p\right)_{nf}=\left(1-\phi\right)\left(\rho C_p\right)_f+\phi\left(\rho C_p\right)_s$ is the heat capacitance

the viscosity of the nanofluid of Brinkman model [10] is $\mu_{nf}=\mu_f\left(1-\phi\right)^{-2.5}$

the thermal conductivity of Maxwell Garnett (MG) model [11] is $k_{nf}=k_f\dfrac{k_s+2k_f-2\phi\left(k_f-k_s\right)}{k_s+2k_f+\phi\left(k_f-k_s\right)}$

The boundary conditions of the computation domain are:

- at all solid boundaries of the riser pipe: $u = v = w = 0$
- at the solid-fluid interface: $k_f\left(\frac{\partial T}{\partial n}\right)_{fluid}=k_a\left(\frac{\partial T}{\partial n}\right)_{solid}$
- at the inlet boundary of the riser pipe: $T=T_{in}$, $w = W_{in}$
- at the outlet boundary: convective boundary condition $p = 0$
- at the top surface of the absorber: heat flux $-k_a\frac{\partial T_a}{\partial z}=q=I\tau\kappa-U_L\left(T_{in}-T_{amb}\right)$
- at the other surfaces of absorber plate: $\frac{\partial T_a}{\partial n}=0$
- at the outer boundary of riser pipe: $\frac{\partial T}{\partial n}=0$

- at the outer boundary of bonding conductance: $\frac{\partial T_a}{\partial n} = 0$

The above equations are non-dimensionalized by using the following dimensionless quantities

$$X = \frac{x}{D}, Y = \frac{y}{D}, Z = \frac{z}{D}, U = \frac{u}{W_{in}}, V = \frac{v}{W_{in}}, W = \frac{w}{W_{in}}, P = \frac{p}{\rho_f {U_{in}}^2}, \theta = \frac{(T - T_{in})k_f}{qD}, \quad \theta_a = \frac{(T_a - T_{in})k_a}{qD}$$

Then the non-dimensional governing equations are

$$\frac{\partial U}{\partial X} + \frac{\partial V}{\partial Y} + \frac{\partial W}{\partial Z} = 0 \tag{7}$$

$$U\frac{\partial U}{\partial X} + V\frac{\partial U}{\partial Y} + W\frac{\partial U}{\partial Z} = -\frac{\rho_f}{\rho_{nf}}\frac{\partial P}{\partial X} + \frac{\nu_{nf}}{\nu_f}\frac{1}{Re}\left(\frac{\partial^2 U}{\partial X^2} + \frac{\partial^2 U}{\partial Y^2} + \frac{\partial^2 U}{\partial Z^2}\right) \tag{8}$$

$$U\frac{\partial V}{\partial X} + V\frac{\partial V}{\partial Y} + W\frac{\partial V}{\partial Z} = -\frac{\rho_f}{\rho_{nf}}\frac{\partial P}{\partial Y} + \frac{\nu_{nf}}{\nu_f}\frac{1}{Re}\left(\frac{\partial^2 V}{\partial X^2} + \frac{\partial^2 V}{\partial Y^2} + \frac{\partial^2 V}{\partial Z^2}\right) \tag{9}$$

$$U\frac{\partial W}{\partial X} + V\frac{\partial W}{\partial Y} + W\frac{\partial W}{\partial Z} = -\frac{\rho_f}{\rho_{nf}}\frac{\partial P}{\partial Z} + \frac{\nu_{nf}}{\nu_f}\frac{1}{Re}\left(\frac{\partial^2 W}{\partial X^2} + \frac{\partial^2 W}{\partial Y^2} + \frac{\partial^2 W}{\partial Z^2}\right) \tag{10}$$

$$U\frac{\partial \theta}{\partial X} + V\frac{\partial \theta}{\partial Y} + W\frac{\partial \theta}{\partial Z} = \frac{1}{RePr}\frac{\alpha_{nf}}{\alpha_f}\left(\frac{\partial^2 \theta}{\partial X^2} + \frac{\partial^2 \theta}{\partial Y^2} + \frac{\partial^2 \theta}{\partial Z^2}\right) \tag{11}$$

$$K\left(\frac{\partial^2 \theta_a}{\partial X^2} + \frac{\partial^2 \theta_a}{\partial Y^2} + \frac{\partial^2 \theta_a}{\partial Z^2}\right) = 0 \tag{12}$$

The corresponding boundary conditions take the following form:

- at all inner solid boundaries of the riser pipe: $U = V = W = 0$,
- at the solid-fluid interface: $\left(\frac{\partial \theta}{\partial N}\right)_{fluid} = K\left(\frac{\partial \theta}{\partial N}\right)_{solid}$
- at the inlet boundary: $\theta = 0$, $U = 0 = V$, $W = 1$
- at the outlet boundary: convective boundary condition $P = 0$
- at the top surface of the absorber: heat flux $\frac{\partial \theta_a}{\partial Z} = -1$
- at the other surfaces of absorber plate: $\frac{\partial \theta_a}{\partial N} = 0$
- at the outer surface of riser tube: $\frac{\partial \theta}{\partial N} = 0$
- at the outer surface of bonding conductance: $\frac{\partial \theta_a}{\partial N} = 0$

where $Pr = \frac{\nu_f}{\alpha_f}$ is the Prandtl number, $K = \frac{k_a}{k_f}$ is thermal conductivity ratio, $Re = \frac{W_{in} D}{\nu_f}$ is the Reynolds number, n and N is the dimensional and non-dimensional distances either along x or y or z directions acting normal to the surface respectively.

The overall heat transfer coefficient (U_l) for the collector system is $Q = U_l \frac{qD}{k_f}$, where Q is the absorbed solar radiation per unit area by the collector surface, q is constant heat flux assigned at the top surface of absorber.

Equation of local Nusselt number for flow through a cylinder is $\overline{Nu} = \frac{U_l D}{k_f} = \frac{Q}{\Delta T}\left(\frac{D}{k_f}\right)$, where D is the inner diameter of cylinder, ΔT is the difference between cylinder surface temperature and ambient temperature, Q is the energy received or lost by the cylinder surface. For a flat plate solar collector constant heat flux is assigned at the absorber top surface. So equation of local Nusselt number for flow at the solid surface of the absorber pipe of a solar flat plate collector can be written as $\overline{Nu} = \frac{U_l D}{k_f} = \frac{Q}{\left(qD/k_f\right)}\left(\frac{D}{k_f}\right)$

For water based nanofluid flow this equation becomes $\overline{Nu} = \frac{-k_{nf}\left(\frac{\partial T}{\partial n}\right)}{\left(qD/k_f\right)}\left(\frac{D}{k_f}\right) = -\left(\frac{k_{nf}}{k_f}\right)\left(\frac{k_f}{q}\right)\left(\frac{\partial T}{\partial n}\right)$

The non-dimensional form of local heat transfer at the riser pipe solid surface is $\overline{Nu} = -\frac{k_{nf}}{k_f}\left(\frac{\partial \theta}{\partial N}\right)$.

The normal temperature gradient can be written as $\frac{\partial \theta}{\partial N} = \sqrt{\left(\frac{\partial \theta}{\partial X}\right)^2 + \left(\frac{\partial \theta}{\partial Y}\right)^2 + \left(\frac{\partial \theta}{\partial Z}\right)^2}$

By integrating the local Nusselt number over the surface of the riser pipe, the average heat transfer rate of the collector can be written from Saleh et al. [12]

$Nu = \frac{\iint_S \overline{Nu}\, ds}{\iint_s dS} = -\frac{1}{\pi DL}\frac{k_{nf}}{k_f}\iint_S \sqrt{\frac{\partial^2 \theta}{\partial X^2} + \frac{\partial^2 \theta}{\partial Y^2} + \frac{\partial^2 \theta}{\partial Z^2}}\, ds$ where L is the height of absorber tube.

The mean bulk temperature and average sub domain velocity of the fluid inside the collector may be written as

$\theta_{av} = \frac{\iiint_v \theta d\mathrm{V}}{\iiint_v d\mathrm{V}} = \frac{4}{\pi D^2 L}\iiint_v \theta d\mathrm{V}$ and $\overline{\mathrm{V}}_{av} = \frac{\iiint_v \overline{\mathrm{V}} d\mathrm{V}}{\iiint_v d\mathrm{V}} = \frac{4}{\pi D^2 L}\iiint_v \overline{\mathrm{V}}\, d\mathrm{V}$, where V is the volume the absorber tube.

A measure of a flat plate collector performance is the collector efficiency (η) defined as the ratio of the useful energy gain (Q_{usfl}) to the incident solar energy. The instantaneous thermal efficiency of the collector is:

$$\eta = \frac{\text{useful gain}}{\text{available energy}} = \frac{Q_{\text{usfl}}}{AI} = \frac{F_R A\left[I(\tau\kappa) - U_L\left(T_{in} - T_{amb}\right)\right]}{AI} = F_R(\tau\kappa) - F_R U_L \frac{\left(T_{in} - T_{amb}\right)}{I}$$

4. Numerical Modeling

The Galerkin finite element method Taylor and Hood [13] and Dechaumphai [14] is used to solve the non-dimensional governing equations along with boundary conditions for the considered problem. The equation of

continuity has been used as a constraint due to mass conservation and this restriction may be used to find the pressure distribution. The finite element method is used to solve the Eqs. (7) - (16), where the pressure P is eliminated by a constraint. The continuity equation is automatically fulfilled for large values of this constraint. Then the velocity components (U, V, W) and temperatures (θ and θ_a) are expanded using a basis set. The Galerkin finite element technique yields the subsequent nonlinear residual equations. Three points Gaussian quadrature is used to evaluate the integrals in these equations. The non-linear residual equations are solved using Newton–Raphson method to determine the coefficients of the expansions. The convergence of solutions is assumed when the relative error for each variable between consecutive iterations is recorded below the convergence criterion such that $\left|\psi^{n+1}-\psi^{n}\right| \le 10^{-4}$, where n is the number of iteration and Ψ is a function of U, V, W, θ and θ_a.

4.1. Mesh Generation

In the finite element method, the mesh generation is the technique to subdivide a domain into a set of sub-domains, called finite elements, control volume, etc. The discrete locations are defined by the numerical grid, at which the variables are to be calculated. It is basically a discrete representation of the geometric domain on which the problem is to be solved. The computational domains with irregular geometries by a collection of finite elements make the method a valuable practical tool for the solution of boundary value problems arising in various fields of engineering. Fig. 2 displays the finite element mesh of the present physical domain.

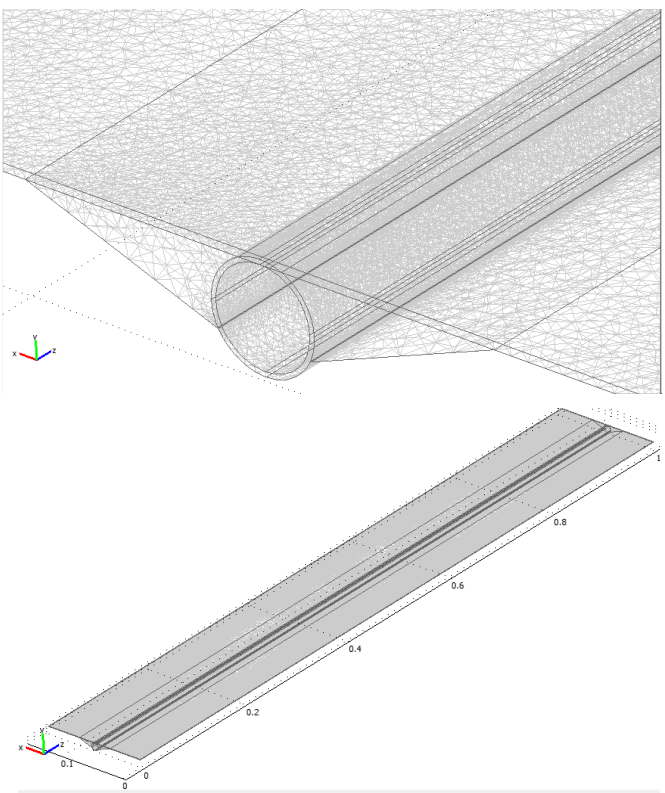

Fig. 2: Mesh generation of the collector (i) partial view and (ii) total view

4.2. Grid In dependent Test

The arrangement of discrete points throughout the domain is simply called a grid. The determination of a proper

grid for the flow through a given geometric shape is important. The way that such a grid is determined is called grid generation. The grid generation is a significant consideration in CFD. Finite element method can be applied to unstructured grids. This is because the governing equations in this method are written in integral form and numerical integration can be carried out directly on the unstructured grid domain in which no coordinate transformation is required. The three dimensional computational domain is modeled using finite element mesh as shown in Fig. 2. The complete domain consists of 14,20,465 elements which include the riser tube and absorber plate. The mesh is composed of tetrahedron element type with ten nodes. The grid independence test is performed to check validity of the quality of mesh on the solution. The influence of further refinement does not change the result by more than 1.25 % which is taken here as the appropriate mesh quality for computation. The thermo-physical properties of the nanofluid are taken from Ogut [15] and given in Table 1.

Table 1: Thermo-physical properties of water and Cu nanoparticles at 295K

Physical Properties	Fluid phase (water)	Cu
C_p(J/kgK)	4181	385
ρ (kg/m^3)	998.0	8933
k (W/mK)	0.606	400
$\alpha\times10^7$ (m^2/s)	1.47	1163.1
$\mu\times10^6$ (Ns/ m^2)	959	-

5. Results and Discussions

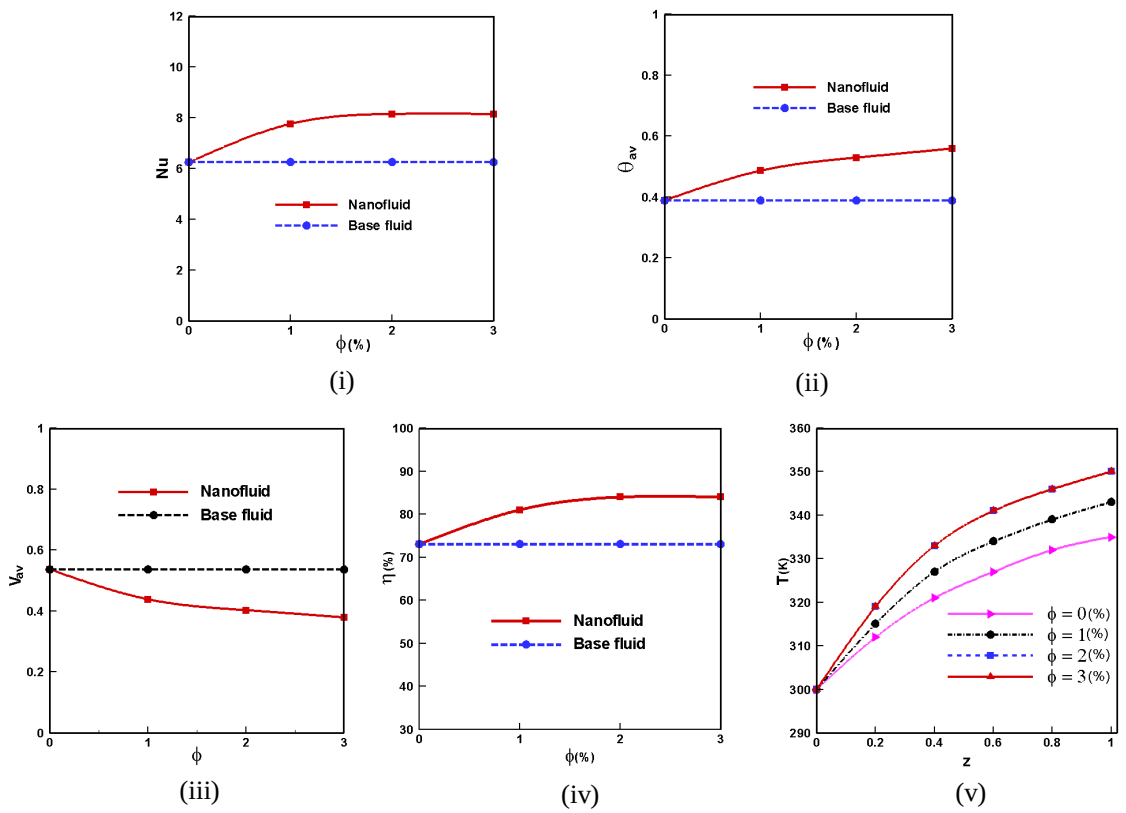

Fig. 3: Effect of solid volume fraction on (i) mean Nusselt number, (ii) mean temperature (iii) mean velocity, (iv) thermal efficiency, (v) mean outlet temperature

Finite element simulation is applied to perform the analysis of laminar forced convection temperature and fluid flow through a riser pipe of a flat plate solar collector filled with water/copper nanofluid. Effect of the solid volume fraction (ϕ) of copper nanoparticles on heat transfer and collector efficiency has been studied. The ranges of ϕ for this investigation vary from 0% to 3%.

The average Nusselt number (Nu), average temperature (θ_{av}), mean velocity ($\overline{V}_{av}$) collector efficiency (η), outlet temperature (T) along with the various solid volume fraction (ϕ) are displayed in Fig. 3 (i)-(v). From Fig. 3(i) it is evident that the mean Nusselt number raises monotonically upto 2% of solid volume fraction. Here rate of heat transfer remains constant for clear water (ϕ = 0%) with the variation of ϕ. Heat transfer rate increases by 30% with the variation of ϕ from 0% to 2% of water-copper nanofluid. And then there is almost no change in Nu-ϕ profile for extra variation of ϕ from 2% to 3%. Thus, adding more nanoparticles is not beneficial.

Fig. 3(ii) shows that θ_{av} along with the solid volume fraction grows sequentially for ϕ = 3%. It is due to the fact that higher concentration of solid particle enhances thermal conductivity as well as temperature of the working Cu-water nanofluid.

Fig. 3(iii) has notable changes in the mean velocity of water-copper nanofluid with the variation of solid volume fraction (ϕ). Growing ϕ devalues mean velocity of the nanofluid through the riser pipe of the flat plate solar collector. This happens because more solid concentrated nanofluid can't move freely.

Fig. 3(iv) expresses the variation of the collector efficiency as a function of nanoparticle concentration. Absorption coefficient of nanofluid can be adjusted by varying the concentration of nanoparticles. The efficiency of flat-plate solar collector with Cu/water nanofluid is higher than the efficiency of flat-plate solar collector with water as working fluid. This can be deduced by comparing the value of outlet temperature of fluid for Cu nanofluid and water, which shows that the removed energy parameter, $F_R U_L$, values for Cu nanofluid and water are close to each other. However, the absorbed energy parameter, value for nanofluid is higher than that for water by 30%. This causes the efficiency of solar collector with 2% particle volume fraction of Cu nanofluid become greater than that with water. Collector efficiency rises from 73% to 84% for the variation of ϕ from 0%-2%. As can be observed from the Fig. 3(iv), increasing nanoparticle concentration initially increases the collector efficiency up to a maximum value. Then, a further increase in the concentration leads to no significant change in the collector efficiency. This phenomenon can be explained as follows. Generally speaking, increasing nanoparticles concentration increases nanofluid absorption coefficient and consequently increases the collector optical absorption. Using a certain concentration causes complete absorption of the incoming solar radiation, but beyond this maximum value, any further increase of the nanofluid absorption coefficient results in a shorter length for the radiation attenuation.

Fig. 3(v) shows temperature of fluids at the middle of the riser pipe. The inlet temperature of water-Cu nanofluid is maintained at 300K and then it increases gradually with the contact of heated solid surfaces of the riser pipe. And finally the mean output temperature of nanofluid becomes 335K, 343K, 350K and 350K for ϕ = 0%, 1%, 2% and 3% respectively.

Acknowledgement

This work is done in the Department of Mathematics, Bangladesh University of Engineering & Technology, Dhaka-1000, Bangladesh.

References

[1] K.V. Karanth, M.S. Manjunath, N.Y. Sharma, Numerical simulation of a solar flat plate collector using discrete transfer radiation model (DTRM) – a CFD approach, Proc. of the World Cong. on Engg., London, U.K., III, 2011.

[2] OA. Bég, A. Bakier, R. Prasad, SK. Ghosh, Numerical modelling of non-similar mixed convection heat and species transfer along an inclined solar energy collector surface with cross diffusion effects, World J. of Mech., 1 (2011) 185-196,.

[3] M.S, Manjunath, K.V. Karanth, N.Y. Sharma, Three dimensional numerical analysis of conjugate heat transfer for enhancement of thermal performance using finned tubes in an economical unglazed solar flat plate collector, Proc. of the World Cong. on Engg., London, U.K., III, 2011.

[4] J. Vestlund, Gas-filled, flat plate solar collector, Ph. D. Thesis, Building Services Engg., Dept. of Energy and Environ., Chalmers University of Technology, Gothenburg, Sweden, 2012.

[5] M.S, Manjunath, K.V. Karanth, N.Y. Sharma, A comparative CFD study on solar dimple plate collector with flat plate collector to augment the thermal performance, World Academy of Sci., Engg. and Tech., 6 (2012) 10-21.

[6] P.W. Ingle, A.A. Pawar, B.D. Deshmukh, K.C. Bhosale, CFD analysis of solar flat plate collector, Int. J. of Emerg. Techn. and Adv. Engg., 3 (2013) 337-342.

[7] S., Basavanna and K.S. Shashishekar, CFD analysis of triangular absorber tube of a solar flat plate collector, Int. J. Mech. Eng. & Rob. Res., 2 (2013) 19-24.

[8] I.A. Tagliafico, F. Scarpa, M.D. Rosa, Dynamic thermal models and CFD analysis for flat-plate thermal solar collectors – a review, Renew. and Sust. Energy Rev., 2 (2014) 526-537.

[9] R. Nasrin and M.A. Alim, Semi-empirical relation for forced convective analysis through a solar collector, Solar Energy, 105 (2014) 455-467.

[10] H.C. Brinkman, The viscosity of concentrated suspensions and solution. J. Chem. Phys. 20 (1952) 571–581.

[11] JC. Maxwell-Garnett, Colours in metal glasses and in metallic films, Philos. Trans. Roy. Soc. A, 203 (1904) 385–420.

[12] H. Saleh, R. Roslan, I. Hashim, Natural convection heat transfer in a nanofluid-filled trapezoidal enclosure, Int. J. of Heat and Mass Transfer, 54 (2011) 194–201.

[13] C. Taylor, P. Hood, A numerical solution of the Navier-Stokes equations using finite element technique, Computer and Fluids, 1(1973) 73–89.

[14] P. Dechaumphai, Finite Element Method in Engineering, 2nd ed., Chulalongkorn University Press, Bangkok, 1999.

[15] EB. Ogut, Natural convection of water-based nanofluids in an inclined enclosure with a heat source, Int. J. of Thermal Sciences, 48 (2009) 2063-2073.

6th BSME International Conference on Thermal Engineering (ICTE 2014)

Effect of Thermal Grashof Number on Heat and Mass Transfer in a Parallel Plate Reactor Channel with Heated Cylinders

Salma Parvin, Rehena Nasrin and M.A. Alim

Department of Mathematics, Bangladesh University of Engineering and Technology, Dhaka-1000, Bangladesh

**E-mail: salpar@math.buet.ac.bd*

Abstract

A numerical study has been carried out for laminar double-diffusive mixed convection in a parallel plate reactor channel with four heated cylinders. An external air flow enters from the left inlet and exits from the right. After entering the reactor, the fluid passes four heated cylinder. The developed mathematical model is governed by the two-dimensional continuity, momentum, energy and concentration equations. The governing equations, written in non-dimensional form are solved by using Galerkin finite element method with triangular grid discretization system. The Reynolds number is fixed at 100 and the working fluid is considered as air. Numerical simulations are carried out for different combinations of the thermal Grashof numbers and results are presented in terms of streamlines, temperature and concentration distributions. The results indicate that the average Nusselt and Sherwood numbers at the heat and contaminant sources strongly depend on the mentioned parameter.

Keywords: Double diffusive mixed convection; parallel plate reactor; finite element method.

1. Introduction

Combined heat and mass transfer problems with chemical reaction are of importance in many processes and have, therefore, received a considerable amount attention in recent years. In processes such as drying, evaporation at the surface of a water body, energy transfer in a wet cooling tower and the flow in a desert cooler, in chemical reaction engineering heat and mass transfer occur simultaneously.

Brown and Lai [1] numerically examined combined heat and mass transfer from a horizontal channel with an open cavity heated from below. Since heat and contaminant sources usually co-exist indoors, the present work is to

Nomenclature

α	thermal diffusivity
β	expansion coefficient
ν	kinematic viscosity
ρ	density
θ	nondimensional temperature
C	nondimensional concentration
c	concentration
D	mass diffusivity
g	gravitational acceleration
Gr	Grashof number
H	height of the reactor
K	Chemical reaction parameter
L	length of the reactor
Le	Lewis number
N	buoyancy ratio
n	outward normal direction
Nu	average Nusselt number
P	nondimesional pressure
Pr	Prandtl number
Re	Reynolds number
Ri	Richardson number
Sh	average Sherwood number
T	temperature
U,V	nondimensional velocity components
u,v	velocity components
X,Y	nondimensional coordinate
x,y	Cartesian coordinate

numerically study the double-diffusive mixed convection in a vented cavity due to the discrete heat and contaminant sources. Parvin et al. [2] analyzed numerically the effect of double-diffusive natural convection of a water–Al_2O_3

nanofluid in a partially heated enclosure with Soret and Dufour coefficients. Azad et al. [3] investigated double diffusive mixed convection in an open channel with a circular heater on the bottom wall. They found that, average Nusselt number at the heat source decreases and overall mass transfer rate in terms of average Sherwood number increases with the rising of Lewis number.

In [4], the unimolecular thermal decomposition mechanism of anti-N,N'-Dinitrourea was studied by an in situ pyrolytic Fourier transform infrared spectroscopy with the temperature program and density functional theory calculations. The thermal unimolecular decomposition of dichloroketene was studied experimentally and computationally in [5]. The authors used the analysis of the experimental data and the computational models to demonstrates that thermal decomposition is a major pathway of destruction for dichloroketene in combustion systems. Muthucumaraswamy and Ganesan [6] studied effect of the chemical reaction and injection on flow characteristics in an unsteady upward motion of an isothermal plate. Deka et at. [7] studied the effect of the first order homogeneous chemical reaction on the process of an unsteady flow past an infinite vertical plate with a constant heat and mass transfer. Chamkha [8] studied the MHD flow of a numerical of uniformly stretched vertical permeable surface in the presence of heat generation/absorption and a chemical reaction. He assumed that the plate is embedded in a uniform porous medium and moves with a constant velocity in the flow direction in the presence of a transverse magnetic field. Ibrahim et al. [9] have studied the effect of chemical reaction and radiation absorption on the unsteady MHD free convection flow past a semi infinite vertical permeable moving plate with heat source and suction. Kesavaiah et al [10] have studied the effect of the chemical reaction and radiation absorption on an unsteady MHD convective heat and mass transfer flow past a semi-infinite vertical permeable moving plate embedded in a porous medium with heat source and suction. Heat and mass transport in tubular packed reactors at reacting and non-reacting conditions was analyzed by Koning [11] where the most common models of wall-cooled tubular packed bed reactors were presented. The two dimensional axial plug flow model was used for a water gas shift reactor to compare heat conduction or mass diffusion with convective effect. Kugai [12] studied Heat and Mass Transfer in Fixed-bed Tubular Reactor. The two dimensional axial plug flow model was used for a water gas shift reactor to compare heat conduction or mass diffusion with convective effect in his study.

The objective of the present work is to investigate the new characteristics of the airflow and heat/contaminant transport mechanism inside a chemical reactor channel in terms of streamlines, isotherms and iso-concentration lines.

2. Analysis

2.1. Physical Model

The domain under analysis is, as sketched in Figure 1(a)-(b), a two-dimensional cross section of a reactor channel of length L and height H with four heated tubes each of radius r, suffering the influence of a gravitational field. The centers of the heaters are located at (L/5, H/2), (2L/5, H/2), (3L/5, H/2) and (4L/5, H/2). The heaters are maintained at constant and uniform temperature T_h and concentration c_h. The air flow is entering from the left with velocity U_i, temperature T_i and concentration c_i, then passes the tubes and then the polluted hot air exhausted from the outlet opening at the right.

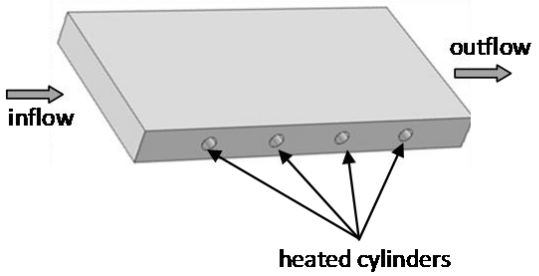

Fig-1(a). 3-D geometry of the considered reactor

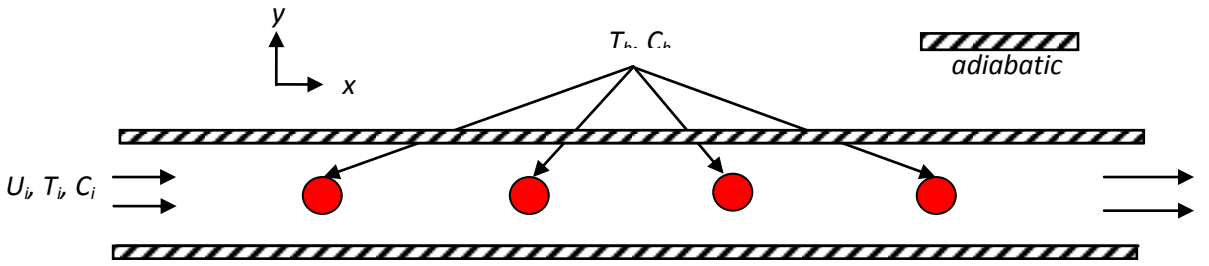

Fig-1(b). Schematic diagram of the problem

2.2. Mathematical Model

The governing mass, momentum, energy and species conservation equations have been presented by Deng et al. [13] for double-diffusive mixed convective flows driven by the combined effect of the internal buoyancy induced from temperature and concentration differences and the external mechanical driven forced flow from the inlet port. With use of the Boussinesq approximation, the dimensionless governing equations under steady-state condition are given by:

Continuity equation: $\frac{\partial U}{\partial X}+\frac{\partial V}{\partial Y}=0$

X-momentum equation: $U\frac{\partial U}{\partial X}+V\frac{\partial U}{\partial Y}=-\frac{\partial P}{\partial X}+\frac{1}{Re}\left(\frac{\partial^2 U}{\partial X^2}+\frac{\partial^2 U}{\partial Y^2}\right)$

Y-momentum equation: $U\frac{\partial V}{\partial X}+V\frac{\partial V}{\partial Y}=-\frac{\partial P}{\partial Y}+\frac{1}{Re}\left(\frac{\partial^2 V}{\partial X^2}+\frac{\partial^2 V}{\partial Y^2}\right)+Ri\left(\theta+NC\right)$

Energy equation: $U\frac{\partial \theta}{\partial X}+V\frac{\partial \theta}{\partial Y}=\frac{1}{RePr}\left(\frac{\partial^2 \theta}{\partial X^2}+\frac{\partial^2 \theta}{\partial Y^2}\right)$

Diffusion equation: $U\frac{\partial C}{\partial X}+V\frac{\partial C}{\partial Y}=\frac{1}{RePrLe}\left(\frac{\partial^2 C}{\partial X^2}+\frac{\partial^2 C}{\partial Y^2}\right)-KC$

The above equations are non-dimensionalized by using the following dimensionless variables

$$X=\frac{x}{L},Y=\frac{y}{L},U=\frac{u}{Ui},V=\frac{v}{Ui},P=\frac{p}{\rho U_i^{\,2}},\theta=\frac{T-T_i}{T_h-T_i},C=\frac{c-ci}{c_h-c_i}$$

and the dimensionless parameters are Reynolds number (*Re*), Grashof number (*Gr*), Richardson number (*Ri*), Prandtl number (*Pr*), Lewis number (*Le*), the buoyancy ratio (*N*) and Chemical reaction parameter (*K*) and they are defined as follows:

$$Re=\frac{U_i L}{\nu}\ ,\ Gr=\frac{g\beta_T\left(T_h-T_i\right)L^3}{\nu^2}\ ,\ Ri=\frac{Gr}{Re^2}\ ,\ Pr=\frac{\nu}{\alpha}\ ,\ Le=\frac{\alpha}{D}\ ,\ N=\frac{\beta_c\left(c_h-c_i\right)}{\beta_T\left(T_h-T_i\right)}\ ,\ K=\frac{kL^2}{D}$$

where ν, α, D and k are kinematic viscosity, thermal diffusivity, solutal diffusivity and reaction coefficient respectively. The buoyancy ratio measures the relative importance of solute and thermal diffusion in creating the density difference to drive the flow. It is clear that N is zero for pure thermally driven flows and infinity for pure solute driven flows.

The boundary conditions are

at the inlet: $U = 1,\ V = \theta = C = 0$
at the circular tube walls: $\theta = C = 1,$
at other surfaces: $\frac{\partial \theta}{\partial n} = 0, \frac{\partial C}{\partial n} = 0$
at all solid boundaries: $U = V = 0$
The average Nusselt and Sherwood number at the tube surface may be expressed as

$$Nu = -\frac{1}{S}\int_0^S \sqrt{\left(\frac{\partial \theta}{\partial X}\right)^2 + \left(\frac{\partial \theta}{\partial Y}\right)^2}\, dS \quad \text{and} \quad Sh = -\frac{1}{S}\int_0^S \sqrt{\left(\frac{\partial C}{\partial X}\right)^2 + \left(\frac{\partial C}{\partial Y}\right)^2}\, dS$$

where S is the non-dimensional length of the heated/contaminant surface.

3. Computational methodology

The numerical procedure used to solve the governing equations for the present work is based on the Galerkin weighted residual method of finite element formulation. The application of this technique is well documented by Zienkiewicz and Taylor [14]. The nonlinear parametric solution technique is chosen to solve the governing equations. This approach will result in substantially fast convergence assurance. In addition, the absolute convergence criteria are set to be 10^{-4} for velocities, energy and concentration.

4. Results and Discussion

The present investigation was carried out with controlling parameter Richardson number *Ri* (= 0.1, 1 and 100) with *Re* = 100, *Pr* = 0.7, *Le* = 1, *N* = 1, *K* = 1. Now in the following section, a detailed description of mixed convection with heat and mass transfer in a parallel plate reactor is given in terms of streamline, thermal and concentration contours for different *Ri*. In addition, the results for both average Nusselt and average Sherwood numbers at various *Ri* will be presented.

Figure 2-4 exhibits the effect of *Ri* on the streamlines, isotherms and iso-concentrations. In fact, the analysis is performed at pure mixed convection regime by fixing *Ri* = 1. Changing Richardson number means the effect of Grashof numbers while the Reynolds number is kept constant. Three sets of Richardson numbers, *Ri* = 0.1, 1 and 10, and the corresponding value of Grashof numbers are *Gr* = 10^3, 10^4 and 10^5 respectively at *Re* = 100 are chosen to examine the evolution of streamline, isotherm and concentration patterns.

From Figures 2, it is observed that there is a common trend of the evolution of streamlines with increasing Richardson numbers. The streamlines are almost parallel to the channel wall and condensed in region between the circular heater and the channel wall. In this condensed area, streamlines change from more to less bended due to increasing Richardson number effect. This happens because of higher thermal buoyancy effect.

It is of interest to note that both θ and *C* develop in a very similar way. This is simply because the *Le* and *N* in the gas flow is taken as unity. As in Figure 3, isothermal lines have slight change due to Richardson number variation. Besides, an increase in the value of *Ri*, through an increase in *Gr*, leads to denser isothermal lines because of the dominance of natural convection. Thus the isothermal lines concentrate at the heat source for *Ri* = 10. It is also seen from the figure that, the lower temperature lines remain at the left potion where as the higher temperature lines at the right exit port. It is also clear that the higher temperature gradient exists at the first heater from the inlet and sequentially it reduces for the second, third and fourth.

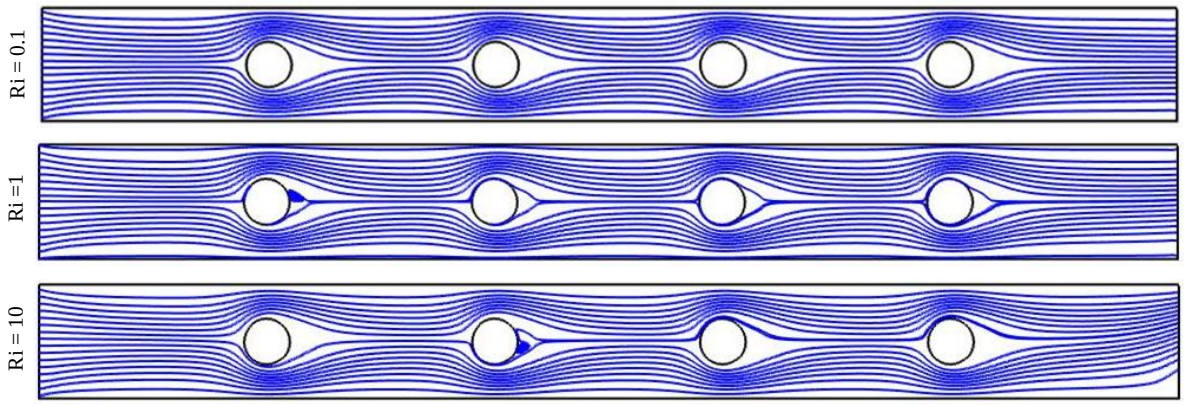

Fig-2. Effect of *Ri* on streamlines

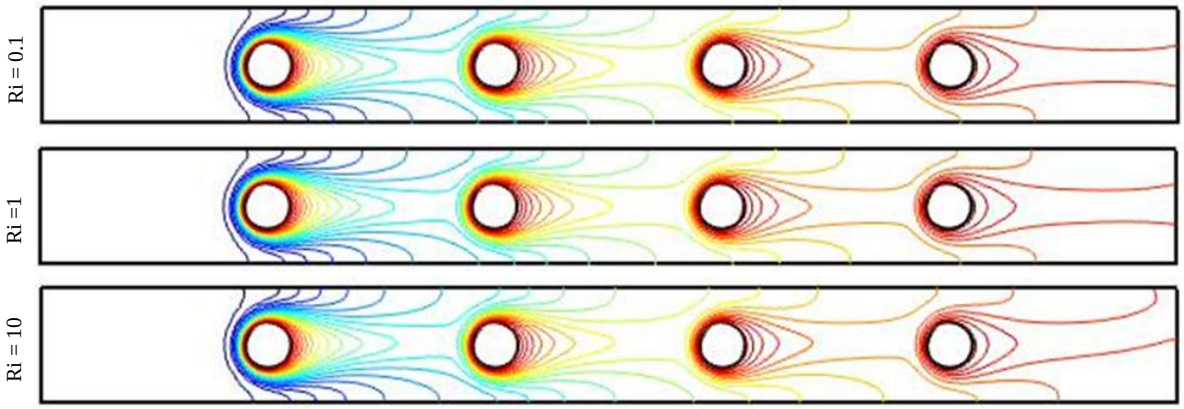

Fig-3. Effect of *Ri* on isotherms

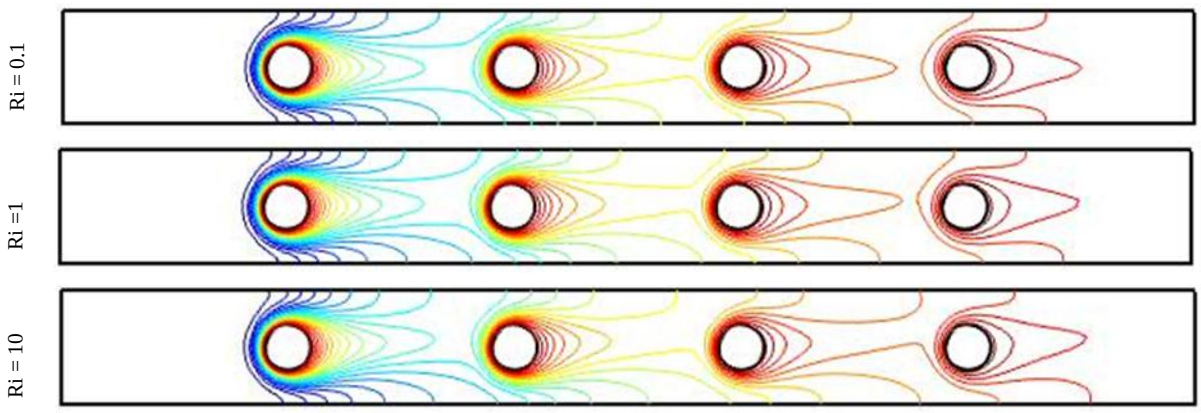

Fig-4. Effect of *Ri* on isoconcentrations

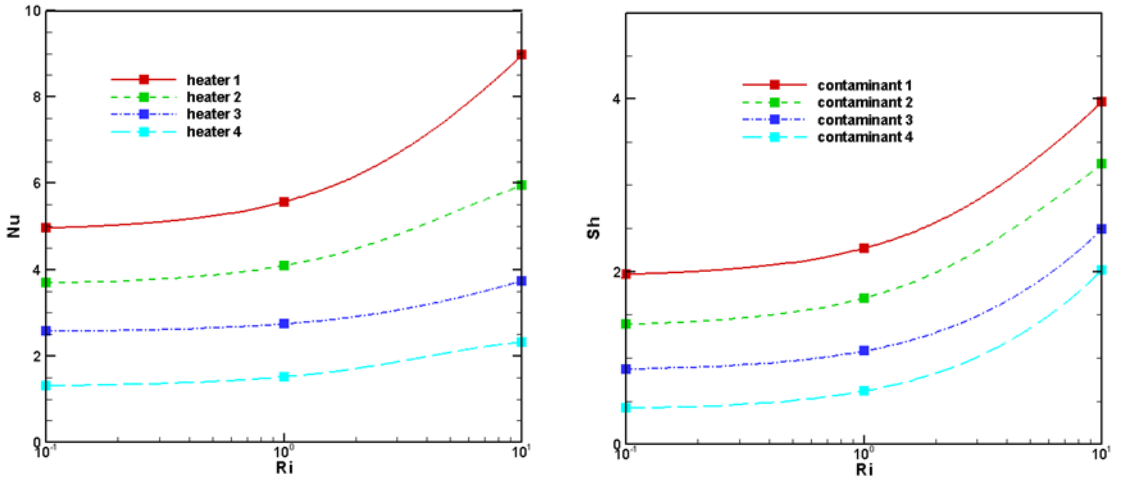

(a) (b)

Fig-5. Effect of *Re* on (a) *Nu* and (b) *Sh*

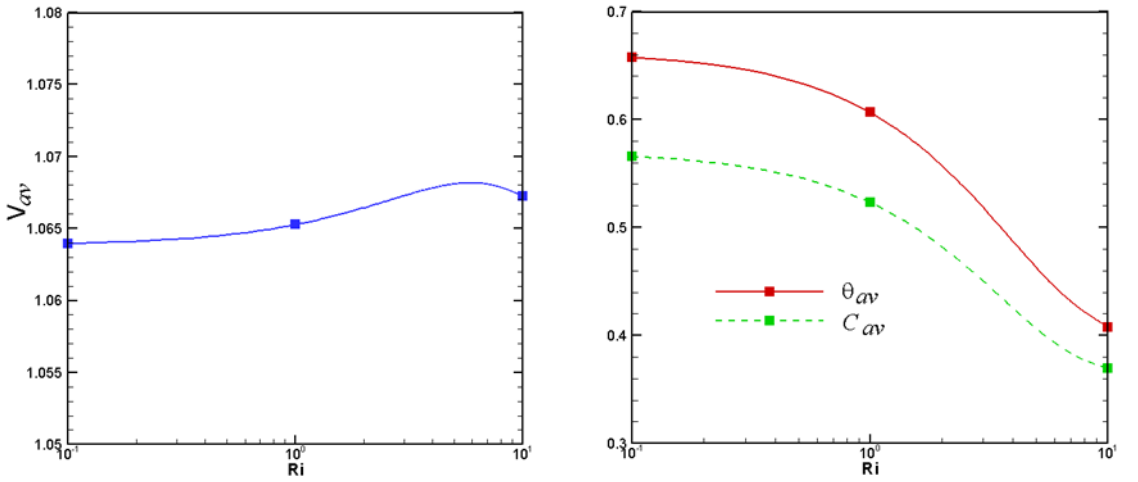

(a) (b)

Fig-6. Effect of *Ri* on average (a) velocity V_{av} (b) temperature Θ_{av} and concentration C_{av}

Iso-concentration lines have also considerable change due to Richardson number variation as shown in Figure 4. Iso-concentration lines have the similar effect as isothermal lines for changing the value Richardson number except the expansion of concentration to the whole domain is slightly less than that of isotherms.

Figure 5(a)-(b) depicts the average heat transfer *Nu* and mass transfer *Sh* at the four consecutive heaters for different *Ri*. Highest heat transfer as well as mass transfer rate are observed for the first heater/contaminant and sequentially these values reduce for second, third and fourth heater/contaminant. This phenomenon is very logical because the flow intensity becomes lower for the last heater due to the obstacles. Increasing *Ri* enhances both the *Nu* and *Sh* but the corresponding values of *Sh* slightly lower than that of *Nu* which indicates greater thermal diffusivity than the solutal diffusivity.

The average velocity magnitude V_{av} , temperature Θ_{av} and concentration C_{av} in the domain of the reactor are presented in Figure 6(a)-(b). It is observed that the average velocity increases due to the increase in the Richardson

number because of higher thermal force. Average temperature and concentration reduce for higher values of *Ri*. The values of mean temperature are lower than that of concentration which indicates temperature gradient is higher than the concentration gradient. This agrees with the phenomena displayed in Figure 5(a)-(b).

Conclusion

The following major conclusions are drawn:

- Increasing Richardson number has significant effects on flow, temperature and concentrations.
- Higher temperature and concentration gradient observe for higher *Ri*.
- Both heat and mass transfer enhance for rising values of *Ri*.
- The position of heat/contaminant source plays an important role in both heat and mass transfer enhancement.

Acknowledgement

The work is supported by the department of mathematics, Bangladesh University of Engineering and Technology, Dhaka.

References

[1] N. Brown and F .Lai, Correlations for combined heat and mass transfer from an open cavity in a horizontal channel, International Communications in Heat and Mass Transfer, 32(8) (2005) 1000–1008.

[2] Salma Parvin, Rehena Nasrin, M.A. Alim, and N.F. Hossain, Double-diffusive natural convection in a partially heated enclosure using a nanofluid, Heat Transfer—Asian Research, 41 (6) (2012) 484-497.

[3] A.K. Azad, M.J.H. Munshi, M.M. Rahman, Double Diffusive Mixed Convection in a Channel with a Circular Heater , Procedia Engineering , 56 (2013) 157–162.

[4] L. Liu, K. Dong, , X. Yao, Z. Li, C. Li, J. Sun, X. Zhang, and S. Zhang, Combustion and Flame, 159 (2012), 1393.

[5] A.A. Shestov, S.A. Kostina and V.D. Knyazev, Proceedings of the Combustion Institute, 30 (2005) 975.

[6] R. Muthucumaraswamy, P. Ganesan, Effect of the chemical reaction and injection on flow characteristics in an unsteady upward motion of an isothermal plate, J. Appl. Mech. Tech. Phys., 42 (2001) 665-671.

[7] R. Deka, U.N. Das, V.M. Soundalgekar, Effects of mass transfer on flow past an impulsively started infinite vertical plate with constant heat flux and chemical reaction, Forschung in Ingenieurwesen, 60 (1994) 284-287.

[8] A.J Chamka, MHD flow of a numerical of uniformly stretched vertical permeable surface in the presence of heat generation/absorption and a chemical reaction. Int. Comm. Heat and Mass Transf., 30 (2003) 413-22.

[9] F.S. Ibrahim, A.M. Elaiw, A.A. Bakr, Effect of chemical reaction and radiation absorption on the unsteady MHD free convection flow past a semi infinite vertical permeable moving plate with heat source and suction, Comm. in Nonlinear Sci. and Num. Simul., 13 (2008) 1056-1066.

[10] DC.H. Kesavaiah, P.V. Satyanarayana and S. Venkataramana, Effects of the chemical reaction and radiation absorption on an unsteady MHD convective heat and mass transfer flow past a semi-infinite vertical permeable moving plate embedded in a porous medium with heat source and suction. Int.J. of Appl. Math. and Mech., 7(1) (2011) 52-69.

[11] B. Koning, Heat and mass transport in tubular packed bed reactors at reacting and non-reacting conditions, Ph.D. Thesis, University of Twente, Netherland, 2002.

[12] J. Kugai, Heat and mass transfer in fixed-bed tubular reactor, May 1st , 2008.

[13] Q. Deng, J. Zhou, C. Mei and Y. Shen, Fluid, heat and contaminant transport structures of laminar double diffusive mixed convection in a two-dimensional ventilated enclosure, International Journal of Heat and Mass Transfer, 47(24) (2004) 5257–5269.

[14] O. Zienkiewicz and R. Taylor, The finite element method, Butterworth-Heinemann, 5th edition, 2000.

6th BSME International Conference on Thermal Engineering (ICTE 2014)

MHD Radiative Boundary Layer Flow of a Nanofluid past a Rotating Stretching Sheet

Mohammad Wahiduzzaman[a,*], Md. Sharif Uddin[b], Pallab Biswas[c]

[a]*Assistant Professor, Mathematics Discipline, Khulna University, Khulna-9208, Bangladesh*
[b]*Associate Professor, Mathematics Discipline, Khulna University, Khulna-9208, Bangladesh*
[c]*Mathematics Discipline, Khulna University, Khulna-9208, Bangladesh*

Abstract

Radiative heat transfer in a nanofluid with the influence of magnetic field over a rotating stretching surface are investigated numerically. The steady laminar boundary layer flow is considered in this study. The governing boundary layer equations are formulated and transformed into nonlinear ordinary coupled differential equations by using similarity variables. The governing equations are solved numerically using the Nactsheim-Swigert Shooting iteration technique together with the Runge-Kutta six order iteration schemes with the help of a computer programming language Compaq Visual Fortran 6.6a. The simulation results are presented graphically to illustrate influence of well known parameters on the velocity, temperature and concentration distributions as well as Skin-friction coefficient, Nusselt and Sherwood number at the sheet.
(ICTE 2014).

Keywords: Radiative heat transfer; Nanofluid, Rotating stretching surface; Nactsheim-Swigert Shooting iteration; Runge-Kutta six order iteration schemes.

1. Introduction

Nanofluid technology has been received a lot of attention due to effective applications in the field of electronics engineerings, transportation, biomedical research etc. Adding nano-sized partical (1-100 nm diameters) suspended in base fluids is named nanofluids. The nanofluid has a higher thermal conductivity that shows significant enhancement due to the rate of heat transfer in industrial applications. The cooling applications of nanofluids show the importance on itself and increased attention worldwide.

On the other hand, the study of Magnetohydrodynamics (MHD) boundary layer flow of a nanofluid over a stretching surface has become several industrial, scientific and engineering applications. Engineers employ MHD principle in the design of heat exchangers, pumps and flow matters, in space vehicle propulsion, thermal protection, controlling the rate of cooling etc.

The point of application view, several scientists have made model studies. Carragher and Crane [1] investigated the heat transfer in the flow over a stretching surface, in the case when the temperature difference between the surface and ambient fluid is proportional to a power of distance from the fixed point. Pop et al. [2] determined the flow over stretching sheet near a stagnation point taking the effect of thermal radiation. The effect of various parameters on nanofluid thermal conductivity has been obtained by Jang and Choi [3]. Murshed et al. [4] and Yu et

al. [5], provide a detail literature review of nanofluids including synthesis, potential aplications, experimental and analytical analysis of effective thermal conductivity, effective thermal diffusivity and convective heat transfer.

The convective heat transfer in a nanofluid past a vertical plate using a model in which Brownian motion and Thermophoresis are accounted with the simplest possible boundary conditions have discussed by Kuznetsov Nield [6] . Khan and Pop [7] have investigated the problem of laminar fluid flow over the stretching surface in a nanofluid.

Hence the objective of this study is to present a similarity analysis of the boundary layer flow of a nanofluid past a rotating stretching sheet with the influence of magnetic field and thermal radiation. The governing equations are transformed into nonlinear ordinary diffential equations which depend on the Magnetic parameter *M*, the Radiation parameter *R*, the Prandtl number *Pr*, the Ekert number *Ec*, the Rotational parameter R', the Lewis number *Le*, the Brownian motion parameter *Nb*, Thermophoresis parameter *Nt*, stretching parameter *b/a* and constant parameter. The obtained nonlinear coupled ordinary differential equations are solved numerically using Nactsheim-Swigert (1965) Shooting technique together with Runge-Kutta six order iteration schemes. The velocity, temperature and concentration distributions are discussed and presented graphically.

2. Mathematical model of the flow

The steady two dimensional boundary layer flow of a nanofluid past a stretching surface of a rotating system is considered with the linear stretching velocity $u_w = ax$, where a is constant and *x* is coordinate measured along the stretching surface. The flow takes place at $y \geq 0$ where *y* is the coordinate measured normal to the stretching surface. A steady uniform stress leading to equal and opposite forces is applied along the *x*-axis, so that the sheet is stretched keeping the origin fixed.

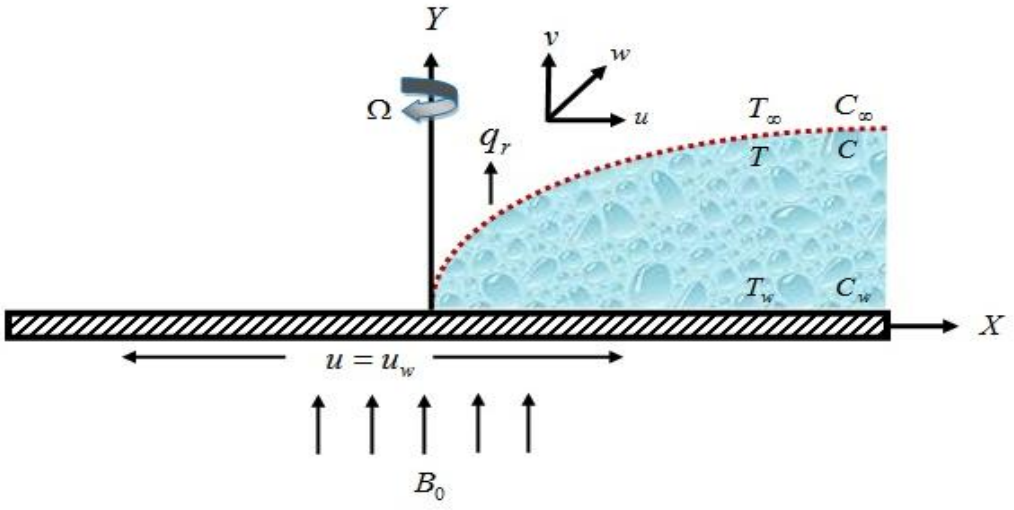

Figure 1. Physical configuration of the flow

It is assumed that at the stretching surface, the temperature T and the concentration C takes constant value T_w and C_w respectively. The ambient values attained as y tends to infinity of T and C are denoted by T_∞ and C_∞ respectively. A uniform magnetic field B is imposed to the plate. The magnetic vector B_0 can be taken as $B = (0, B_0, 0)$ and q_r is the radiative heat flux in the y-direction. The velocity of the plate (uniform velocity) considered as *U*. Also *a* and *b* are the linear constant parameter, *l* is the characteristics length and A_1, A_2 is the constant whose values depends on the properties of the fluid. Under this assumption and usual boundary layer approximation MHD nanofluid flow is governed by the following equations [8];

$$\frac{\partial u}{\partial x} + \frac{\partial v}{\partial y} = 0 \tag{1}$$

$$u\frac{\partial u}{\partial x}+v\frac{\partial u}{\partial y}=U\frac{dU}{dx}+\upsilon\frac{\partial^2 u}{\partial y^2}+2\Omega w+\frac{\sigma B_0^2}{\rho}\left(U-u\right) \tag{2}$$

$$u\frac{\partial w}{\partial x}+v\frac{\partial w}{\partial y}=\upsilon\frac{\partial^2 w}{\partial y^2}-2\Omega u-\frac{\sigma B_0^2 w}{\rho} \tag{3}$$

$$u\frac{\partial T}{\partial x}+v\frac{\partial T}{\partial y}=\alpha\frac{\partial^2 T}{\partial y^2}-\frac{\alpha}{k}\left(\frac{\partial q_r}{\partial y}\right)+\frac{\upsilon}{C_p}\left(\frac{\partial u}{\partial y}\right)^2+\tau\left[D_B\left(\frac{\partial C}{\partial y}.\frac{\partial T}{\partial y}\right)+\frac{D_T}{T_\infty}\left(\frac{\partial T}{\partial y}\right)^2\right] \tag{4}$$

$$u\frac{\partial C}{\partial x}+v\frac{\partial C}{\partial y}=D_B\frac{\partial^2 C}{\partial y^2}+\frac{D_T}{T_\infty}\frac{\partial^2 T}{\partial y^2} \tag{5}$$

and the boundary condition for the model is

$$\left.\begin{aligned} &u=u_w=ax, v=0, w=0, T=T_w=T_\infty+A_1\left(\frac{x}{l}\right)^m, C=C_w=C_\infty+A_2\left(\frac{x}{l}\right)^m && \text{at } y=0\\ &u=U=bx, w=0, T\to T_\infty, C\to C_\infty && \text{as } y\to\infty \end{aligned}\right\} \tag{6}$$

where, α is the thermal diffusivity, k is the thermal conductivity, D_B is the Brownian diffusion coefficient, D_T is the thermophoresis diffusion coefficient, x is the coordinate measured along stretching surface, u_w is the stretching velocity, U is the uniform velocity, a and b the linear constant parameter, l is the characteristics length and A_1, A_2 is the constant whose values depends on the properties of the fluid.

2.1. Method of solution

In order to find a similarity solution to the equations (2) to (5) with boundary conditions (6), the following similarity transformations, dimensionless variables are used in the rest of analysis;

$$\eta=y\sqrt{\frac{a}{\upsilon}}, \psi=x\sqrt{a\upsilon}\,f\left(\eta\right), g_0\left(\eta\right)=\frac{w}{U}, \theta=\theta\left(\eta\right)=\frac{T-T_\infty}{T_w-T_\infty}, \varphi=\varphi\left(\eta\right)=\frac{C-C_\infty}{C_w-C_\infty}$$

$$\text{and } u=\frac{\partial\psi}{\partial y}, v=-\frac{\partial\psi}{\partial x} \tag{7}$$

From the above transformations the non-dimensional, nonlinear, coupled ordinary differential equations are obtained as;

$$f'''+ff''-f'^2+M\left(\frac{b}{a}-f'\right)+2R'g_0+\frac{b^2}{a^2}=0 \tag{8}$$

$$g_0''+fg_0'-2R'f'+Mg_0=0 \tag{9}$$

$$\left(1+R\right)\theta''+E_cP_r f''^2+P_r f\theta'-mP_r f'\theta+P_rN_b\theta'\varphi'+P_rN_t\theta'^2=0 \tag{10}$$

$$\varphi''+L_e f\varphi'+\frac{N_t}{N_b}\theta''-L_e mf'\varphi=0 \tag{11}$$

The transformed boundary conditions are as follows;

$$\left.\begin{aligned} &f = 0, f' = 1, g_0 = 0, \theta = 1, \varphi = 1 \quad \text{at } \eta = 0 \\ &f' = \frac{b}{a}, g_0 = 0, \theta = 0, \varphi = 0 \qquad \text{as } \eta \to \infty \end{aligned}\right\} \tag{12}$$

where the notation primes denote differentiation with respect to η and the parameters are defined as;

$M = \dfrac{\sigma B_0^2}{\rho a}$ is the Magnetic parameter

$R = \dfrac{16\sigma_S T_\infty^3}{3k\overset{*}{\kappa}}$ is the Radiation parameter

$P_r = \dfrac{\upsilon}{\alpha}$ is the Prandtl number

$E_C = \dfrac{u_w^2}{c_p\left(T_w - T_\infty\right)}$ is the Eckert number

$R' = \dfrac{\Omega x}{U^2}$ is the Rotational parameter

$L_e = \dfrac{\nu}{D_B}$ is the Lewis number

$N_b = \dfrac{\left(\rho c\right)_p D_B\left(C_w - C_\infty\right)}{\upsilon\left(\rho c\right)_f}$ is the Brownian motion parameter

$N_t = \dfrac{\left(\rho c\right)_p D_T\left(T_w - T_\infty\right)}{\upsilon T_\infty\left(\rho c\right)_f}$ is the Thermophoresis parameter

$\dfrac{b}{a}$ is the Stretching parameter

and m is the Constant parameter.

The physical quantities of the skin-friction coefficient, the reduced Nusselt number and reduced Sherwood number are calculated respectively by the following equations,

$$C_f\left(R_e\right)^{\frac{1}{2}} = -f''(0) \tag{13}$$

$$C_{g_0}\left(R_e\right)^{\frac{1}{2}} = -g_0'(0) \tag{14}$$

$$N_u\left(R_e\right)^{-\frac{1}{2}} = -\theta'(0) \tag{15}$$

$$S_h\left(R_e\right)^{-\frac{1}{2}} = -\varphi'(0) \tag{16}$$

where $R_e = \frac{Ux'}{\upsilon}$ is the Reynolds number.

The governing equations are transformed into nonlinear ordinary differential equations which depends on the Magnetic parameter, the Radiation parameter, the Prandtl number, the Eckert number, the Rotational parameter, the Lewis number, the Brownian motion parameter, the Thermophoresis parameter, Stretching parameter and constant parameter respectively. The obtained non-linear coupled ordinary differential equations (8) to (11) are solved numerically using Nactsheim-Swigert shooting technique together with Runge-Kutta six order iteration schemes.

3. Results and discussion

A The heat and mass transfer problem associated with laminar flow of the nanofluids past a stretching surface of a rotating system has been studied. In order to investigated the physical representation of the problem, the numerical values of primary velocity, secondary velocity, temperature and species concentration with the boundary layer have been computed for different parameters as the Magnetic parameter *M*, the Radiation parameter *R*, the Prandtl number P_r, the Eckert number E_c, the Rotational parameter R', the Lewis number L_e, the Brownian motion parameter N_b, the Thermophoresis parameter N_t, the Stretching parameter b/a, and the Constant parameter *m* respectively.

In the fig. 2-3, dimensionless primary velocity distribution is plotted for different values of Magnetic parameter *M*. Here consider the values of Stretching parameter $b/a = 0.0, 0.1$. It is observed that as the Magnetic parameter increases the primary velocity decreases gradually when $b/a = 0.0$ and the primary velocity increases gradually when $b/a = 0.1$.

In the fig. 4-7, dimensionless secondary velocity distribution is plotted for different values of Magnetic parameter *M*, Here consider the values of Stretching parameter $b/a = 0.0, 0.5, 1, 1.5$. It is observed that as the Magnetic parameter increases the secondary velocity increases gradually when $b/a = 0.0$ and the secondary velocity decreases gradually when $b/a = 0.5, 1.0, 1.5$.

In the fig. 8, dimensionless secondary velocity distribution is plotted for different values of Rotational parameter R'. It is observed that as the Rotational parameter increases the secondary velocity decreases gradually.

In the fig. 9, the dimensionless temperature distribution is plotted for different values of Stretching parameter b/a. It is observed that as the Stretching parameter increases the temperature decreases gradually.

In the fig. 10, the dimensionless temperature distribution is plotted for different values of Brownian parameter N_b. It is observed that as the Brownian parameter increases the temperature increases gradually.

In the fig. 11, the dimensionless temperature distribution is plotted for different values of constant parameter *m*. It is observed that as the constant parameter increases the temperature increases gradually.

In the fig. 12, the dimensionless temperature distribution is plotted for different values of Eckert number E_c. It is observed that as the Eckert number increases the temperature increases gradually.

In the fig. 13, the dimensionless temperature distribution is plotted for different values of Lewis number L_e. It is observed that as the Lewis number increases the temperature decreases gradually.

In the fig. 14, the dimensionless temperature distribution is plotted for different values of Lewis number L_e. It is observed that as the Lewis number increases the temperature decreases gradually.

In the fig. 15, the dimensionless temperature distribution is plotted for different values of Magnetic parameter *M*. It is observed that as the Magnetic parameter increases the temperature increases gradually.

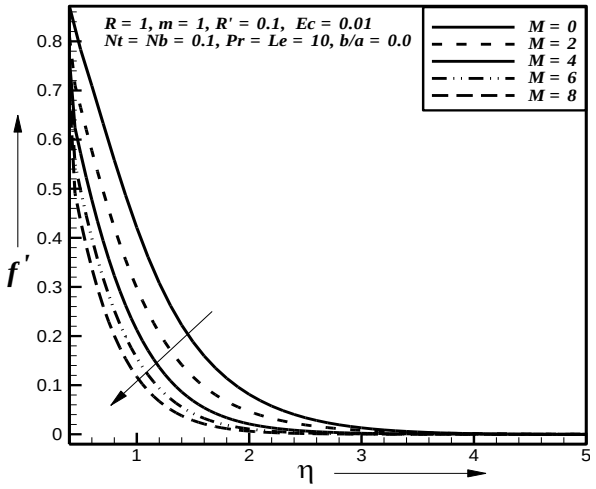

Fig. 2. Effect of M on primary velocity profiles when $b / a = 0.0$

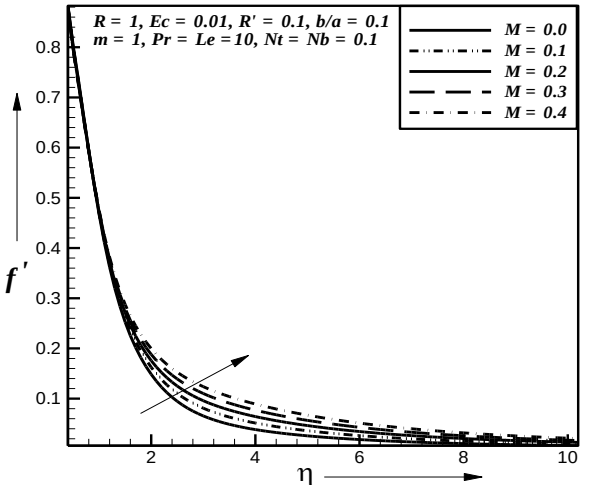

Fig. 3. Effect of M on primary velocity profiles when $b / a = 0.1$

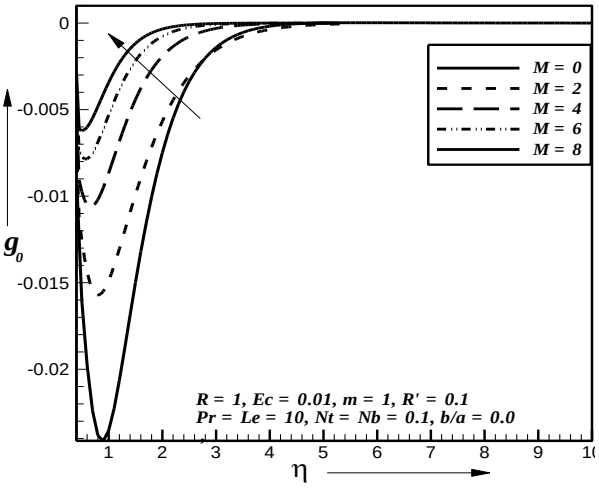

Fig. 4. Effect of M on secondary velocity profiles when $b / a = 0.0$

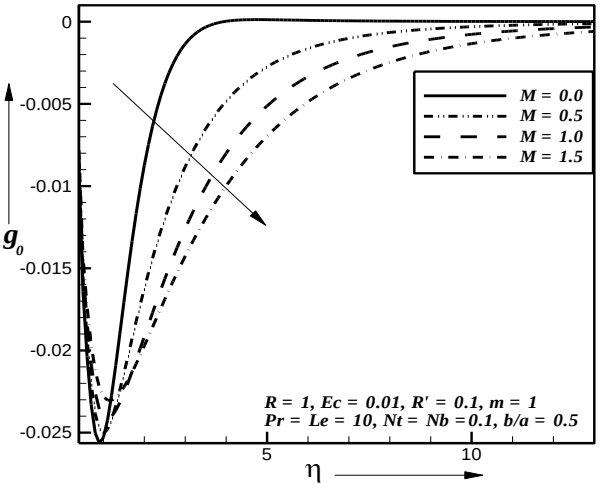

Fig. 5. Effect of M on secondary velocity profiles when $b / a = 0.5$

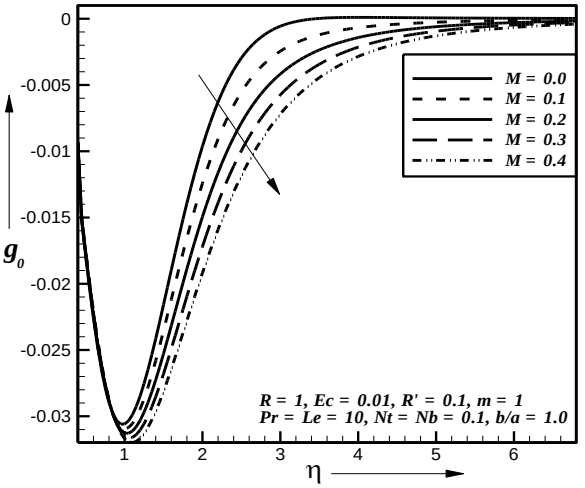

Fig. 6.Effect of M on secondary velocity profiles when $b / a = 1.0$

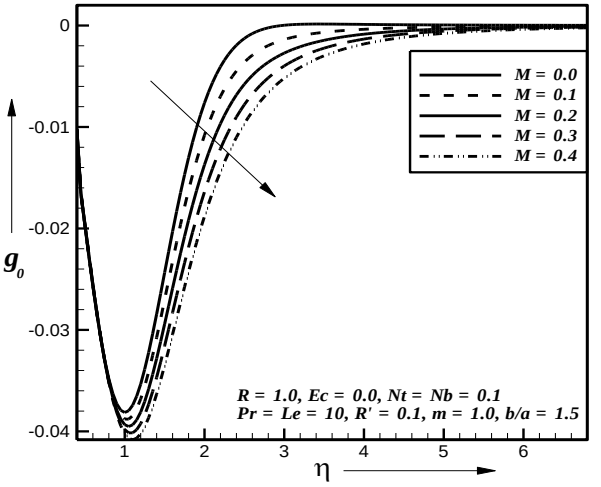

Fig. 7. Effect of M on secondary velocity profiles when $b / a = 1.5$

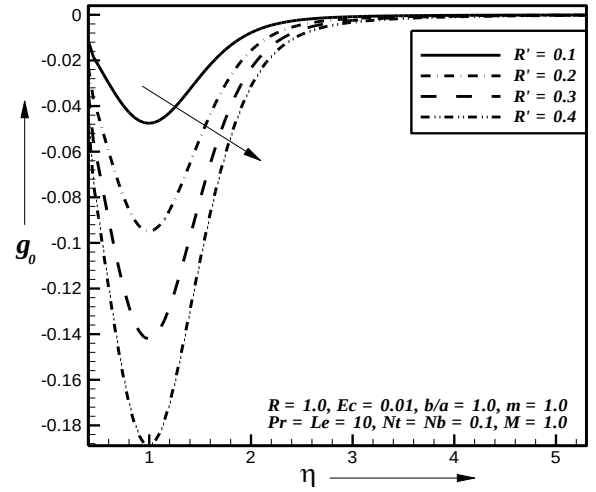

Fig. 8. Effect of R' on secondary velocity profiles

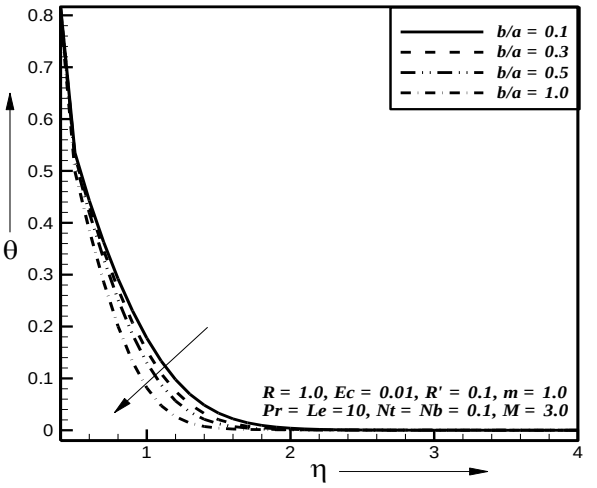

Fig. 9. Effect of b / a on temperature profiles

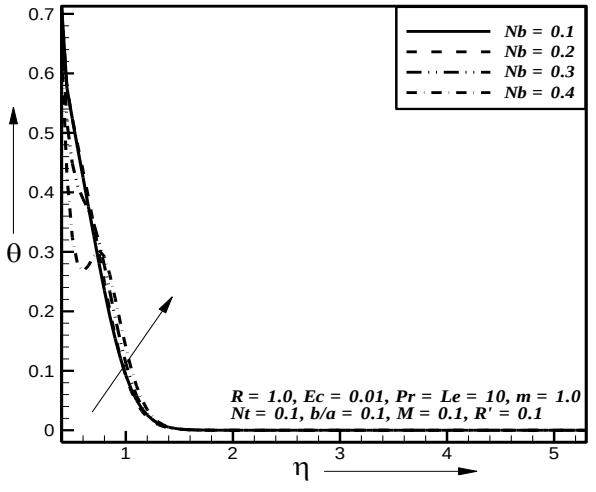

Fig. 10. Effect of N_b on temperature profiles

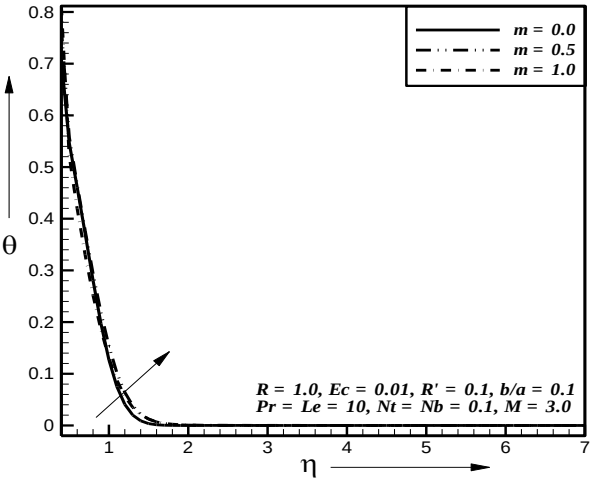

Fig. 11. Effect of m on temperature profiles

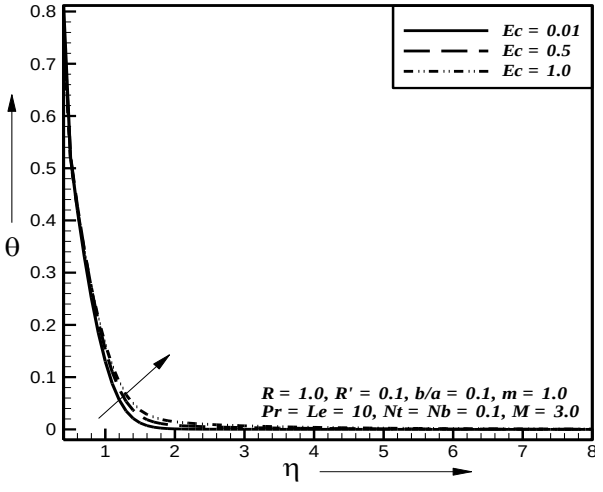

Fig. 12. Effect of E_c on temperature profiles

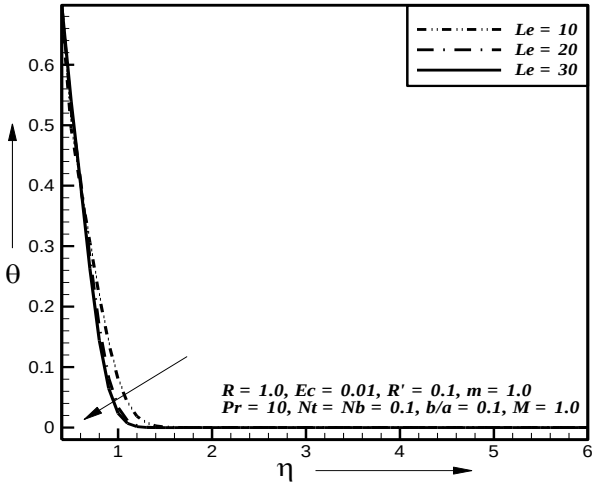

Fig. 13. Effect of L_e on temperature profiles

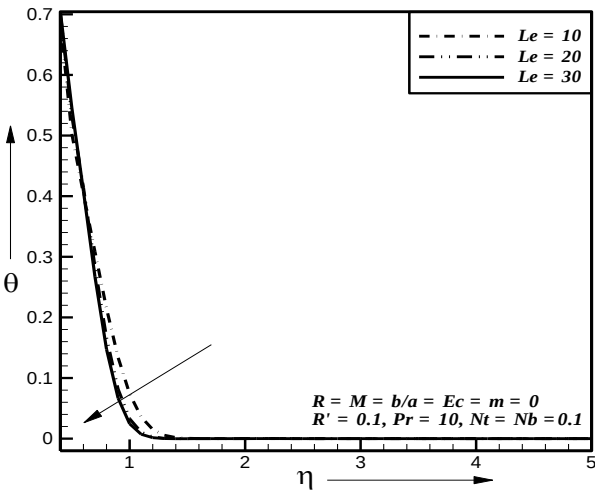

Fig. 14. Effect of L_e on temperature profiles

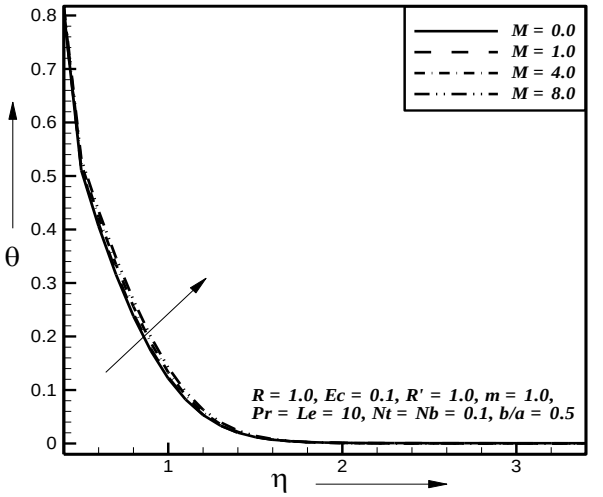

Fig. 15. Effect of M on temperature profiles

In the fig. 16, the dimensionless temperature distribution is plotted for different values of Prandtl number P_r. It is observed that as the Prandtl number increases the temperature increases gradually.

In the fig. 17, the dimensionless temperature distribution is plotted for different values of Radiation parameter R. It is observed that as the Radiation parameter increases the temperature increases gradually.

In the fig. 18, the dimensionless temperature distribution is plotted for different values of Rotational parameter R'. It is observed that as the Rotational parameter increases the temperature increases gradually.

In the fig. 19, the dimensionless concentration distribution is plotted for different values of Stretching parameter b/a. It is observed that as the Stretching parameter increases the concentration decreases gradually.

In the fig. 20, the dimensionless concentration distribution is plotted for different values of constant parameter m. It is observed that as the constant parameter increases the concentration decreases gradually.

In the fig. 21, the dimensionless concentration distribution is plotted for different values of Eckert number E_c. It is observed that as the Eckert number increases the concentration decreases gradually.

In the fig. 22, the dimensionless concentration distribution is plotted for different values of Magnetic parameter M. It is observed that as the Magnetic parameter increases the concentration increases gradually.

In the fig. 23, the dimensionless concentration distribution is plotted for different values of Radiation parameter R. It is observed that as the Radiation parameter increases the concentration decreases gradually.

In the fig. 24, the dimensionless concentration distribution is plotted for different values of Lewis number L_e. It is observed that as the Lewis number increases the concentration decreases gradually.

In the fig. 25, the dimensionless concentration distribution is plotted for different values of Thermophoresis parameter N_t. It is observed that as the Brownian parameter increases the temperature increases gradually.

In the fig. 26, the dimensionless concentration distribution is plotted for different values of Brownian parameter N_b. It is observed that as the Brownian parameter increases the temperature increases gradually.

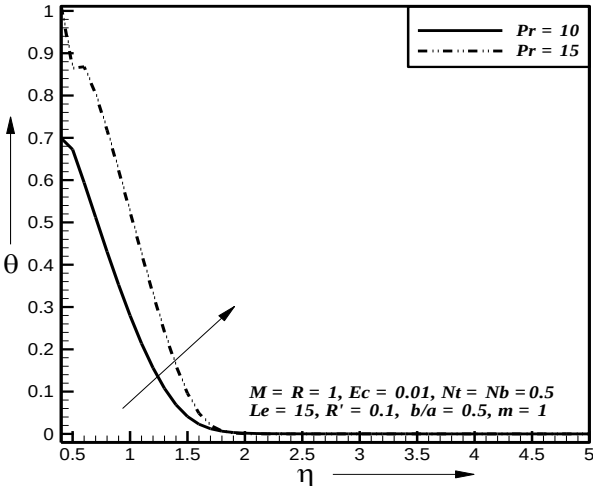

Fig. 16. Effect of P_r on temperature profiles

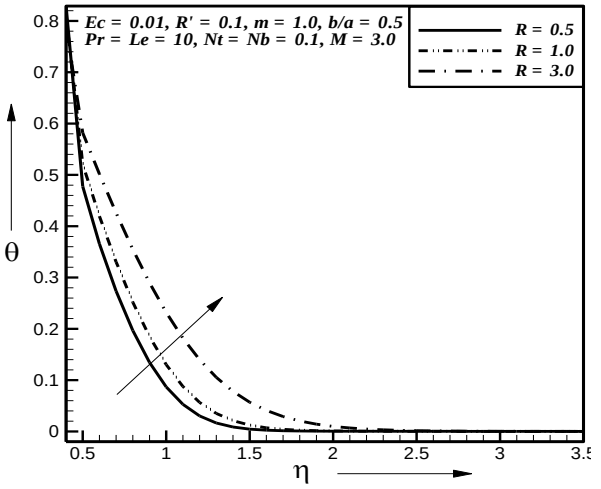

Fig. 17. Effect of R on temperature profiles

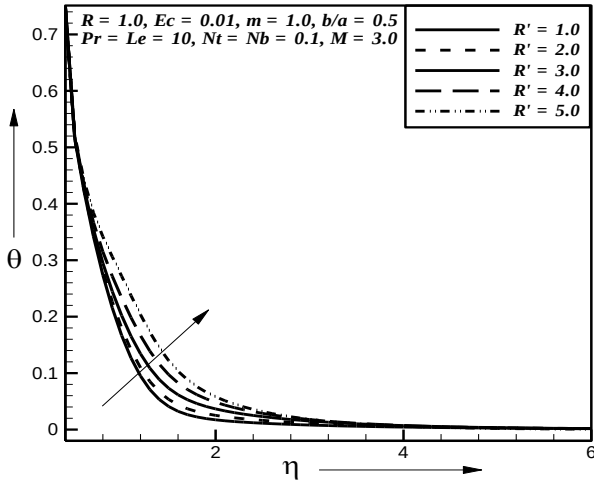

Fig. 18. Effect of R' on temperature profiles

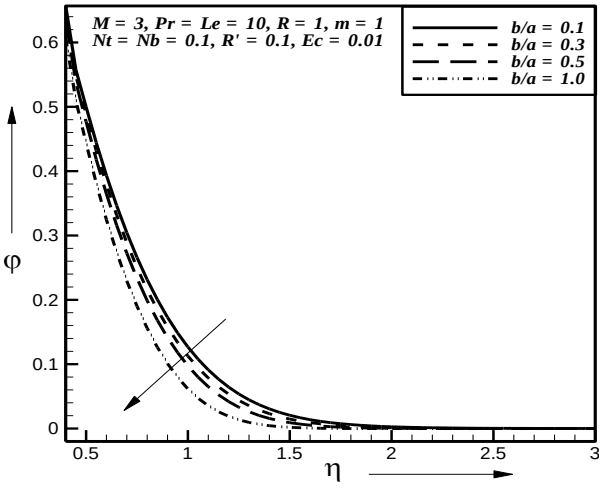

Fig. 19. Effect of b / a on concentration profiles

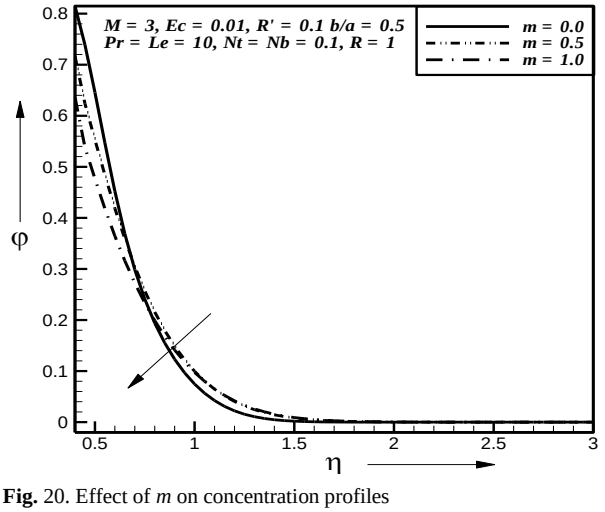

Fig. 20. Effect of m on concentration profiles

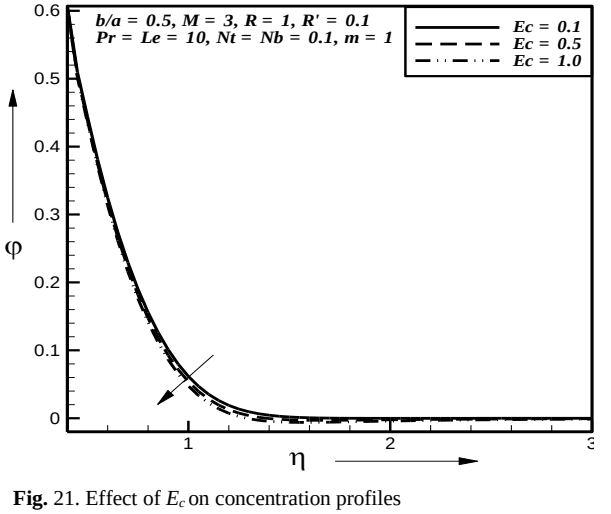

Fig. 21. Effect of E_c on concentration profiles

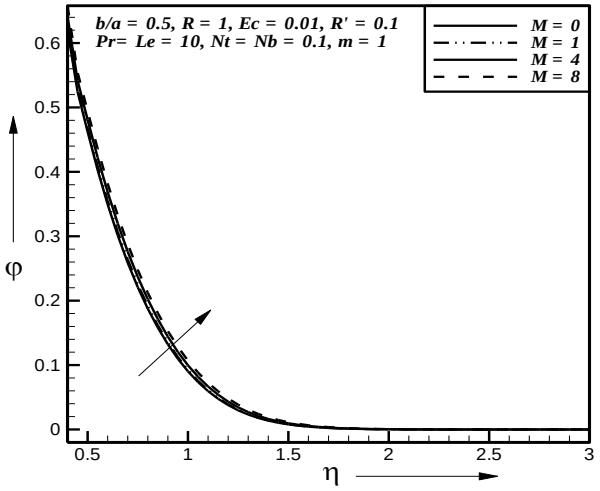

Fig. 22. Effect of M on concentration profiles

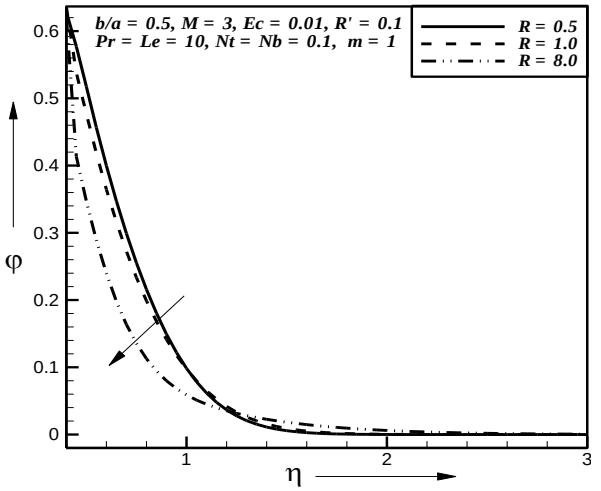

Fig. 23. Effect of R on concentration profiles

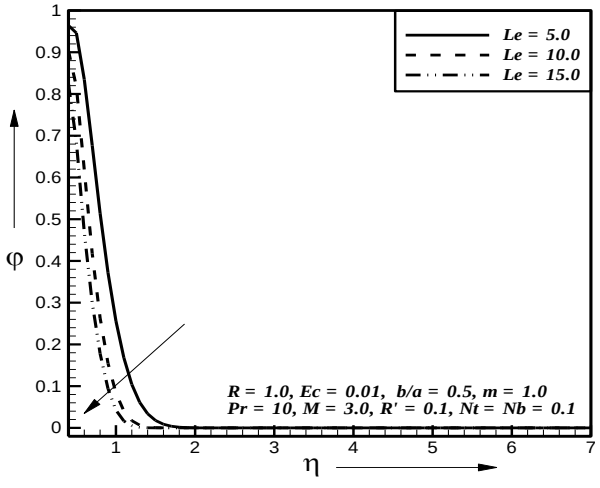

Fig. 24. Effect of L_e on concentration profiles

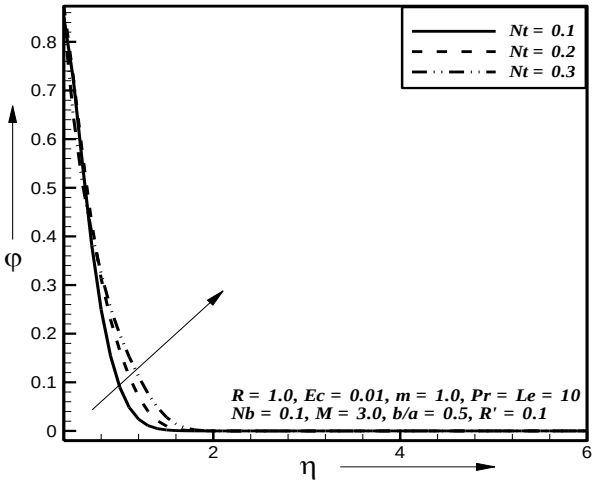

Fig. 25. Effect of N_t on concentration profiles

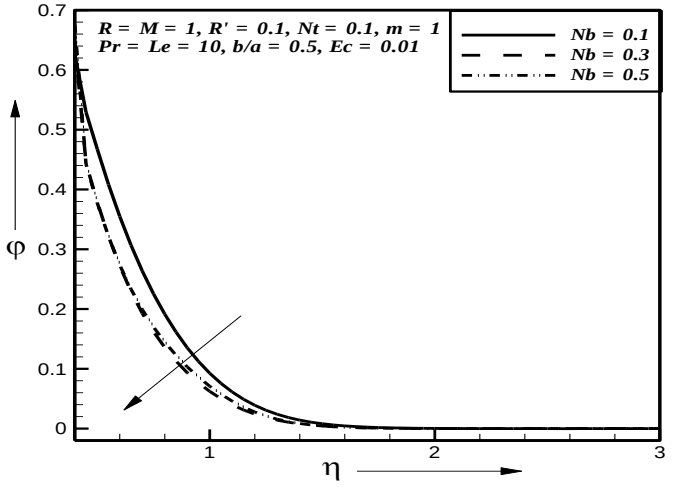

Fig. 26. Effect of N_b on concentration profiles

For the physical interest of the problem, the dimensionless skin-friction coefficient $\left(-f''\right)$ and $\left(-g_0'\right)$, the dimensionless heat transfer rate $\left(-\theta'\right)$ at the sheet and the dimensionless mass transfer rate $\left(-\varphi'\right)$ at the sheet are plotted against Thermophoresis parameter $\left(N_t\right)$ and illustrated in Figures 27 to 40.

Fig. 27 represents the primary shear stress $\left(-f''\right)$ plotted against the Thermophoresis parameter $\left(N_t\right)$ for different values of Magnetic parameter M. It is observed that as the Magnetic parameter increases the primary shear stress decreases gradually.

Fig. 28 represents the primary shear stress $\left(-f''\right)$ plotted against the Thermophoresis parameter $\left(N_t\right)$ for different values of Magnetic parameter M. It is observed that as the Magnetic parameter increases the primary shear stress increases gradually.

Fig. 29 represents the secondary shear stress $\left(-g_0'\right)$ plotted against the Thermophoresis parameter $\left(N_t\right)$ for different values of Magnetic parameter M. It is observed that as the Magnetic parameter increases the secondary shear stress increases gradually.

Fig. 30 represents the secondary shear stress $\left(-g_0'\right)$ plotted against the Thermophoresis parameter $\left(N_t\right)$ for different values of Magnetic parameter M. It is observed that as the Magnetic parameter increases the secondary shear stress decreases gradually.

Fig. 31 represents the secondary shear stress $\left(-g_0'\right)$ plotted against the Thermophoresis parameter $\left(N_t\right)$ for different values of Magnetic parameter M. It is observed that as the Magnetic parameter increases the secondary shear stress decreases gradually.

Fig. 32 represents the secondary shear stress $\left(-g_0'\right)$ plotted against the Thermophoresis parameter $\left(N_t\right)$ for different values of Rotational parameter R'. It is observed that as the Rotational parameter increases the secondary shear stress decreases gradually.

Fig. 33 represents the dimensionless heat transfer rate $\left(-\theta'\right)$ plotted against the Thermophoresis parameter $\left(N_t\right)$ for different values of Constant parameter m. It is observed that as the Constant parameter increases the heat transfer rate decreases gradually.

Fig. 34 represents the dimensionless heat transfer rate $\left(-\theta'\right)$ plotted against the Thermophoresis parameter $\left(N_t\right)$ for different values of Eckert number E_c. It is observed that as the Eckert number increases the heat transfer rate increases gradually.

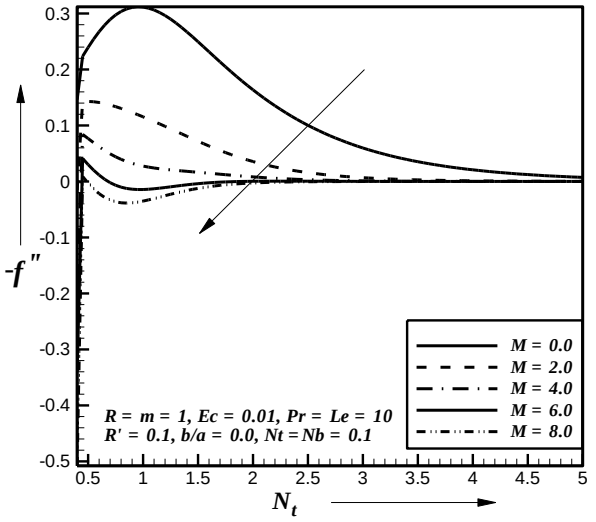

Fig. 27. Effect of *M* on primary shear stress

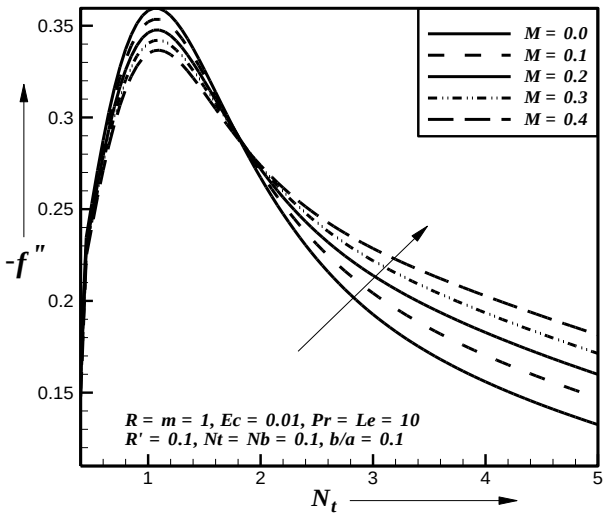

Fig. 28. Effect of *M* on primary shear stress

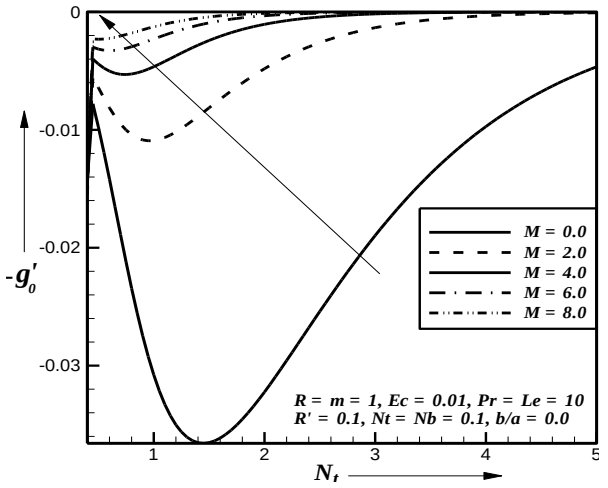

Fig. 29. Effect of *M* on secondary shear stress

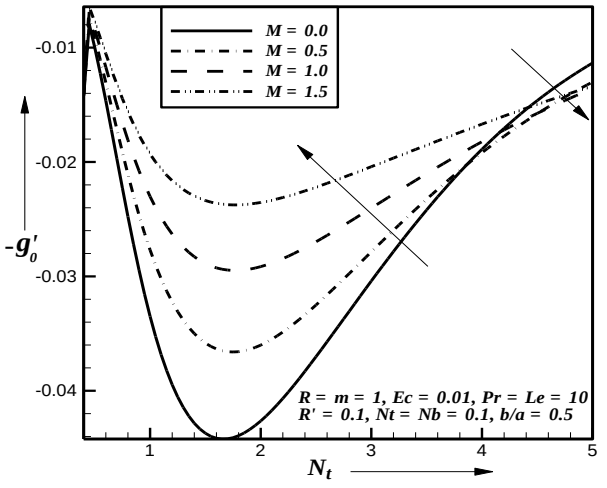

Fig. 30. Effect of *M* on secondary shear stress

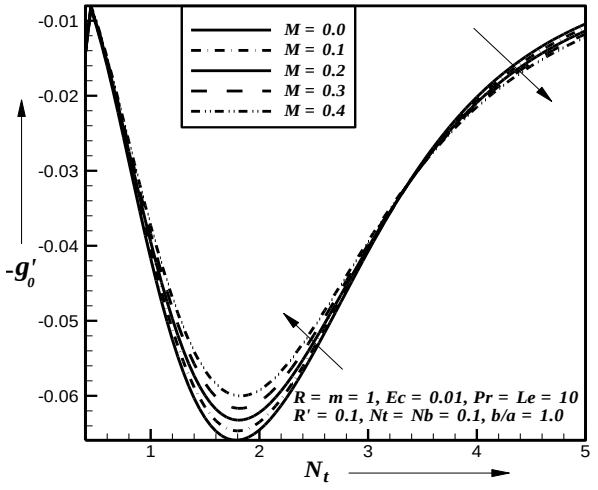

Fig. 31. Effect of *M* on secondary shear stress

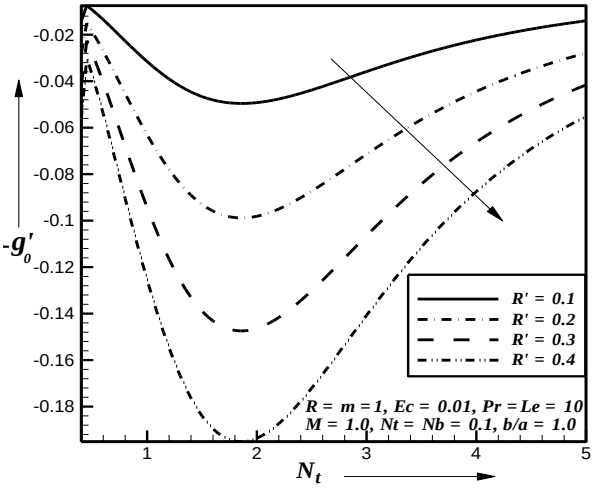

Fig. 32. Effect of R' on secondary shear stress

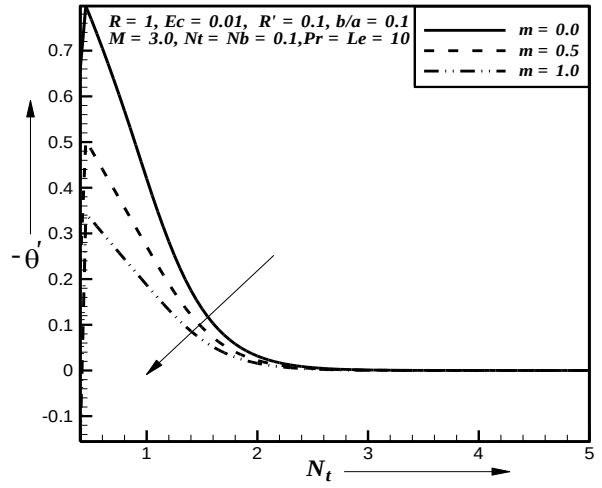

Fig. 33. Effect of *m* on heat transfer rate

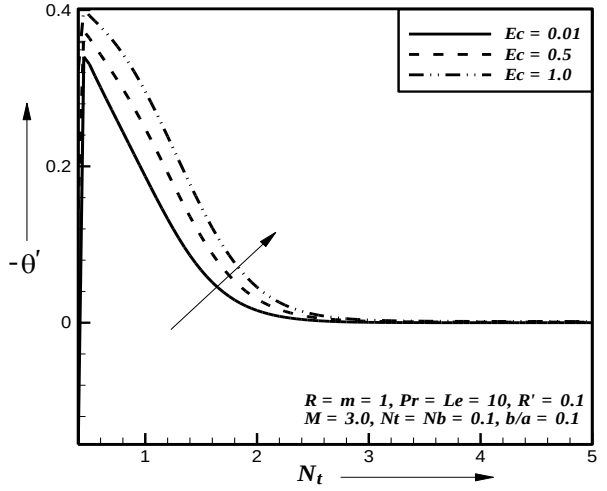

Fig. 34. Effect of E_c on heat transfer rate

Fig. 35 represents the dimensionless heat transfer rate $\left(-\theta'\right)$ plotted against the Thermophoresis parameter $\left(N_t\right)$ for different values of Brownian parameter N_b. It is observed that as the Brownian parameter increases the heat transfer rate increases gradually.

Fig. 36 represents the dimensionless heat transfer rate $\left(-\theta'\right)$ plotted against the Thermophoresis parameter $\left(N_t\right)$ for different values of Thermophoresis parameter N_t. It is observed that as the Thermophoresis parameter increases the heat transfer rate increases gradually.

Fig. 37 represents the dimensionless heat transfer rate $\left(-\theta'\right)$ plotted against the Thermophoresis parameter $\left(N_t\right)$ for different values of Prandtl number P_r. It is observed that as the Prandtl number increases the heat transfer rate increases gradually.

Fig. 38 represents the dimensionless heat transfer rate $\left(-\theta'\right)$ plotted against the Thermophoresis parameter $\left(N_t\right)$ for different values of Radiation parameter R. It is observed that as the Radiation parameter increases the heat transfer rate increases gradually.

Fig. 39 represents the dimensionless mass transfer rate $\left(-\varphi'\right)$ plotted against the Thermophoresis parameter $\left(N_t\right)$ for different values of Lewis number L_e. It is observed that as the Lewis number increases the mass transfer rate decreases gradually.

Fig. 40 represents the dimensionless mass transfer rate $\left(-\varphi'\right)$ plotted against the Thermophoresis parameter $\left(N_t\right)$ for different values of Brownian parameter N_b. It is observed that as the Brownian parameter increases the mass transfer rate decreases gradually.

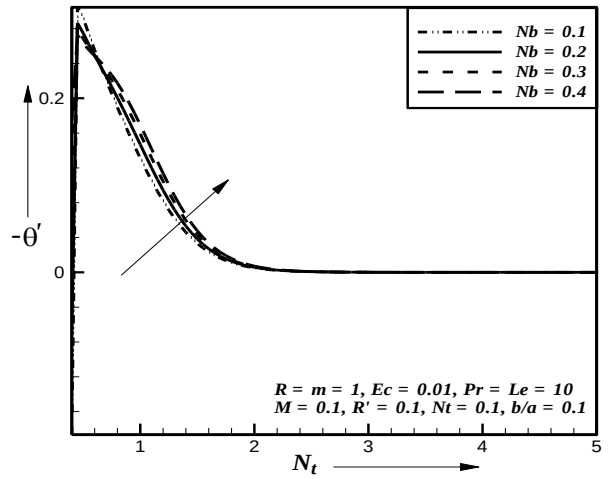

Fig. 35. Effect of N_b on heat transfer rate

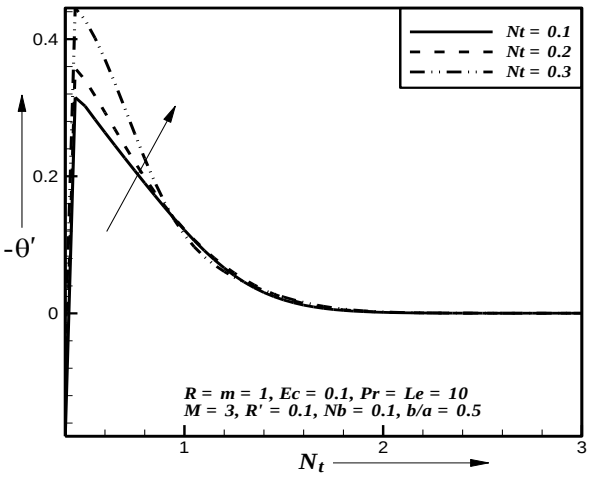

Fig. 36. Effect of N_t on heat transfer rate

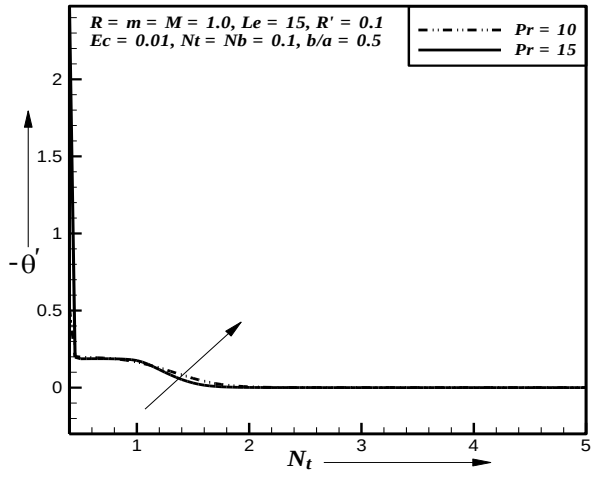

Fig. 37. Effect of P_r on heat transfer rate

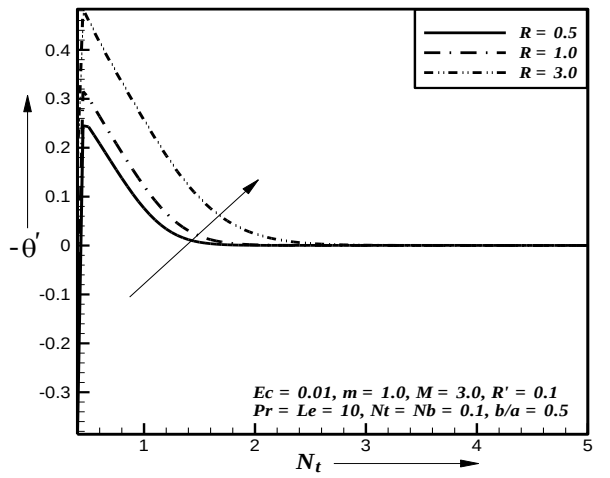

Fig. 38. Effect of R on heat transfer rate

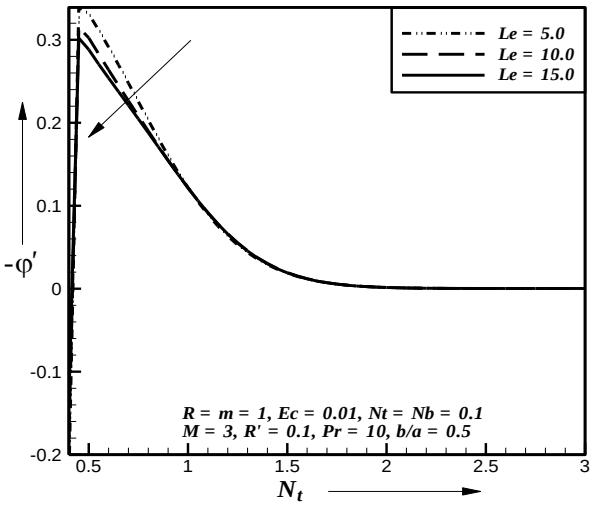

Fig. 39. Effect of L_e on mass transfer rate

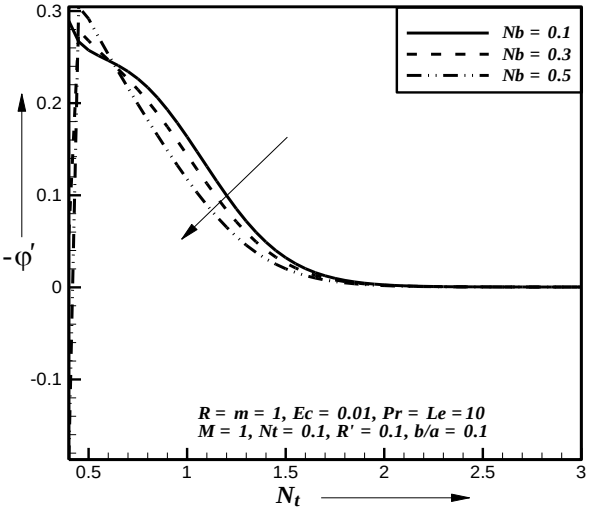

Fig. 40. Effect of N_b on mass transfer rate

4. Conclusion

Laminar boundary layer flow of a nanofluid has been investigated for steady flow past a stretching surface of rotating system with the influence of magnetic field and thermal radiation. The results are presented for various parameters. The velocity, temperature and concentration distributions for different parameters are shown graphically. The important findings of the investigation from graphical representation are listed below:

The temperature and concentration boundary layer thickness increases due to increase of magnetic parameter for nanofluids.

The temperature boundary layer thickness increases due to increase of Brownian motion parameter. Also the heat transfer rate at the sheet increases for increasing value of Brownian motion parameter and Thermophoresis parameter. The concentration boundary layer thickness increases due to increase of thermophoresis parameter and concentration boundary layer thickness decreases due to increase of Brownian motion parameter. Also the mass transfer rate at the sheet decreases due to decrease of Brownian motion parameter.

The temperature and concentration boundary layer thickness decreases due to increase of Stretching parameter.

The temperature boundary layer thickness increases due to increase of constant parameter and concentration boundary layer thickness decreases due to increase of constant parameter. Also the surface heat transfer rate is decreased.

The temperature boundary layer thickness increases due to increase of Radiation parameter where as concentration boundary layer thickness decreases due to increase of Radiation parameter. Also the surface heat transfer rate is increased.

The temperature boundary layer thickness increases due to increase of Eckert number where as concentration boundary layer thickness decreases due to increase of Eckert number. Also the surface heat transfer rate is increased.

The temperature boundary layer thickness increases due to increase of Rotational parameter for nanofluids.

The temperature boundary layer thickness as well as the concentration boundary layer thickness decreases due to increase of Lewis number. Also the mass transfer rate at the sheet decreases.

The primary velocity profiles decreases for increasing Magnetic parameter when the stretching parameter takes the value zero but.when the Stretching parameter takes value 0.1 then the primary velocity profiles increases. The secondary velocity profiles increase for increasing Magnetic parameter when the stretching parameter takes the value zero, but when the Stretching parameter takes the value (0.5 to 1.5 in present study) then the secondary velocity profiles decreases.

References

[1] P. Carragher, L. Crane, Heat Transfer on Continuous Stretching Sheet, ZAMM, vol. 10, (1982), No. 62, pp. 564-565.
[2] S. R. Pop, Radiation effect on the flow near the stagnation point of a stretching sheet, Technische Mechanik, vol. 25, (2004), pp. 100-106.
[3] S. P. Jang, S. U. S. Choi, Effects of Various Parameters on Nanofluid Thermal Conductivity, Journal of Heat Transfer, vol. 129, (2007), pp. 617-623.
[4] S. M. S. Murshed, Thermophysical and electrokinetic properties of nanofluids – a critical review, Applied Thermal Energy, vol. 28, (2008), pp. 2109-2125.
[5] W. Yu, Review and comparison of nanofluid thermal conductivity and heat transfer enhancements, Heat Transfer Engineering, vol. 29, (2008), No. 5, pp. 432-460.
[6] A. V. Kuznetsov, D. A. Nield , The Cheng-Minkowycz Problem for Natural Convective Boundary-layer Flow in a Porous Medium Saturated by a Nanofluid, International Journal of Heat and Mass Transfer, vol. 52, (2009), pp. 5792-5795.
[7] W. A. Khan, I. Pop, Boundary-Layer Flow of a Nanofluid Past a Stretching Sheet, International Journal of Heat and Mass Transfer, vol. 53(2010), pp. 2477-2483.

6th BSME International Conference on Thermal Engineering (ICTE 2014)

Energy and exergy analysis of a coal based thermal power plant

A.K.M. Nazrul Islam, Farhana Alam, Md. Ashraful Islam

Department of Mechanical Engineering, Bangladesh University of Engineering and Technology, Dhaka-1000, Bangladesh.

Abstract

This paper addresses the energetic and exergetic efficiencies and losses in different components and the overall system of a 250 MW coal based thermal power plant. The plant is operated under Bangladesh Power Development Board (BPDB), which is located at Barapukuria, Bangladesh and consists of 2 units (2 x 125 MW). The analyses have been carried out by considering design data for different designed and loading conditions of the plant. The overall energy efficiencies of the plant are 35.48%, 56.77%, 70.96% and 75.67% and the overall exergy efficiencies were 44.25%, 33.31%, 30.78 % and 30.21% for 50%, 80%, 100% and 106% loading conditions respectively for the design data. However, the overall energy and exergy efficiencies of the power plant during operation are 39.2%, 46.6% and 27.9 %, 27.2% for 57% and 67% loading conditions respectively, which are lower than the design value. The distribution of the exergy losses in power plant components has been assessed to locate the process irreversibility. The comparison between the energy losses and the exergy losses of the individual components of the plant shows that the maximum energy losses (~49.92%) occur in the condenser, whereas the maximum exergy losses (~68.27%) occur in the boiler. Exergy analysis can be particularly effective in identifying ways to optimize the performance of existing operations and designing the plant while energy balance gives heat transfer between the system and its surrounding.

Keywords: Energy efficiency; exergy destruction; coal base power plant; thermal power plant.

1. Introduction

Energy consumption is one of the most important indicators showing the development stages of countries and living standards of communities. Population increment, urbanization, industrializing and technological development result directly in increasing energy consumption. To achieve the maximum utilization of energy resources and reliability of the plant, researchers have the great interest on energy and exergy analysis of the power plant. In generally, the performance of thermal power plants is evaluated through energetic performance criteria based on the first law of thermodynamics, including electrical power and thermal efficiency [1]. In recent decades, the exergetic performance based on the second law of thermodynamics has found as useful method in the design, evaluation, optimization and improvement of thermal power plants. The majority of the causes of thermodynamic imperfection of thermal processes are not accounted for by energy (or the first law of thermodynamics), whilst the exergy (or second law of thermodynamic analysis) accounts the irreversibilities like heat transfer through a finite temperature difference, chemical reactions, friction, mixing, and unrestrained expansion. Practical devices involving energy conversion and transfer always observe energy conservation law, but the quality of energy degrades. Degradation of energy is equivalent to the irretrievable loss of exergy due to all real processes being irreversible. The loss of exergy or irreversibility provides a quantitative measure of process inefficiency [2].

Nomenclature

Cp	Specific heat at constant pressure
En	Energy flow (kW)
Ex	Exergy flow (kW)
HPT	High pressure turbine
IPT	Intermediate pressure turbine
DFLP	Differential low pressure turbine
CW	Cooling water
CEP	Condensate extraction pump
BFP	Boiler feed pump
HTR	Heater
LHV	Lower Heating Value

Subscript

g	Flue gas
in	Inlet
j	Species /stream identification
out	Outlet
o	Reference state

Superscript

a	air
f	fuel
g	Flue gas

The exergy consumption during a process is proportional to entropy creation, which accounts for inefficiencies due to irreversibilities. Therefore, exergy analysis is as important as energy analysis for design, operation and maintenance of different equipment and systems of a power plant. An exergy analysis can identify locations of energy degradation and rank them in terms of their significance. This knowledge is useful in directing the attention of process design, researchers, and practicing engineers to those components of the system being analyzed that offers the greatest opportunities for improvement [3].

At present 1880 GW of total electricity (5940 GW) is generated from coal (Source: IEA, June 2014) which is the 31.64% of total generation. As per statistics June 2014 of BPDB, the electricity production by coal is about 2.40% of total electricity generation of country [4]. Bangladesh has up to 2.7 billion short tons of high-quality coal reserves [5] and thus coal-based thermal power plants can play an important role for Bangladesh. Extensive research have been carried out concerning energetic and exergetic performances of coal-fired thermal power plants. Datta et al. [6] presented work on exergy analysis of a coal-based thermal power plant using the design data from a 210 MW thermal power plant. The exergy efficiency is calculated using the operating data from the plant at different conditions, viz. at different loads, different condenser pressures, with and without regenerative heaters. Rosen [7] presented energy and exergy-based comparison of coal-fired and nuclear steam power plants. The results show overall energy and exergy efficiencies are 37% and 36% respectively for the coal-fired and nuclear process. Ganapathy et al. [8] determined the energy losses and the exergy losses of the individual components of the lignite fired thermal power plant. The results represent the maximum energy losses of 39% occur in the condenser, whereas the maximum exergy losses of 42.73% occur in the combustor. Suresh et al. [9] provides insight to find out efficiency improvement in various components of a power generating system. The performance of the plant was estimated by a component-wise modeling followed by computer program, "Cycle-Tempo" was used for the study. The maximum exergy loss was found to be in steam generation unit followed by turbine. The off-design simulation resulted in an overall energy efficiency of 28.5% at 40% load factor compared to 31.5% at design rating. Rudra et al. [10] examined to increase coal-fired steam power plant efficiency by advance steam parameters. Although a considerable amount of research have been carried out, but more effective research is essential to investigate results on coal based thermal power plant using sub-critical, supercritical and ultra-supercritical steam conditions. This study represents the results considering both the energetic and exergetic performance criteria, efficient and effective usage of fuel resources by taking into account the quality and quantity of the energy used in the generation of electric power in coal based thermal power plants, which is operating on sub-critical steam conditions.

2. Process Description

Coal fired thermal power plant generally operates on Rankine cycle [11]. The schematic arrangement of equipments of this power plant is shown in Fig. 1. The major components of the plant are high, intermediate and differential low pressure turbines (HPT, IPT and DFLP), boiler (B), pumps (P), deaerator (D), generator (G), condenser (C), low and high pressure feed water heaters etc. The thermodynamic models of this power plant are based on fundamental mass, energy and exergy balances.

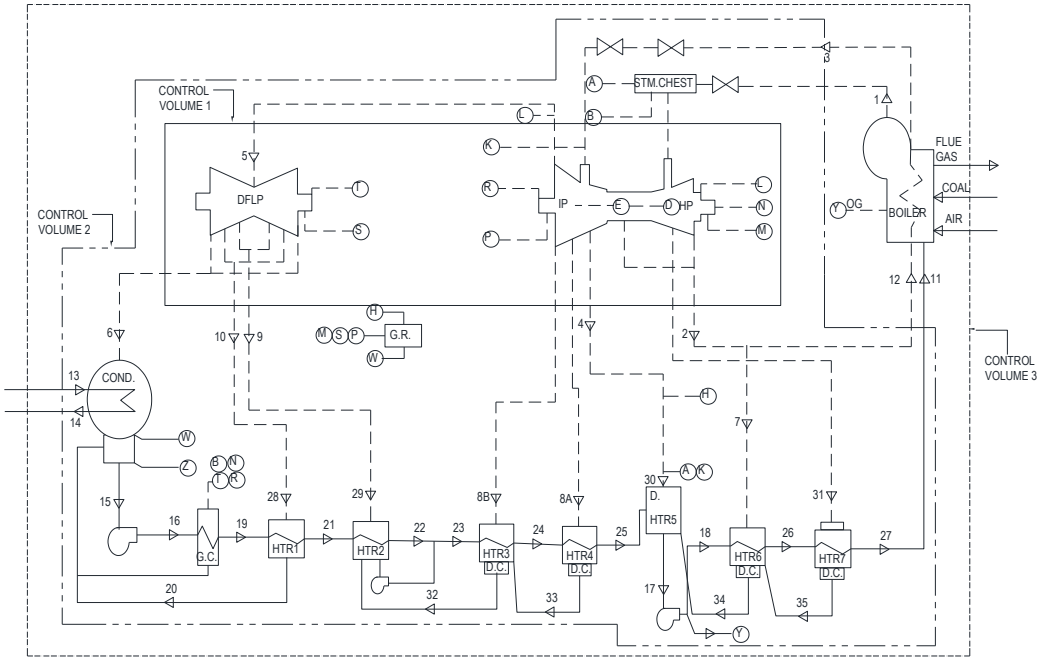

Fig. 1. Flow diagram of Barapukuria 2 x 125 MW coal based thermal power plant.

The plant consists of three turbines, namely high, intermediate and low pressure (HP, IP and LP) which are connected to the generator. Steam flows to HP turbine (point 1) with high energy and high exergy, after producing work on expansion in HP turbine, cold reheat steam (point 12) with low energy and exergy flows back to boiler for reheating, hot reheat steam (point 3). Wet steam (vapour fraction = 0.92) is exhausted from LP turbine to condenser at a very low pressure (86 kPa). Circulating water flows to the condenser (point 13) almost at ambient temperature takes away heat of condensation and flows back to the river (point 14). The condensate exits the condenser (point 15) with low energy and is pumped by the condensate extraction pump (CEP) to the deaerator through LP heaters (HTR1 to HTR4). Deaerator feeds (point 17) to BFP, which raise the pressure of feed water flow (point 18) to high value to flow through high pressure heaters (HTR6 and HTR7) and back to the boiler (point 11) for generation of steam and the cycle continues. Final feed water (point 11) temperature rises across feed heaters by transferring heat from turbine extraction steam and facilitates high temperature heat addition in boiler.

Table 1. Some baseline data of the Barapukuria 250 MW coal based power plant (Source: BPDB)

Coal flow	55 t/h
Ash production	6.6 t/h
Flue gas flow	700,000 Nm^3/h
Flue gas temperature	150 ^oC
Emission SO_x on average	0.600 t/h
Emission SO_x max	0.735 t/h
Emission NO_x max	500 mg/Nm^3
Particulate matter	50 mg/Nm^3
Stack height	95m
Circulating cooling water	14,000 m^3/h

Following additional considerations are made for calculation of the energy and exergy of the different components:

- Total auxiliary power consumption in the plant is considered in a consolidated manner as a percentage of the generated power.
- Atmospheric pressure and temperature are 25°C temperature and 1 atmospheric pressure.
- The relative humidity of the ambient air is assumed to be 80%.
- Incoming fuel temperature is 25°C.

3. Results and discussion

The design and operating data of Barapukuria 2 x 125 MW coal based thermal power plant have been used for the energy and exergy analysis at different state points. The total cycle of the power plant consists of six closed feed water heaters and one open feed water heater (deaerator). The T-s diagram is shown in Fig. 2. For this cycle, the working fluid passes isentropically through the turbine stages and pumps. The T-S diagram shows the principal states of the cycle. The steam (temp. 515 ^{o}C, 14.00 Mpa) enters the HP turbine at state 1 and expands to state 2, where a fraction of the total flow is extracted, or bled, into two closed feed water heater HTR6 and HTR7 (state 7 and state 31). Then the steam is reheated (temp. 510 ^{o}C, 1.078 Mpa) and enters the IP turbine at state 3 and expands to state 5. A fraction of the total flow is extracted, or bled, into one open feed water heater HTR5 (deaerator, state 30) and two closed feed water heater HTR3 and HTR4 (state 8B and state 8A). The rest of the steam expands through the LP turbine to state 6. Finally, after increasing the temperature by the feed water heater and increasing the pressure by the boiler feed pump to the steam generator pressure and enters the steam generator at state 27.The cycle is completed as the working fluid is heated in the steam generator at constant pressure from state 27 to 1.

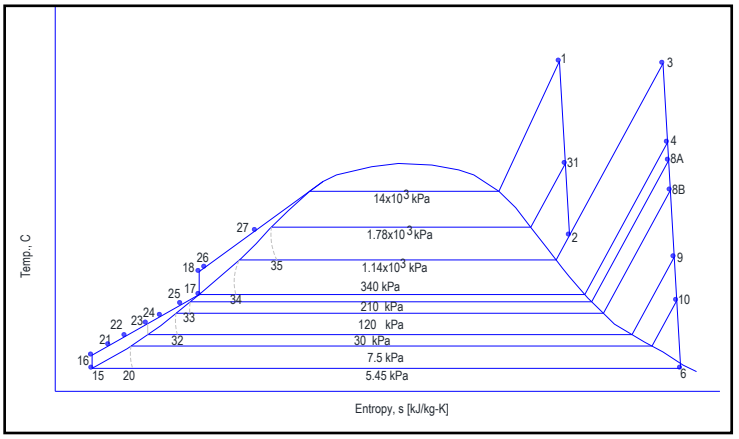

Fig. 2. T-s diagram of total power cycle.

Energy and exergy efficiencies of the overall power plant are shown in Fig. 3(a) as function of 100%, 80% and 50% loading condition for the design data condition. The decrease in exergy efficiency is attributed to the loss of exergy in the steam generation unit (boiler) and turbine. Energy and exergy efficiencies of the overall power plant are shown in Fig. 3(b) as function of 57% and 67% loading condition for the operation condition. From the comparison of design and operating data of the overall power plant, it is found that the efficiency of the operating condition is low than the design condition.

(a)

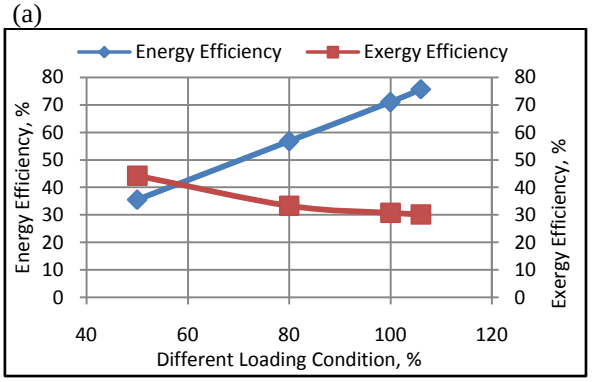

(b)

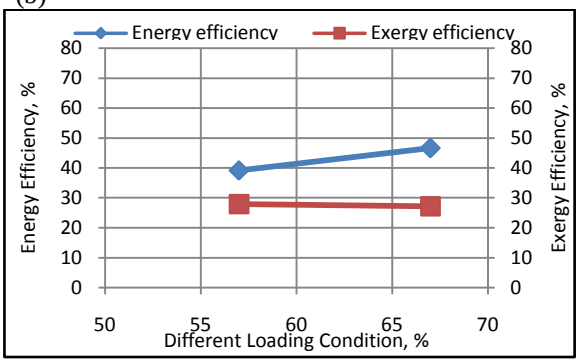

Fig. 3. Energy and exergy efficiencies of the overall power plant for (a) design data (b) operating data.

The comparison of energy efficiency and exergy efficiency between different components of the power plant is specified in Fig. 4(a) - 4(c) for different loading conditions.

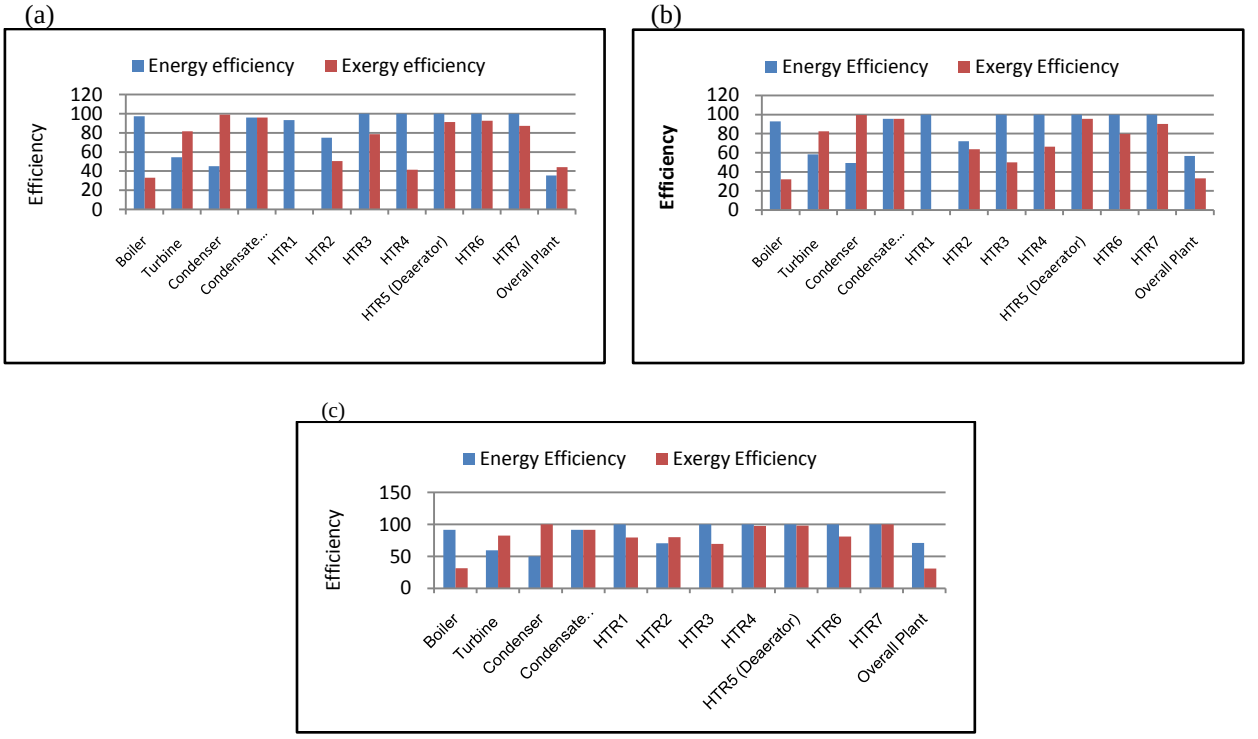

Fig. 4. Comparison of efficiency in the plant and components at (a) 50%; (b) 80%; (c) 100% load.

The comparisons of energy and exergy losses between the different subsystems of the plant are shown in Fig 5. It is noted that the maximum exergy loss occurs in the boiler subsystem (68.27% at 100% load). This might be due to the irreversibility of the combustion process in the combustor. The exergy destruction of the condenser is only 0.21%. The real loss is primarily back in the boiler where entropy was produced. Contrary to the first law analysis, this demonstrates that significant improvements exist in the boiler system rather than in the condenser. The calculated exergy efficiency of the cycle is 30.78% at 100% load. This indicates that remarkable opportunities are available for improvement. Energy efficiency of the turbine cycle is low (47.25% at 100% load) due to a large quantity of energy rejection in the condenser. But the derived exergy efficiency of the turbine is high (83.14 % at 100% load), this is due to the reason that a little exergy associated with turbine exhaust steam enters condenser, part of which is rejected to CW and partly consumed due to irreversibility.

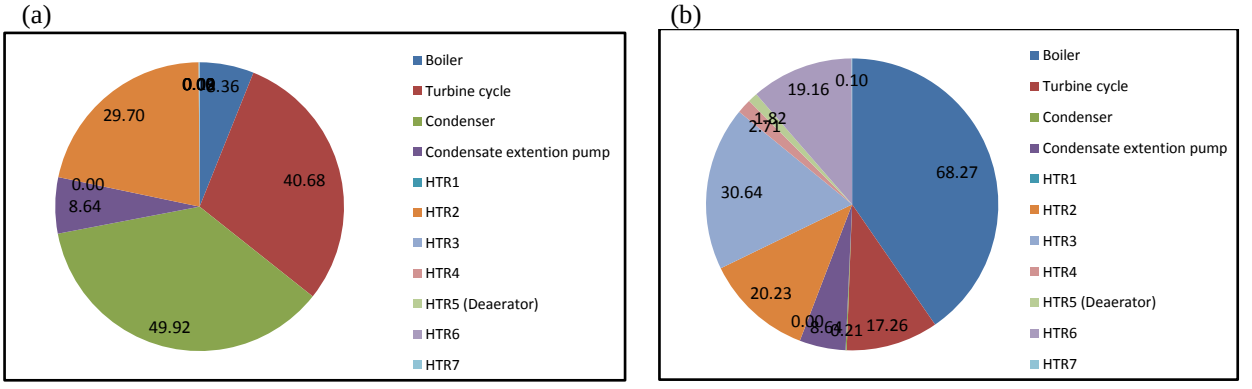

Fig. 5. (a) Energy (b) Exergy loss of different components of the plant at 100% loading condition.

Exergy analysis can also be effectively used to take important decisions pertaining to operation and maintenance. Any operation decisions based on the energy analysis will be incorrect for the overall plant performance. This corroborates to the overall plant performance degradation. First law analysis alone also often does not reflect properly the performance deterioration level of a single component. Exergy analysis can benefit by pinpointing the sources of irreversibility in different components of a power cycle.

4. Conclusions

Energy and exergy analyses are presented in this study to understand the performance of coal fired thermal power plants and identify design possible efficiency improvements. From the data presented and the subsequent analysis, following conclusions can be drawn:

- Exergy efficiency is lower than energy efficiency of the plant. Boiler is the main part that contributed to lower the exergy efficiency.
- It has been observed that 68.27% exergy loss occur in combustor (boiler) which represents combustor is not fully adiabatic and combustion might be incomplete. The large exergy loss is mainly due to the combustion reaction and to the large temperature difference during heat transfer between the combustion gas and steam. Other factors that might contribute to the high amount of exergy loss are tubes fouling, defective burners, fuel quality, inefficient soot blowers, valves steam traps and air heaters fouling.
- The major energy destruction occurs in the condenser which leads to inefficient heat transfer between hot stream (flue gas) and cold stream (water and air).
- Thus, energy analysis results lead to erroneous conclusion that major loss is associated with the heat rejection at the condenser, while exergy analysis quantitatively demonstrates that only a very small amount of work potential is lost in the condenser. Operation and maintenance decisions based on exergy analysis of the power plants proved more effective. Power station equipment involves high density of exergy transfer and therefore, it is important that exergy destruction is minimized in such devices. Exergy-based approach of performance monitoring in operating power plants helps in better management of energy resources and environment.

Acknowledgements

The authors would like to acknowledge the authority of Barapukuria 250 MW coal based thermal power plant and Bangladesh power development board (BPDB) for helping during the collection of data from the plant and conduct research.

References

[1] H.E. Hasan, V.A. Ali, Burhanettin, D. Ahmet, H.S. Suleyman, S. Bahri, T. Ismail, G. Cengiz, A. Selcuk, Comparative energetic and exergetic performance analyses for coal-fired thermal power plants in Turkey, International journal of thermal sciences 48 (2009), pp. 2179–86.

[2] T.J. Kotas, The exergy method of thermal plant analysis, Butterworth's: London, 1985.

[3] K.N. Sachdeva, Karun, Performance optimization of steam power plant through energy and exergy analysis, International journal of current engineering and technology, Vol.2, No.3, Sept, 2012.

[4] Bangladesh power development board, key statistics, June 2014.

[5] http://www.eoearth.org/article/Energy_profile_of_Bangladesh, 2007.

[6] A. Datta, S. Sengupta, S. Duttagupta, Exergy analysis of a coal based 210 MW thermal power plant, International journal of energy research, Vol. 31, No. 1, pp. 14-28, 2007.

[7] M.A. Rosen, I. Dincer, Thermoeconomic analysis of power plants: an application to the coal fired electrical generating station, Energy conversion and management 44 (2003), pp. 2473-2761.

[8] T. Ganapathy, N. Alagumurthi, R.P. Gakkhar, K. Murugesan, Exergy analysis of operating lignite fired thermal power plant, Journal of engineering science and technology review, Vol. 2, No. 1 (2009), pp. 123-130.

[9] M.V. Suresh, K.S. Reddy, A.K. Kolar, Energy and exergy based thermodynamic analysis of a 62.5 MW coal based thermal power plant, International conference on energy and environment, August 28-30, Malaysia, 2006.

[10] S. Rudra, H.M. Shim, H.T. Kim, Exergetic analysis of coal fired thermal power plants based advance steam parameters, 4th BSME-ASME International conference on thermal Engineering, 27-29 December, 2008.

[11] J. Beér, High efficiency electric power generation; the environmental role, Massachusetts Institute of Technology (MIT), October 17, 2006, http://mitei.mit.edu/system/files/beer-combustion.pdf

6th BSME International Conference on Thermal Engineering (ICTE 2014)

Control of Production and Process Using Optimal Control Technique

M. H. A. Biswas*, Mithun Mondal

Mathematics Discipline, Science Engineering and Technology School,
Khulna University, Khulna- 9208, Bangladesh.

Abstract

Sustainable and efficient control management is the key to the production and process in industrial engineering. The maintenance of process performance ensuring the quality products after a long time operation of the system is desirable in any industry. Appropriate model design and control strategy is the crucial concern in such management of the process. In this paper we study a mathematical model controlling the production and process arising in industrial engineering. We analyze the model using the optimal control technique in the form of maximum principle to control the quality products in the operation processes. We show that introduction of state constraint can be of advantageous for obtaining good products during the longer operation process. We investigate the model numerically using some known nonlinear optimal control solvers and the simulation results are well illustrated. We compare the model to illustrate the significant effect of introducing state constraint to the dynamics of the model.

Peer-review under responsibility of organizing committee of the 6th BSME International Conference on Thermal Engineering (ICTE 2014).

Keywords: Optimal control; state constraint; production and process; industrial engineering; numerical application.

1. Introduction

Optimal control theory has a long history in the literature for diverse applications in engineering science. There may have some controversy about the birth of the optimal control theory [26], but not about its necessity in practice and it is now widely accepted that optimal control theory has dominant role in applications of many real life problems arising in science, engineering, biology and biomedicine. According to the argument of Sussmann and Willems [26], the fundamental research in optimal control theory came to light more than three centuries ago with the publication of Johann Bernoulli's solution of the Brachystochrone problem in 1697. However the main theoretical developments in this field occurred in the 1950s about more than 60 years ago. The development of optimal control has gained strength by treating multivariable, time varying systems, as well as many nonlinear problems arising in control engineering, biology and medicine. Several authors contributed to the basic foundation of a very large scale research effort initiated in the end of the 1950's, which continues to the present day. The

* Corresponding author. Tel.: +88 01711 948396
*E- mail address:*mhabiswas@yahoo.com

Pontryagin Maximum Principle is a milestone in optimal control theory [23]. It extends the classical Euler and Weierstrass conditions from the classical calculus of variations to control settings [27]. The development of Nonsmooth Analysis [15] has enhanced a wide scope of research and it has opened a new horizon in the optimal control theory. However, Due to the beyond of the scope of this paper we omit the detailed descriptions of the theoretical development of nonsmooth maximum principle for optimal control problems referring the readers to [3, 7, 11-13] and references therein) for some recent developments in this area.

It is now well recognized that in parallel to the theoretical developments, the numerical solutions as well as applications of optimal control problems have been one of the most challenging as well as demanding areas of research since the few decades due to the diverse applications specially in biology and medicine. Particularly to bridge the gap between the theory and application is the crucial issue of the present day research on optimal control theory. The necessary conditions of optimality (NCO) for optimal control problems are powerful tool in the determination of the optimal solution. Indeed, they are widely used to develop solvers. Moreover, they can provide qualitative information on the solution and are the basis for the study of regularity of the optimal solution (see, for example, [13, 27]). Necessary condition of optimality for optimal control problems with state constraints have been studied since the very beginning of optimal control theory and it appeared in a very natural way when modelling many real life engineering applications in engineering, life science, biology and medicine. This paper focuses on some applications of optimal control arising in real life problems. Because of multidimensional applications of optimal control theory in diverse areas, it has become one of the most challenging area of researches in the last few decades. Since the first application of optimal control in biomedical engineering around 1980s [21] several control and vaccination strategies for the treatment of infectious diseases in a certain population over a period of time has been successfully modelled as optimal control problems. Some of those applications in biomedicine include modelling of infectious diseases and obtain optimal control strategies for treatments of HIV/AIDS (see for examples, [1, 2, 5, 6, 17, 19]; for modelling and control of deadly nipah virus infections in [4]; for control of SEIR epidemic disease in [8] as well as modelling and control of cancer treatments in [14, 24]). Some of other important applications of optimal control theory attracting attention to the readers are soft landing and fuel consuming of space vehicles in aerospace engineering [9] and efficient and sustainable managements of forest and ecosystems in life science [10].

Our aim in this study is concerned with one such application of optimal control in production and process of industrial engineering. We study a mathematical model of process in the form of optimal control problem in turns of ordinary differential equations (ODE) and represent here only the numerical investigations of the problem (omitting the theoretical details) arising in production and process managements in industrial engineering. We also discuss the necessity of introducing state constraints in the model and show how it influences in management for obtaining "good" (quality) products over a certain time of operations.

2. Mathematical model

It is well-known that the rate of production of "good" (or quality/non-defective) products in a process management becomes slow down after a long time operation of the systems due to the absence of maintenance. However, in some cases, an appropriate introduction of state constraints can be of help in preventing the declination of "good" items produced over time. Mathematical model can be used to describe this production process in terms of ODEs. This problem is an application of optimal control in management and industrial engineering where the state constraints play an influential role in maintaining the performance of the production process. The dynamic model describing the process is taken as in [20] in turns of the following differential equations:

$$\frac{dx_1}{dt} = x_2(t)u_1(t) - d(t),$$
$$\frac{dx_2}{dt} = -(\alpha + u_2(t))x_2(t) + u_2(t),$$
$$x_1(t) \geq 0, \quad a.e.\ t \in [0, T],$$

with the initial conditions

$$x_1(0) = x_{10} > 0, \quad x_2(0) = x_{20} > 0,$$

and the control constraints

$$0 \le u_1(t) \le U_1, \quad 0 \le u_2(t) \le U_2, \quad a.e.\ t \in [0,T].$$

In the above dynamical model one can see that the process consists of two state variables and two control variables. Here in the systems, we suppose that the state variable $x_1(t)$ represents inventory level at time $t \in [0,T]$ for a fixed final time $T > 0$ and $x_2(t)$ represents the proportion of 'good' units of end items produced at time t (also known as process performance). The two control variables $u_1(t)$ and $u_1(t)$ represent scheduled production rate and preventive maintenance rate to reduce the proportion of defective units produced respectively. $\alpha(t)$ denotes the obsolescence rate of the process performance in the absence of maintenance and $d(t)$ is the demand rate. With the above system of differential equations, a production process in industrial engineering is efficiently described. It is worth mentioning that the negative sign in second dynamic equation shows how the productions of 'good' (or non-defective) units of items decrease over time in absence of maintenance. However, appropriate preventive measure can be applied to the process to slow down the rate of declination of process performance. In this preventive measure, an introduction of lower bound on the number of 'good' items produced over time can be imposed as *state constraints* to improve the process performance which may be of help keeping the 'good' items produced in a minimum level. Thus we introduce the following state constraint (i.e. a lower bound) on the number of 'good' items:

$$x_2(t) \ge l_{\min}, \quad a.e.\ t \in [0,T] \ , \tag{1}$$

where $l_{\min}$ is the lower bound of the "good" items produced at time t and taking values in $\mathbb{R}$.

We observe that the constraint $x_1(t) \ge 0, \quad a.e.\ t \in [0,T]$ is imposed because of the fact that all demands must be satisfied and the state constraint in (1) is crucial in our analysis because it is a lower bound on the number of 'good' items produced at time t.

Our objectives in this optimal control problem is to maximize the total discounted cost as well as the salvage cost with the following objective functional:

$$J(x_1, x_2, u_1, u_2) = \int_0^T \left(wd - hx_1(t) - \phi(u_1(t)) - cu_2(t) \right) e^{-\rho t} dt + bx_2(T) e^{-\rho T}, \tag{2}$$

where the function $\phi(u_1(t))$ is called the production cost function and is defined either as the *quadratic function*

$$\phi(u_1(t)) = ru_1^{\,2}, \quad r > 0, \tag{3}$$

or the *linear function*

$$\phi(u_1(t)) = qu_1, \quad q > 0, \tag{4}$$

and all other parameters and constants (also sometimes regarded as weight parameters balancing the cost) along with their values used in the objective function are presented in Table 1. We note that in our analysis we will consider and investigate the *quadratic function* only. Observe also that in the objective function, the other control function $u_2(t)$, representing the maintenance cost appears as *linear function*. Thus we are considering the quadratic production cost function and linear maintenance cost functions. Maurer *et al.* studied such problem in [20] without introducing any state constraint in the model. They investigated state constrained model when both the production cost function and maintenance cost function are linear. In this study, we investigate the state constrained model when the production cost function is quadratic and maintenance cost function is linear. We treat this problem based on numerical analysis omitting the theoretical details. Before presenting the results of numerical simulations, we sketch the idea of optimality conditions for the optimal solutions of our problem referring readers to [20, 22, 27) for detailed study.

3. Characterization of optimal control

The above mentioned dynamical model along with the state constraint can be rewritten in the following optimal control problem:

$$(P)\begin{cases} \underset{(u_1,u_2)\in U}{\text{Maximize}}\ \ l(x(T))+\int_0^T L(t,x(t),u(t)) \\ \text{subject to} \\ \dot{x}(t)=f(t,x(t),u(t)), \\ h(t,x(t)\le 0,\ \ \forall\ t\in[0,T], \\ (u_1(t),u_2(t))\in U\ \ a.e.\ t\in[0,T], \\ x_1(t)\ge 0,\quad a.e.\ t\in[0,T], \\ x(0)=x_0, \end{cases}$$

where $x(t)=(x_1(t),x_2(t))$,

$f(x)=(x_2(t)u_1(t)-d(t),-(\alpha+u_2(t))x_2(t)+u_2(t))$,

$h(t,x(t))=-x_2(t)+l_{\min}$,

$l(x(T))=bx_2(T)e^{-\rho T}$, $L(t,x(t),u(t))=(wd-hx_1(t)-2u_1{}^2(t)-cu_2(t))e^{-\rho t}$

and the control functions representing the percentage are measurable functions defined in the set

$$U=\{(u_1,u_2):0\le u_1(t)\le U_1,\ \ 0\le u_2(t)\le U_2,\ \ a.e.\ t\in[0,T]\}.$$

Here problem (P) is a well-known optimal control problem with state constraint which coincides with *standard* optimal control problem in absence of state constraint. However, the optimal solutions of such problem can be characterized by the Pontryagin Maximum Principle (PMP), the pioneer works of Pontryagin *et al.* [23], which satisfies the necessary conditions of optimality for optimal control problems having the novelty of being sufficient conditions for the normal linear convex problems. The optimality systems are characterized by the two dynamic equations associated with two adjoins equations in turns of multipliers. For the optimality systems, we define the pseudo Hamiltonian in normal form (i.e. for $\lambda=1$):

$$H(x_1,x_2,u_1,u_2,p,1)=\langle p,f(t,x,u)\rangle-L(t,x,u) \tag{5}$$

Suppose that (x^*,u^*) is the optimal solution of the problem (P) . Then the maximum principle in [27] asserts the existence of an absolutely continuous function p and a scalar λ such that

$(i)\ \|p\|_\infty+1=0,$

$(ii)\ (-\dot{p}(t),0)=p(t).f_{x,u}(t,x^*(t),u^*(t))-L_{x,u}(t,x^*(t),u^*(t)),$

$(iii)\ \forall(u_1,u_2)\in U,$

$p(t).f_u(t,x^*(t),u(t))-L_u(t,x^*(t),u(t))\le p(t).f_u(t,x^*(t),u^*(t))-L_u(t,x^*(t),u^*(t))\ a.e.,$

together with the transversality conditions $p(T)=(\nu,b)$ where $\nu\in\mathbb{R}$.

Now consider that $p(t)=(p_{x1},p_{x2})$. We deduce from (iii) an explicit characterization of the optimal control for the production cost given in terms of the multipliers p:

$$u_1^* = \frac{p_{x1}(t)x_2(t)}{2r}.$$

Observe a special feature of (P) that the dynamics is linear both in the state and control variables separately and the cost is convex with respect to the production cost (control) function. For such problem we can a priori get an explicit optimal control. However, although we refrain from writing here the necessary conditions in the form of a maximum principle, it is well known that the presence of explicit state constraints introduces an additional multiplier which, a priori, is a non-negative Radon measure (see, for example, [27]). This fact itself complicates any analytical analysis and prevents the determination of a closed form for the optimal control. Given the special features of (P) we could hope to get some additional information taking into account some literature like [18, 25] on the regularity of the optimal control. We also refer readers to [22] for the study of both necessary and sufficient conditions of optimality for such state constrained problems. We are now in position to illustrate our numerical results and discussions in the next section.

4. Numerical results and discussions

We solve the optimality systems by numerical simulations to obtain the optimal performance of the process for our model in different scenarios; for example, without state constraint and with state constraint. To do these simulations we used the Imperial College London Optimal control Software – ICLOCS—version 0.1b [16]. ICLOCS is an optimal control interface, implemented in Matlab, for solving the optimal control problems with general path and boundary constraints and free or fixed final time. ICLOCS uses the IPOPT—Interior Point OPTimizer—solver which is an open-source software package for large-scale nonlinear optimization [28]. Considering a fixed time $T=1$, a time-grid with 1000 nodes was created, i.e., for $t \in [0,1]$ we get $\nabla t = 0.001$. According to [20], the values for all parameters and constants we use in this model are presented in Table 1.

Table 1: Definitions and values of parameters and constants:

Parameters and constants	Definitions	Values
d	Demand rate	4
α	Obsolescence rate of process performance in absence of maintenance	2
x_{10}	Initial value of inventory level	3
x_{20}	Initial value of process performance	1
U_1	Upper limit of scheduled production rate	3
U_2	Upper limit of preventive maintenance rate	4
ρ	Discount rate (positive constant)	0.1
w	Positive constant	8
h	Positive constant	1
c	Positive constant	2.5
b	Positive constant	10
r	Positive constant	2
q	Positive constant	4
$l_{\min}$	Lower bound on number of ‘good’ items	0.5

(Source: [20])

Since we used a direct method and consequently, an iterative approach, we imposed an acceptable convergence tolerance at each step of $\varepsilon_{rel} = 10^{-9}$ (see [16] for more details).

We first solve the optimality systems for our problem (P) when the state constraint is not imposed . We run the program in Matlab code using the aforementioned solver 'ICLOCS' and found the optimal solution. The simulation results for the optimal states and controls are presented in Fig. 1. Fig. 1(a) shows how the state trajectories for stocks and productions of 'good' items become slow down in absence of maintenance during the operations of the process over time. Fig. 1(b) represents the behaviours of the control functions where the production cost control is singular while the maintenance cost control is bang-bang with some strange behaviours from 0.5 to 0.7 in the time interval.

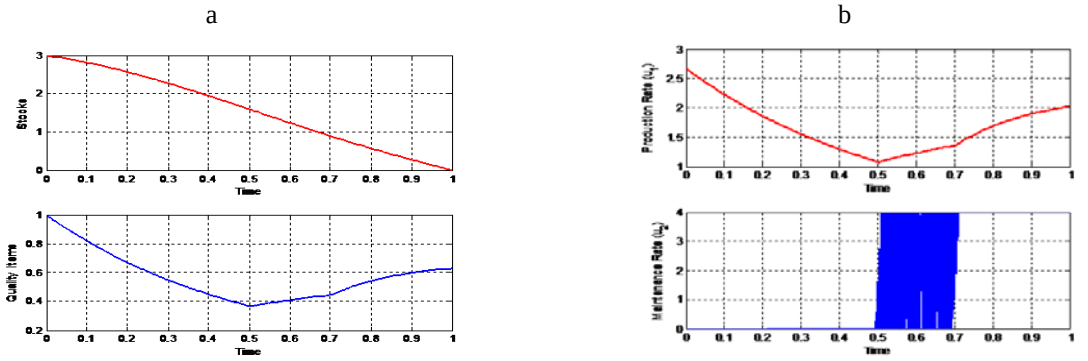

Fig. 1. (a) Optimal processes of stocks and quality products (i.e. 'good' items) without state constraint; (b) Optimal control representing the production rate and maintenance rate without state constraint.

Now we run the program for the optimality systems of problem (P) in presence of state constraint. Here we again found the optimal solution satisfying the necessary conditions of optimality. Our results show that the rate of declination of the number of 'good' items produced over time can be halted from being slow down at a certain minimum level. The simulation results of the optimal trajectories for state and control have been illustrated in Fig. 2. From Fig. 2(a), we see that the number of quality products can be halted from becoming slow down at $l_{\min} = 0.5$ due to imposing state constraint and thus increases again over a fixed interval of time. The behaviors of control functions presented in Fig. 2(b) are quite better than those in Fig. 1(b).

Our simulation results show that state constrained model can provide more information as well as better performance for maintenance a production process in industry if appropriate deign of controller for better approximation can be made. As we omit here the detailed analytical investigations, so further extensive study requires for more accurate control strategy. Moreover, due to the presence of state constraint and thus the involvement measure require the validation of sufficient conditions of optimality as well as the regularity of minimizers. Our future work will focus on these directions.

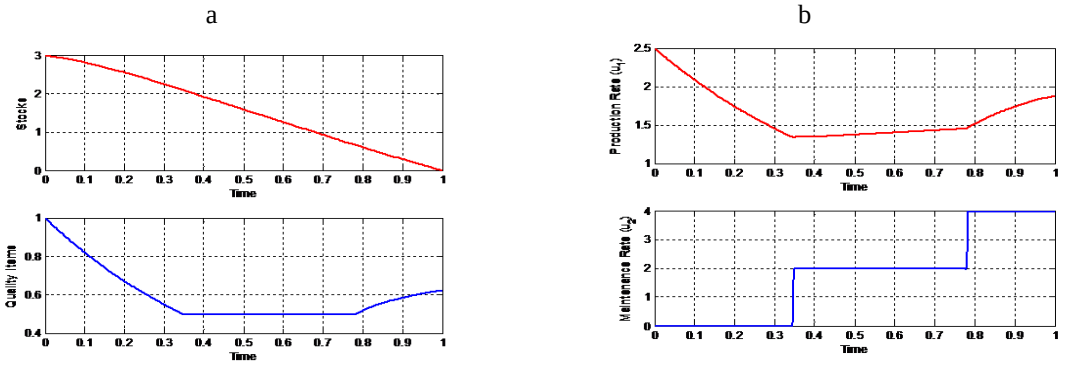

Fig. 2. (a) Optimal processes of stocks and quality products (i.e. 'good' items) with state constraint; (b) Optimal control representing the production rate and maintenance rate with state constraint.

5. Conclusions

This paper mainly focuses on the application of optimal control theory in some real life problems emphasizing on the process management in industrial engineering. A mathematical model describing the production process over time has been studied and a numerical solution for the optimality systems has been presented. A feature of this paper is that the model is discussed introducing state constraint showing that such constraint can be of advantageous for the maintenance of process performance to ensure the quality (or 'good' items) products after a long time operation of the system. As this result is only based on numerical treatment, further analytical investigation is needed, specially because of the presence of state constraint. Our future research on the validation of sufficient optimality conditions and the regularity of minimizers will be focused based on both detailed theoretical and numerical approaches.

Acknowledgements

The authors would like to thank Mathematics Discipline of Khulna University, Bangladesh for all sorts of logistic supports while preparing this manuscript.

References

[1] M. H. A. Biswas, On the Evolution of AIDS/HIV Treatment: An Optimal Control Approach. *Current HIV Research*, 12(1), (2014), 1—12.

[2] M. H. A. Biswas, On the Immunotherapy of HIV Infections via Optimal Control with Constraint. Proceedings of the 18th International Mathematics Conference 2013, March 20—22, (2014), 51—54.

[3] M. H. A. Biswas, Necessary Conditions for Optimal Control Problems with State Constraints: Theory and Applications, PhD Thesis, Department of Electrical and Computer Engineering, Faculty of Engineering, University of Porto, Portugal, 2013.

[4] M. H. A. Biswas, Model and Control Strategy of the Deadly Nipah Virus (NiV) Infections in Bangladesh. *Research & Reviews in BioSciences*, 6(12): 370-377, 2012.

[5] M. H. A. Biswas,*Optimal Chemotherapeutic Strategy for HIV Infections– State Constrained Case*. Proceedings of the 1st PhD Students' Conference in Electrical and Computer Engineering organized by the Department of Electrical and Computer Engineering, Faculty of Engineering, University of Porto, Portugal on 28-29 June, 2012.

[6] M. H. A. Biswas,AIDS Epidemic Worldwide and the Millennium Development Strategies : A Light for Lives. *HIV & AIDS Review* , 11(4): 87-94 (2012).

[7] M. H. A. Biswas,Necessary Conditions for Optimal Control Problems With and Without State Constraints: A Comparative Study. *WSEAS Transactions on Systems and Control*, Vol. 6, No. 6, p. 217–228, June 2011.

[8] M. H. A. Biswas, Paiva, L. T. and de Pinho, M. d. R. A SEIR Model for Control of Infectious Diseases with Constraints. Mathematical Biosciences and Engineering, 11(4): 761—784, 2014.

[9] M. H. A. Biswas, Huda, M. A., Ara, M. and Rahman, M. A., Optimal Control Theory and Its Applications in Aerospace Engineering. *International Journal of Academic Research*, Vol. 3, No. 2, Part II, pp. 349-357, 2011.

[10] M. H. A. Biswas,Ara, M., Haque, M. N. and Rahman, M. A., Application of Control Theory in the Efficient and Sustainable Forest Management. *International Journal of Scientific and Engineering Research*, Vol. 2, No. 3, March, 2011.

[11] M. H. A. Biswas and de Pinho, M.d. R. A Maximum Principle for Optimal Control Problems with State and Mixed Constraints. *ESAIM: Control, Optimization and Calculus of Variations*, 2014 (accepted).

[12] M. H. A. Biswas and de Pinho, M.d. R. Variant of nonsmooth maximum principle for state constrained problems, IEEE Proc. of the 51st CDC, pp. 7685—7690, 2012.

[13] M. H. A. Biswas and de Pinho, M.d. R. A Nonsmooth Maximum Principle for Optimal Control Problems with State and Mixed Constraints-Convex Case. *Discrete and Continuous Dynamical Systems, Special issue*, pp. 174–183, September 2011.

[14] T. Burden, Ernstberger, J. and Fister, K. R. Optimal Control Applied to Immunotherapy. Discrete and Continuous Dynamical Systems—Series B, Vol. 4, No. 1, pp. 135—146, 2004.

[15] F. H. Clarke, "*Optimization and Nonsmooth Analysis"*. John Wiley & Sons New York. 1983.

[16] P. Falugi, Kerrigan, E. and Wyk, E. Van. Imperial College London Optimal Control Software User Guide (ICLOCS), Department of Electrical and Electronic Engineering, Imperial College London, London, England, UK, 2010.

[17] K. R. Fister, Lenhart, S. and McNally, J. S., Optimizing Chemotherapy in an HIV Model, *Electronic Journal of Differential Equations*, Vol. 1998, No. 32, pp. 1-12, 1998.

[18] G. N. Galbraith and R. B. Vinter (2003). Lipschitz continuity of optimal controls for state constrained problems. *SIAM J. Control Opt.*, 42, pp. 1727–1744.

[19] D. Kirschner, Lenhart, S. and Serbin, S., Optimal Control of the Chemotherapy of HIV, *J. Math. Biol*, 35, 775-792, 1997.

[20] H. Maurer, Kim, Jang-Ho R. and Vossen, G. 2005. On a State-Constrained Control Problem in Optimal Production and Maintenance, C. Deissenberg and R.F. Hartl (eds.), *Optimal Control and Dynamic Games*, Chapter 17, 289—308, Springer, The Netherlands, 2005.

[21] D. S. Naidu, Fernando, T. and Fister, K. R. 2011. Optimal control in diabetes, *Optim. Control Appl. Meth.*, 32, (2011), pp. 181-184.
[22] N. P. Osmolovskii and Maurer, H. "*Applications to Regular and Bang-Bang Control: Second-Order Necessary and Sufficient Optimality Conditions in Calculus of Variations and Optimal Control*", SIAM, 2012.
[23] L. S. Pontryagin, Boltyanskii, V. G., Gamkrelidze, R. V. and Mischenko, E. F. "*The Mathematical Theory of Optimal Processes*", John Wiley, New York, 1962.
[24] H. Schättler and Ledzewicz, U., "*Geometric Optimal Control: Theory, Methods and Examples"*, Springer, 2012.
[25] Ilya A. Shvartsman and R. B. Vinter (2006). Regularity properties of optimal controls for problems with time-varying state and control constraints. *Nonlinear Analysis, Theory, Meth. and Applic*,. 65, pp. 448–474.
[26] H. J. Sussmann and J. C. Willems, 300 Years of Optimal Control: From the Brachystochrone to the Maximum Principle. *Control Systems Magazine, IEEE***,** Vol.17, Issue 3, pp. 32-44, 1997.
[27] R. B. Vinter, *Optimal Control*. Birkhauser, Boston, 2000.
[28] A. Wachter and Lorenz T. Biegler, On the implementation of an interior-point _lter line-search algorithm for large-scale nonlinear programming, *Mathematical Programming*, 106, pp. 25—57, (2006).

6th BSME International Conference on Thermal Engineering (ICTE 2014)

Power generation with vertical axis wind turbine, in respect of Bangladesh

Sanjib Kumar Nandi1

Bachelor of Science in Electrical & Electronic Engineering, American International University- Bangladesh (AIUB), Banani, Dhaka 1213, Bangladesh

Abstract

Power crisis is one of the major problems in Bangladesh which is increasing day by day. In such situation renewable sources could be the best possible solution. But the power of the renewable sources varies with day time and climate. Electrical energy plays a vital role in development of civilization. The advancement of a country is measured in terms of per capital consumption of electrical energy. It is quite impossible to solve over all power crisis but possible to control load demand by using compact fluorescent lamp, transferring holiday, transfer from peak to off-peak hour only through proper planning by load management, encouraging Independent Power Producers, reducing transmission loss, more utilization of renewable energy sources. So, vertical axis wind turbine can play a vital role against this power crisis. This system is very much cost effective in the long run and also very much environmental friendly.

(ICTE 2014)

Keywords: Energy Crisis; Power; Renewable Energy; Wind Power; Vertical axes wind turbine; Wind Speed.

1. Introduction

Bangladesh is one of the world's poorest and most densely populated nations. Today only an estimated 49% of the Bangladesh population is connected to the electricity grid. The electricity supply is not reliable though and peak demand cannot be met. In the rural areas, where more than 70% of the population lives, only about 25% have electricity. Here is a huge scarcity of electric power. So steps must be taken to reduce this problem. One of the solutions is to increase the use of renewable energy. And that's why vertical axis wind turbine is one of the better options. Power plays a great role wherever people lives and works in industry, agriculture, and transportation etc. The living standard and prosperity of a nation vary directly with increase in use of power. As technology is advancing the consumption of power is steadily rising. Sufficient and reliable source of electricity is a major

* Sanjib Kumar Nandi. Tel.: +8801727449956;
E-mail address: sanjib.eee.aiub@gmail.com

prerequisite for a sustained and successful economic development effort and poverty reduction. In Bangladesh, 70 million of the populations out of 160 million do not have direct access to electricity and remaining 90 million people have access but reliable and quality power is still beyond their reach (BPDB, 2013). In order to achieve the growth rate, availability of a reasonably priced and reliable source of electricity is a prerequisite. Present generation of electric power in Bangladesh is not sufficient to meet the consumers growing demand. So it is not possible to ensure a constant supply of electric power to all consumers throughout the country. Moreover the demand is increasing day by day. It is essential to set up Renewable plants for over demanding load. So, Vertical axis wind turbine plant can be chose to meet up this demand.

2. Wind Power

Wind is a form of solar energy. Wind power is a power that is producing from the Wind turbine. Wind turbines convert the kinetic energy in the wind into mechanical power. The Turbine rotates by the Energy of the wind and extracts power from the Wind. Wind is a form of solar energy. The terms “Wind energy” or “Wind power” describe the process by which the wind is used to generate mechanical power or electricity.

3. Vertical-axis Wind Turbine

Vertical-axis wind turbines (VAWTs) are a type of wind turbine where the main rotor shaft is set vertically and the main components are located at the base of the turbine. Among the advantages of this arrangement are that generators and gearbox can be placed close to the ground which makes these components easier to service and repair and that VAWTs do not need to be pointed into the wind . Major drawbacks for the early designs (savonius, darrieus and giromill) included the pulsatory torque that can be produced during each revolution and the huge bending moments on the blades.

Figure 1: A simple vertical axes wind turbine

4. Design Process of Vertical Axis Wind Turbine

4.1. Basic Working Principle:

A wind turbine is quite simple in design. There are the propellers just mentioned, a shaft and a generator. The propellers catch the wind and help rotate the shaft. The turning of the shaft helps to power the generator and create electricity. A generator will normally consist of magnets and a conductor such as coiled copper wire. The arrays of magnets are connected to the shaft and surround the coil of wire. When the magnets rotate around the copper wire it produces a different in electrical potential creating voltage and an electric current. This process is called induction and it is how generators of all types produce electricity[6]. In order to analyse the aerodynamics of a rotor and to get information about its power generation, it’s necessary to start by considering that a wind turbine works converting the kinetic energy of a wind flow in electricity, following several steps:

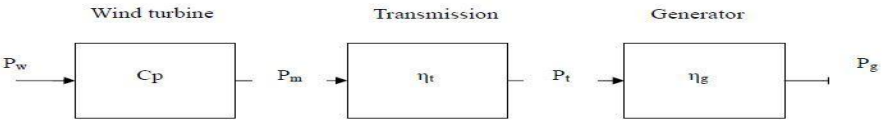

Figure 2: Block diagram of the working principle of a wind turbine

The power of the wind is described by:

$P_{kin} = (1/2)*m*v^2$

Where:

P_{kin} = kinetic power [W];

m= mass flow = ρ*A*v [kg/s];

ρ = density [kg/m^3];

A = area [m^2];

v = speed [m/s];

The formula of the power in the wind can be written also as: $P_{kin} = (1/2)* \rho * A * v^3$

The density of the air varies with the height above sea level and temperature. The standard value for Sweden used usually is density at sea level (1 bar) and a temperature of 900C. Using these values, the density of the air is 1.25 kg/m3. The maximum mechanical power that can be got from a wind turbine depends on both the rotational speed and on the undisturbed wind speed, as shown in the picture below.

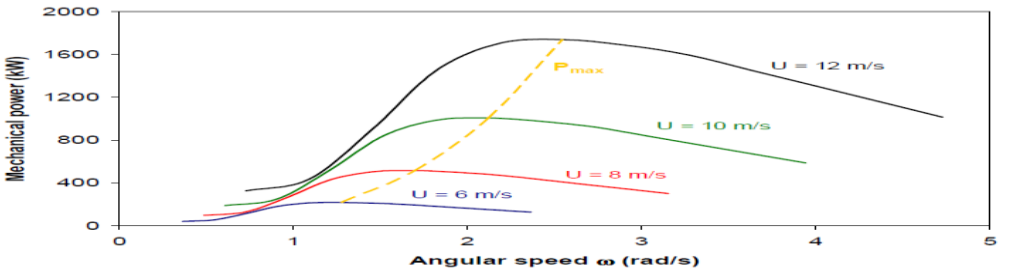

Figure 3: Mechanical power and rotational speed for different wind speed

4.2. Drag and Lift Force of the Rotor:

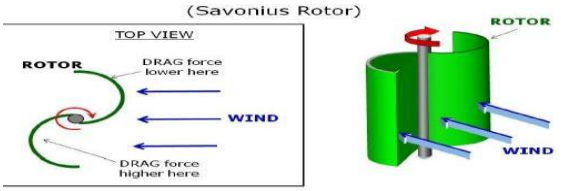

Figure 4: Drag Based wind turbine concept

Figure 5: Lift Based wind turbine concept

Airflow over any surface creates two types of aerodynamic forces— drag forces, in the direction of the airflow, and lift forces, perpendicular to the airflow. Either or both of these can be used to generate the forces needed to rotate the blades of a wind turbine.

5. simulation and result

Wind data from last three years was collected with the help of anemometer. The data collected, was compiled using HOMER. The wind pattern was studied very carefully. It was observed that the wind velocity is quite low. The challenge lies within the proper design of windmill that can be used at this low wind velocity. With the help of HOMER, the wind data was compiled for different types of wind turbines and found that A Savonius rotor (S-rotor), a vertical axis turbine, is the most suitable for the wind pattern . A Savonius Turbine is simple in construction, pollution free, having low operating speed and extremely cost effective. It was found that this S-rotor can be used for small power generation which can be used for domestic purpose in rural based communities. Thus solving the energy crisis to some extent.

Wind Data At Mirpur, Dhaka:

Wind is used as wind energy which is extracted with wind machines like wind turbines. To install a wind turbine we need sufficient wind velocity so that we get maximum of power density. Site selection is necessary in this case. For this we need to collect wind data. After collection of wind data, the compilation of that wind data is very important as it decides the type, design, and location of wind turbine. Wind data were collected at Mirpur, Dhaka(Latitude: 23° 47’10.59" N, Longitude: 90° 22’37.06"E) of Bangladesh. Wind data were collected with the help of anemometer. The data collected were compiled using the HOMER. Data recorded for the last three years and the sample data were depicted. After the analysis various graphs in HOMER for that particular data, we observed that wind velocity is quite low. The maximum wind velocity is obtained in summer.

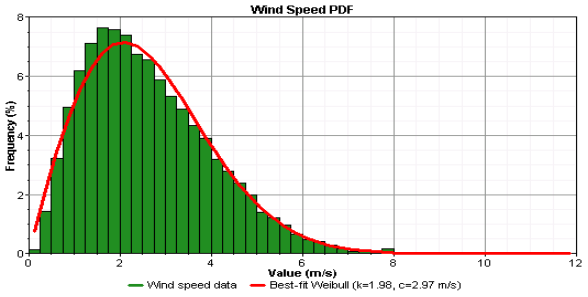

Figure 6: Sample Wind data from Mirpur, Dhaka

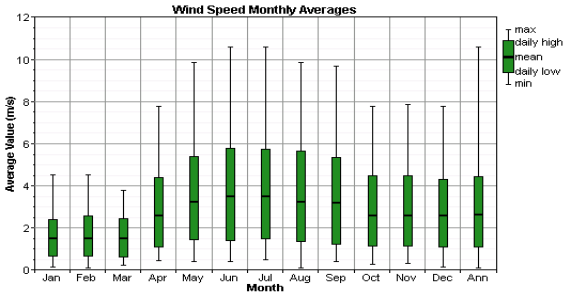

Figure 7: Wind Speed Monthly Average

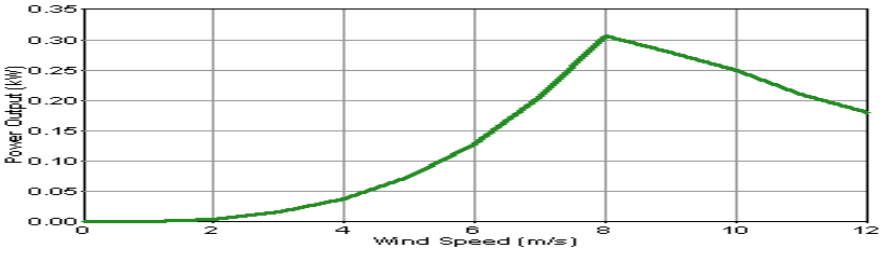

Figure 8: Power curve w.r.t wind speed

Considering these advantages of Savonius turbine, we conducted varies experiments on Savonius prototype in wind tunnel. The simple Savonius was a four-bladed system having 18 inch bucket diameter & 15 inch in height

with provision for overlap variation. The material used was aluminium. The experiments were carried out in a low speed open circuit wind tunnel which provides an air velocity adjustable between 0 and 30 m/sec.

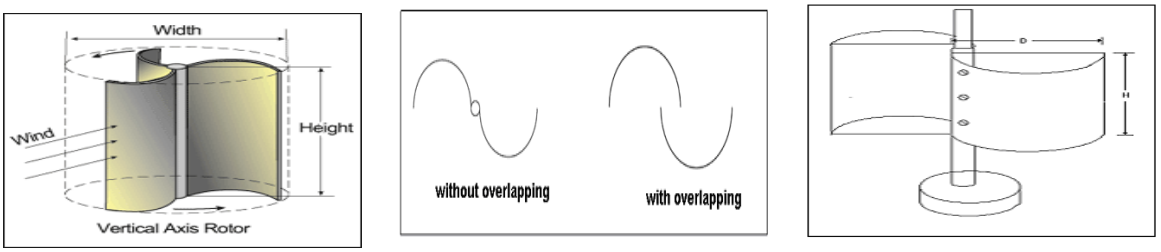

(a) (b) (c)

Figure 9: Savonius rotor model, with and without overlap

Tests were conducted for S-rotor with and without overlap. The overlap variation was 16.2 % & 20% for both the cases. The rotor speed was measured using a digital tachometer having a least count of 1 rpm and the wind velocity was determined via the Pitot static tube. The purpose of the study was to find out different observations for S-rotor with and without overlapping. The data collected during the experiments, were compiled with the help of HOMER and also by legacy system. The performance of the machine can be expressed in the form of Power Coefficient (C_p) versus tip-speed ratio (λ). For analysis, the following relations were used:-

i) Co-efficient of Performance, $C_p = \dfrac{Protor}{.5\rho V^2}$

ii) Tip speed ratio (λ) = $\dfrac{Velocity\ of\ blade\ tip}{Free\ stream\ velocity}$

From the experimental data and graphs [Fig.10], we concluded that S-rotor with 20% overlap will give the maximum co-efficient of performance (i.e. C_p= 21 % at 0.24 TSR). So while constructing the real Savonius rotor, 20 % overlap will give the best results. In this Output and Simulation part, At first wind data were collected where the experiment was done.

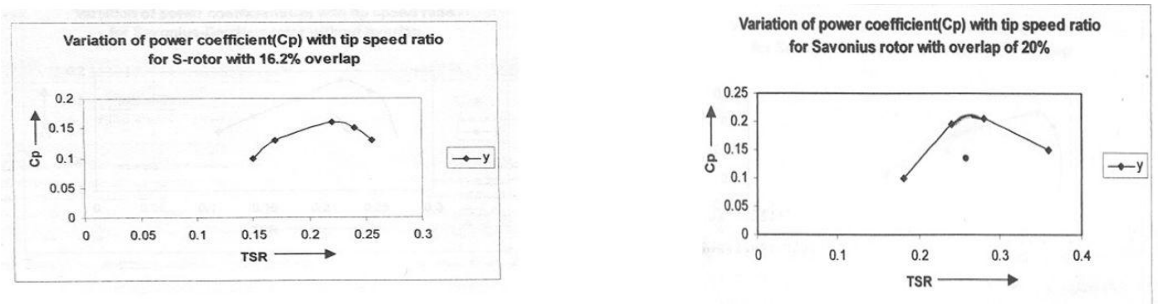

(a) (b)

Figure 10: Graphs showing experimental results for different overlapping

The data were collected from Bangladesh meteorology department. Then the data is modified in Homer simulation software. By using this data the power of coefficient was calculated. From the theoretical part 21% of power coefficient was calculated. And from the practical part the coefficient of power was get 28%.If 20% overlapping is given in the blade the efficiency will increase more. Otherwise, the cost of this project is 6000Tk.If the bearing and dynamo were high rated the efficiency will increase more.

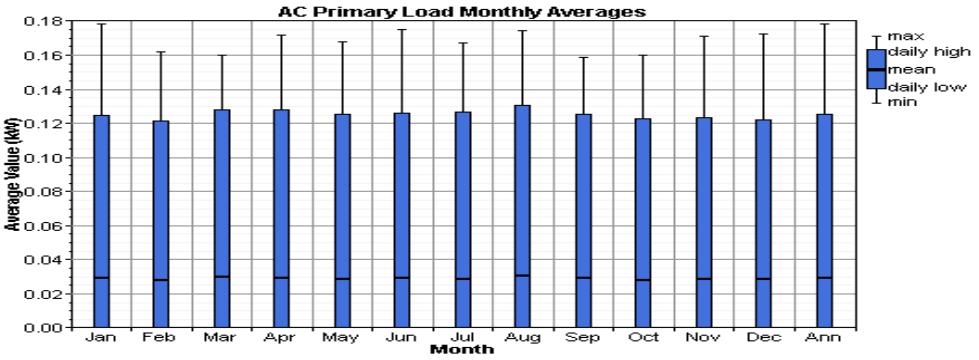

Figure 11: Sample Graphs form HOMER for a SAVONIUS Wind Turbine, 1 Battery and 1 inverter

The Experimental result shows that,

Average wind speed at Mirpur,Dhaka is 2.63 m/s

Savonius Turbine gives best results with 20% overlapping

Co-efficient of performance of S-rotor is 21% at 20% overlapping.

Cost of construction of SAVONIUS Wind Turbine is around Tk:6000

6. Conclusion & Future Work

Owing to acute energy crisis that most developing countries including Bangladesh are facing today, the interest in alternative energy sources has increased in the recent past. Wind being a non-polluting and nontoxic energy source, will go a long way in solving energy requirements. The initial research and analysis portion of the thesis provided its share of complications; however, once completed it provided valuable information about the final design. To date, the major components of the turbine have been settled on; in particular, full-scale aluminium blades have been chosen. There are still some final design options that must be finalized. However, in Bangladesh few designs were developed but could not sustain. An important reason could be that wind velocity in Bangladesh, apart from the coastal region, is relatively low and varies appreciably with seasons. This low velocity and seasonal winds imply a high cost of exploitation of wind energy. The calculation of the Cost of construction of SAVONIUS Wind Turbine is around Tk: 6000. Due to unavailability of necessary equipment total cost increased, as well as per unit energy generation cost increased. During gear design, gear ratio 120/16 was chosen. But if 120/10 that will be more efficient design. The blade design is not totally perfect, though it was by hand. The curvature in the blade may be improved by designing the blade by using machine. So if this problem can be solved then an efficient VAWT can be built which was the main goal. By building efficient VAWT power problem can be solved.

References

[1] U.S. Department of Energy. “Wind and Hydropower Technologies Program”. Retrieved from http://eereweb.ee.doe.gov/windandhydro/wind_how.html in November, 2005.

[2] Kirke, Brian Kinloch, 1998. “Evaluation of Self-Starting Vertical Axis Wind Turbines for Stand-Alone Applications”. Griffith University, Australia. Retrieved from http://www4.gu.edu.au:8080/adt-root/public/adt-QGU20050916.120408/ on November 1, 2005.

[3] Information retrieved from http://www.bpdb.gov.bd/bpdb

[4] Weekly Blitz, 2012, “Power crisis in Bangladesh”. Retrieved from http://www.weeklyblitz.net/2214/power-crisis-turns-unbearable-in-bangladesh

[5] Luethi enterprise limited, January 2011, “ Silent wind turbine” http://www.silentwindturbine.com/design.htm

[6] Jonny Hylander, Göran Sidén, May 2010, “Vertical Axis Wind Turbines: History, Technology and Applications” retrieved from http://hh.diva-portal.org/smash/get/diva2:326493/FULLTEXT01

6th BSME International Conference on Thermal Engineering (ICTE 2014)

Theoretical study of homogeneous boiling of ethanol at liquid superheat limit: the case of high heat flux pulse heating

Mohammad Nasim Hasan*[a], S. M. Shavik[a], Y. Mitsutake[b], M. Monde[b]

[a]*Department of Mechanical Engineering, Bangladesh University of Engineering & Technology, Dhaka-1000, Bangladesh*
[b]*Department of Mechanical Engineering, Saga University, Saga, 840-8502, Japan*

Abstract

Recent developments in bubble actuated micro electro-mechanical systems have put a significant importance on the superheat induced micro boiling explosion of a metastable liquid. In the present study, we studied the homogeneous boiling phenomena of ethanol under high heat flux boundary condition by applying a newly developed theoretical model. In this model, a finite liquid control volume or cluster at the liquid boundary has been considered where energy is stored due to external heating while some energy is consumed due to bubble nucleation and subsequent growth. The state of boiling explosion of the liquid under heating has been defined as the moment when massive scale vaporization causes the liquid sensible energy to decrease with time. As the size of liquid cluster, the size of a critical vapor embryo ($2r_c$) has been considered. The obtained results have been presented and discussed in terms of the average liquid temperature rise inside the liquid cluster, maximum attainable cluster temperature and time to reach the boiling explosion condition for a wide range of boundary heat flux (0.1-10^3 MW/m^2) and liquid initial temperature (25-78.3 °C). The present study shows that, the occurrence of the boiling explosion in ethanol i.e. the time and temperature of the liquid cluster greatly depend on the boundary heat flux for a given liquid initial temperature. The predicted superheat limits of ethanol prior to boiling explosion at different boundary heat fluxes are found in reasonable agreement with the superheat limit reported in the literature. Moreover, the boiling explosion condition predicted by the present model has been found to satisfy the theoretical upper bound of maximum evaporative heat flux in terms of the heat flux across the liquid-vapor interface.

Keywords: Homogeneous Boiling; Boiling Explosion

Nomenclature

J	nucleation event rate (m^{-3}s^{-1})	t	time (s)
L	latent heat of vaporization (J/kg)	t'	Time of bubble generation (s)
M	molecular weight (kg/kmol)	t^*	time of boiling explosion (s)
N^*	number of bubbles generated at the boiling explosion per unit area (m^{-2})	T	temperature (K)
P_0	system pressure (Pa)	T_0	liquid initial temperature (°C)
P_s	saturation pressure (Pa)	T_{avg}	average temperature in the liquid cluster (K)
q_w	boundary heat flux (W/m^2)	T^*_{avg}	maximum cluster temperature (K)
$q_{max,max}$	upper limit of evaporative heat flux (W/m^2)		

q_c	energy consumption rate in the cluster (W/m^2)		Greek symbols
q_d	energy deposition rate in the cluster (W/m^2)	α	thermal diffusivity (m^2/s)
$q_{l\text{-}v}$	heat flux across the liquid-vapor interface (W/m^2)	ρ	density(kg/m^3)
$q^*_{l\text{-}v}$	heat flux across liquid-vapor interface at the boiling explosion, $t = t^*$ (W/m^2)	λ	thermal conductivity (W/m.K)
r	bubble radius (m)	Γ	vapor generation rate ($kg/m^3.s$)
$r(t, t')$	bubble radius at time t generated at t'(m)		
r_c	radius of critical vapor embryo (m)	σ	Surface tension (N/m)
			Subscript
R	universal gas constant (J/kg.K)	l	Liquid
x	distance from the boundary (m)	v	Vapor
x_e	liquid cluster size (m)		

1. Introduction

The study of explosive boiling of liquids induced by intense heat and laser pulse has become an emerging topic in current heat transfer research due to its practical applications in many microscale systems. Recent development of bubble actuated micro-electromechanical systems (MEMS), bubble jet printers and their commercial success have encouraged the researchers to study and explore the mechanism of bubble formation under the condition of rapid liquid heating. The fundamental research regarding explosive boiling is also important because of its far-reaching applications like the development of technologies required for the safety operation of nuclear reactors, the storage and transformation of liquefied natural gas (LNG), acoustic cavitation and laser-assisted phase change phenomena.

The explosive boiling under an extreme liquid heating condition differs from the usual nucleate boiling from many points of views. Skripov [1] showed a particular condition (impact condition) for explosive boiling during high heat flux pulse heating and following his research, many experimental and analytical studies on explosive boiling have been performed by several research groups which were principally devoted to determine the dominating mechanism of boiling namely the boiling incipience temperature and its dependency on the parametric variation of the heating condition. Iida et al. [2] experimentally observed the boiling nucleation phenomenon occurring at high rates of boundary temperature rise and obtained a good agreement between the heater temperature at the boiling incipience and the homogeneous nucleation temperature for ethyl alcohol and concluded that boiling during rapid liquid heating is mainly due to spontaneous nucleation or homogeneous nucleation. Okuyama et al. [3] investigated the dynamics of boiling following spontaneous nucleation on a small film heater immersed in water and ethyl alcohol for boundary temperature rising rates ranging from 10^7 K/s to 10^9 K/s and noticed the dominancy of spontaneous nucleation in the incipience of boiling. Gold et al. [4] used a short and ultrathin platinum wire with the pulse heating to study the explosive boiling in water and found the boiling incipience temperature to be 303 °C which is consistent with the corresponding superheat limit predicted by homogeneous nucleation theory. Asai et al. [5] proposed a model for bubble growth and liquid flow in bubble jet printers and later, he [6] presented another model based on the classical nucleation theory for the nucleation process in the bubble jet printers. One of the most important conclusions of Asai's model study [6] is that the heat flux should be in the order of 100 MW/m^2 for the nucleation process to be reproducible. Hong et al. [7] studied the explosive boiling phenomena of water using microheater (25 μm × 80 μm) with high heat flux boundary condition, observed that there were no nucleate bubble for a heat flux below 240 MW/m^2 at the heater-liquid interface and experimentally determined that the nucleation temperatures were slightly below the superheat limit as predicted by the classical nucleation theory and showed a weak linear dependency on the heat flux. Zhao et al [8] obtained the criterion for the minimum heat flux at the heater-liquid boundary for explosive boiling which corresponds to a value of about 220 MW/m^2 for water at atmospheric pressure. The aforementioned experimental studies have been done [1-8] to understand the incipience of bubble generation, the mechanism of boiling nucleation and the effect of bubble coalesces on bulk liquid motion under non-equilibrium heating condition, but experimental determination of

the point at which explosive boiling occurs is very difficult and for sufficiently faster liquid heating cases, it is almost impossible. .Incidentally, the authors have developed a new theoretical model for homogeneous nucleation boiling and applied it for water heating cases at high rates of boundary temperature rise of 10^7 K/s to 10^9 K/s. As reported in [9], the model prediction of the time of the boiling explosion is in good agreement with the experimental observations as reported by the other researchers.

In the present study, the same model [9] has been applied to investigate the characteristics of homogeneous boiling explosion in ethanol at atmospheric pressure under high heat flux pulse heating boundary condition. A wide range of range of boundary heat flux (0.1-10^3 MW/m^2) for three different liquid initial temperatures (T_0 = 25°C, 50°C and 78.3°C) have been considered in the present study. The results have been presented in terms of the average liquid temperature rise inside a finite liquid control cluster, maximum attainable liquid temperature before boiling explosion and the time required to achieve the boiling explosion condition for different boundary heat fluxes and initial temperatures. Also, the heat flux across the liquid-vapor interface of bubble is calculated and compared with the theoretical upper bound of maximum evaporative heat flux.

2. Model for Boiling Explosion

To analyse the boiling explosion due to homogenous nucleation during liquid heating at the boundary [9], a finite size liquid control volume or cluster (x_e) adjacent to the boundary as shown in the Fig. 1, is considered where heat has been deposited by conduction (q_d), while some of the stored heat in the cluster will be consumed to generate bubbles and their growth (q_c). The energy balance equation for the stationary control can be given for instance as:

$$\frac{dT_{avg}}{dt} = \frac{d}{dt}\left(\frac{1}{x_e} \int_0^{x_e} T(x,t)dx \right) = \frac{1}{\rho_l c_{pl} x_e}\left[q_d(t) - q_c(t) \right] \tag{1}$$

In this model, a particular stage of liquid heating (t^*) is defined as the homogeneous nucleation boiling explosion at which bubble generation and growth due to homogeneous nucleation inside a characteristic liquid cluster, x_e, causes the average cluster temperature, T_{avg}, to decrease when $q_c \geq q_d$. With the approximation of 1D semi-infinite heat conduction in the liquid the transient energy flux, deposited inside a finite size liquid cluster q_d (W/m^2) can be obtained as:

$$q_d(t) = -\lambda_l \left[\left.\frac{\partial T}{\partial x}\right|_{x=0} - \left.\frac{\partial T}{\partial x}\right|_{x=x_e} \right] \tag{2}$$

The solution of 1-D heat conduction for constant high heat flux boundary condition is given by:

$$T(x,t) = T_0 + \frac{q_w \sqrt{4\alpha t}}{\lambda} ierfc\left(x/\sqrt{4\alpha t} \right) \tag{3}$$

The rate of energy consumption in the liquid cluster due to homogeneous boiling, $q_c(t)$, can be obtained as follows:

$$q_c(t) = L\Gamma_G(t) x_e \tag{4}$$

Considering homogeneous nucleation boiling and assuming all of the bubbles generated during different stages of liquid heating grow up independently, $\Gamma_{G,}(t)$ can be given as:

$$\Gamma_G(t) = \int_0^t \left\{ 4\pi r^2 \frac{dr(t,t')}{dt} \rho_v \right\} J(t')dt' \tag{5}$$

For the rate of homogeneous nucleation events Carey [10] proposed Eq. (5) that has been graphically demonstrated in Fig. 2 for ethyl alcohol at atmospheric pressure:

$$J = 1.44 \times 10^{40} \left(\frac{\rho_l^2 \sigma}{M^3} \right)^{1/2} \exp\left\{ \frac{-1.214 \times 10^{24} \sigma^3}{T_l \left[\eta P_s(T_l) - P_0 \right]^2} \right\}; \eta = \exp\left\{ \frac{\left[P_0 - P_s(T_l) \right]}{RT_l \rho_l} \right\} \tag{6}$$

According to Skripov [1] bubble radius at any time *t*, generated at time *t′* can be given as:

$$r(t,t') = \phi\sqrt{t-t'};\ \phi = 2\sqrt{\frac{3}{\pi}}\frac{\sqrt{\lambda_l \rho_l c_l}}{L\rho_v}(T_l - T_s) \tag{7}$$

By incorporating the expressions of $q_d(t)$ and $q_c(t)$in Eq. (1)further simplification leads to:.

$$\frac{dT_{avg}}{dt} = \frac{1}{\rho_l c_l x_e}\left[-\lambda_l\left\{\left.\frac{\partial T}{\partial x}\right|_{x=0} - \left.\frac{\partial T}{\partial x}\right|_{x=x_e}\right\} - 2\pi L x_e \int_0^t \phi^3(T_{avg})\rho_v J(T_{avg})\sqrt{t-t'}\,dt'\right] \tag{8}$$

As indicated by Eq. (7), temperature history as well as the attainment of boiling explosion condition depends ($q_c(t) \geq q_d(t)$) on the liquid cluster size under consideration. The cluster size model that has been used in this study is proposed by Carey [10] which states that size of critical vapor embryo at maximum cluster temperature, $x_e = 2r_c(T^*_{avg})$ and,

$$r_c(T_l) = \frac{2\sigma(T_l)}{p_s(T_l)\exp\left[\{p_0 - p_s(T_l)\}/\rho_l R T_l\right] - p_0} \tag{9}$$

Variation of r_c with liquid temperature for ethanol at atmospheric pressure has been depicted in Fig. 2.

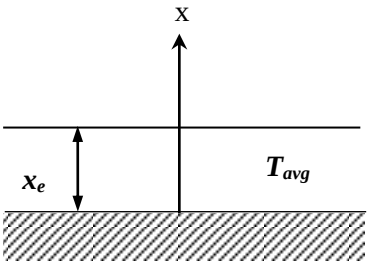

Fig. 1. Liquid cluster at the boundary

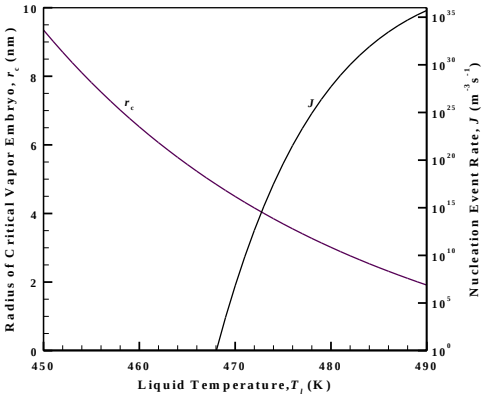

Fig. 2. Variation of r_c and J for ethanol at atmospheric pressure

3. Results and Discussion

The model used in the present study has been applied to the case of ethanol heating with linearly increasing boundary temperature with initial and boundary conditions identical to the case of Okuyama et. al. [3]. As depicted in Fig. 3, the model predicted time of boiling explosion has been found to be in good agreement with experimental observation. As no experimental/theoretical work on explosive boiling of ethanol under high heat flux boundary heating has reported in the literature, the present study focused on the case of ethanol heating with high heat flux boundary condition. The summary of the present study has been described in the next.

3.1 Minimum boundary heat flux for boiling explosion

Fig. 4 shows the temperature escalation inside the liquid cluster during heating of ethyl alcohol at various boundary heat fluxes for an initial temperature of 25 °C. As shown in Fig. 4, the boiling explosion at maximum liquid superheat takes place much earlier at higher boundary heat fluxes. For a characteristic time of 1 ms for the occurrence of boiling explosion, the limiting boundary heat flux for ethanol has been found to be in the order of 1 MW/m^2 which for water has been reported to be 15 MW/m^2 [11]. The liquid superheat limit at various boundary heat fluxes obtained in the present study are found to be in good agreement with the superheat limit reported for ethanol under pulse heating condition [12]. Fig. 5 depicts the effect of the boundary heat flux on the boiling explosion time, t* and maximum cluster temperature, T^*_{avg} for an initial temperature of 25°C. As shown in Fig. 5, the

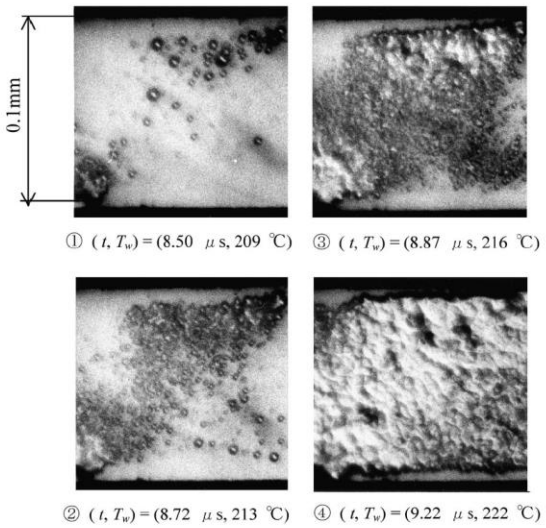

Fig. 3: Boiling bubbles immediately on the film heater immersed in ethanol; T_0 = 25 °C, $b = 2.2\times10^7$ K/s. Model predicted time of boiling explosion: $t^* = 8.12$ μs

variation of the time of boiling explosion with boundary heat flux is drastic; for a variation of four order of magnitude of boundary heat flux, q_w (0.1-1000 MW/m^2) the boiling explosion time, t^* undergoes a variation of ten orders of magnitude (0.743s - 9.93ns).

3.2 Effect of boundary heat flux on boiling explosion characteristic

The time of the occurrence of boiling explosion, t^* depends on the initial temperature of the liquid, T_0 for a particular boundary heat flux, q_w. For higher initial temperature of liquid, T_0, the nucleation occurs much earlier. However, as mentioned in Table 1, the variation of boiling explosion time, t^* with boundary heat flux, q_w is of similar order for all liquid initial temperature, T_0 ranging from 25°C to 78.3°C. Moreover, significant decrease of the attainment of the time of boiling explosion, t^* is caused by the increasing boundary heat flux, q_w. Therefore, the time of homogeneous boiling explosion, t^* is dependent on both the boundary heat flux, q_w and the liquid initial temperature, T_0. From the present study, the following equation has been approximated for the time of boiling explosion, t^*(μs), as a function of the boundary heat flux q_w (MW/m^2) and initial temperature of the liquid, T_0 (K)

$$t^* = (1.0 - 0.008\,(T_O - 273\,)) \times 10^4 \times q_w^{-1.96} \qquad 0.1 < q_w < 1000 \text{ MW/m}^2;\ 273 \text{ K} < T_0 < 351\text{K} \qquad (10)$$

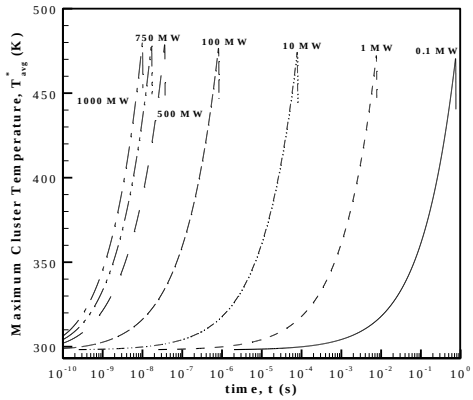

Fig. 4. Temperature escalation inside the liquid cluster at various boundary heat fluxes (T_0= 25 °C)

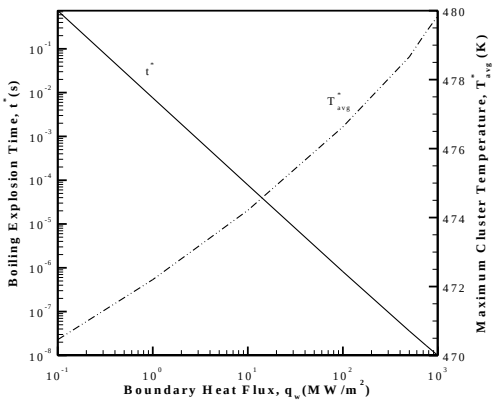

Fig. 5. Boiling explosion time and maximum cluster temperature at various boundary heat fluxes (T_0= 25 °C)

As mentioned in table 1, the variation of maximum cluster temperature, T^*_{avg}, with the boundary heat flux, q is quite small compared to the variation of time of boiling explosion, t^* with the boundary heat flux, q. As obtained in the present study for the variation of the boundary heat flux from 0.1 to 1000 MW/m^2, the maximum attainable cluster temperature, T^*_{avg} increases only about 10 K (470 - 480 K). However, T^*_{avg} does not vary much with the change of initial temperature of the liquid, T_0, for a particular boundary heat flux, q_w. This is because the homogeneous nucleation occurs at much higher temperature range than the liquid initial temperature (25-78.3°C).As there is no significant influence of liquid initial temperature, T_0, on the maximum cluster temperature, T^*_{avg}, therefore, the variation of maximum cluster temperature, T^*_{avg} (K) can be expressed as a function of boundary heat flux, q_w (MW/m^2) only, as given by the following equation:

$$T^*_{avg} = 473.2 + 1.02 \ln(q_w) \qquad 0.1 < q_w < 1000 \text{ MW/m}^2 \tag{11}$$

3.3 Theoretical boiling explosion and $q_{max,max}$

The boiling explosion conditions predicted by the present model is compared with the theoretical explosion condition denoted by the upper bound of the evaporative heat flux, $\boldsymbol{q_{max,max}}$ as given by Gambill and Lienhard [13],

$$q_{max,max} = \rho_v L \sqrt{RT/2\pi} \tag{12}$$

The maximum heat flux across the liquid-vapour interface of a bubble at the time of boiling explosion, $t = t^*$ can be obtained as follows:

$$q^*_{l-v} = \rho_v L \left.\frac{dr}{dt}\right|_{t=t^*} \tag{13}$$

Fig. 6 depicts the variation of maximum heat flux across the liquid-vapour interface at the boiling explosion ($q^*_{l\text{-}v}$) and the corresponding upper limit of evaporative heat flux, $q_{max,max}$ for various boundary heat fluxes. The $q^*_{l\text{-}v}$ and $q_{max,max}$ depends on the liquid temperature at the boiling explosion. As shown in the Table-1, the liquid temperature at the boiling explosion, T^*_{avg} does not vary much with the boundary heat flux, therefore, $q^*_{l\text{-}v}$ and $q_{max,max}$ remains nearly constant with the change of boundary heat flux. In addition, for all cases, $q^*_{l\text{-}v}$ is lower than $q_{max,max}$. This happens because $q_{max,max}$ is obtained with the assumption of no condensation at the liquid-vapour interface while in reality there must be some condensation in parallel with vaporization.

4. Conclusion

The boiling explosion condition of ethanol subjected to high heat flux pulse heating has been determined by applying a theoretical model based on homogeneous nucleation theory and heat conduction. The present model has been found to conform to the theoretical explosion condition corresponding to the upper bound of the evaporative heat flux across the liquid-vapor interface. A wide range of heat flux for liquid heating has been considered in the present study and it is found that the time of boiling explosion depends greatly on the heat flux while the temperature at the boiling explosion does not change significantly with the heat flux. At any particular heat flux,

Table 1. Homogeneous boiling explosion characteristics of ethanol under different boundary heat fluxes and liquid initial temperatures

q_w (MW/m^2)	x_e (nm)			t^* (s)			T^*_{avg} (K)		
	T_0 (°C)								
	25	50	78.3	25	50	78.3	25	50	78.3
0.1	8.83	8.81	8.77	0.743	0.5443	0.3563	470.46	470.54	470.64
1	8.26	8.23	8.19	7.59×10^{-3}	5.576×10^{-3}	3.673×10^{-3}	472.20	472.29	472.41
10	7.63	7.60	7.56	7.77×10^{-5}	5.737×10^{-5}	3.804×10^{-5}	474.21	474.31	474.45
100	6.92	6.89	6.84	8.15×10^{-7}	6.063×10^{-7}	4.072×10^{-7}	476.63	476.76	476.93
500	6.37	6.33	6.28	3.60×10^{-8}	2.724×10^{-8}	1.873×10^{-8}	478.66	478.80	478.99
750	6.18	6.15	6.09	1.69×10^{-8}	1.282×10^{-8}	8.914×10^{-8}	479.38	479.52	479.72
1000	6.06	6.03	5.98	9.93×10^{-9}	7.596×10^{-9}	5.326×10^{-9}	479.85	479.99	480.19

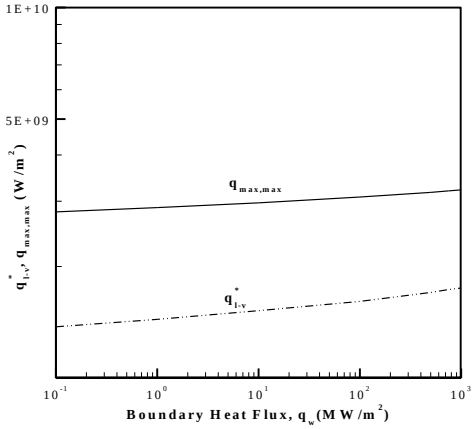

Fig. 6. Variation of the maximum heat flux across the liquid vapor interface (q^*_{l-v}) and the upper bound of evaporative heat flux ($q_{max,max}$) with boundary heat flux (T_0 = 25 °C)

higher liquid initial temperature results in earlier occurrence of the boiling explosion but the temperature limit at the boiling explosion does not change substantially with liquid initial temperature. Considering a characteristic time period of 1 millisecond for the occurrence of the homogeneous boiling explosion, the model predicts a heat flux of 0.1 MW/m^2 as the minimum heat flux at the liquid-heater interface required for the boiling explosion for a liquid initial temperature of 25 °C. The present study provides a possible way to explore the characteristics of boiling explosion for liquid heating with extremely high heat fluxes for which the experimentations are quite difficult due to the practical reasons involved.

Acknowledgement

The authors would like to appreciate the PROPATH group for offering the PROPATH software for calculation of thermodynamic properties of ethanol. We also gratefully acknowledge Professor K. Okuyama of Yokohama national university Japan, for offering the valuable photos.

References

[1] V. P. Skripov, Metastable Liquids, John Wiley & Sons, New York, U.S.A, 1974.

[2] Y. Iida, K. Okuyama, K. Sakurai, Boiling nucleation on a very small film heater subjected to extremely rapid heating, Int. J. Heat and Mass Transfer 37 (1994) 2771–2780.

[3] K. Okuyama, S. Mori, K. Sawa, Y. Iida,Dynamics of boiling succeeding spontaneous nucleation on a rapidly heated small surface, Int. J. Heat and Mass Transfer, 49 (2006) 2771-2780

[4] S. Glod, D. Poulikakos, Z. Zhao, G. Yadigaroglu, An investigation of microscale explosive vaporization of water on an ultrathin Pt wire, Int. J. Heat and Mass Transfer, 45 (2002) 367-379

[5] A. Asai, T. Hara, I. Endo, One- dimensional model of bubble growth and liquid flow in bubble jet printers, Japanese J. Applied Physics, 26–10 (1987) 1794–1801.

[6] A. Asai, Bubble dynamics in boiling under high heat flux pulse heating, J. Heat Transfer, 113 (1991) 973-979.

[7] Y. Hong, N. Ashgriz, J. Andrews, Experimental study of bubble dynamics on a micro heater induced by pulse heating, J. Heat Transfer, 126 (2004) 259–271.

[8] Z. Zhao, S. Gold, D. Poulikakos, Pressure and power generation during explosive vaporization on a thin film microheater, Int. J. Heat and Mass Transfer, 43 (2000) 281–296.

[9] M. N.Hasan, M. Monde, Mitsutake, Y., Model for boiling explosion during rapid liquid heating, Int. J. Heat and Mass Transfer, 54 (2011) 2844-2853.

[10] V. P. Carey, Liquid-Vapor Phase-Change Phenomena, Hemisphere Publishing Corporation, U.S.A, 1992.

[11] Mohammad Nasim Hasan, Masanori Monde and Yuichi Mitsutake, "Boiling Explosion of Water during Iso-flux Pulse Heating" Thermal Science and Engineering, 19 (2011) 95-102.

[12] C. T. Avedisian, "The Homogeneous Nucleation Limits of Liquids", J. Phys. Chem. Ref. Data, 14 (1985) 3.

[13] W. R. Gambill, and J. H. Lienhard, An upper bound for the critical boiling heat flux, J. Heat Transfer, 111(1989) 815-818.

6th BSME International Conference on Thermal Engineering (ICTE 2014)

MHD effect on free convection flow in porous media filled equilateral triangular cavity with heat generation

R. Chowdhury[a,b,*], S. Parvin[b], M. A. H. Khan[b]

[a]*Department of Natural Science, Stamford University Bangladesh, Dhaka-1209, Bangladesh.*
[b]*Department of Mathematics, Bangladesh University of Engineering & Technology, Dhaka-1000, Bangladesh.*

Abstract

Unsteady-state free convection heat transfer in an equilateral triangular cavity, filled with a fluid-saturated porous medium and with heat generation in presence of magnetic field has been considered in this study. The horizontal wall of the cavity is heated at a constant temperature, the left inclined wall is non-isothermal and the right inclined wall is differentially cold. The governing equations are solved numerically by finite element method. The effect of MHD and heat generation on the streamlines and isotherms are investigated for the fluid of Prandtl number (Pr = 0.7) and Rayleigh number (Ra = 10^5). The average temperature of the cavity and the rate of heat transfer of the bottom surface of the cavity are also presented.
(ICTE 2014).

Keywords: Porous medium; Free convection flow; Magnetic field; Heat generation; Equilateral triangular cavity

1. Introduction

Free convection heat transfer occurs in cavities filled with fluid saturated porous media due to buoyancy can be found in many applications of engineering. These applications are well described in the literature by Nield and Bejan[1], Ingham and Pop[2].

Natural convection has analyzed for different shaped cavities by many researchers. The phenomena of natural convection in cavities can be classified into two main groups as rectangular and non-rectangular cavities. Most of the researchers study the rectangular shaped cavities [3-6] because of the simplicity of solutions for these geometrical shapes. Some researchers investigate the effects of the geometric shapes on natural convection in enclosures such as triangle [7-10], parallelogram [11], trapezoidal [12], and wavy shapes [13]. In these studies they show that both flow and temperature fields are affected by the geometrical parameters.

Triangular cavities with differentially heated isothermal wall have received a considerable attention because of its applicability in various fields such as: design of industrial equipments, crude oil production, cooling of electronic devices [9, 14], energy related applications, for example: thermal insulation of building using air gaps, furnaces and fire control in building, [16, 17], geothermal applications, for example: differential heating and cooling in lakes [19] etc.

* Corresponding author.
E-mail address:raju_chy_23@yahoo.com (R. Chowdhury)

Nomenclature

B_0	applied magnetic field strength	[T]
C_p	specific heat at constant pressure	[$\mathrm{Jkg^{-1}K^{-1}}$]
Da	Darcy parameter	
g	gravitational acceleration	[$\mathrm{ms^{-2}}$]
Ha	Hartmannn number	
k	thermal conductivity of the media	[$\mathrm{Wm^{-1}K^{-1}}$]
l	length of the inclined wall	[m]
L	height of the triangle	[m]
Nu	Nusselt number	
p	fluid pressure	[Pa]
Pr	Prandtl number	
Ra	Rayleigh number	
t	time	[s]
T	temperature	[^{o}C]
u	velocity in x-direction	[$\mathrm{ms^{-1}}$]
U_0	reference velocity, α/L	
v	velocity in y-direction	[$\mathrm{ms^{-1}}$]
x, y	Cartesian coordinates	[m]
X, Y	dimensionless coordinates	

Greek symbols

α	thermal diffusivity	[$\mathrm{m^2s^{-1}}$]
β	thermal expansion coefficient of fluid	[$\mathrm{K^{-1}}$]
θ	dimensionless temperature	
γ	fluid ratio of specific heat	
λ	dimensionless heat generation parameter	
μ	dynamic viscosity	[$\mathrm{Pas^{-1}}$]
υ	kinematic viscosity, μ/ρ	[$\mathrm{m^2s^{-1}}$]
ρ	fluid density	[$\mathrm{kgm^{-3}}$]
τ	dimensionless time	
κ	permeability of the porous media	[$\mathrm{m^2}$]
ε	porosity	
σ	electrical conductivity of the fluid	[$\mathrm{Sm^{-1}}$]

Subscript

c	cold
h	hot

The characteristics of heat and fluid flow for a configuration of isothermal vertical walls, maintained at different temperatures and with adiabatic horizontal walls are well understood [3]. Less work has been carried out for more complex thermal boundary conditions such as an imposed thermal gradient that is neither purely horizontal nor purely vertical. The problem of natural convection heat transfer in a triangular enclosure filled with a porous medium has been first considered by Bejan and Poulikakos [21]. They investigated that the porous material can reduce heat transfer in attic space cavity. It has been shown the flow consists primarily of an elongated horizontal counter flow driven by the cold wall of the cavity. Later, Varol et al. [10] made a study on natural convection in a right angle triangular enclosure filled with a porous medium by taking into account all possibilities of thermal

boundary conditions. Recently, Basak et al.[22] have made a numerical analyzes using finite element method to investigate the effects of non-isothermal boundary conditions on flow fields and temperature distribution in a triangular enclosure filled with a porous medium.

Earlier studies were mainly devoted on physics of the various flow systems in triangular cavity. Akinsete and Coleman [9] have studied the laminar natural convection in triangular enclosure. Karyakin and Sokovishin [24] presented convection patterns in isosceles triangular enclosure. Finite difference method is used to solving the Navier-Stokes and energy equations. They observed that the maximum values of stream functions and Nusselt numbers perform damping oscillations around the steady state values. Koushik et al. [17] studied the performance of a triangular built-in-storage solar water heater under winter conditions.

A considerable number of experimental and numerical studies have been carried out for natural convection in triangular enclosure for various applications. Flack et al. [23] predicted free convection velocities with finite element method and measured velocities using laser velocimetry for three triangular enclosure. Holtzman et al. [14] studied laminar natural convection for isosceles triangular enclosures heated from below and symmetrically cooled from above. Asan and Namil [7] studied the natural convection in pitched roof of triangular cross-section for summer day boundary conditions. Lei and Patterson [19] carried out a model experiment to visualize the convection process in a shallow triangular cavity .

A few recent studies on natural convection in triangular enclosures have also been carried out for various applications. Varol et al. [26], Ridouane et al. [25], Tzeng et al. [8], Joudi et al. [16] studied numerically, the performance of a prism shaped solar collector with a right angled triangular cross-sectional area. The effect of horizontal adiabatic partition was studied. Tzeng et al. [8] carried out numerical simulation and parametric studies for triangular enclosures. The aim of this study was to establish efficient energy management. Ridouane et al. [25] studied natural convection within attic spaces of houses and buildings with sloped roofs and horizontally suspended ceilings. The efficient heating strategies have been proposed for various seasons.

The effect of the magnetic field on the convective heat transfer and the free convection flow of the fluid are of vital importance in engineering. Several numerical and experimental method have been developed to investigate flow characteristics inside cavities because these geometries have practical engineering and industrial applications, such as in the design of solar collectors, thermal design of building, air conditioning, cooling of electronic devices, furnaces, lubrication technologies, chemical processing equipment, drying technologies etc. Garandet et al. [28] analyzed the buoyancy driven convection in a rectangular enclosure with a transverse magnetic field. Oh et al. [29] considered the conducting body generated heat within the cavity. In this study, the flow was driven by a temperature difference across the cavity and a temperature difference caused by a heat generating source. Kahveci and Oztuna [30] studied MHD natural convection to investigate the heat transfer in a horizontally heated subdivided enclosure by applying differential quadrature method. Oztop et al. [31] numerically investigated magnetic field effects on natural convection in an enclosure with non-isothermal heater. Rahman et al. [32] analyzed magnetic field effect on mixed convection in a lid driven cavity and found average Nusselt number decreases with increasing Hartmannn number and joule heating parameter. Similar application can be found for open channels under magnetic field [33]. Sivasankaran and Ho [34] studied natural convection of maximum density water in the presence of magnetic field with temperature dependent properties in a cavity and investigated that the external magnetic field direction is an important parameter for fluid flow as well as heat transfer.

According to the knowledge of the authors and the literature given above, there is no study on natural convection heat transfer in equilateral triangular enclosure with both effect MHD and heat generation. The main purpose of this study is to investigate the effect of MHD on free convection heat transfer in porous medium filled equilateral triangular enclosure with heat generation. The enclosure is heated from bottom wall, non-isothermal left inclined wall and differentially heated right inclined wall. The tests were performed for different Hartmannn number and heat generation parameter.

2. Physical model

The physical model is considered as shown in Fig. 1 with the corresponding boundary conditions. It is a equilateral triangular cavity of height L filled with a fluid-saturated porous medium. The bottom wall is heated

isothermally with temperature T_h. The temperature of the left inclined wall is T_h at the bottom and reduces linearly to T_c at the top. The upper portion of the right wall is at temperature T_c. The boundary condition at the lower portion of the right inclined wall deserves some explanation as: l_1 is the length of a small gap (l is the total length of the inclined wall) where the temperature varies linearly from T_h to T_c. A magnetic field of strength B_0 is applied horizontally to the right side wall.

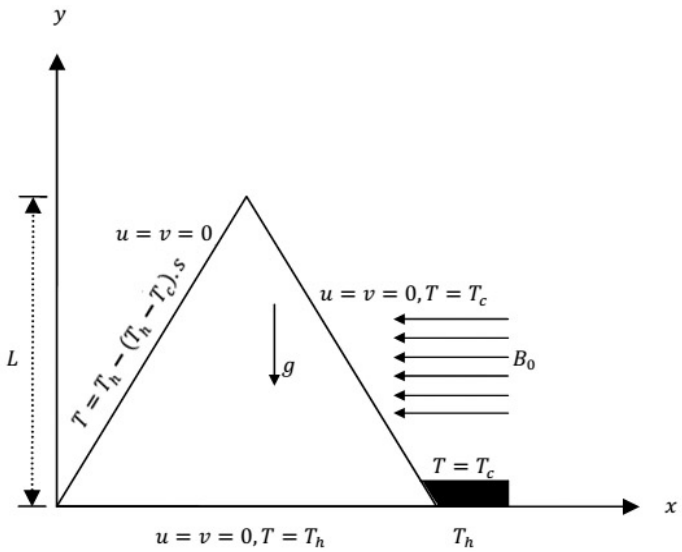

Fig. 1. Physical model of the problem with boundary conditions.

We also bring into account the effect of temperature-dependent heat generating flow region. The volumetric heat generation, Q, is assumed to be:

$$Q = \begin{cases} Q_0(T - T_c), & T \geq T_c \\ 0, & T \leq T_c \end{cases} \tag{1}$$

where Q_0 is the heat generation constant. The above relation, as explained by Vajravelu and Hadjinicolaou [36], is valid as approximation of the state of some exothermic process, which means that heat flows from the surface to the cavity.

3. Mathematical formulation

We assume unsteady laminar flow of a viscous incompressible fluid having constant properties. The effect of buoyancy is included through the well-known Boussinesq approximation. The gravitational force acts in the cavity vertically downward direction as indicated in Fig. 1. Under the above assumptions, the governing equations for mass, momentum and energy in a two-dimensional Cartesian co-ordinate system are:

$$\frac{\partial u}{\partial x} + \frac{\partial v}{\partial y} = 0, \tag{2}$$

$$\frac{\partial u}{\partial t} + u\frac{\partial u}{\partial x} + v\frac{\partial u}{\partial y} = -\frac{1}{\rho}\frac{\partial p}{\partial x} + \nu\left(\frac{\partial^2 u}{\partial x^2} + \frac{\partial^2 u}{\partial y^2}\right) - \frac{\nu}{K}u, \tag{3}$$

$$\frac{\partial v}{\partial t} + u\frac{\partial v}{\partial x} + v\frac{\partial v}{\partial y} = -\frac{1}{\rho}\frac{\partial p}{\partial y} + \nu\left(\frac{\partial^2 v}{\partial x^2} + \frac{\partial^2 v}{\partial y^2}\right) - \frac{\nu}{K}v + g\beta(T - T_c) - \frac{\sigma B_0^2}{\rho}v, \tag{4}$$

$$\frac{\partial T}{\partial t} + u\frac{\partial T}{\partial x} + v\frac{\partial T}{\partial y} = \alpha\left(\frac{\partial^2 u}{\partial x^2} + \frac{\partial^2 u}{\partial y^2}\right) + \frac{Q_0}{\rho C_p}(T - T_c). \tag{5}$$

where u and v are the fluid velocity components in the x- and y-direction, respectively. t is the time, p is the fluid pressure, β is the volumetric thermal expansion coefficient, K is the permeability of the porous medium, ρ is the density of the fluid, $\alpha = \frac{k}{\rho C_p}$ is the thermal diffuisivity and c_p is the specific heat at constant pressure. In the present investigation, porous medium inertia effects have been neglected in the momentum equations and the effect of viscous dissipation are neglected from the energy equation.

In equation (3) and (4), K is the measure of permeability of the porous medium defined by

$$K = \frac{\varepsilon^{+3}}{180(1-\varepsilon^{+})^2} d^2 \tag{6}$$

where d is the diameter of the solid sphere and ε^{+} is known as the porosity of the media and is defined by

$$\varepsilon^{+} = \frac{V_f}{V_c} \tag{7}$$

where V_f is the volume of the fluid and V_c is the control volume.

The following dimensionless variables are constructed:

$$X = \frac{x}{L}, \quad Y = \frac{y}{L}, \quad P = \frac{p}{\rho U_0^2}, \quad \ell = \frac{l}{L}, \quad \ell_1 = \frac{l_1}{L}, \quad \tau = \frac{tU_0}{L}, \quad U = \frac{u}{U_0}, \quad V = \frac{v}{U_0}, \quad \theta = \frac{T-T_c}{T_h-T_c} \tag{8}$$

where $U_0 = \frac{\alpha}{L}$ is the reference velocity. Introducing the above dimensionless dependent and independent variables in the governing equations (2)-(5) the following equations are obtained:

$$\frac{\partial U}{\partial X} + \frac{\partial V}{\partial Y} = 0, \tag{9}$$

$$\frac{\partial U}{\partial \tau} + U\frac{\partial U}{\partial X} + V\frac{\partial U}{\partial Y} = -\frac{\partial P}{\partial X} + Pr\left(\frac{\partial^2 U}{\partial X^2} + \frac{\partial^2 U}{\partial Y^2}\right) - \frac{Pr}{Da}U, \tag{10}$$

$$\frac{\partial V}{\partial \tau} + U\frac{\partial V}{\partial X} + V\frac{\partial V}{\partial Y} = -\frac{\partial P}{\partial Y} + Pr\left(\frac{\partial^2 V}{\partial X^2} + \frac{\partial^2 V}{\partial Y^2}\right) - \frac{Pr}{Da}V + RaPr\theta - Ha^2 Prv, \tag{11}$$

$$\frac{\partial \theta}{\partial \tau} + U\frac{\partial \theta}{\partial X} + V\frac{\partial \theta}{\partial Y} = \left(\frac{\partial^2 \theta}{\partial X^2} + \frac{\partial^2 \theta}{\partial Y^2}\right) + \lambda\theta. \tag{12}$$

where $Pr = \frac{\nu}{\alpha}$ is the Prandtl number, $Ra = \frac{g\beta(T_h-T_c)L^3}{\alpha\nu}$ is the Rayleigh number, $Da = \frac{1}{\gamma} = \frac{K}{L^2}$ is the Darcy number, $Ha = B_0 L\sqrt{\frac{\sigma}{\mu}}$ is the Hartmannn number and $\lambda = \frac{Q_0 L^2}{\rho\nu C_p}$ is the heat generation parameter.

In the present investigation, the value of the Prandtl number is choosen as 0.7, the Rayleigh number is taken to be 10^5 and the Darcy number is 0.4.

The dimensionless initial and boundary conditions are as follows:
All boundaries are rigid and no-slip;
$U = V = \theta = 0$ for $\tau = 0$
On the bottom wall: $\theta = 1$
On the left inclined wall: $\theta = 1 - \ell$
On the upper portion of the right inclined wall: $\theta = 0$
On the lower portion of the right inclined wall: $\theta = 1 - \ell_1$.

Local and mean Nusselt numbers of the bottom wall are calculated via Eqn.(13) and (14) respectively,

$$Nu_x = \left(-\frac{\partial \theta}{\partial Y}\right)_{Y=0} \tag{13}$$

$$\text{and } Nu = \int_0^b Nu_x dX \tag{14}$$

where b is the nondimensional base of the triangular enclosure.

4. Solution Methodology

The Galerkin weighted residual method of finite element formulation is used to solve the governing equations (9)-(12). This procedure is well described by Taylor and Hood [37] and Dechaumphai [38]. In this method, the solution domain is descritized into finite element meshes, which are composed to non-uniform triangular elements. Then the nonlinear governing partial differential equations (i.e., mass, momentum and energy equations) are transferred into a system of integral equations by applying Galerkin weighted residual method. The integration involved in each term of these equations is performed by using Gauss's quadrature method. The nonlinear algebraic equations so obtained are modified by imposition of boundary conditions. These modified non-linear equations are transferred into linear algebraic equations by using Newton's method. Finally these equations are solved by using triangular factorization method.

5. Code validation

The corresponding problem for pure fluid without the effect of MHD has been investigated by Saha and Gu [27] for different values of heat generation parameter, $Ra = 10^5$ and $Pr = 0.7$. A test was made to compare the results obtained by the present code with earlier study [27]. The results of streamlines and isotherms are given in Fig. 2 for natural convection in a porous triangular closure. The left column belongs to result of Saha and Gu [27] and right column gives result for present study. The comparison shows that the present's results agree with the numerical solution of Saha and Gu [27].

6. Result and discussion

Magnetohydrodynamic free convection heat transfer inside a equilateral cavity is studied for different number of Hartmann number *Ha* and dimensionless heat generation parameter λ while $Ra = 10^5, Pr = 0.7$ and $Da = 0.4$.

Fig. 3 shows the effect of magnetic field of the cavity on flow field and temperature distribution. They are presented as streamline (on the left column) and isotherm (on the right column). As can be seen from the left side of fig. 3 (a), it is found that a triangle shaped flow distribution is formed. Also a cell is formed in the absence of magnetic field ($Ha = 0$) and $\lambda = 0$ and located near the centre of the cavity. By the increasing of Hartmann number *Ha* the center of the cell moves towards the bottom wall of the cavity because the magnetic field tends to slow down the motion.

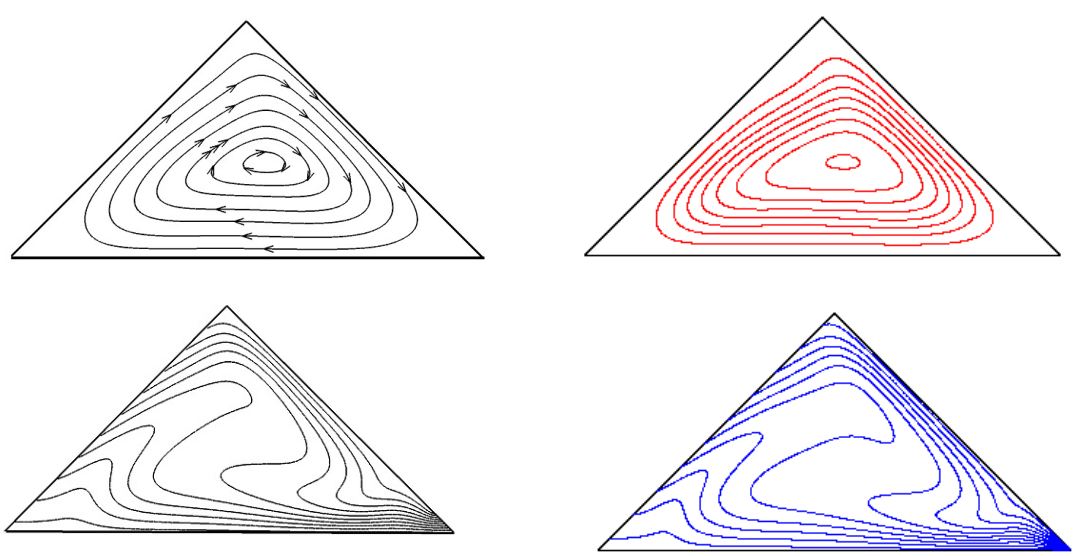

Fig. 2. A comparison for streamlines (top row) and isotherms (bottom row) between Saha and Gu [27] (on the left) and present study (on the right) for $Ra = 10^5, Pr = 0.7,\ Da = 0.4,\ \lambda = 0$ and $Ha = 0$.

a) Ha = 0

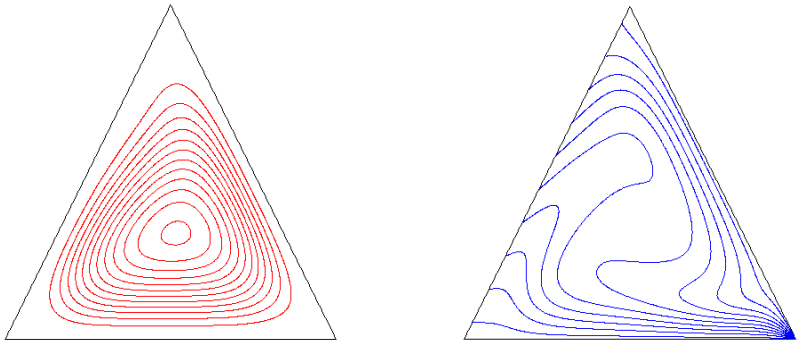

b) Ha = 20

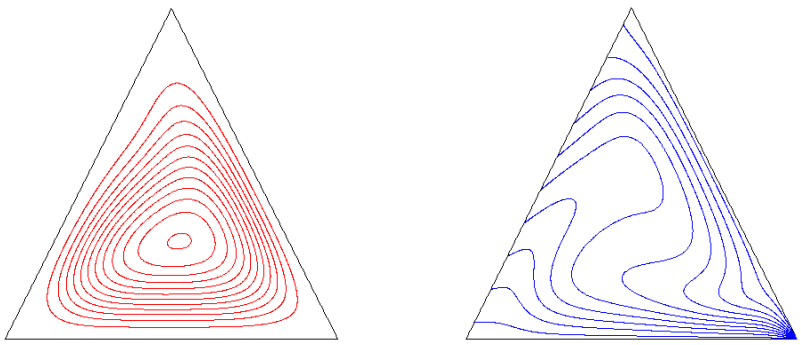

c) Ha = 40

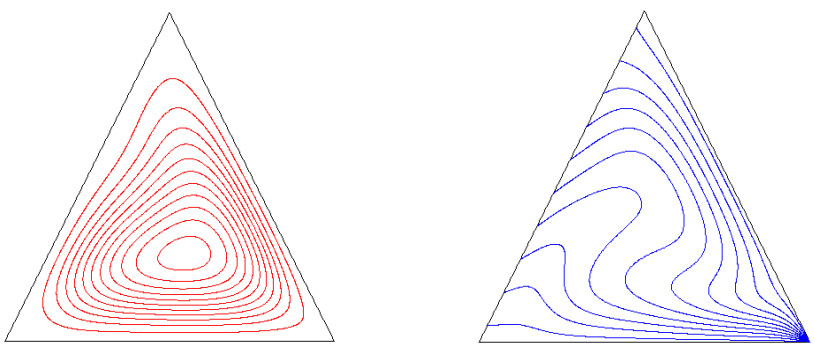

d) Ha = 60

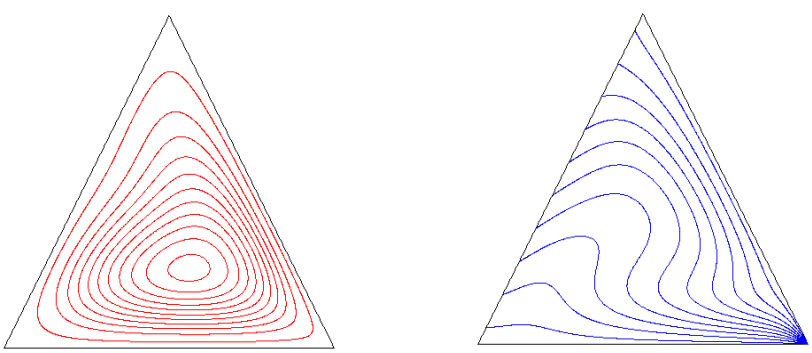

e) $Ha = 80$

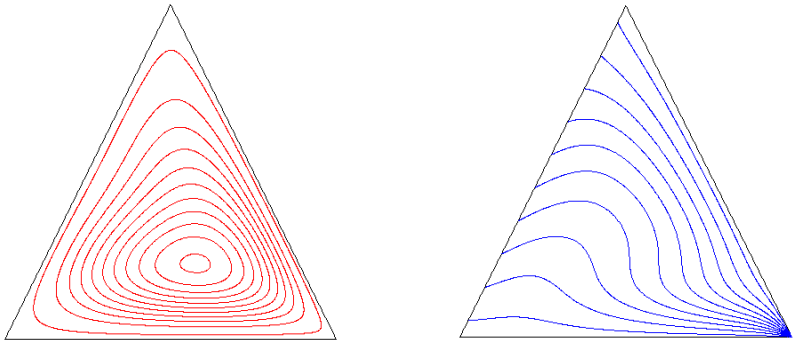

Fig. 3. Streamlines (left) and isotherms (right) for different Hartmann numbers at $Ra = 10^5, Pr = 0.7, Da = 0.4$ and $\lambda = 0$; a) $Ha = 0$, b) $Ha = 20$, c) $Ha = 40$, d) $Ha = 60$, e) $Ha = 80$.

a) $\lambda = 5$

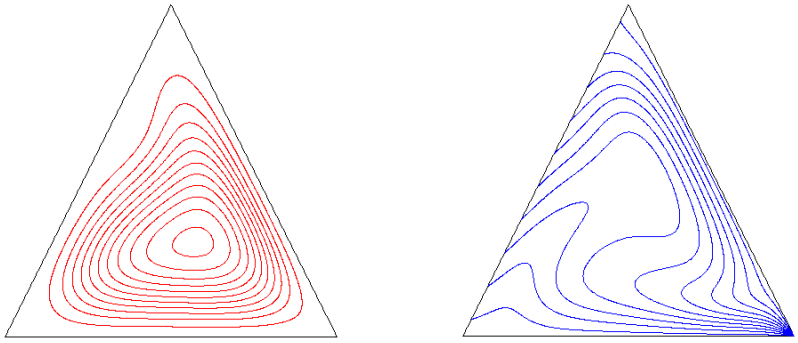

b) $\lambda = 10$

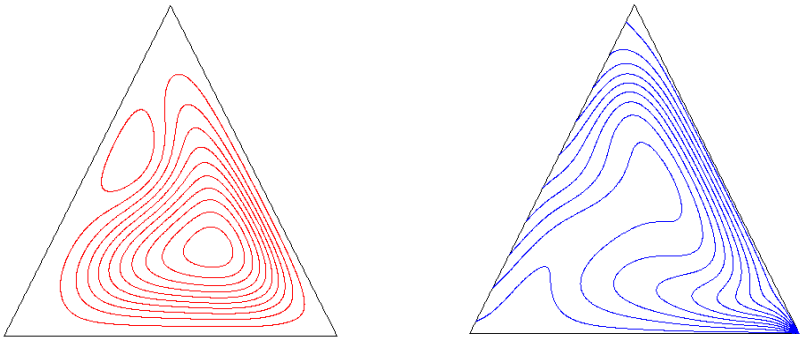

c) $\lambda = 15$

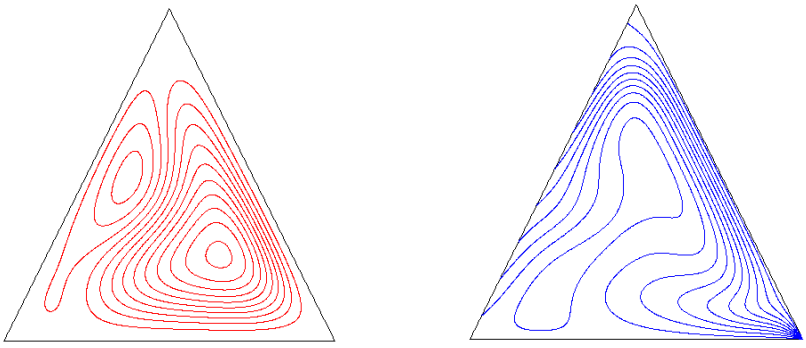

d) λ = 20

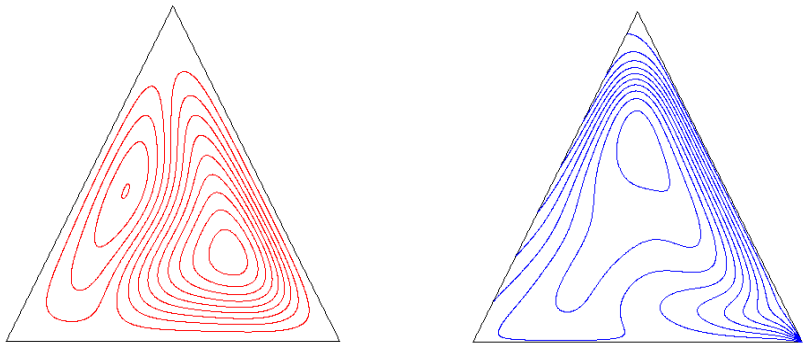

e) λ = 25

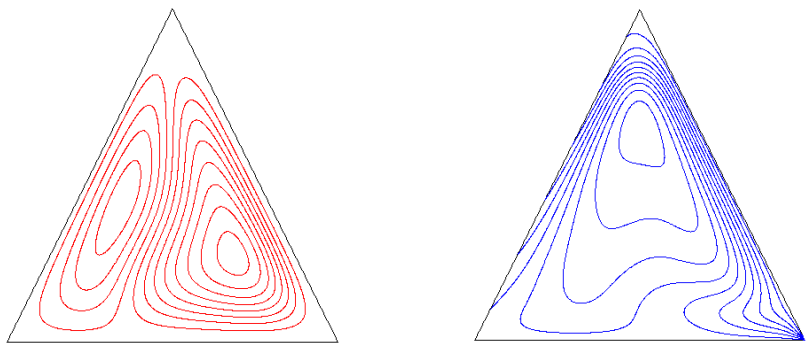

Fig. 4. Streamlines (left) and isotherms (right) for different value of heat generation parameter λ at $Ra = 10^5$, $Pr = 0.7$, $Da = 0.4$ and $Ha = 20$; a) $\lambda = 5$, b) $\lambda = 10$, c) $\lambda = 15$, d) $\lambda = 20$, e) $\lambda = 25$.

The right side of fig. 3 shows the temperature fields in the flow region. The high temperature region remains near the left wall of the cavity and isotherms lines are clustered close to bottom surface that indicates the existence of steep temperature gradient in the vertical direction of this region. In the center of the cavity, the temperature gradients are weak. From the isotherm of fig. 3, it shows that in the presence of magnetic field and for increasing values of Hartmann number *Ha* the temperature distributions are being regular.

Fig. 4 represents the streamline and isotherm for the pure fluid for different values of heat generation parameter λ. A heated boundary layer is formed adjacent to the bottom surface as the surface is heated isothermally. As a result of buoyancy effect, the hot fluid moves toward the uphill from the bottom within the cavity. Non-isothermal heating effect of the left inclined wall of the cavity triggers the hot fluid to move upward and disperse into the core of the cavity. The left side of fig. 4 (a) shows that a large convecting cell is formed through the whole cavity. From fig. 4 (b) (left side) we see that a secondary cell is developed at the left top corner with increasing the value of the heat generation parameter λ. It may further be seen that the size of secondary vortex increases as λ increases.

In fig. 3 (a), from the right side it can be seen that the isotherms are clustered close to the right corner of the bottom surface without presence of the heat generation ($\lambda = 0$). Fig. 4 (right part) shows that the presence of heat generation the clustered isotherms move to the right and towards the right cold surface to the cavity. For increasing the value of heat generation parameter λ, the temperature gradient in the middle of the cavity also appears to increase. It may predict that isotherms become clustered in the region near the top surface as the value of the heat generation parameter increases.

Fig. 5 shows the effect of magnetic field on the rate of heat transfer on the bottom wall of the cavity. The average Nusslet number is plotted as a function a heat generation parameter for different Hartmann number ($Ha = 0, 20, 40, 60, 80, 100$) while $Ra = 10^5$, $Pr = 0.7$ and $Da = 0.4$. It is observed that the average Nusselt number Nu decreases with the increasing of heat generation parameter λ and for little increasing of Hartmann number Ha. In the case of Hartmann number, initially the average Nusselt number Nu decreases for further increasing of the Hartmann number Ha. Then after a certain value ($\lambda = 15$) of heat generation parameter λ, Nu increases as Ha increases.

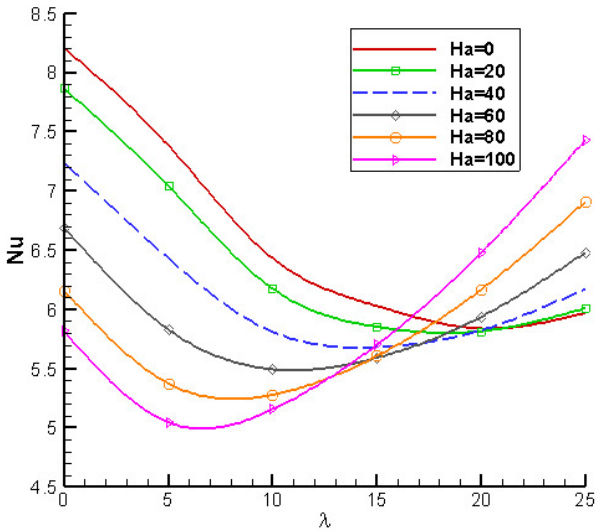

Fig. 5. Variation of average Nusselt number of the bottom surface with heat generation parameter λ for different Hartmann numbers *Ha*.

Fig. 6 represents the average temperature of the cavity as a function of heat generation parameter λ for various Hartmann number Ha while $Ra = 10^5$, $Pr = 0.7$ and $Da = 0.4$. The average temperature θ increases for increasing values of *H*a and heat generation parameter λ.

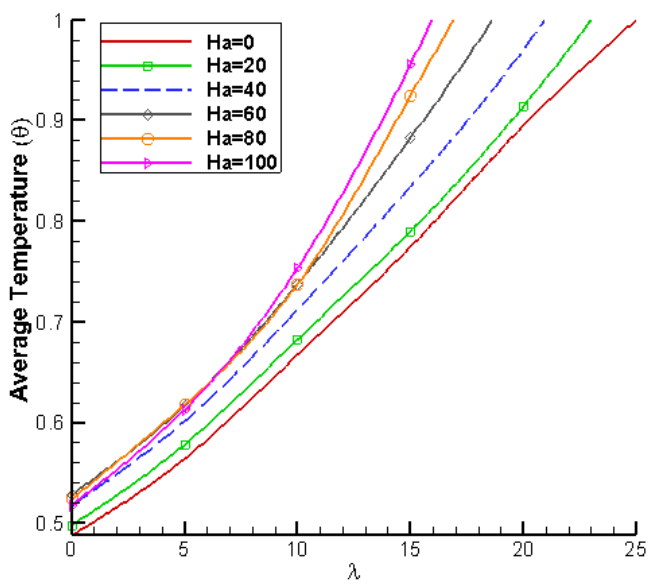

Fig. 6. Variation of average temperature θ with heat generation parameter λ for different Hartmann numbers *Ha*.

7. Conclusion

In this investigation, the effect of MHD on free convection at a equilateral triangular cavity with heat generation is numerically studied. The finite element method was employed for the solution of the present problem. Some important findings can be drawn as follows:

- Increasing the strength of magnetic field, decreases the flow strength inside the cavity and heat transfer.
- Magnetic field can be a control parameter for both heat and fluid flow at constant value of heat generation parameter.
- Increasing heat generation in the fluid reduces the thermal gradients near the heated bottom wall of the cavity.
- The strength of dominant vortex induced by buoyancy effect reduced due to increasing internal heat generation.

Acknowledgements

This work is fully supported by the Department of Mathematics, Bangladesh University of Engineering and Technology.

References

[1] D. A. Nield, A. Bejan, Convection in Porous Media, second ed., Springer, NY, 2006.
[2] D. B. Ingham, I. Pop, Transport Phenomena in Porous Media II, Pergamon, 2005.
[3] S. Ostrach, Natural convection in enclosures, Adv. Heat Transfer 8 (1972) 161-227.
[4] M. A. Hossain, M. Wilson, Natural convection flow in a fluid-saturated porous medium enclosed by non-isothermal walls with heat generation, Int. J. Therm. Sci. 41 (2002) 447-454.
[5] B. Goyeau, J. P. Songbe, D. Gobin, Numerical study of double-diffusive natural convection in a porous cavity using the Darcy-Brinkman formulation, Int. J. Heat Mass Transfer 39 (1996) 1363-1378.
[6] D. M. Manole, J. L. Lage, Numerical benchmark results for natural convection in a porous medium cavity, in: Heat Mass Transfer Porous Media, ASME Conf., 1992, pp. 55-60.
[7] H. Asan, L. Namli, Laminar natural convection in a pitched roof of triangular cross-section: Summer day boundary conditions, Energy and Building 33 (2000) 69-73.
[8] S. C. Tzeng, J. H. Liou, R. Y. Jou, Numerical simulation-aided parametric analysis of natural convection in a roof of triangular enclosures, Heat Transfer Engrg. 26 (2005) 69-79.
[9] V. A. Akinsete, T. A. Coleman, Heat transfer by steady laminar free convection in triangular enclosures, Int. J. Heat Mass Transfer 25 (1982) 991-998.
[10] Y. Varol, H. F. Oztop, A. Varol, Free convection in porous media filled right-angle triangular enclosures, Int. Comm. Heat Mass Transfer 33 (2006) 1190-1197.
[11] A. C. Baytas, I. Pop, Free convection in oblique enclosures filled with a porous medium, Int. J. Heat Mass Transfer 42 (1999) 1047-1057.
[12] Y. varol, A. Koca, H. F. Oztop, Laminar natural convection in saltbox roofs for both summerlike and winterlike boundary conditions, J. Appl. Sci. 6 (2006) 2617-2622.
[13] Y. Varol, H. F. Oztop, Free convection in a shallow wavy enclosure, Int. Comm. Haet Mass Transfer 33 (2006) 764-771.
[14] G. A. Holtzman, R. W. Hill, K. S. Ball, Laminar natural convection in isosceles triangular enclosure heated from bellow and symmetrically cooled from above, J. Heat Transfer-Transactions of the ASME 122 (2000) 485-491.
[15] F. P. Incropera, Convection heat transfer in electronic equipment cooling, J. Heat Transfer 110 (1988) 1097-1111.
[16] K. A. Joudi, I. A. Hussein, A. A. Farhan, Computational model for a prism shaped storage solar collector with a right triangular cross section, Energy Conservation and Management 45 (2004) 391-409.
[17] S. C. Kaushik, R. Kumar, H. P. Grag, J. Prakash, Transient analysis of a triangular built in storage solar water eater under winter conditions, Heat recovery Systems & CHIP 14 (1994) 337-341.
[18] O. Laguerre, S. Ben Amara, D. Flick, Experimental study of heat transfer by natural convection in a closed cavity: application in a domestic refrigerator, J. Food Engrg 70 (2005) 523-537.
[19] C. W. Lei, J. C. Patterson, Unsteady natural convection in a triangular enclosure induced by absorption of radiation, J. Fluid Mechanics 460 (2002) 181-209.
[20] M. A. R. Sharif, T. R. Mahammad, Natural convection in cavities with constant flux heating at the bottom wall and isothermal cooling from the sidewalls, Int. J. Thermal Sci. 44 (2005) 865-878.
[21] A. Bejan, D. Poulikakos, Natural convection in an attic-shaped space filled with porous material, J. Heat Transfer 104 (1982) 241-247.

[22] T. Basak, C. Thirumalesha, S. Roy, Finite element simulations of natural convection in a right-angle triangular enclosure filled with a porous medium: effects of various thermal boundary conditions, J. Porous Media 11 (2008) 159-78.
[23] R. D. Flack, K. Brun, R. J. Schnipke, Measurement and prediction of natural convection velocities in triangular enclosures, Int. J. Heat and Fluid Flow, 16 (1995) 106-113.
[24] YU. E. Karyakin, YU. A. Sokovishin, Transient natural convection in triangular enclosures, Int. J. Heat Mass Transfer 31 (1988) 1759-1766.
[25] E. Ridouane, A Campo, M. Hasnaoui, Benefits derivable from connecting the bottom and top walls of attic enclosure with insulated vertical side walls, Nemer. Heat Transfer Part A-Applications 49 (2006) 175-193.
[26] Y. Varol, A. Koca, H. F. Oztop, Numerical convection in a triangle enclosure with flush mounted heater on the wall, Int. Comm. Heat Mass Transfer 33 (2006) 951-958.
[27] Suvash C. Saha, Y. T. Gu, Free convection flow in a triangular enclosure with fluid-saturated porous medium enclosed with heat generation, J. ANZIAM 53 (2012) C127-C141.
[28] J. P. Garandet, T. Albousssiere, R. Moreau, Buoyancy driven convection in a rectangular enclosure with transverse magnetic field, Int. J. Heat Mass Transfer 35 (1992) 741-748.
[29] J. Y. Oh, M. Y. Ha, K. C. Kim, Numerical study of heat transfer and flow of natural convection in an enclosure with a heat generating conducting body, Numer. Heat Transfer A-Application 31 (1997) 289-304.
[30] K. Kahveci, S. Oztuna, MHD natural convection flow and heat transfer in a laterally heated partitioned enclosure, Euro. J. Mechanics B/Fluids 28 (2009) 744–752.
[31] H.F. Oztop, M. Oztop, Y. Varol, Numerical simulation of Magnetohydrodynamic buoyancy-induced flow in a non-isothermally heated square enclosure, Commu. Nonlinear Sci.e and Numerical Simulation 14 (2009) 770–778.
[32] M.M. Rahman, M.A.H. Mamun, R. Saidur, Analysis of magnetohydrodynamic mixed convection and joule heating in lid-driven cavity having a square block, J. Chinese Institute of Engs. 34 (2011) 585–599.
[33] M.M. Rahman, S. Parvin, R. Saidur, N.A. Rahim, Magnetohydrodynamic mixed convection in a horizontal channel with an open cavity, Int. Commu. Heat Mass Transfer 38 (2011) 184–193.
[34] S. Sivasankaran, C.J. Ho, Effect of temperature dependent properties on MHD convection of water near its density maximum in a square cavity, Int. J. of Thermal Sci. 47 (2008) 1184–1194.
[35] M. Hasanuzzaman, H. F. Oztop, M. M. Rahman, N. A. Rahim, R. Saidur, Y. Varol, Magnetohydrodynamic natural convection in trapezoidal caveties, Int. Comm. Heat Mass Transfer 39 (2012) 1384-1394.
[36] K. Vajravelu, A. Hadjinicolaou, Convective heat transfer in an electrically conducting fluid at a stetching surface with uniform free stream, Int. J. Engrg. Sci. 34 (1997) 1237-1244.
[37] C. Taylor, P. Hood, A numerical solution of the Navier-Stokes equations using finite element technique I, Comput. Fuids, 1 (1973) 73-89.
[38] P. Dechaumphai, Finite element method in Engrg., 2nd edi., Chulalongkorn University Press, Bangkok, 1999.

6th BSME International Conference on Thermal Engineering (ICTE 2014)

Natural convection inside a Nanofluid filled square enclosure in presence of an external transverse magnetic field

Mohammad Nasim Hasan[1], Khondokar Samiuzzaman, S. M. Shavik, Sumon Saha, Md. Quamrul Islam

Department of Mechanical Engineering, Bangladesh University of Engineering and Technology, Dhaka-1000, Bangladesh.

Abstract

Steady, laminar and two-dimensional natural convection inside a square enclosure filled with Cu-water nanofluid in presence of an external transverse magnetic field has been investigated in the present study. The two-dimensional square enclosure under consideration is selected with adiabatic top and bottom walls, while the left and the right vertical walls are maintained at constant high and low temperature, respectively. The Galerkin Finite Element method has been adopted to solve the non-dimensional governing equations (continuity, momentum and energy) of the problem and the effect of various governing parameters, namely, Raleigh number ($10^3 \leq Ra \leq 10^7$), Hartmann number ($0 \leq Ha \leq 60$) and solid-volume fraction of the nanoparticles ($0 \leq \varphi \leq 0.2$) on the heat transfer process inside the enclosure are examined. Results obtained from the present simulation are presented in terms of streamline and isotherm contours inside the enclosure. The average Nusselt number over the hot left wall of the enclosure is evaluated in order to assess the performance of the natural convection heat transfer. The present study shows that in presence of an external transverse magnetic field, addition of nanoparticle to the base fluid does not necessarily enhance the heat transfer rather it depends on both the Richardson number and Hartmann number.
(ICTE 2014).

Keywords: Nanofluids; Natural Convection Heat Transfer; Transverse Magnetic Field, Hartmann Number, Finite Element Method

Nomenclature

C_p	specific heat, $Jkg^{-1}k^{-1}$	*Greek Symbols*	
k	thermal conductivity, $Wm^{-1}k^{-1}$	β	thermal expansion co-efficient, K^-
L	side of the square cavity, m	θ	non-dimensional temperature
T	temperature, K	μ	dynamic viscosity, Pa.s
p	dimensional pressure, Pa	ψ	Streamfunction
P	non- dimensional pressure	α	thermal diffusivity, m^2s^{-1}
u, v	dimensional velocity components, ms^{-1}	ρ	density, kgm^{-3}
U, V	non-dimensional velocity components	φ	soid-volume fraction of nanoparticles
x, y	dimensional Cartesian coordinate	*Subscripts*	
X, Y	non dimensional coordinates	f	basefluid
B_0	magnetic field strength	nf	nanofluid

* Corresponding author. Tel.: +88-02-9665636; fax: +88-02-9665636

E-mail address: nasim@me.buet.ac.bd

Ha	Hartmann number	*c*	cold
Pr	Prandtl number	*h*	hot
Ra	Rayleigh number	*s*	solid particles
Nu	Nusselt number	*avg*	Average value

1. Introduction

The problem of natural convection in square enclosures has many engineering applications such as the cooling systems of electronic components, thermal insulation systems, solar collectors, nuclear reactor systems [1].
In some of the practical cases like in crystal growth in fluids, metal casting, fusion reactors natural convection occurs under the influence of an external magnetic field [2]. Convection heat transfer in the presence of a uniform magnetic field often known as MHD (magneto-hydrodynamic) convection has been studied extensively in the recent years. Sivasankaran and Ho [3] numerically investigated the effects of variable fluid properties on MHD convection of cold water in a square cavity. They found that the average Nusselt number decreases with an increase of the Hartmann number. Sivasankaran et al. [4] numerically examined the MHD convection of cold water near its density maximum in an open cavity with variable fluid properties. They observed that convection heat transfer is enhanced by thermo-capillary force when buoyancy force is weakened. The steady and laminar natural convection flow in the existence of a magnetic field is also examined by Ece and Buyuk [5]. They found that the applied magnetic field suppressed the convective flow and its direction also influenced the flow pattern. Similar results are also reported by Kahveci and Oztuna [7] for the natural convection flow inside a laterally heated partitioned enclosure. Sathiyamoorthy and Chamkha [6] used different thermal boundary conditions to examine the steady laminar two-dimensional natural convection in presence of inclined magnetic field in a square enclosure filled with a liquid gallium. These investigations in fact reveal that a heat transfer improvement method is needful for natural convection in presence of magnetic field. Addition of nano particle to a fluid may be a good solution in these cases and hence study of MHD convection with nanofluid has become one of the frontier topics in current heat transfer research [8-9].

In the present study, parametric investigations are carried out in order to examine the effect of an external transverse magnetic field on the natural convection inside a square enclosure filled with Cu-waternanofluid. The non-dimensional governing equations describing the problem are formulated and then numerically solved by using Galerkin finite element method. The results obtained in the present study are first validated with previous numerical results and the developed model is then applied to investigate the effects of various governing parameters (such as Raleigh number, Hartman number and solid volume fraction of the nano particle) on the flow and thermal field inside the enclosure.

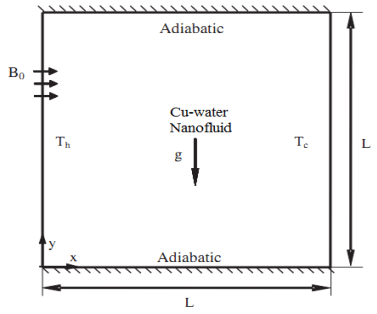

Fig. 1. Physical model and co-ordinate system

2. Mathematical Formulation

Figure 1 depicts the configuration of the two-dimensional square enclosure. The left and right vertical walls of the enclosure are considered to be at constant high and low temperature, respectively while the top and the bottom walls are assumed to be thermally adiabatic. A uniform magnetic field of constant magnitude, B_0 is applied in the direction of x-direction. It is assumed that the induced magnetic field produced by the motion of the electrically

conducting fluid is negligible compared to the applied magnetic field. It is also assumed that the nanofluid inside the cavity is sufficiently dilute such that it is considered incompressible, Newtonian and the flow to be laminar. The Boussinesq approximation is adopted to account for the variations of temperature as a function of density and to couple the temperature field to the flow field. Neglecting the viscous dissipation and the Joule heating effect, the non-dimensional conservation equations of mass, momentum and energy of a 2D enclosure can be given as:

$$\frac{\partial U}{\partial X}+\frac{\partial V}{\partial Y}=0 \tag{1}$$

$$U\frac{\partial U}{\partial X}+V\frac{\partial U}{\partial Y}=-\frac{\partial P}{\partial X}+\frac{\mu_{nf}}{\rho_{nf}\alpha_f}\left(\frac{\partial^2 U}{\partial X^2}+\frac{\partial^2 U}{\partial Y^2}\right) \tag{2}$$

$$U\frac{\partial V}{\partial X}+V\frac{\partial V}{\partial Y}=-\frac{\partial P}{\partial Y}+\frac{\mu_{nf}}{\rho_{nf}\alpha_f}\left(\frac{\partial^2 V}{\partial X^2}+\frac{\partial^2 V}{\partial Y^2}\right)+\frac{(\rho\beta)_{nf}}{\rho_{nf}\beta_f}Ra*\Pr*\theta-Ha^2*\Pr*V \tag{3}$$

$$U\frac{\partial \theta}{\partial X}+V\frac{\partial \theta}{\partial Y}=\frac{\alpha_{nf}}{\alpha_f}\left(\frac{\partial^2 \theta}{\partial X^2}+\frac{\partial^2 \theta}{\partial Y^2}\right) \tag{4}$$

Various non-dimensional parameters that appear in these above equations are defined as follows:

$$X=\frac{x}{L},Y=\frac{y}{L},\mathrm{U}=\frac{uL}{\alpha_f},V=\frac{vL}{\alpha_f},\theta=\frac{T-T_c}{T_h-T_c},P=\frac{pL^2}{\rho_{nf}\alpha_f^2}.\qquad \mathrm{Ra}=\frac{g\beta_f(T_h-T_c)\mathrm{L}^3}{\nu_f\alpha_f},Ha=B_0L\sqrt{\frac{\sigma_{nf}}{\rho_{nf}\nu_{nf}}},Pr=\frac{\nu_f}{\alpha_f} \tag{5}$$

In Eqs.2-4, the density, specific heat and thermal expansion coefficient of nanofluid are defined based on the properties of the base fluid and nano particle as well as the volume fraction of the nano particle (φ) defined as:

$$\rho_{nf}=(1-\varphi)\rho_f+\varphi\rho_s \tag{6}$$

$$(\rho C_p)_{nf}=(1-\varphi)(\rho C_p)_f+\varphi(\rho C_p)_s \tag{7}$$

$$(\rho\beta)_{nf}=(1-\varphi)(\rho\beta)_f+\varphi(\rho\beta)_s \tag{8}$$

Moreover, dynamic viscosity μ_{nf} and effective thermal conductivity of the nanofluid and can be determined as:

$$\mu_{nf}=\frac{\mu_f}{(1-\varphi)^{2.5}};\qquad k_{nf}=k_f\left(\frac{k_s+2k_f-2\varphi(k_f-k_s)}{k_s+2k_f+\varphi(k_f-k_s)}\right) \tag{9}$$

The boundary conditions of the present problem are specified as:

Horizontal walls: $\frac{d\theta}{dX}=0,U=0,V=0$ *Left wall:* $\theta=1,U=V=0$ *Right wall:* $\theta=0,U=V=0$

Finally, the average Nusselt number over the hot left wall of the enclosure may be determined as:

$$Nu=\int_0^1\left(-\frac{k_{nf}}{k_f}\right)\frac{\partial\theta}{\partial X}dY \tag{10}$$

Various thermo-physical properties of base fluid and nano particles used in the present study tabulated in Table 1.

Table 1. Thermo-physical properties of base fluid and nano particles [8]

Properties	Pure Water	Cu
C_p (Jkg $^{-1}$ K $^{-1}$)	4179	385
k (Wm $^{-1}$K $^{-1}$)	0.613	401
ρ (kgm $^{-3}$)	997.1	8933
β (K^{-1})	21×10 ^{5}	1.67×10 ^{5}
μ (Pa.s)	9.09×10^{-4}	--

3. Numerical Procedure

The numerical procedure used to solve the governing equations of the present problem is the finite element method. It provides the smooth solutions at the interior domain including the corner regions. The non-linear parametric solution method has been chosen to solve the governing equations. This approach will result in substantially fast convergence assurance. A non-uniform triangular mesh arrangement is implemented in the present investigation especially near the heated wall to capture the rapid changes in the dependent variables. As the dependent variables vary greatly in magnitude, manual scaling of the dependent variables is used to improve numerical convergence. The manual scaling values are kept constant and selected in such a way that the magnitudes of the scaled degrees of freedom become one.

3.1. Grid sensitivity test

Test for the accuracy of grid sensitivity is examined for the arrangements of five different number of elements shown in the table. The test was conducted for the model with $\varphi = 0.1$, $Ra = 10^7$ and $Ha = 15$. From Table 2 it is observed that 3520 elements are sufficient enough to produce accurate result.

Table 2. Grid sensitivity test

Number of elements	Nu_{avg}
850	21.0517
1610	19.3259
2328	19.0864
3520	19.0586
4480	19.0439

3.2. Code Validation

Since the validation against experimental data is not possible in the present case, the computational code is validated with the results obtained for natural convection with a transverse magnetic field in a square enclosure as mentioned by Kefayati [9]. The comparison of the result is shown in Table 3 and it has been observed that the present numerical solution is almost in complete agreement with the aforementioned one in terms of the average Nusselt number. Therefore, it can be decided that the present code can be used to predict the flow and thermal field for the present problem accurately.

Table 3. Comparison of the present work and Kefayati [9] for different Ha numbers and at $Ra = 10^5$, $\varphi = 0$

	Nu	
Ha	Kefayati's work [9]	Present work
0	4.79	4.82
30	3.22	3.18
60	1.9	1.85
90	1.35	1.33

4. Result and Discussion

4.1 Effect of the Rayleigh number

Table 4 presents the effect of solid volume fraction (φ) on the average Nusselt number (Nu_{avg}) and the maximum stream function ($|\psi_{max}|$) at different values of Rayleigh number (Ra). The Hartman number is assumed to be constant at $Ha = 30$. For all values of solid volume fraction, the results show that Nu_{avg} and $|\psi_{max}|$ increase as the Ra number increases. This happens because strength of buoyancy-driven flow within the cavity for a fixed strength of magnetic field increases as the Rayleigh number increases. At lower Ra number the heat transfer is mainly dominated by

conduction process that results in lower values of Nu_{avg} and $|\psi_{max}|$. For these low values of Ra, the buoyant forces are weak and mainly diffusion governs the behavior of the fluid. But at higher Ra number (10^6, 10^7) the values of Nu_{avg} and $|\psi_{max}|$ are much higher as stronger convective flows govern the heat transfer process. The addition of nano particle has been found to weaken the flow strength for Ra = 10^3-10^5, while that results in stronger flow field for Ra = 10^6 and 10^7.

Table 4. Average Nusselt number and max. Stream functions at various *Ra* and φ (*Ha* = 30)

		φ = 0	φ = 0.1	φ = 0.2
Ra=10^3	Nu	1.002	1.332	1.746
	$\|\psi_{max}\|$	0.127	0.070	0.047
Ra=10^4	Nu	1.182	1.382	1.763
	$\|\psi_{max}\|$	0.191	0.069	0.470
Ra=10^5	Nu	3.137	2.834	2.708
	$\|\psi_{max}\|$	5.693	4.726	3.914
Ra=10^6	Nu	7.813	7.8678	7.884
	$\|\psi_{max}\|$	13.940	14.068	14.472
Ra=10^7	Nu	16.355	17.685	18.794
	$\|\psi_{max}\|$	29.900	31.840	33.950

As shown in Fig.2, it is very obvious that lower values of *Ra*, results in a conduction dominated convection heat transfer process in which the temperature gradient near the hot and cold wall is very small as indicated by almost straight parallel vertical isotherms. As Ra increases, convection mode of heat transfer becomes prominent and the isotherms near the hot and cold sidewalls gradually become higher.

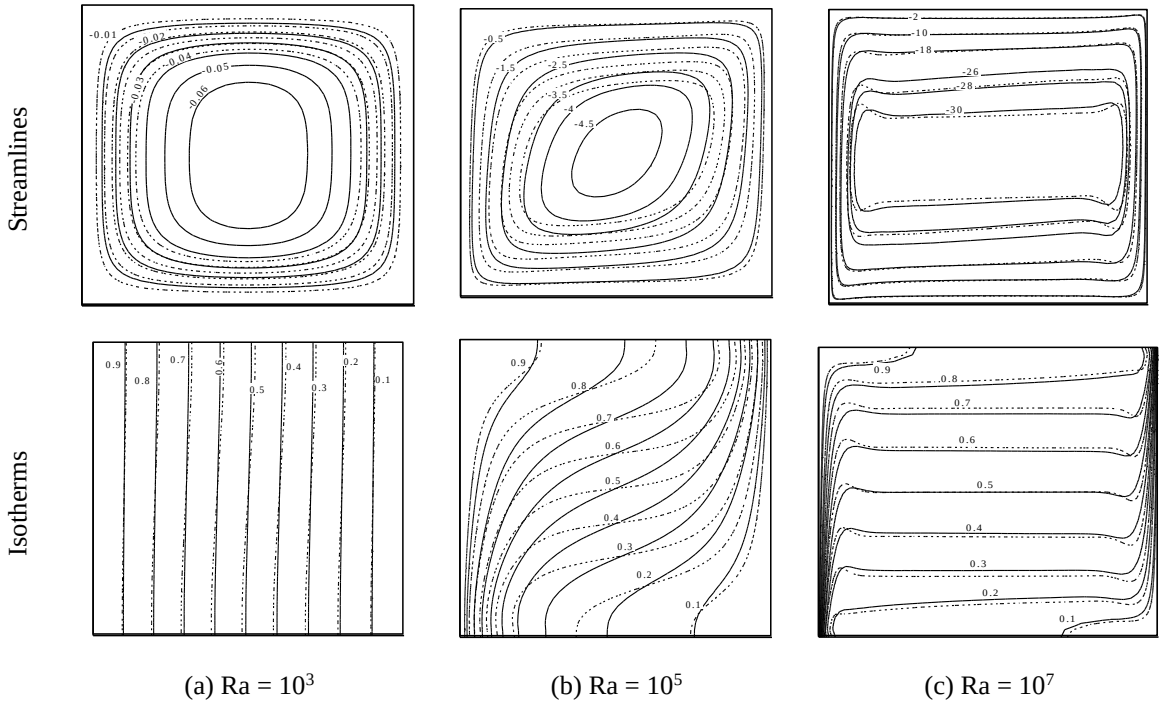

Fig. 2: Streamlines (ψ) and isotherms (θ) for base fluid (dashed line) and nanofluid (φ = 0.1)with *Ha* = 30

4.2 Effect of the Hartmann number

The distributions of streamlines and isotherms are also affected with the variation of the Hartmann number (*Ha*). If we focus the case of *Ra* =10^5 as shown in Fig. 3, it is clear that an increase in Hartmann number results in a weaker flow field with the isotherms being less distorted similar to a conduction dominated heat transfer process. It means the flow field becomes weak and the dominating heat transfer mode shifts from convection to conduction at higher Hartmann numbers. A look at Table 5 clearly reveal out these phenomena.

Table 5. Average Nusselt number and max. Stream functions at various *Ha* (*Ra* = 10^5)

		$\varphi = 0$	$\varphi = 0.1$	$\varphi = 0.2$
Ha = 0	Nu	4.720	5.222	5.633
	$\lvert\psi_{max}\rvert$	11.01	12.329	13.609
Ha = 15	Nu	4.126	4.182	4.201
	$\lvert\psi_{max}\rvert$	8.438	8.45	8.268
Ha = 30	Nu	3.137	2.834	2.708
	$\lvert\psi_{max}\rvert$	5.693	4.726	3.914
Ha = 45	Nu	2.360	2.052	2.095
	$\lvert\psi_{max}\rvert$	3.807	2.701	2.017
Ha = 60	Nu	1.844	1.677	1.886
	$\lvert\psi_{max}\rvert$	2.61	1.691	1.204

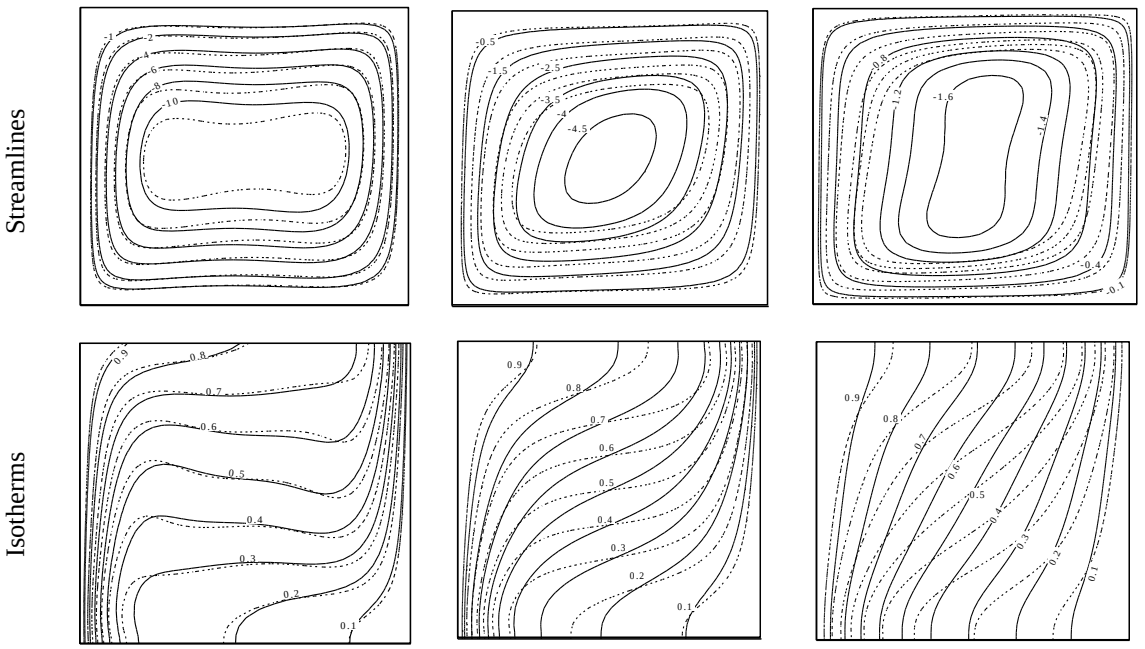

(a) Ha = 0 (b) Ha = 30 (c) Ha = 60

Fig. 3: Streamlines (ψ) and isotherms (θ) for base fluid (dashed line) and nanofluid (φ = 0.1)with *Ra* = 10^5

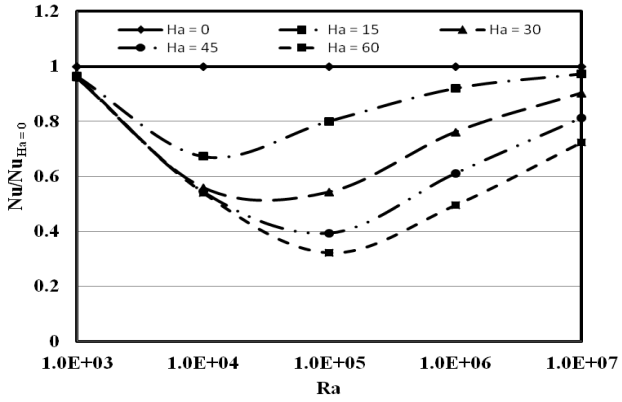

Fig 4: Variation of average Nusselt number ratio ($Nu_{avg}/Nu_{avg,\,Ha=0}$) with Hartman number ($\varphi = 0.1$)

Figure 4 shows the variation of $Nu_{avg}/\ Nu_{avg,Ha=0}$ with respect to the Rayleigh number at different values of the Hartmann number. The average Nusselt number ratio ($Nu_{avg}/Nu_{avg,\,Ha=0}$) shows that the effects of the magnetic field on the heat transfer performance of the enclosure. The average Nusselt number ratio at Ha = 0 is the reference value and the solid volume fraction is assumed to be constant at φ = 0.1. As shown in the Fig. 4, for a fixed value of the Ha, with the increase of the *Ra*, the Nusselt number ratio at first decreases with Ra and this trend of variation continues up to a critical value of *Ra* after which further increase in *Ra* results in an increase of the Nusselt number ratio. This critical value of the *Ra* has been found to depend on the strength of the applied magnetic field i.e. *Ha* number. For instance, at *Ha* = 15, the critical *Ra* number is found to be 10^4 while for the case *Ha* = 60, the critical *Ra* number is found to be 10^5. The trend of variation of the Nusselt number ratio with *Ra* for different Ha also points out the fact that, effect of the magnetic field is insignificant either at very lower values of *Ra* or at very higher values of *Ra*. However, at other values of *Ra*, the magnetic field suppresses the convection flows, therefore, the Hartmann number can be seen to have a significant effect on the average Nusselt number ratio.

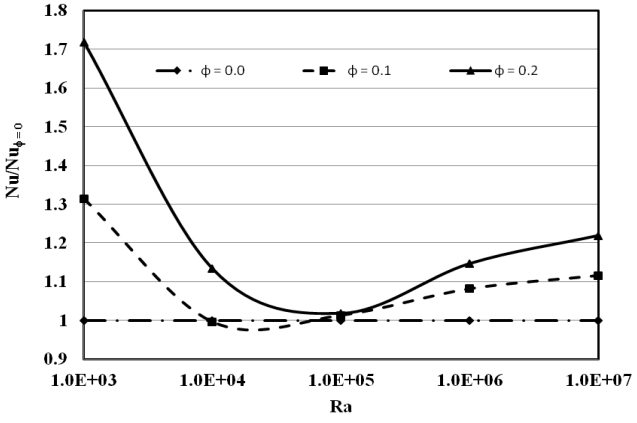

Fig. 5. Variation of average Nusselt number ratio with Raleigh number at different solid volume fraction (*Ha* = 30)

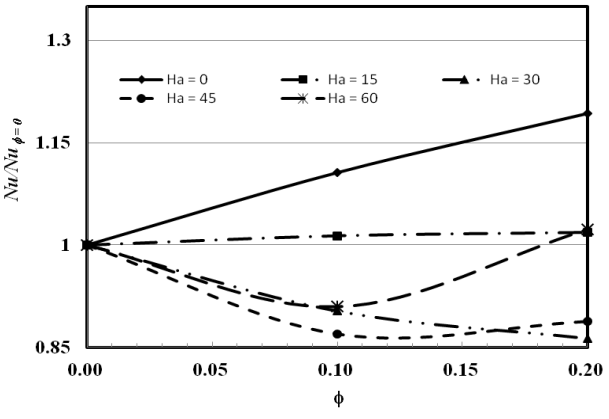

Fig. 6. Variation of average Nusselt number ratio with Hartmann number at different solid volume fraction ($Ra = 10^5$)

4.3 Effect of the nano-particle volume fraction

Fig. 5 depicts the variations in the average Nusselt number ratio ($Nu_{avg}/Nu_{avg,\,\varphi=0}$) with the Rayleigh number at different values of the solid volume fraction. The average Nusselt number ratio at $\varphi = 0$ is the reference value and the Hartmann number is assumed to be constant (*Ha* = 30) for this part of the study. The results show that for the

nanofluid, which is influenced by a magnetic field, there is a critical Rayleigh number (for this case, $Ra = 10^5$) that minimizes the average Nusselt number ratio regardless of the value of the solid volume fraction. For Rayleigh number higher than this critical value, addition of nanoparticle results in an increase in heat transfer rate. However, the effect of nano particle volume fraction on the Nusselt number ratio has been found to deem at higher values of Ra regardless of the magnitude of φ.

Fig. 6 represents the variations of the average Nusselt number ratio ($Nu_{avg}/Nu_{avg,\ \varphi=0}$) with the solid volume fraction at different Hartmann numbers. The results, as presented here for $Ra = 10^5$, show that for Ha = 0, addition of nano particle results in increased heat transfer while for Ha = 15, no significant enhancement of the heat transfer is obtained with the addition of nano particle. However, for Ha = 30, addition of nano particle results in lower heat transfer for all values of φ. For Hartmann number, Ha = 45 and 60, the average Nusselt number ratio has been found to decrease with the solid volume fraction initially and then starts increasing. This behaviour might be due to the greater effect of the magnetic field and the stronger suppression of the buoyancy-driven flows of the nanofluid at higher densities of the solid nanoparticles in the nanofluid.

5. Conclusion

Finite element based simulations on natural convection characteristics inside a square enclosure filled with Cu-water nanofluid have been performed to understand the effect of an external transverse magnetic field. The effects of various parameters such as the Rayleigh number, the solid volume fraction and the Hartmann number on the flow and temperature fields as well as the heat transfer rate have been examined. The present study led to the following conclusions.

i. The heat transfer mechanism and the flow characteristics inside the enclosure greatly depend greatly upon both the strength of the applied magnetic field strength and the Rayleigh number.
ii. As the strength of external magnetic field increases, the heat transfer inside the enclosure decreases for any values of the Rayleigh number.
iii. The effect of magnetic field becomes prominent for the intermediate values of Rayleigh numbers. For very low or for very high Rayleigh number, effect of external magnetic field becomes insignificant.
iv. In presence of external magnetic field, addition of nanopaticle does not always contribute to higher heat transfer. Rather it depends both on the Rayleigh number and Hartmann number.

References

[1] S. Ostrach, Natural convection in enclosures, Journal of Heat Transfer 110 (1988) 1175-1190.
[2] M. Moreau, Magnetohydrodynamics. Kluwer Acadamic Publishers, The Netherlands, 1990.
[3] S. Sivasankaran, C.J. Ho, Effect of temperature dependent properties on MHD convection of water near its density maximum in a square cavity, Int. J. Thermal Sciences 47 (2008) 1184–1194.
[4] S. Sivasankaran, M. Bhuvaneswari, Y.J. Kim, C.J. Ho, K.L. Pan, Numerical study on magneto-convection of cold water in an open cavity with variable fluid properties, Int. J. Heat Fluid Flow 32 (2011) 932–942.
[5] Ece, M. C. and Büyük, E., Natural-convection flow under a magnetic field in an inclined rectangular enclosure heated and cooled on adjacent walls, Fluid Dynamics Research, 38 (2006) 564-590.
[6] M. Sathiyamoorthy, A. Chamkha, Effect of magnetic field on natural convection flow in a liquid gallium filled square cavity for linearly heated side wall(s), International Journal of Thermal Sciences 49 (2010) 1856-1865.
[7] K. Kahveci, S. Oztuna, MHD natural convection flow and heat transfer in a laterally heated partitioned enclosure, European Journal of Mechanics Fluids 28 (2009) 744-752.
[8] SM Aminossadati and B Ghasemi. Natural convection cooling of a localised heat source at the bottom of a nanofluid-filled enclosure, European Journal of Mechanics-B/Fluids 28 (2009) 630–640.
[9] G. R. Kefayati., Lattice Boltzmann simulation of natural convection innanofluid-filled 2D long enclosures at presence of magnetic field, Theoretical and Computational Fluid Dynamics 27 (2013) 865-883.

6th BSME International Conference on Thermal Engineering (ICTE 2014)

A Simulant Method to Analyze the Effects of Different Add-on Devices on Vehicle's Aerodynamics

Tawsif Ahmed

Department of Mechanical Engineering, Bangladesh University of Engineering and Technology (BUET), Dhaka, Bangladesh.

Abstract

At the recent time people's increasing need for speed along with fuel crisis has created an interest for vehicle aerodynamics among automotive engineers. The redesign of car frames and bodies to reduce the total weight, and the modification of car bodies to improve the overall aerodynamic characteristics for improved cruising conditions, reliability of navigation and lower energy consumption have become the major concern for today's automotive engineers. This simple work aims to obtain the flow structure around a passenger car with different add-on devices using the Computational Fluid Dynamics (CFD). A model of general passenger car was developed using SolidWorks and the simulation has been performed in ANSYS Fluent for the evaluation of drag coefficient and lift coefficient. Result shows that the addition of those add-on devices are reducing both drag and lift coefficient reasonably. Hence, the drag and lift force on a car can be reduced by using proper add-on devices on vehicle and thus fuel economy, traction and stability of a passenger car can be improved significantly.
(ICTE 2014).

Keywords: Drag, lift, aerodynamics; fuel economy; add-on devices; CFD; traction; simulation;

1 Introduction

1.1 Overview

Recent hike in energy cost and demand along with people increasing thrust for speed around the globe has led to a renewed interest in vehicle's aerodynamics. In this paper we have basically focused on the lift and drag coefficient. Drag force is a resistive force which increases fuel consumption. On the other hand due to high lift force the car loses its traction. So only a perfectly shaped car body which has both low drag and lift coefficient can ensure reliability of navigation and fuel economy.

1.2 Objectives

In general, add-on devices are usually installed on cars to reduce the lift and improve traction leading to stability and smoother control. However, the aerodynamics performance corresponding to the add-on devices could deteriorate severely. For this reason, this work aims to analyze the effect of different add-on devices on a general passenger car by analyzing the drag coefficient, lift coefficient, turbulent intensity etc. Thereafter, the installation of add-on devices that leads to lower aerodynamic drag will be carefully evaluated.

* Corresponding author.
E-mail address: tawsif.ahmed.buet@gmail.com

2 Methodology

Aerodynamic evaluation of airflow over an object can be easily done using analytical method or CFD approach. Analytical method can be done when the flow is laminar but if air flow gets turbulent then it becomes impossible to solve Navier-Stokes and continuity equations analytically. In the present work the k-ε turbulence model with non-equilibrium wall function has been used to analyze the flow over the passenger car model. This k-ε turbulence model is very robust, having reasonable computational turnaround time, and widely used by the auto industry.

3 Steps for simulation

- Design a basic car model in SolidWorks with proper dimensions and import it in ANSYS workbench.
- Create the wind tunnel and generate mesh using ANSYS mesh solver for simulation.
- CFD solver setup: apply all the boundary conditions.
- Simulate and test the basic car model for drag coefficient and lift coefficient.
- Then simulate and test the car with vortex generators (VGs), spoiler; tail plates and with both spoiler and VGs.
- Analyze the effect of add-on devices on the car.

4 Simulation of basic car model for drag coefficient and lift coefficient

4.1 Design of Basic Car Model

Fig.1 shows the basic model of the general passenger car used for the CFD simulation is a 1:100 scale model has been designed in SolidWorks. To analyze the effect of air flow an air domain is necessary which will work as a theoretical wind tunnel. The general concept is that the domain should be 8 to 10 times larger in the front , 5 to 7 times larger in the back side and 3 to 5 times larger in the top and left or right side of the car than the its length. To include the effect of road in analysis the length of domain in bottom has kept small similar to the road clearance (i.e., 12in). The dimensions of the car and air domain has been given in Table 1.

Table 1. Dimensions of basic car model and theoretical wind tunnel.

Basic car model		Theoretical wind tunnel or air domain	
Length	36mm	Length	550mm
Width	17mm	Width	200mm
Height	11mm	Height	103mm
Plane of Symmetry	xy-plane	Ground Clearance	3mm

4.2 Meshing of Basic Car Model

The meshing of the car along with the wind tunnel which was performed in the ANSYS Fluent mesh solver has been shown in Fig.2. A tetrahedrons type meshing was generated throughout the whole air domain. A surface mesh sizing of 0.5 mm was created on the vehicle surface. A body mesh of 1mm size was also applied throughout 65x18x12 mm^3 volume around the car. All meshing parameters has been shown in Table 2.

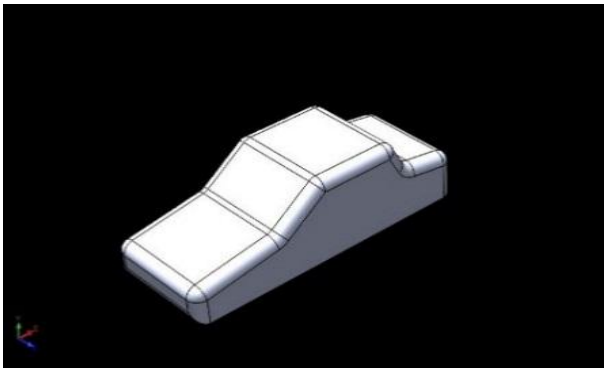

Fig.1. Basic car model.

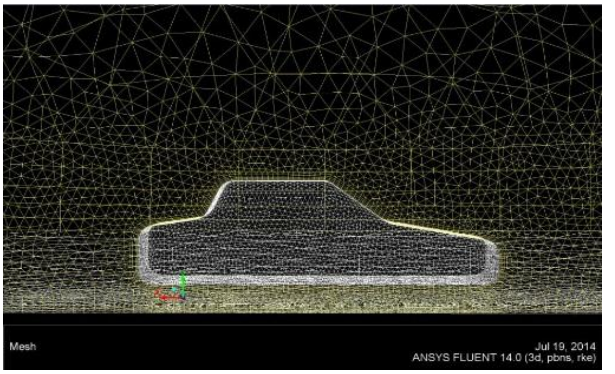

Fig.2. Meshing of the basic model.

Table 2. Global and face sizing for meshing.

Defaults	Physics preference	CFD
	Solver preference	Fluent
	Relevance	100
Sizing	Use advanced size function	Proximity and Curvature
	Relevance Center	Medium
	Initial size seed	Active assembly
	Smoothing	High
	Translation	Slow
	Span angle center	Fine
	Curvature normal angle	12^0
	Proximity accuracy	0.5
	Number of cell across gap	5
	Min size	0.5mm
	Proximity min size	0.5mm
	Max face size	40mm
	Max size	50mm
	Growth rate	1.2
Inflation	Use automatic inflation	Program controlled
	Inflation Option	First aspect ratio
	First aspect ratio	5
	Maximum Layers	5
	Growth rate	1.2
Face sizing	Type	Element size
	Element size	0.5mm
	Behavior	Soft

4.3 CFD Solver Setup for Basic Car Model

The CFD simulation done by Ram Bansal and R. B. Sharma [1] has been reproduced in this paper to analyze the effect of different add-ons on general passenger car. Tables 3 shows the solver setup, boundary condition settings, viscous model, solution method and solution controls for present simulation, respectively.

Table 3. Problem setup for CFD solver.

General	Solver	Type	Pressure-based
		Velocity Formulation	Absolute
		Time	Steady
Models	Viscous laminar	Model	Viscous k-epsilon (2 eqn)
		k-epsilon model	Realizable
		Near wall treatment	Non-equilibrium wall function
		Other parameters	Default
Boundary conditions	Velocity inlet	Velocity specification method	Component
		X-velocity	5 m/s
		Turbulence specification model	Intensity and viscosity ratio
		Turbulent intensity	1%
		Turbulent viscosity ratio	10%
		Backflow direction	Normal to boundary
		Turbulence specification model	Intensity and viscosity ratio
		Backflow turbulent intensity	5%
		Backflow turbulent viscosity ratio	10%
Reference values		Compute from	Velocity inlet
		Area	7.6542×10^{-5} m^2
		Density	1.225 kg/m^3
		Viscosity	1.7894×10^{-5} kg/m.s
		Reference zone	air
Solution method	Pressure velocity coupling	Scheme	coupled
	Special discretization	Gradient	Least square cell based
		Pressure	Standard
		Momentum	Second order upwind
		Turbulent kinetic energy	Second order upwind
		Turbulent dissipation rate	Second order upwind

	Flow courant number	50
Solution control	Momentum relaxation factor	0.25
	Pressure relaxation factor	0.25
	Turbulent viscosity	0.95

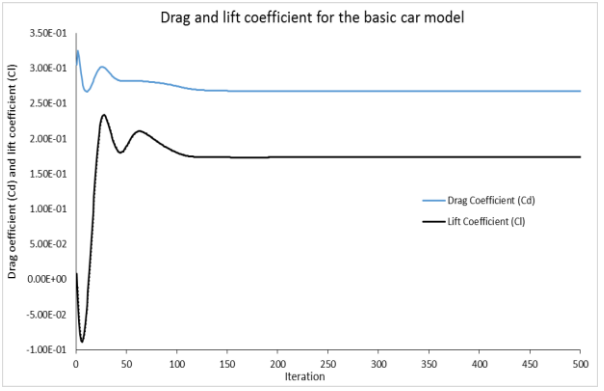

Fig.3. Drag coefficient for the basic model.

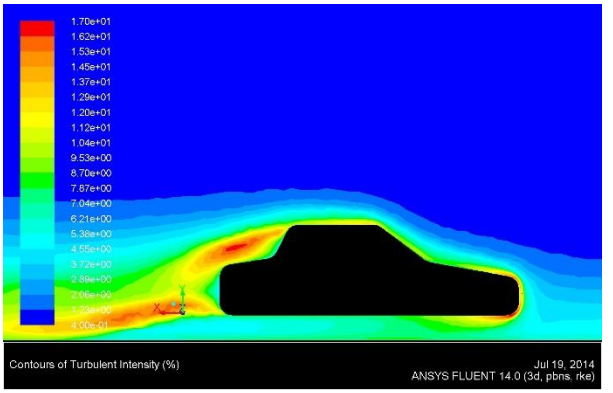

Fig.4. Turbulent intensity for the basic model.

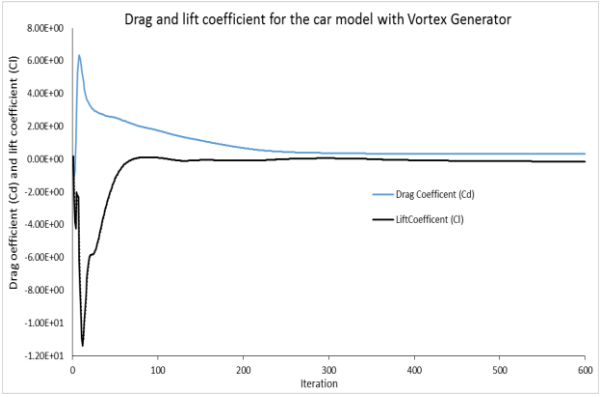

Fig.5. Drag coefficient for car with VGs.

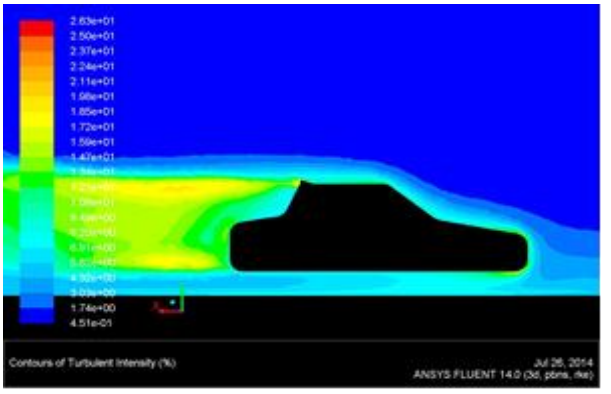

Fig.6. Turbulent intensity for the car with VGs.

4.4 Simulation of Basic Car Mode

Fig.3 shows drag coefficient and lift coefficient acting on the basic car body. From those graph we get that the coefficient of drag is 0.267146, coefficient of lift is 0.173601. Fig.4 shows that how turbulent intensity changes around the car on the symmetry plane or xy-plane.

5 Simulation of car model with vortex generators for drag coefficient and lift coefficient

After completing the simulation of basic car model it has been added with vortex generators (VGs) to study the effect VGs on the lift and drag coefficient. CFD simulations has been performed on the modified models to examine changes. Fig.5 shows drag and lift coefficient acting on the basic car body and Fig.6 shows that how turbulent intensity changes around the car on the symmetry plane or xy-plane. From those graph we get that the coefficient of drag is 0.306942 and coefficient of lift is -0.148453. It is clear that lift and turbulent intensity have been decreased but drag has been increased by adding VGs. So it seems that VGs reduces lift but cannot reduce drag.

6 Simulation of model car with spoiler for drag coefficient and lift coefficient

A Spoiler, 11 mm long and 2.5 mm wide has been attached to the boot of the car at an inclination angle of 10^0. It is expected that the spoiler will delay the separation of flow that normally occurs at the rear edge of the boot. To examine changes simulations has been performed using the same CFD solver and meshing setup as the previous one. Fig.9 shows drag and lift coefficient acting on the car. From this graph we get that the coefficient of drag is 0.252126

and coefficient of lift is 0.0423661. It is clear that both lift and drag has been decreased by adding spoiler. From Fig.10 it seems that by adding spoiler turbulence has been decreased considerably at the back end. So it supposes that spoiler can reduce both lift and drag.

7 Simulation of model car with tail plates for drag coefficient and lift coefficient

In order to decrease the velocity of airflow from the underbody to the rear of the vehicle, a diffuser type tail plate was mounted at the rear of the vehicle. A 0.75 mm long plate was attached to the floor of the vehicle and a 1.5 mm long plate was attached to the top outer edge of the roof at 15^0 inclination angle. CFD simulations has been performed on the modified models to examine changes using the same CFD solver and meshing setup as the previous one. Fig.7 shows drag and lift coefficient acting on the basic car body. From those graph we get that the coefficient of drag is 0.342146 and coefficient of lift is 0.248552. It is clear that both lift and drag has been increased tremendously by adding tail plates. But Fig.8 shows that how turbulent intensity decreases considerably around the car on the symmetry plane. It seems that using tail plates with car may be a good choice.

8 Simulation of model car with spoiler and vortex generators for drag coefficient and lift coefficient

In order to decrease the drag and lift on the car a combination of spoiler and VGs has been applied on the car surface and studied in ANSYS. Fig.11 shows drag and lift coefficient acting on the car body respectively. From those graph we get that the coefficient of drag is 0.242355 and coefficient of lift is -0.0633009. It is clear that both lift and drag has been decreased tremendously by adding spoiler and VGs together. Fig.12 also shows that by adding spoiler turbulence has been decreased considerably at the back end. It seems that spoiler and VGs together can reduce both lift and drag considerably.

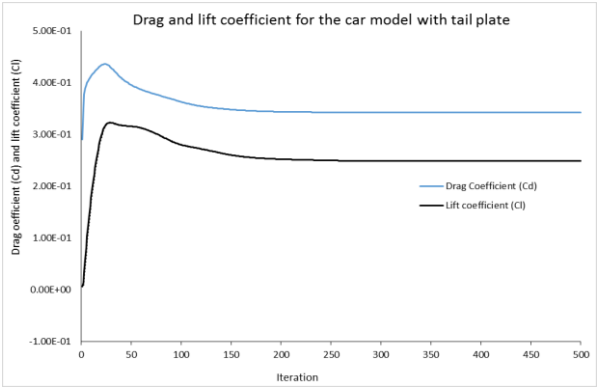

Fig.7. Drag coefficient for car with tail plate.

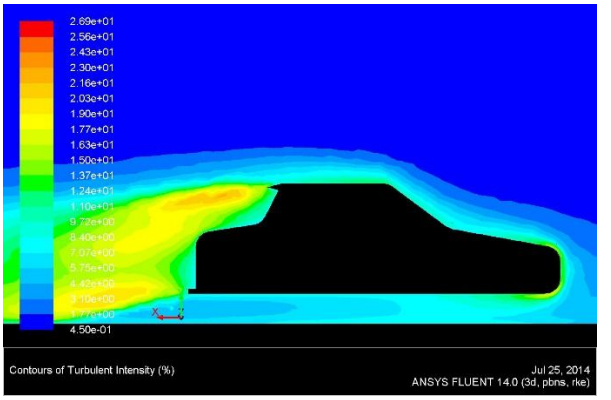

Fig.8. Turbulent intensity for car with tail plate.

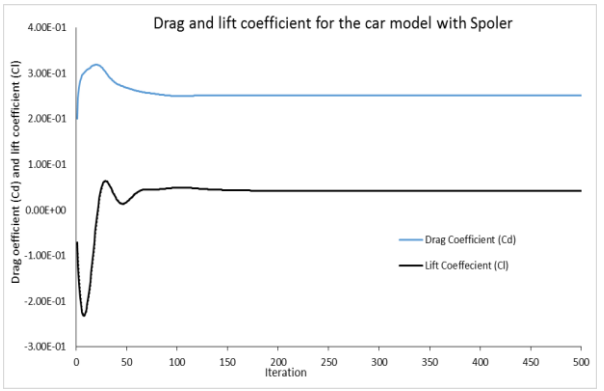

Fig.9. Drag coefficient for car with spoiler.

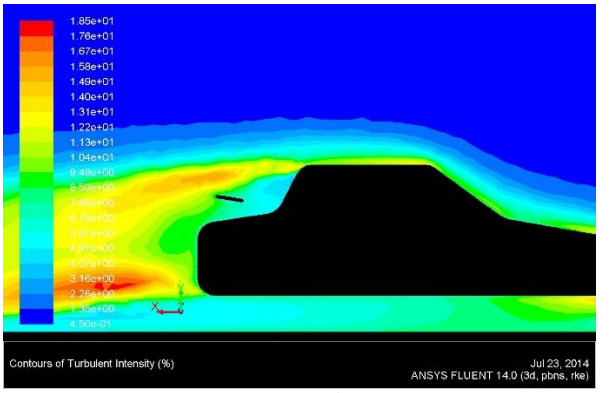

Fig.10. Turbulent intensity for car with spoiler.

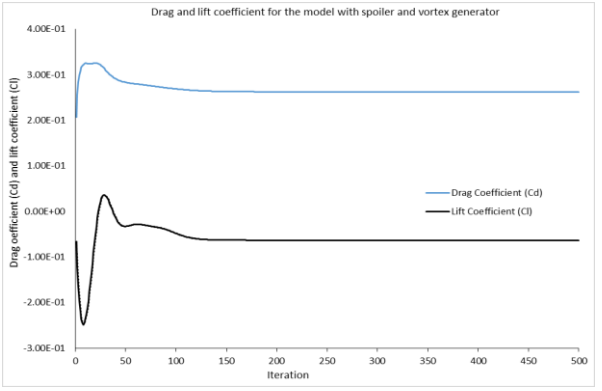

Fig.11. Drag coefficient for car with Spoiler and VGs.

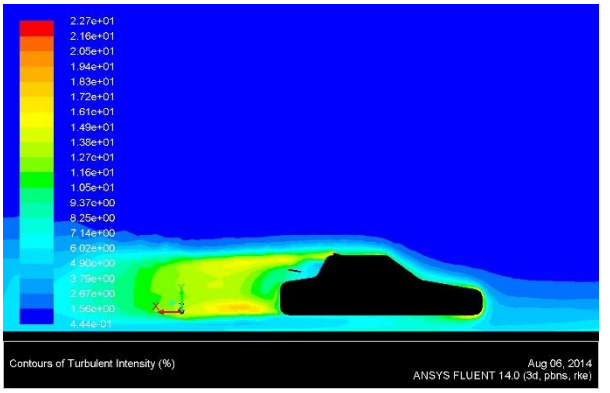

Fig.12. Turbulent intensity for car with Spoiler and VGs.

9 Results

In the above analysis there are different types of aerodynamic add-on devices used on the basic car model to study the effect of add-on devices on the coefficient of drag and coefficient of lift. The comparative results between the basic car and car with various add-on devices have been shown in Table 4.

Table 4. Lift and drag coefficient for all add-ons.

Configurations	Drag Coefficient (C_d)	% change in C_d	Lift Coefficient (C_l)	% change in C_l
Basic car model	0.267146	0	0.173601	0
Along with vortex generators (VGs)	0.306942	14.897	-0.148453	-185.341
Along with spoiler	0.252126	-5.622	0.042366	-75.595
Along with tail plate	0.342146	28.075	0.248552	43.174
Along with spoiler and VGs	0.242355	-1.793	-0.063301	-136.463

From the above analysis, it is found that spoiler with VGs is more effective add-on device to reduce the drag coefficient, lift coefficient and moment which are applied on the passenger car when the car is running on the road. The drag coefficients and drag forces are proportional to each other so when the drag forces are reduced, lift forces are also reduced because it is proportional to the lift coefficient.

10 Conclusion

Computational fluid dynamics (CFD) simulations of the steady flow field around passenger car models with and without add-on devices both were presented comparing the simulated data to each other. The ANSYS Fluent with the analyses during CFD approach. The objective is to reduce aerodynamic drag acting on the vehicle and thus improve the fuel efficiency of passenger car. Hence, the drag force can be reduced by using add-on devices on vehicle and fuel economy, and stability of a passenger car can be improved.

References

[1] Ram Bansal and R. B. Sharma, "Drag Reduction of Passenger Car Using Add-On Devices", Journal of Aerodynamics, Volume 2014, Article ID 678518,13 pages, Hindawi Publishing Corporation, Received 12 July 2013; Revised 15 December 2013; Accepted 15 December 2013; Published 23 March 2014.

[2] J.R.CallisterandA.R.George,"Windnoise,"inAerodynamics of Road Vehicles, W. H. Hucho, Ed., SAE International, Warrendale, Pa, USA, 1998.

[3] F. R. Bailey and H. D. Simon, "Future directions in computing and CFD," AIAA Paper 92-2734, 1992.

[4] Fluent6.1User'sGuide, Fluent, Lebanon, NH, USA, 2003.

[5] TGrid 3.4 User's Guide, Fluent, Lebanon, NH, USA, 2001.

[6] Z. Yang and B. Khalighi, "CFD simulation for flow over pickup trucks," SAE Paper 2005-01-0547, 2005.

6th BSME International Conference on Thermal Engineering (ICTE 2014)

Numerical Study of the Performance of Three and Four Bladed Savonius Wind Turbine

Md. Azimur Rahman[1], Wasi Uddin Ahmed[2], Muhammad Junayed Hasan Zahed[3], Dr Mohammad Mamun[4]
Bangladesh University of Engineering & Technology
Dhaka 1000, Bangladesh

Abstract

The aim of this paper is to present a numerical study of three and four bladed Savoius rotor with different overlap ratios. The models with 0%, 20%, and 30% overlap having the same blade diameter and height are used for the comparison. The CFD simulations were first used to validate with the experimental results. Then the same procedure was repeated to find the static torque characteristics, power coefficients and the flow field around the rotor blades to analyse the aerodynamic performance of the rotor. The dimensionless parameter torque coefficient of the wind turbine as a function of the wind velocity and the rotor's angle of rotation and power coefficient vs tip speed ratio was plotted to compare between models. The pressure contour and velocity contour were used to analyse the flow field around the rotor. In this analysis authors have found that the torque co-efficient of the rotors decreases with the increase in blade number and with the increase in blade overlap ratio the negative torque co-efficient is reduced.

Keywords: Savonius;Wind Turbine; VAWT; CFD; FLUENT

Introduction

Proper utilization renewable energy is one of the most important issues to solve the energy shortage and to control environmental pollution as the growing use of fossil fuel is leading ourselves to rapid climate change and global warming. In spite of its rising cost and detrimental environmental effects fossil fuels are still considered as the major source of power generation which indicates global warming will be inevitable if alternate sources of energies are not prioritized. Green energy technologies like wind is the most appropriate solution to this problem to meet the production and demand of electric energy on commercial and industrial applications, since it is a clean, economic and renewable energy source with a great availability in the environment. Wind turbines converts the kinetic energy available in the wind to produce electricity. It is classified into two broad classes Vertical Axis Wind Turbine (VAWT) and Horizontal Axis Wind Turbine (HAWT), former one being the most popular device for electricity generation for its higher efficiency due to high rotational speed. But the HAWTs require a more complicated structure than the VAWTs and are only feasible to the regions where permanent winds of high speeds are available. But in regions where the speed and direction of wind is continuously changing VAWTs provides a better utility. Unlike HAWTS, the VAWTS are characterized by their simplicity in construction, low rotational speed with a high torque and no effects of wind direction. Savonius Wind Turbine is the simplest form of VAWT originally invented by a Finish engineer Sigurd J. Savonius in 1922 [1]. Menet J. et al [2] performed a parametric investigation on the power coefficient of two-bucket Savonius rotor and found that the power coefficient can be significantly increased by selecting its important geometric parameters like height, diameter, overlap ratio, end plate dimensions etc. wind, thereby reducing the computational time and effort. Cochran et al. [3] numerically simulated the flow patterns

Md. Azimur Rahman Tel.: +8801676950334;
E-mail address: azimur.rahman.buet@gmail.com

around a two-bucket Savonius rotor of thirteen different configurations to optimize the blade configuration by using Reynolds-stress 5-equation turbulence model. They further concluded that 2D CFD simulation was sufficient as the blades rotate in the same plane as the approaching Numerical and experimental study of Savonius wind turbines both in static and dynamic conditions, can be found widely in literature. R. Gupta et al [4] also analysed the flow field around a three bladed Savonius wind turbine using k-ε turbulence model and found that overlap of 19.87% is the optimum overlap at which both pressure and velocity differences across the rotor are the highest for which high performance of three-bucket Savonius rotor can be expected at that overlap condition. Katsuya I. et al [5] simulated numerically the flow over a two-bucket Savonius rotor by solving 2D finite volume equations using an upwind scheme for unstructured mesh. Their results showed good matching with the experimental values of power coefficient, aerodynamic coefficients. Tong Zhou et al [6] did a 2D CFD simulation to analyse the detailed flow field and performance of a Savonius rotor

Nomenclature

A	Area
D	Rotor Diameter
d	Blade Diameter
H	Rotor Height
a	Overlap Ratio (OR)
V	Velocity`
N	RPM
λ	Tip Speed Ratio (TSR)
T	Torque
P	Power
Cq	Torque Coefficient
Cp	Power Coefficient
Re	Reynold's Number

using the commercial code Star-CCM+. They solved the unsteady Reynolds Averaged Navier-Stokes equations using the SIMPLE (Semi-Implicit Method for Pressure-Linked Equations) algorithm for pressure-velocity coupling and realizable k-ε model for turbulence modelling. They concluded that The Bach-type rotor have better performance than the conventional Savonius-type rotor. Khondoker Niaz Morshed et al [7] performed a numerical and experimental investigation on three bladed Savonius rotor with different overlap ratio. They solved the 2D Navier Stokes equations using SIMPLE algorithm and k-ε model for turbulence modelling using the commercial software Fluent. Their results showed the significant effect of overlap ratio and Reynold's number on the performance of Savonius rotor.

In this paper authors have compared the performance of two and three bladed Savonius Wind Turbine using CFD techniques. The results show the change in torque coefficient, power coefficient with the change in tip speed ratio and Reynolds number.

2. Rotor Models:

Three and Four bladed rotor models having overlap ratio of 0%, 10% and 20% were designed for the numerical study to observe the effect of blade numbers and overlap ratio on torque and power characteristics of the model.

Figure 1 shows the three bladed rotor models having blade diameter (d) of 100mm and three overlap ratios of 0%, 20% and 30%. Model 1(a), 1(b) and 1(c) have rotor diameter (D) of 200mm, 166mm and 154 mm respectively. All of the models have a height (H) of 300mm. Fig 2 shows the four bladed models with same overlap ratios, blade diameter and height as the previous model. Corresponding rotor diameters of Model 2(a), 2(b) and 2(c) being 200mm, 160mm and 146mm.

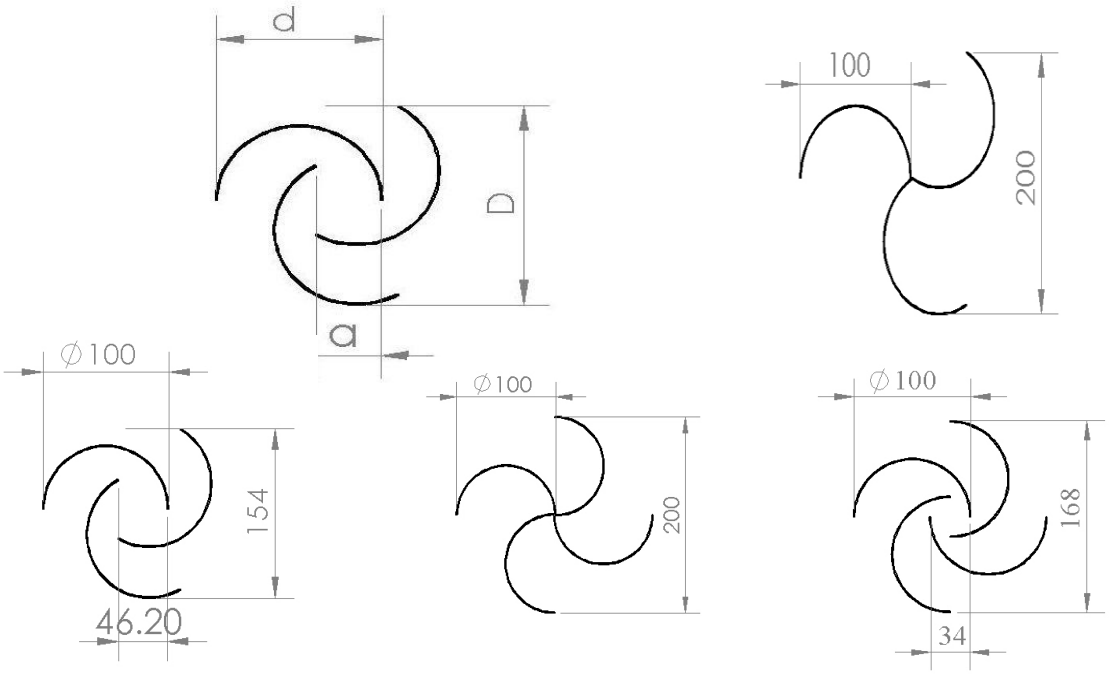

Fig 1. Rotor Models

3. Performance Parameters:

Performance parameters used in aerodynamics of wind turbines are in commonly found in dimensionless form. To compare between the models, the Torque coefficient, power coefficient and the tip speed ratio (TSR) are good indicators to rate the performance of a particular model which are calculated by the following equations

Torque Coefficient, $C_q = \frac{T}{\frac{1}{2}\rho A R V^2}$

Power Coefficient, $C_p = \frac{P_t}{\frac{1}{2}\rho V^3 A} = C_q \times \lambda$

TSR, $\lambda = \frac{\omega R}{V}$

Reynolds Number, $Re = \frac{\rho V D}{\mu}$

4. Numerical Procedure:

Since VAWTs are inherently a 2D device each one of the models was built in a 2D computational domain. Moving Reference Frame (MRF) technique was used in CFD analysis for solving the 2D incompressible Navier-Stokes equations. The size of the total computational domain was 7m in stream wise direction and 2.3m in perpendicular to stream direction. Total number of nodes was around 49415. The whole computational domain was discretized using the triangular unstructured mesh. ANSYS Mesh was used for the generation of mesh around the rotor models.A size function was introduced with the rotor blade to achieve better computational results adjacent to the blade surface. Edge sizing was done in two steps. First the span wise length of the blade was divided into 100 divisions. Then the interior fluid region was sized by controlling the size of the elements as 15mm, outer fluid region as 30 mm. These generated meshes were then exported in FLUENT for post processing. Figures 2 shows 2-D mesh generated within a

computational domain around the models of Savonius wind turbine using ANSYS Mesh .Commercially available software ANSYS FLUENT was used to solve the turbulent flow field. Numerical simulation provides the pressure and velocity values at all nodal points of flow domain around the rotating blades. The pressure-velocity coupling was achieved using the COUPLED algorithm. In order to achieve accurate results without excessive computational effort, the realizable k-ε turbulence model of second order upwind scheme was adopted. This model contains a new transport equation for the turbulent dissipation rate ε. Also, a critical coefficient of the model, Cm, is expressed as a function of mean flow and turbulence properties, rather than assumed to be constant as in the standard model. The realizable k-ε model is substantially better than the standard k-ε model for many applications. The transport equations for realizable k-ε model are

For turbulent kinetic energy k

$$\frac{\partial}{\partial t}(\rho k) + \frac{\partial}{\partial x_i}(\rho k u_i) = \frac{\partial}{\partial x_i}\left[\frac{\left(\mu + \frac{\mu_t}{\sigma_k}\right)\partial k}{\partial x_j}\right] + P_k + P_b - \rho\varepsilon - Y_M + S_k$$

For dissipation ε

$$\frac{\partial}{\partial t}(\rho\varepsilon) + \frac{\partial}{\partial x_i}(\rho\varepsilon u_i) = \frac{\partial}{\partial x_j}\left[\frac{\left(\mu + \frac{\mu_t}{\sigma_\varepsilon}\right)\partial_\varepsilon}{\partial x_j}\right] + \frac{C_{1\varepsilon}\varepsilon}{k}(P_k + C_{3\varepsilon}P_b) - \frac{C_{2\varepsilon\rho}\varepsilon^2}{k} + S_\varepsilon$$

Turbulent viscosity is modelled as $\mu_t = \frac{\rho C_\mu k^2}{\varepsilon}$, Production of k, $P_{k=} - \frac{\rho u_i u_j \partial u_j}{\partial x_i}$, $P_k = \mu_t S^2$

Where is the modulus of the mean rate-of-strain tensor, defined as $S \equiv \sqrt{2S_{ij}S_{ij}}$

Effect of Buoyancy is obtained from, $P_b = \frac{\frac{\beta g_i \mu_t}{Pr_t}\partial T}{\partial x_i}$, where Pr_t is the turbulent Prandtl number for energy and g_i is the component of the gravitational vector in the with direction. For the standard and realizable - models, the default value of Pr_t is 0.85. The coefficient of thermal expansion,β, is defined as $\beta = -\frac{1}{\rho}\left(\frac{\partial\rho}{\partial T}\right)_p$

Model Constants are $C_{1\varepsilon} = 1.44, C_{2\varepsilon} = 1.92, C_{3\varepsilon} = -0.33, C_\mu = 0.09, \sigma_k = 1.0, \sigma_\varepsilon = 1.3$

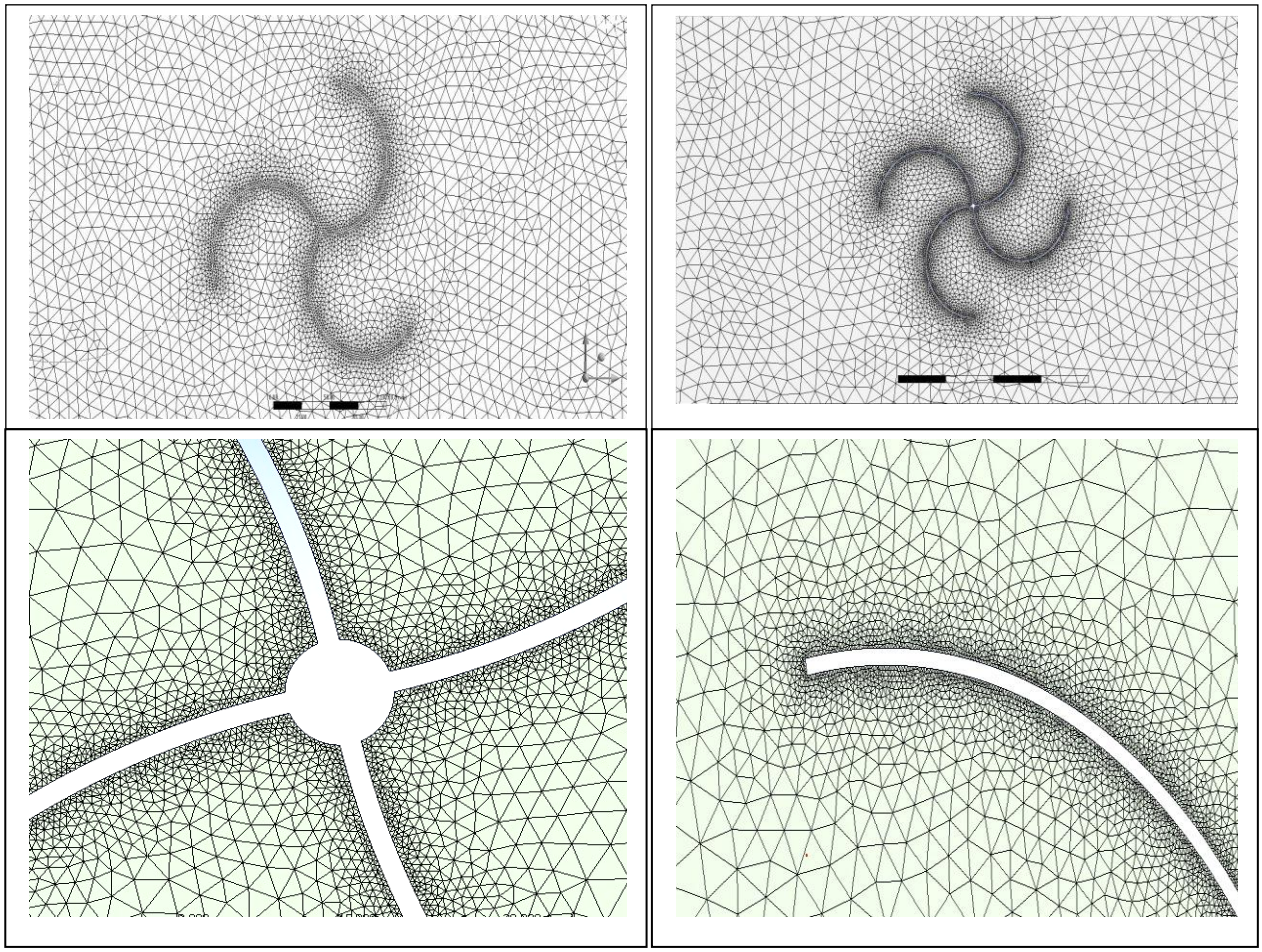

Fig 2 Generated mesh closer view

Boundary conditions were assigned top and bottom as symmetry, the inlet with inlet free stream velocity and the outlet is pressure outlet. Inlet air velocity was considered as 13 m/s. For the static torque analysis the blades were assigned as stationary wall and for achieving the power coefficient vs TSR the blades were assigned as moving walls with relative velocity of zero with respect to the adjacent cell zone. Again to capture the velocity, pressure and turbulent contours the cell zone conditions were defined. Fluid-inner-core was given an rpm of the corresponding TSR. Table 1 shows the reference values that has been used for the simulation

Table 1. Reference Values

Property	Value
Density (Kg/m^3)	1.225
Viscosity (Kg/m-s)	1.7895×10^{-5}
Temperature (K)	288.16
Pressure (atm)	1
Inlet Velocity (m/s)	13

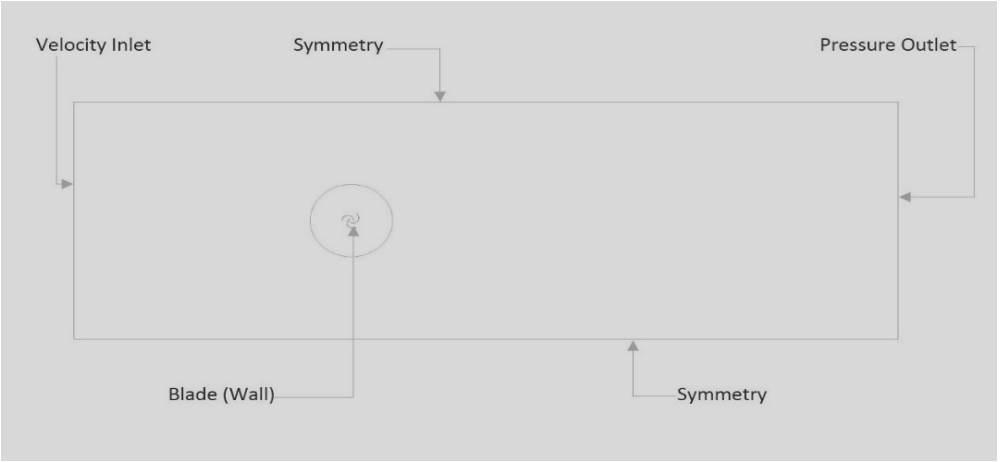

Fig 3.Boundary Conditions

5. Results and Discussion:

CFD analysis of two and three bladed Savonius rotors was performed to validate with the experimental results. The validation has been done by comparing the torque coefficient obtained by both CFD and experimental data. Again, the same simulation model was performed to analyse characteristics of the models.

5.1 Experimental Validations:

Figure 4 represents the validation of two bladed model with the experimental study by M.H Ali [8]. For this validation a rotor with the same diameter (D=200mm), height (H=200mm) and overlap ratio (O.D=0) was designed and the physical properties were kept the same. The torque co-efficient found from CFD analysis follows the same path as the experimental one. Maximum value of torque coefficient in CFD was found .68 where the experimental value is .64 at blade angles of 30^0, 210^0 which matches with the experimental one. In the range from 110^0 to 160^0 and 270^0 to 340^0 blade angle the result deviates slightly and it finds a negative torque at 150^0 and 330^0 blade angle which is not obtained in experiment which shows a 6.24% variation with the experimental data. Figure 0-B shows the validation of the three bladed rotor model with the experimental study of Anik Adhikery [9]. Same procedure was followed like the previous model. CFD results shows good match with the results by experiment. Maximum value of Cq for the experimental result was found at 30^0, 150^0 and 270^0 and for CFD it was found at 40^0, 160^0 and 280^0 and the minimum torque was found at 90^0 for both CFD and experimental. Slight deviation in torque coefficient was noticed at blade angle 0^0, 120^0 and 240^0. The maximum value of torque coefficient was .58 for the experimental result and .56 for the CFD which shows a variation of only 3.45%.

(a) (b)

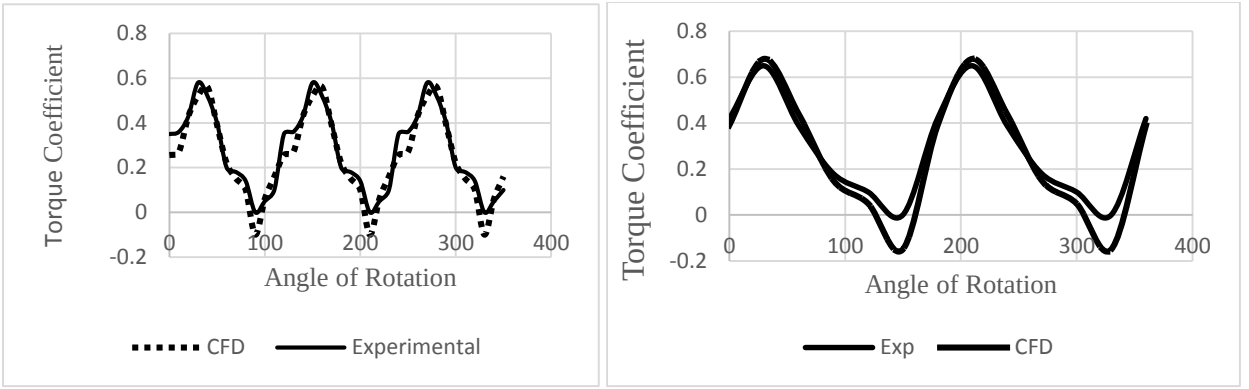

Fig 4. Experimental validation of (a) Three bladed Savonius Rotor (b) Four bladed Savonius Rotor

5.2 Results

Torque coefficient variation with the angle of rotation for three models of three bladed rotor at wind speed of 13 m/s and with a 10° interval from 0° to 360° is shown in Fig 5(a) and 5(b). For the three bladed rotor it can be

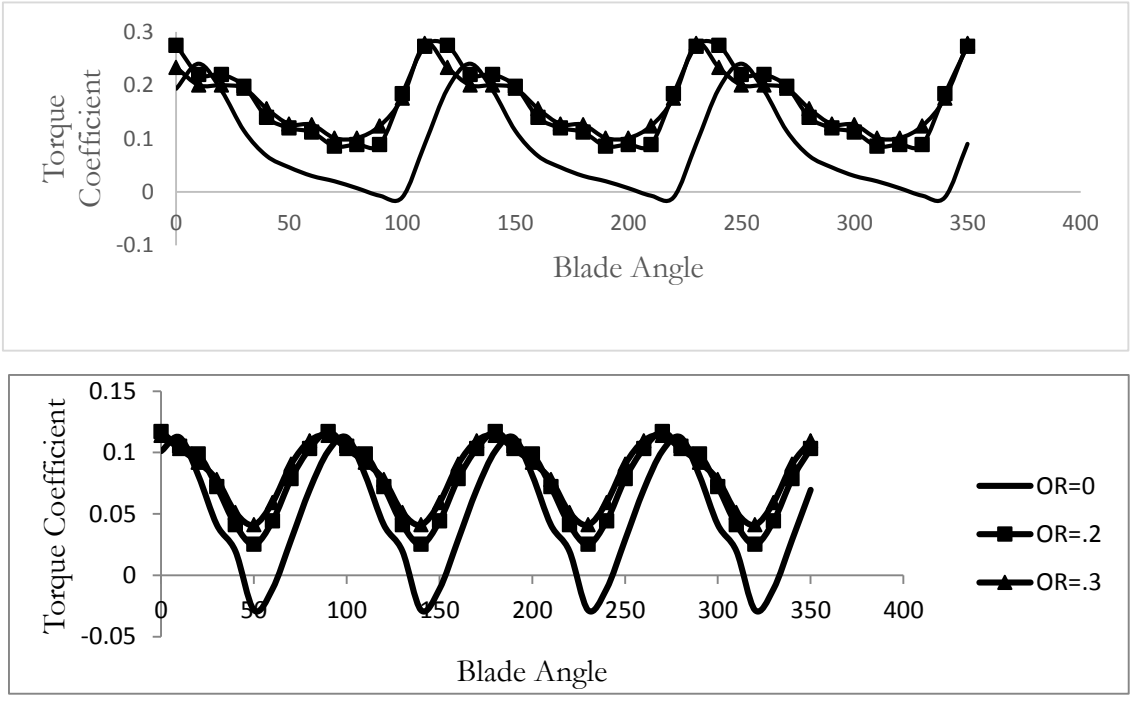

Fig 5 Torque Coefficient vs angle of rotation of the rotor (a) three blade on top (b) Four blade on bottom

seen from Fig 5(c) that the highest value of C_q occurs at 110 degree for models with OR 0.2 and 0.3 and for the

model with no overlap highest value of $C_q$occurs at 120 degree. With the introduction of overlap ratio of 20% C_q increases about 8.69%. Most importantly the negative torque is eliminated. All the graph shows the same pattern with a decrease in the value of C_q from 0° to 100°. Then the value increases until 110°. Same pattern repeats for the rest of angle. Basically for three bladed rotor the cycle of 0°to 110° repeats three times. For four bladed rotors maximum value of C_q occurs at 0°, 90°, 180°, 270° and 360° for models with overlap ratio of 20% and 30%. The graph pattern can be easily predicted from Fig 5(d) as all three models show the same pattern. The value of C_q decreases from 0° to 50° and increases upto 90° to reach the maximum value of C_q. This cycle repeats four times between 0° to 360°.

Fig 6 shows the numerically computed Cq versus Reynolds Number for the three bladed Savonius rotors. It can be

(a) (b)

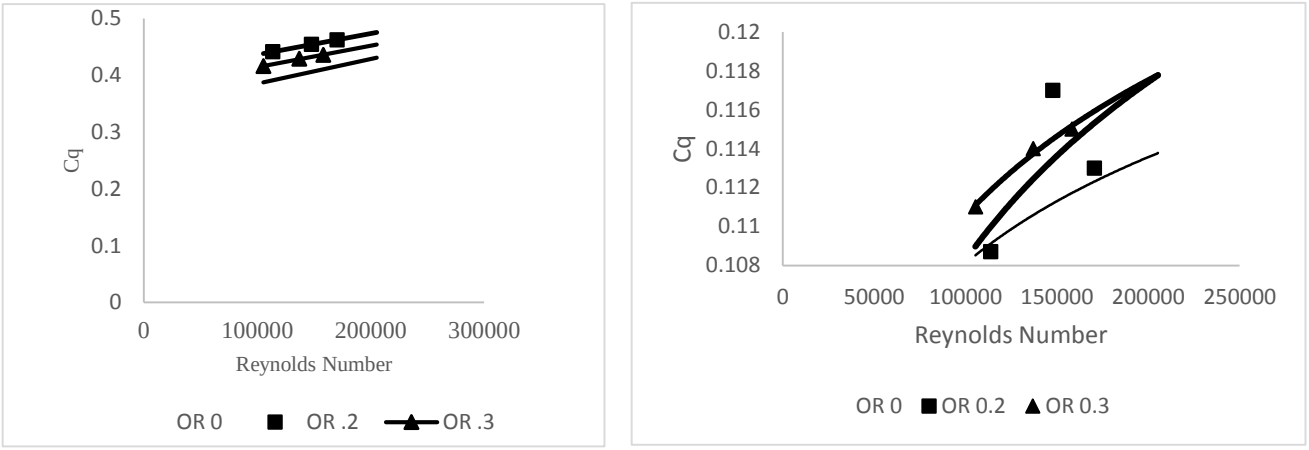

Fig 6. Torque Coefficient Vs Reynold's number (a) three blade (b) four blade

(a) (b)

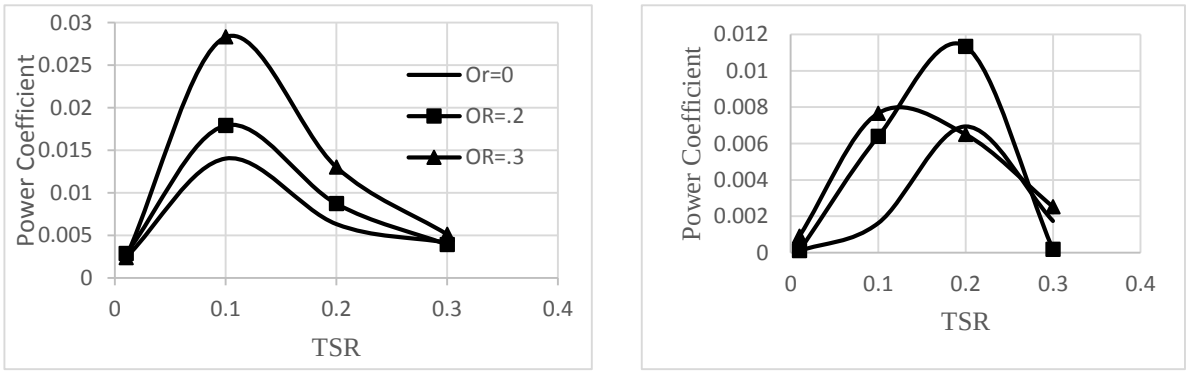

Fig 7. Power Coefficient Vs Tip Speed Ratio TSR (a) Three blade (b) Four blade

seen from the graph that the torque coefficient increases slightly with the increase in Reynolds number. Rotor with OR 0.2 gives better performance than the other two models.

Power coefficients at different TSR has been plotted in Fig 7. Power coefficients has been calculated by multiplying C_q with λ. For the three bladed models with the maximum C_p being 0.014, 0.017 and 0.028 for models with 0%, 20% and 30% overlap respectively. In case of the three blades, model with OR 0.3 shows the highest Power Coefficient and in case of the four blades the model with OR 0.2 shows the highest power coefficient.

Conclusion:

Six Savonius wind turbine scale models with different overlap ratios (0, 0.2, 0.3) and blade numbers (3 and 4) were designed for the current study. Aerodynamic characteristics of these models were numerically investigated using the CFD techniques. Major findings of this study are listed below.

- The number of period per rotor revolution increase as the numbers of blade increases. The number of period per rotor revolution is equal to the number of blades of a Savonius rotor.
- Savonius rotors have a period per rotor revolution each 120º and 90º rotor angle for the cases three bladed and four bladed rotors.
- The amplitude of torque coefficient decreases with the increase in blade numbers. Rotor with three blade exhibits the higher torque than the four bladed model.
- The rotors with no overlap exhibits a negative torque at a certain angle of rotation.
- Presence of overlap ratios in Savonius rotors eliminates the negative torque and the increase of overlap ratio increases the lowest value of torque coefficient.
- In each models, higher torque coefficient is observed in higher Reynolds number. The value of torque coefficient increases linearly as the Reynolds number increases.
- The power coefficient increases as tip speed ratio increases until it reaches a maximum value then it starts to decrease the value of power coefficient decreases with the increase in blade number of a Savonius rotor.

Acknowledgments:

We feel indebted to our supervisor, Dr. Mohammad Mamun, Professor, Department of Mechanical Engineering, Bangladesh University of Engineering and technology for his invaluable encouragement and guidance throughout this thesis and study period. We are sincerely and specifically thankful to him for his continuous patience and trust for upon us

References:

1. S. J. Savonius, “The S rotor and its application,” Journal of Mechanical Engineering, vol. 53, pp. 333-338, 1931.
2. Menet, J.L.; Bourabaa, N. “Increase in the Savonius turbines power coefficient via a parametric investigation”. Technical paper series, University of Valenciennes, France, 2001
3. B. Cochran, B. David and S. J. Taylor, "A three-tiered approach for designing and evaluating performance characteristics of novel WECS," AIAA, vol. 18, pp. 2004-1362, 2004.
4. Dr. R. Gupta, K.K Sharma "Flow Physics of a Three-Bucket Savonius Rotor using Computational Fluid Dynamics (CFD)," IJRMET, vol. 1, no. 1, pp. 46-51, 2011
5. I. Katsuya and S. Toshio, "Simulation of flow around rotating Savonius turbines," in Proceedings the sixth National Symposium on Computational Fluid Dynamics, 2001..
6. Tong Zhou,Dietmar Rempfer, "Numerical study of detailed flow field and performance of Savonius wind turbines," Renewable Energy, vol. 51, pp. 373-381, 2013.
7. K.N. Morshed, Mosfequr Rahman, Gustavo Molina and Mahbub Ahmed, “Wind Tunnel Testing and Numerical Simulation on Aerodynamic performance of a Three Bladed Savonius Wind Turbine”, International Journal of Energy and Environmental Engineering 2013, Volume 4, no18,
8. M. H. Ali, "Experimental Comparison Study for Savonius Wind Turbine of Two & Three blades at Low Wind Speed," International Journal of Modern Engineering Research , vol. 3, no. 5, pp. 2978-2986, 2013
9. A. Adhikery, "Aerodynamic Characteristics of a Savonius Rotor with Three Blades of Circular Arc Profile," in *Msc Thesis*, BUET, 2014.

6th BSME International Conference on Thermal Engineering (ICTE 2014)

A Study on Machine Vision Technology – An Automated Aid for Industrial Product Inspection

Md. Saidur Rahman[a], J. U. Ahamed[b*]

[a]*M. Sc. In Management Technology, Institute of Appropriate Technology, Bangladesh University of Engineering and Technology (BUET), Dhaka, Bangladesh*

[b*]*Department of Mechanical Engineeirng, Chittagong University of Engineering and Technology (CUET), Chiittagong-4349,Chittagong, Bangladesh. Email: jamal293@yahoo.com*

Abstract

An efficient integration of automated systems into high speed, complex manufacturing processes is today's main demand and it is possible by the development of modern automation technologies. This article presents a study of machine vision technology using image processing and an application of software based automatic industrial product inspection system. The background of visual inspection technology and related works before describing the system are discussed in thisarticle. The developed vision inspection system with a camera that was integrated into a station has a capability to inspect a product of wooden piece. The description of the algorithms used to perform the image processing and the inspection system are discussed. A microcontroller based control circuit unit is used in this research work, which can communicate with computer system through serial communication protocol.

Keywords: Automation; Edge Detection; Machine Vision; Product Inspection.

1. Introduction

In these days of modern technology, business must boost using the help of automation technologies. The machine vision technology is also such thing which can be efficiently integrated into manufacturing system and can increase the productivity of the production by reducing cost and time. In an era of high labor costs, it is very much cost economic for any production that automated visual inspection can be used as a replacement of human inspection. While manufacturing of any product, manufacturers need to maintain high levels of quality inspection with maximization of productivity and also maintain less consumption of time.

Now machine vision systems are widely used in both small and high-volume production line. Because of the low costs and non-destructiveness, it increases the demand of visual inspection system for high level of quality management and process control [1]. In many different industrial sectors machine vision technology has now been used as an innovative technology for products quality inspection and measurement. Bazin *et al.* (2006) describes a method of automated contact lens inspection [2]. Jia (2009) developed a machine vision system for inspecting medical syringes, which has been integrated with a PLC based automatic system to check and control the fault

Corresponding Author: Dr. Jamal Uddin Ahamed, Associate Professor, Department of Mechanical Engineering, Chittagong University of Engineering and Technology (CUET), Chittagong-4349, Mobile-+8801720641636, E-mail: jamal293@yahoo.com

product from the production line [3]. Huajun *et al.* (2012) developed a software based automatic system of mechanical geometry parts fault detection by using the recognition of product shape and size measurement. They uses image processing technology for complete automation and rapid production, which will help to achieve the high efficiency and precision [4]. Singh and Bharti [5] described a method for inspecting fault connections of industrial PCB board.

Industrial product offers many challenges for visual inspection. Because of the complexity of their shape and size, manufacturer must ensure the excellent dimensional precision of any product. High speed, real time, non-contact and high precision automatic inspection of products geometrical dimensions plays an important role in the manufacturing floor. But the traditional manual inspection or measurement methods cannot meet such requirements. In order to ensure the stringent quality demands of industrial product, machine vision technology is a logic choice for automated manufacturing system. And this is very much efficient because of the programmability of a vision system and the repeatable measurement capability. The most advantages of computerized visual inspection system are that, it can be integrated into the manufacturing system for inspection, measurement, verification with design database and can provide many quality based information during the operation of quality controls. This paper presents a method of inspecting industrial products, which has a 'T' like shape. The user interface software is developed using the image processing system. The vision inspection hardware system, control interface and the implementation of visual inspection system will be presented.

2. Methods & Materials:

2.1 Design of the Inspection System

Figure 1 shows the basic work flow diagram of the mechanical parts dimension measurement system.

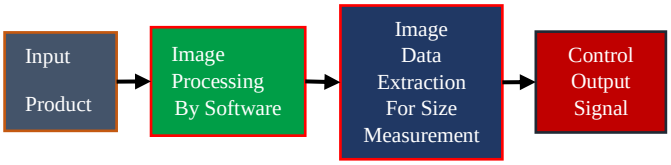

Figure 1: Basic work-flow diagram.

This process shows four steps and these are as follows:

Firstly, the input is our required product image and it is done by a web camera. Any other high resolution camera can be used for better image quality which will give a better performance. *Secondly*, this input image is processed by a dedicated computer software program namely as CVI (Computerized Visual Inspection), which is developed in Visual Basic 6.0. This process includes the grayscale conversion of input image, edge detection, thresholding and feature extraction etc. *Thirdly*, the image data is extracted using this software for measuring the size of our product and check the product whether it is ok or not. *Finally*, a control signal is constructed on the basis of inspection result for accepting or rejecting the product and it is done by a microcontroller based control unit using the RS-232 serial communication protocol.

2.2 Edge Detection

This is the important part of image processing system. Firstly, the RGB image is converted into grayscale image because it reduces the complexities of the processing [6]. Then this gray image is used to convert into edge image

Corresponding Author: Dr. Jamal Uddin Ahamed, Associate Professor, Department of Mechanical Engineering, Chittagong University of Engineering and Technology (CUET), Chittagong-4349, Mobile-+8801720641636, E-mail: jamal293@yahoo.com

and it is done by the edge detection algorithm. There are numerous number of edge detection algorithms and they yields slightly different results, depends upon the necessity of the work.

We use masks to make the required edge image, which is worked like a high-pass filters. Because edges create higher frequencies in the spectrum, so they can be easily separated by high-pass filter mask. Laplacian1 is such type of mask, which is used to make an edge image from the grayscale image [6]. Figure 2 shows a typical high-pass edge detector mask of Laplacian1, which is used to make the edge image.

0	-1	0
-1	4	-1
0	-1	0

Figure 2: Edge detector (Laplacian1) mask [6].

2.3 Thresholding of Edge Image

It is the process of dividing any image into different portions by using a threshold value and comparing with each pixel. This is used in the edge image to make it more sharpening and reduces the unexpected pixels. This is done by settling a threshold value (***T***) and comparing this value with every pixel of *f(x, y)* location in the edge image. This process checks whether the pixel's grayness level is below the threshold or above the threshold. If it founds the pixel's value of below threshold value, then it replaces that pixel with '0' i.e. "off" pixel or the elimination of that pixel and if it found any pixel value of above threshold value then it replaces that pixel with "255" i.e. "on" pixel [6].

$$f_{new}(x, y)=\begin{cases}255, iff(x, y) \geq T \\ 0, if \ \ f(x, y) < T\end{cases} \qquad (1)$$

State 1 of equation 1 gives the white edge pixel of value "255" and the State 2 of equation 1 gives an off pixel of value "0" in the edge image. It makes the image very sharp for further processing. The threshold value (***T***) is founded by using trial and error system.

2.4 Materials

Table 1 shows the materials list of the computerized visual inspection system used in this research work.

Table 1: Components List used in the System

No.	Components (Quantity)	Description
1.	Lights (1)	LED lighting used for system illumination.
2.	Camera (1)	Web camera for image capture.
3.	Software (1)	Namely as CVI (Computerized Visual Inspection) used to control the all processes.
4.	Control Unit (1)	Microcontroller based control circuit to communicate with computer via RS-232 protocol.
5.	Servo Motor (1)	For product rejection actuator.
6.	Serial-RS232 (1)	Serial to USB converter.

Corresponding Author: Dr. Jamal Uddin Ahamed, Associate Professor, Department of Mechanical Engineering, Chittagong University of Engineering and Technology (CUET), Chittagong-4349, Mobile-+8801720641636, E-mail: jamal293@yahoo.com

3. Results & Discussions:

3.1 User Interface Description

The dedicated user interface of the inspection system consists of the following panels:

- Main Panel
- Camera Control Panel
- Automatic/Manual Mode Selection Panel
- Dimension Measurement Panel
- Detection Alarm Panel

Figure 3 shows the screenshot of main screen panel of the user interface. The processed image and associated with the measurement result will be shown on this panel during the operation.

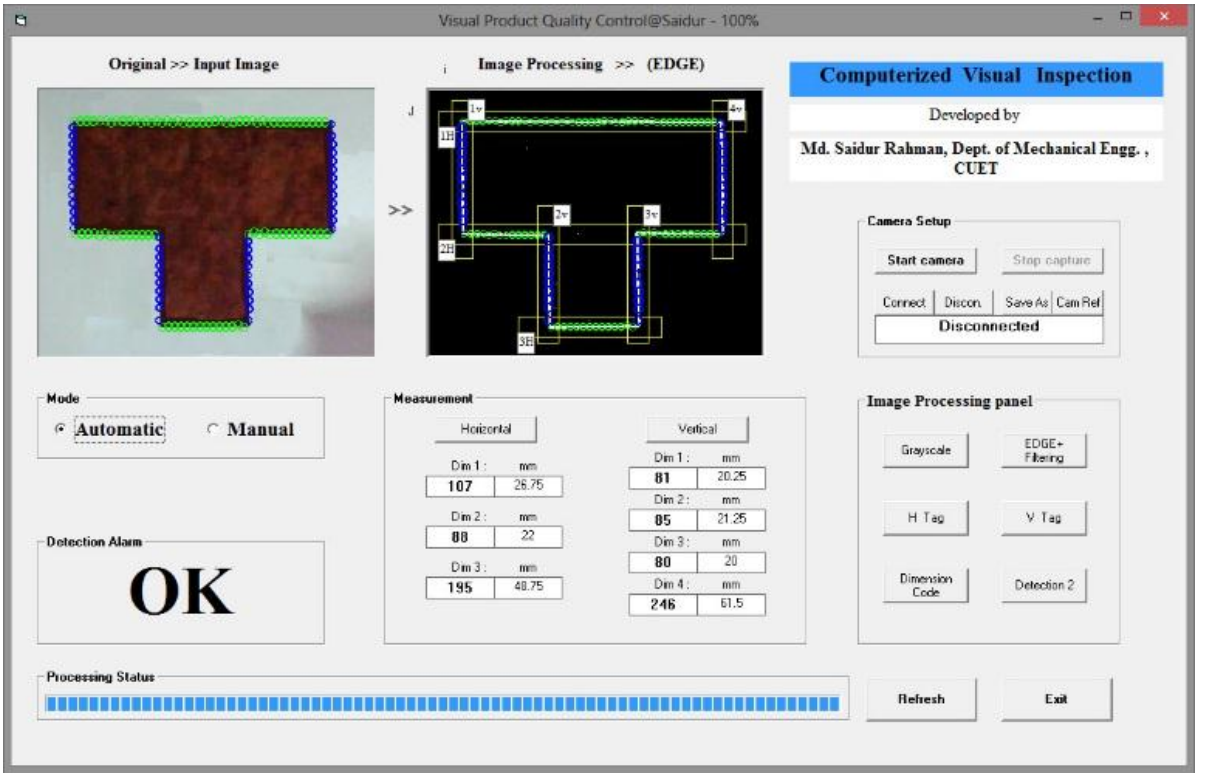

Figure 3: Screenshot of Main User Interface.

Only one camera has been used for inspecting front side of the required product. The "**Start camera**" push button is used to initialize and start the webcam camera to capture the product image. The input image will be displayed in the main panel. The white text box displayed the text "**Connected**" in the camera setup panel, when the user interface established the connection with the control circuit via the RS-232 serial communication port. By this time, it will

Corresponding Author: Dr. Jamal Uddin Ahamed, Associate Professor, Department of Mechanical Engineering, Chittagong University of Engineering and Technology (CUET), Chittagong-4349, Mobile-+8801720641636, E-mail: jamal293@yahoo.com

display the text "**Object Found**" when the external control system found any object for measurement process. A light proximity sensor is used to detect the presence of object and send this signal via serial communication port.

The image processing panel and the command buttons associated with this panel is used to done the software processing by manually. The "**Automatic**" option button can be used to do the all inspection & measurement operations instead of "**Manual**" mode. After the inspection operation and image processing, the measurement panel will show the all dimensions of that product and if it found the dimensions matched with the predefined dimensions from the database then it will show the text "**OK**" in the detection alarm panel, otherwise it will show the text "**Fault**". So if the product will be found as fault then the software will send a signal to the control circuit to run the actuator and reject the product from the inspection line. This actuator is made with a servo motor (SG-5010).

3.2 Processing Tools for Front View Inspection

The processing tools used for front view inspection of the required product are as follows:

- Grayscale conversion
- Applying edge detection mask
- Filter the edge image using threshold value
- Tagging the horizontal & vertical pixel points

The image has been captured by the camera is a RGB color image. But it is very much complicated to handle the color image. So we need to convert it in grayscale image. This grayscale image contains only 8 bit data (i.e. 0~255). Figure 4(a) shows the original image and Figure 4(b) shows the converted grayscale image.

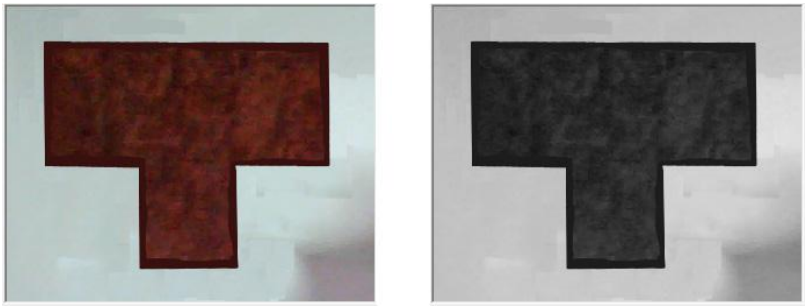

(a) (b)

Figure 4: (a) Input image (b) after the grayscale conversion.

Then this gray image has been passed through the edge detection mask of Laplacian1 to make the edge image as we have described before. Figure 5(a) shows the result of edge image using the mask. But this image is not enough sufficient to extract the feature data, because there are many false edge pixels remain in the edge image. So, to reduce the false pixels, a predefined threshold value has been used to filter the edge image. The thresholding system has been applied by using the Equation 1 from the previous section we have described. Figure 5(b) shows the result of applying the threshold value in the edge image.

Corresponding Author: Dr. Jamal Uddin Ahamed, Associate Professor, Department of Mechanical Engineering, Chittagong University of Engineering and Technology (CUET), Chittagong-4349, Mobile-+8801720641636, E-mail: jamal293@yahoo.com

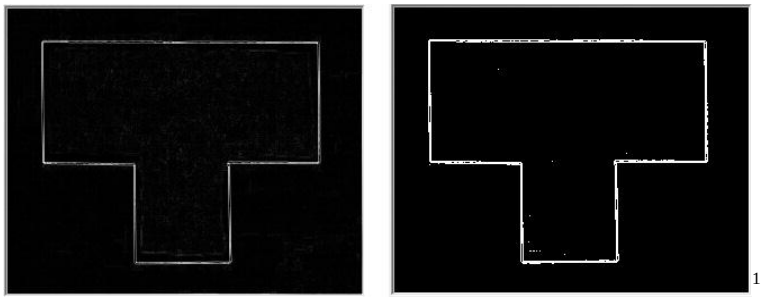

(a) (b)

Figure 5: (a) Edge image (b) after using threshold.

Now, we need to find out the horizontal & vertical pixels from the edge image, because these pixels create a continuous horizontal and vertical lines respectively in the edge image. Figure 6 shows the horizontal pixel location tagging in the edge image. Figure 7 shows the vertical pixel location tagging in the edge image. Finally it will help us to measure the dimensions.

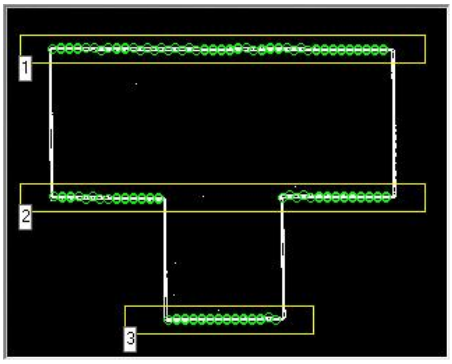

Figure 6: Horizontal pixel tagging of edge image.

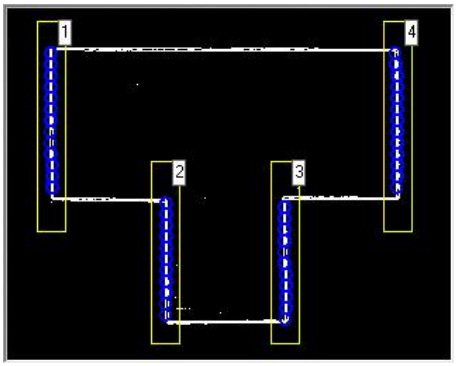

Corresponding Author: Dr. Jamal Uddin Ahamed, Associate Professor, Department of Mechanical Engineering, Chittagong University of Engineering and Technology (CUET), Chittagong-4349, Mobile-+8801720641636, E-mail: jamal293@yahoo.com

Figure 7: Vertical pixel tagging of edge image.

The yellow rectangles and their corresponding number value indicates the number of lines it detected. The perpendicular distance among these lines has been used for dimension measurement of the required product.

3.3 Measurement Results

The dimension measurement system is done by the horizontal and vertical lines based on their corresponding pixels found in the edge image after the completion of processing. The results will be displayed on the measurement panel in pixel and mm format. A calibration factor has been used based on the perpendicular distance between the camera lens plane and the target object. The factor is found as 0.25 used in this system. The factor will be constant for a same machine vision system. However, the better performance of the measurement result will be depends on the camera resolution. High resolution will give a good performance. Table 2 shows the measurement results of the product size, which has been taken from the user interface software after complete processing.

Table 2: Measurement Results

Horizontal Measurements			**Vertical Measurements**		
	In Pixel	In mm		In Pixel	In mm
Dim_1	107	26.75	Dim_1	81	20.25
Dim_2	88	22	Dim_2	85	21.25
Dim_3	195	48.75	Dim_3	80	20
			Dim_4	246	61.5

After the dimension measurement, the software will compare these data with the database that whether the dimensions are ok or not and then send a response signal on the basis of this analysis.

3.4 Control Output System

After the measurement, the program will send a signal on the basis of fault products' dimension analysis. This output signal is then received by a control circuit. The circuit has been constructed by using a microcontroller of PIC16F877A, MAX-232, an oscillator of 8 MHz, voltage regulator 7805 and some capacitors and resistors. This control board is mainly used for sending and receiving the signal from computer. The actuator response is based on this signal. A Universal Synchronous Asynchronous Receiver & Transmitter (USART) system has been used for this control system. The data comes from the computer is in 8 bit asynchronous format, which is received by the control circuit using the USART module of the microcontroller. The baud rated for serial data communication system is normally 300, 1200, 2400, 9600, 192000, 384000, 115200 [7]. A servo motor (SG-5010) has been used as a rejecting actuator. If the control board receives signal for any fault product, then it will run the actuator to reject the fault product from the production line.

4. Conclusion:

In this paper the developed machine vision technology for the industrial product inspection system has been presented, which can be used for 100% inspection of the product and it will also ensure the quality of whole production system. This system only demonstrates the front view inspection of the specific product. But in this way of similar methods and technology, other views of the mechanical products like side or top view can be measured. A very efficient measurement result will depends on the good quality of light illumination system, because it helps to capture good quality of image. Another fact of the system performance relied on the high resolution of camera, which will give a very fine quality of image with a reduced number of noises. However, the advances of

Corresponding Author: Dr. Jamal Uddin Ahamed, Associate Professor, Department of Mechanical Engineering, Chittagong University of Engineering and Technology (CUET), Chittagong-4349, Mobile-+8801720641636, E-mail: jamal293@yahoo.com

computerized visual inspection system has been providing and supporting the technical progresses in many industrial manufacturing and production system.

References

[1] T. Petkovic, D. Juric and S. Loncaric, "Flexible Visual Quality Inspection in Discrete Manufacturing," Proceedings of Computer Vision Workshop, *CCVW* '13, pp.58-62, 19 Sept. 2013.

[2] A.I. Bazin, T. Cole, B. Kett, and M.S. Nixon, "An Automated System for Contact Lens Inspection," *Visual Computing*, 2006. *ISVC* '06. Second Intl. Symposium on, vol. 4291, pp.141-150, 6-8 Nov. 2006. doi: 10.1007/11919476_15

[3] J. Jia, "A Machine Vision Application for Industrial Assembly Inspection," *Machine Vision*, 2009. *ICMV* '09. Second Intl. Conference on, vol., no., pp.172-176, 28-30 Dec. 2009; doi: 10.1109/ICMV.2009.51

[4] D. Huajun, Y. Haijun, H. Guohui, "Researches on the Size Measurement of Mechanical Parts Based on Image Processing," Advanced Matrials Reasearch, vol. 605-607, pp.915-918, Dec. 2012; doi: 10.4028/www.scientific.net/AMR.605-607.915

[5] S. Singh, M. Bharti, "Image Processing Based Automatic Visual Inspection System for PCBs," IOSR Journal of Engineering (*IOSRJEN*), vol. 2, issue 6, pp.1451-1455, June 2012; ISSN: 2250-3021.

[6] S. B. Niku, Introduction to Robotics, Analysis, Systems, Applications, ISBN-81-203-2379-7. New Jersey, Peason Prantice Hall, USA, 2001.

[7] J. Axelson, "Serial port Complete Programming fro RS-232 and RS-485 Links and Networks", Lakeview Research, USA. ISBN-0-9650819-7-4, pp.43-45, 2000.

Corresponding Author: Dr. Jamal Uddin Ahamed, Associate Professor, Department of Mechanical Engineering, Chittagong University of Engineering and Technology (CUET), Chittagong-4349, Mobile-+8801720641636, E-mail: jamal293@yahoo.com

6th BSME International Conference on Thermal Engineering (ICTE 2014)

Analysis of Effects of Surface Roughness on Muffler Performance

Erfanul Alam[a], Farhan Arafin[b], M Ashiqur Rahman[a,b] *

[a]*Room -318 , Ahsanullah Hall, BUET, Dhaka-1211 , Bangladesh*
[b]*70/a 2nd lane , Kalabagan, Dhaka-1415, Bangladesh*

Abstract

Internal combustion engines are typically equipped with an exhaust muffler to suppress the acoustic pulse generated by the combustion process. A high intensity pressure wave generated by combustion in the engine cylinder propagates along the exhaust pipe and radiates from the exhaust pipe producing undesirable loud noise. Hence, mufflers are important parts of engine system which are commonly used to minimize sound transmissions caused by exhaust gases. In our study, a reactive muffler which attenuates the noise of a diesel engine is investigated. This paper deals with a practical approach to design, develop and test muffler with different surface roughness of the muffler material. The variation in performance characteristics, i.e. noise reduction capability of the muffler with five different surface roughnesses is measured experimentally and the results have been compared with the smooth surface to study the effects.

Peer-review under responsibility of organizing committee of the 6th BSMEInternational Conference on Thermal Engineering (ICTE 2014).

Keywords: Automotive muffler; Reactive silencer; Surface roughness; Noise reduction

* Corresponding author. Tel.: +8801710467996 .
E-mail address: irfan_0810028@yahoo.com

Peer-review under responsibility of organizing committee of the 6th BSME International Conference on Thermal Engineering (ICTE 2014).

Nomenclature

Hz	Hertz
dB	Decibel
TL	Transmission Loss

1. Introduction

A muffler (silencer) is a device for reducing the amount of noise typically emitted by an engine. In internal combustion engines, the engine exhaust blows out through the muffler. They are typically installed along the exhaust pipe as part of the exhaust system of an internal combustion engine of a vehicle to reduce its exhaust noise. The level of exhaust noise reduction depends upon the construction and the working procedure of mufflers. Muffler technology has not changed very much over the past years. The exhaust is passed through a series of chambers in reactive type mufflers or straight through a perforated pipe wrapped with sound attenuating material in an absorptive type muffler. A significant number of research and experimentation has been conducted to study the performance and flow characteristics of exhaust muffler. Bhat and Sharma [1] studied on design and analysis of expansion chamber mufflers. They found that three chamber muffler provides higher attenuation of sound pressure compare to one and two chamber mufflers. Sabah and Ameen [2] did experimental test for noise attenuation in gasoline engine with different types of mufflers and compared among three different types of exhaust muffle for noise attenuation of single cylinder four stroke air-cooled gasoline engine. They found that the length of muffler's chamber is proportionate with sound attenuation. The higher muffler's chamber wall thickness the greater noise reduction. Jadhav [3] found that combined reactive and dissipative muffler give better results in sound attenuation. Mohiuddin, Ideres and Hashim [4] presented experimental study of noise and back pressure for silencer design characteristics. They concluded that the relationship between the noise and the back pressure is inversely proportional. Rahman and Sharmin [5] designed a combination muffler which had absorptive part, reflective part, resonator and tailpipe. They concluded that hybrid muffler works better both in high and low frequency noises. They also stated that the side branch resonator attenuates residual low frequency noise and if residual frequency exceeds the range, the resonator becomes largely ineffective.

It was seen that the effect of surface roughness on noise attenuation in muffler is not analyzed earlier. The objective of our research was to focus on surface roughness effect on noise attenuation whether it increases muffler efficiency or not. Experimentation of this research measures the sound level with muffler which has internal rough surface and determines the transmission loss. Transmission loss is the difference between sound pressure level without muffler and with muffler. Then the transmission loss for rough surface and smooth surface were compared to study the effect of surface roughness of muffler in noise reduction. The study will help the researchers to get the idea for optimum muffler design considering surface roughness.

2. Materials and Methods

2.1 Equipments and instrumentation

The various basic equipment used in the experimentation includes a manufactured muffler, various grades of emery paper, sound generator and sound level meter.

Emery paper: Emery paper was used to make the internal surface rough. Emery papers with five largest particle sizes were selected and they are of grade: P60, P50, P40, P36 and P24. The average grit particle sizes for them were

260 micron, 326 micron, 412 micron, 524 micron, 740 micron respectively. Emery paper was adhered with the internal surface of muffler using silicon glue. After collecting data with one grade of emery paper, it was removed and another was placed for collecting data.

Sound generator: Sound generator was used to produce sound of different frequencies. One terminal of speaker was connected to digital pin 9 of microcontroller through a 100 ohm resistor, and its other terminal to ground. Photoresistor was powered with 5V and was connected to analog 0 with the addition of a 4.7K resistor to ground. An analog input value ranged from about 100Hz to about 2000Hz input was taken and value was mapped to a range of audible pitches.

Manufactured muffler: A muffler of 15cm diameter and 35.5cm length with 3.3cm inlet and outlet pipe diameter was manufactured. At the middle of the muffler, a flange system was designed so that the muffler can be opened and surface roughness can be changed to collect data. Flange distance from the inlet of the muffler body is 18cm. The muffler was made of mild steel and the thickness was 18 SWG.

Figure 1: Manufactured muffler

Sound level meter: For measuring the sound level, a digital Sound Level Meter was used. It was set at A-weighted filter. Sound pressure level (SPL) or sound level is a logarithmic measure of the effective sound pressure of a sound relative to a reference value. It is measured in decibels (dB) above a standard reference level. The standard reference sound pressure in air or other gases is 20μPa, which is usually considered the threshold of human hearing (at 1 kHz).

2.2 Experimental procedures

A sound generator was placed at the inlet of the muffler. Sound of particular frequency was generated and sound level was measured from sound level meter which was placed at 1m distance from the muffler outlet. Then sound level was measured again without the muffler. Sound level difference between two data is the transmission loss.

After collecting data with one grade of emery paper, it was removed and another was adhered with the internal surface of the muffler. Then sound level and transmission loss were measured in similar process. Thus sound level and transmission loss for five different grade of surface roughness were measured. Base level of sound was 48 dB. Measuring time span for each reading was 5 sec.

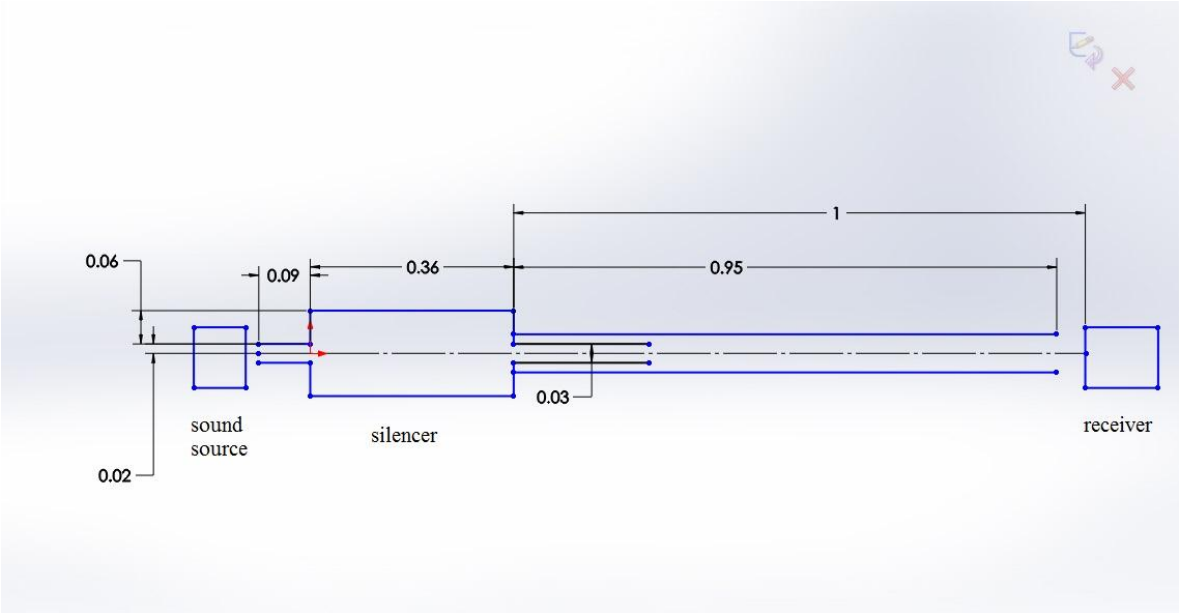

Figure 2: Block diagram of experimental setup (dimensions in meter)

3. Results and discussion

In figure 3, effect of surface roughness is depicted by the difference in two curves. Data is collected from 100Hz to 1000Hz with 50Hz step and 1000Hz to 2000Hz with 100Hz step. By studying the graph, it is found that transmission loss (TL) for rough surface gets higher and lower than smooth surface in different discrete frequency ranges. But this increase and decrease occur consecutively. TL is slightly lower in rough surface than in smooth surface for 100-350Hz range. But in 400-700Hz range, TL is higher in rough surface than in smooth surface. An average 3.41dB greater TL is found in this range for rough surface. Again, in a small range of 700-850Hz, smooth surface gives better attenuation. In 900-1300Hz range, attenuation is greater for rough surface. It should be mentioned that the highest difference in TL between smooth and rough surface is found in this range. It is 19dB higher for rough surface than smooth surface at 1000Hz. Then again TL decreases and increases for 1400-1500Hz and 1600-2000Hz respectively.

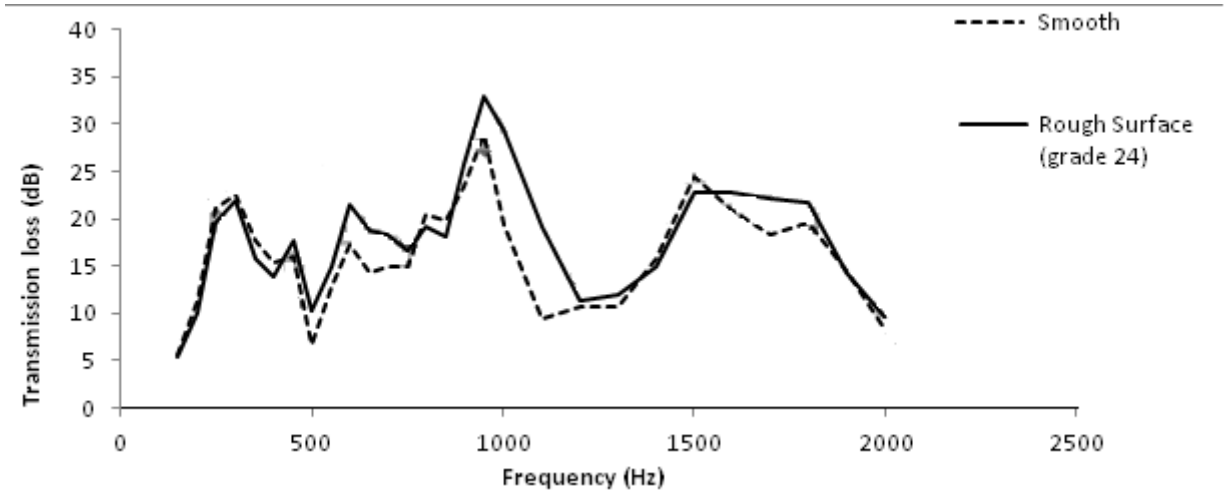

Figure 3: Transmission Loss vs. Frequency graph for smooth surface and rough surface of Grade P24

By studying the figure 4, it is found that, it is found that transmission loss (TL) for rough surface gets higher and lower than smooth surface in different discrete frequency ranges consecutively. TL slightly decreases for rough surface in 150-350Hz range. In 400-700Hz range, TL is higher in rough surface than in smooth surface. An average 3.94dB greater TL is found in this range for rough surface. Again, in a small range of 700-850Hz, smooth surface gives better attenuation. In 900-1300Hz range, attenuation is greater for rough surface while highest TL is found at 1000Hz for rough surface which is 31.1dB. It is 19.8dB higher than smooth surface at 1000Hz. Then again TL decreases and increases for 1300-1500Hz and 1600-2000Hz respectively.

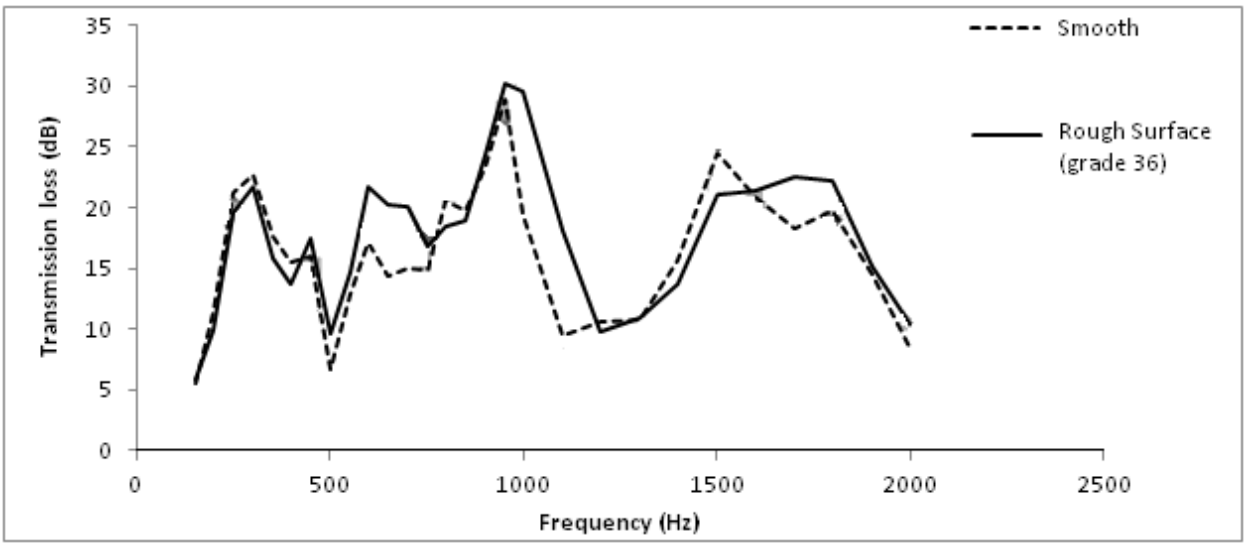

Figure 4: Transmission Loss vs. Frequency graph for smooth surface and rough surface of Grade P36

Figure 5 depicts that the transmission loss (TL) increases and decreases with surface roughness in different discrete frequency ranges. TL is lower in rough surface than in smooth surface for 100-350Hz range. In 400-700Hz range,

TL is higher in rough surface than in smooth surface. An average of 2.9dB greater TL is found in this range for rough surface. Again, in 900-1200Hz range, attenuation is greater for rough surface. The highest TL of 32.3dB is found again at 1000Hz for rough surface which is 21dB higher than in smooth surface. Beyond this frequency TL for rough surface increases and decreases than smooth surface so randomly that we cannot find any trend to show the relation with surface roughness.

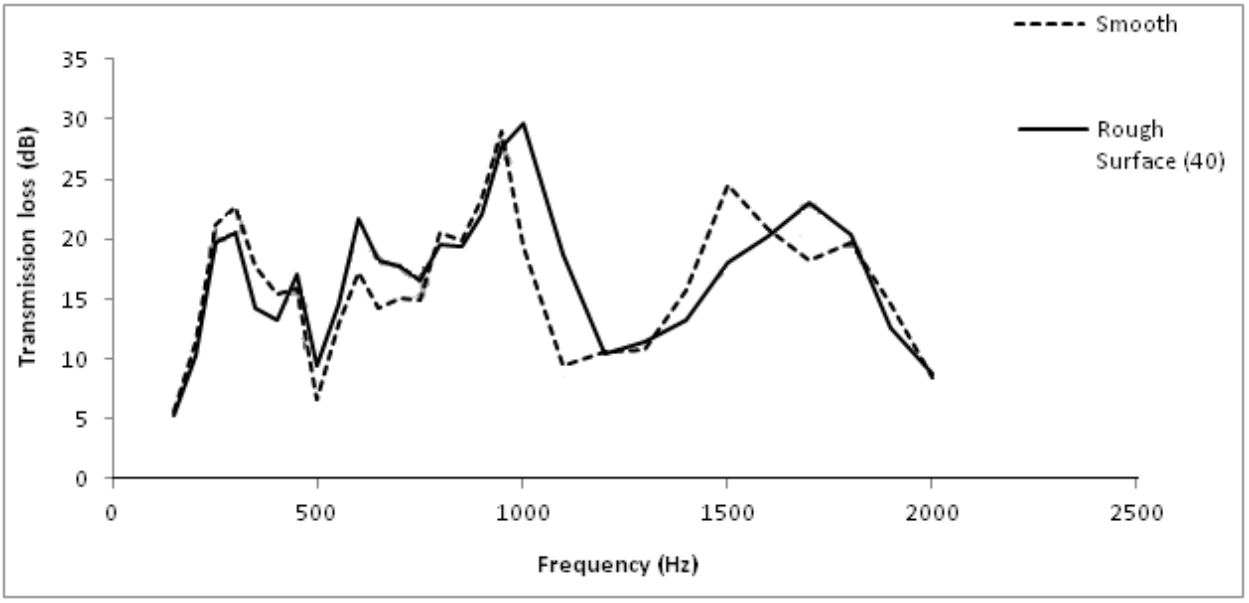

Figure 5: Transmission Loss vs. Frequency graph for smooth surface and rough surface of Grade P40

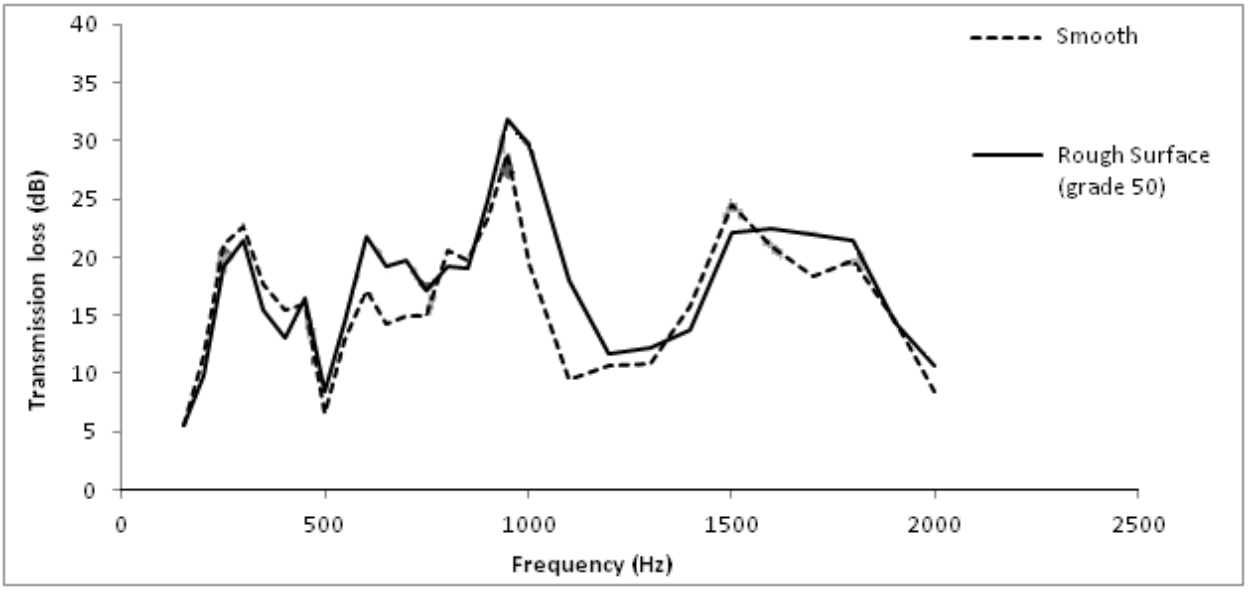

Figure 6: Transmission Loss vs. Frequency graph for smooth surface and rough surface of Grade P50

By studying the figure 6**,** it is found that transmission loss (TL) for surface roughness increases and decreases in different discrete frequency ranges consecutively. TL is slightly lower in rough surface than in smooth surface for

100-350Hz range. In 400-700Hz range, TL is higher in rough surface than in smooth surface. An average of 3.51dB greater TL is found in this range for rough surface. Again, in a small range of 700-850Hz, smooth surface gives slightly better attenuation. From 900Hz to 1400Hz, attenuation is greater for rough surface. Highest difference in TL between smooth and rough surface is found at 1000Hz and it is 18.3dB higher in rough surface than smooth surface. Then again TL for rough surface decreases and increases than smooth surface for 1400-1600Hz and 1600-2000Hz respectively.

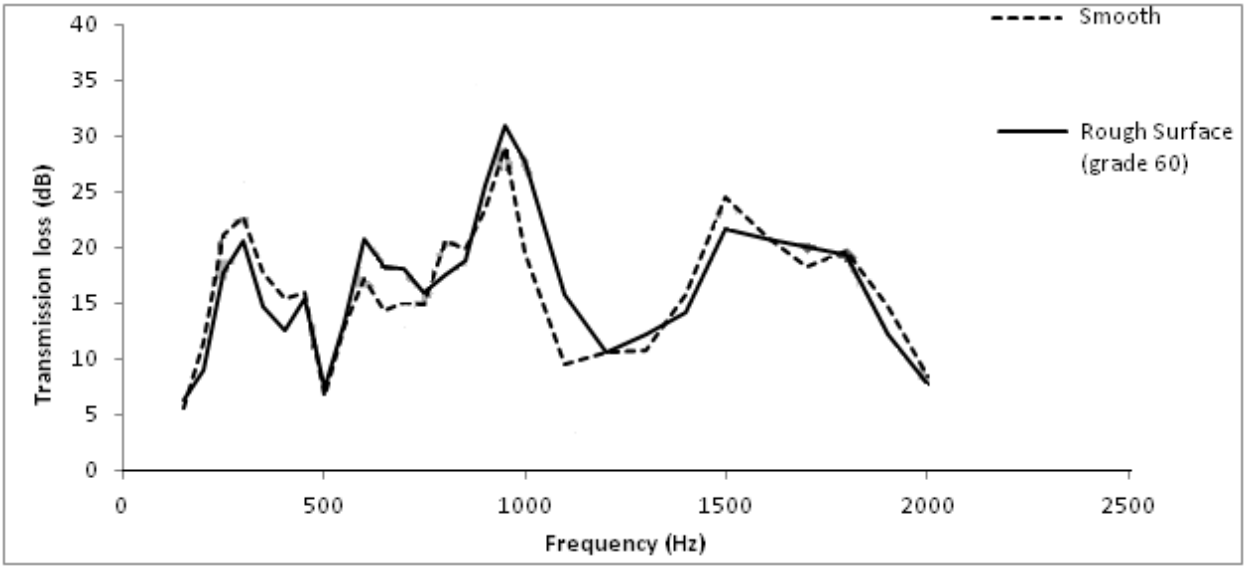

Figure 7: Transmission Loss vs. Frequency graph for smooth surface and rough surface of Grade P60

In figure 7, TL is slightly lower in rough surface than in smooth surface for 150-400Hz range. From 400Hz to 700Hz, TL is higher in rough surface than in smooth surface. An average of 2.46dB greater TL is found in this range for rough surface. Again, in a small range of 750-800Hz, smooth surface gives slightly better attenuation. From 850Hz to 1400Hz, attenuation is greater for rough surface. Like every grade of surface roughness, highest difference in TL between smooth and rough surface is found at 1000Hz and it is 16dB higher in rough surface than smooth surface. After this frequency, TL for rough surface gets lower and higher than smooth surface rapidly but consecutively in discrete frequency range.

Five grades of rough surfaces were used to investigate the effects of surface roughness on transmission loss in muffler. Each grade of rough surface showed almost similar result. We have found that the transmission loss for rough surface gets higher and lower than smooth surface consecutively in different discrete frequency ranges. In our designed muffler, surface roughness improves the sound attenuation significantly from 400Hz to 1300Hz range. Higher transmission loss for rough surface than for smooth surface can also be found beyond this range, but the increase and decrease occur rapidly and for shorter frequency ranges. In each grade of rough surface, highest increase in transmission loss for surface roughness is found at 1000Hz.

4. Conclusion

This paper is focused on the experiment to determine if there is any contribution of surface roughness to noise attenuation in muffler. Throughout this study it was found that sound attenuation for surface roughness increases and decreases consecutively in different discrete frequency ranges. Surface roughness improves sound attenuation in some particular range of frequency. From 400Hz to 1300Hz, sound attenuation is greater for rough surface than for smooth surface. As we know that reactive muffler works better at lower frequency range and is designed considering that range, it can be helpful to make the internal surface rough.

References

[1] Bhat C. and Sharma S. S. (2010): “Design and Analysis of a Expansion Chamber Mufflers‟. –World Journal of Engineering, volume 7, supplement 3, 2010, ISSN: 1708-5284.

[2] Sabah E. and Ameen M. A. (2013): “Experimental Test for Noise Attenuation in Gasoline Engine with Different Types of Mufflers”. Journal of Engineering and Development, Vol. 16, No.4, Dec. 2012 ISSN 1813- 7822

[3] Jadhav V.S. and Ghatage D.M. (2002): "Noise Attenuation of Diesel Engine with Different Types Mufflers". – Mech. Eng. Dept. Govt. COE, KARAD – INDIA

[4] Mohiuddin A.K.M., Ideres M.R. and Hashim S. M. (2005); ‟Experimental study of noise and backpressure for silencer design characteristics” – Journal of Applied Science 5(7):1292-1298, 2005 ISSN 1812-5654

[5] Rahman M., Sharmin T. and Nur M.A. (2005): “Design & Construction of a Muffler for Engine Exhaust Noise Reduction”– ICME05-TH-47

6th BSME International Conference on Thermal Engineering (ICTE 2014)

Understanding of Host-Pathogen Interaction of HIV Infections Using Mathematical Modelling

S. K. Sahani*, A. Islam, P. Gain and M. H. A Biswas,1

Mathematics Discipline, Khulna University, Khulna-9208, Bangladesh

Abstract

The most urgent public health problem today is to devise effective strategies to minimize the destruction caused by the AIDS epidemic. We have discussed the concepts and methodologies in developing HIV modelling. Here we are not discussing about any invention of HIV modelling rather we focused in bringing the awareness to medical epidemiologists and public health providers of how to use mathematical model in epidemiology. We discuss the mathematical representation of HIV model and shown the shown if the basic reproduction number $R_0 \leq 1$, then HIV infection is cleared from the T-cell population. Whereas if $R_0 \geq 1$ the HIV infection persists. Within the parameter values, the chronic infection equilibrium W^* can be stable and periodic solution may exist. Our aim was to make an understanding between the mathematical model of HIV and the real life situation.

Keywords: Mathematical modelling; Host-pathogen; HIV; CD4+ T cells; Stability analysis.

1. Introduction

Mathematical modeling is basically referred to as a method of simulating real-life situations with mathematical equations to forecast their future behavior. Mathematical models have become the most important tools in analyzing the dynamics of infectious diseases over the years. An efficient preventive and control measure of the spread of a life-threatening pathogen mainly depends on an essential understanding of the mechanisms of that pathogen. Acquired Immunodeficiency Syndrome (AIDS) was first discovered in 1981 since then it has been considered as the most as most leading cause of mortality. To be practical mankind has never faced such a devastating, mysterious pandemic disease. At present, the most burning issue as the same time most dangerous phenomena is Human Immunodeficiency Virus (HIV). HIV is a retrovirus and a member of the lentivirus genus. A detailed background and survey on HIV is described in [4]. Numerous mathematical model has been developed to identify the characteristics of Human immunodeficiency virus. Most these models are generally formed with three compartments such as susceptible class, infective class and recovered class.HIV dynamic model, a set of ordinary differential equations (ODE) that describes the interaction between HIV virus and human body cells, has been proven useful for understanding the pathogenesis of HIV infection and developing treatment strategies. HIV mainly targets CD4+ T cells. The continuous attack of Human Immunodeficiency virus causes the depletion of CD4+ T cells and this leads people to gradually become a victim of Acquired Immunodeficiency Syndrome (AIDS). For this reason the count of CD4+ T cells is considered as the primary indicator of progression of HIV.

* Tel.:+88 01717-966483.
E-mail address: santosh.ku091205@gmail.com

1.1 Host-Pathogen interaction

Host–pathogen interactions are the interactions taking place between a pathogen (e.g. virus, bacteria) and their host (e.g. humans, plants). Host-pathogen interactions can be described on the population level (virus infections in a human population), on the organismal level (e.g. virus infects host), or on the molecular level (e.g. virus protein binds to receptor on human cell.

2. Mathematical model for HIV

Every basic model has three compartments and they are systematically studied to form a mathematical model. Since the way back to history and in present time there has been remarkable changes in modelling a real life phenomena to build a basic model. The HIV affect our system's CD4+ T cells and letter it leads to AIDS. Here we present a three compartmental model of HIV which has been taken from [17], letter it was developed by [21]. The CD4+ T cells grow in bone marrow and it has a production rate s and T cells have a death rate α , T cells multiply through mitosis with a rate r the T cell equation was developed in [21] was

$$\frac{dT}{dt} = s - \alpha T + rt(1 - \frac{T + T^*}{T_{\max}}) - KVT$$

Where $T_{\max}$ is the maximum level of CD4+ T-cell concentration in the body [11]. We then added the drug efficacy parameter ε whose value is in the range between [0 1] [1]. Our modified CD4+ T cell is

$$\frac{dT}{dt} = s - \alpha T + rt(1 - \frac{T + T^*}{T_{\max}}) - (1-\varepsilon)KVT$$

Hence our modified three compartmental model as

$$\begin{aligned} \frac{dT}{dt} &= s - \alpha T + rt(1 - \frac{T + T^*}{T_{\max}}) - (1-\varepsilon)KVT \\ \frac{dT^*}{dt} &= (1-\varepsilon)KVT - \beta T^* \\ \frac{dV}{dt} &= N\beta T^* - \gamma V \end{aligned} \qquad (2.1)$$

In this model T is concentrated as susceptible CD4+ T cells and T^*, V are infected CD4+ T cells and HIV virus. Parameters α , β and γ are natural turnover rate of uninfected CD4+ T cells, infected CD4+ T cells and virus. The population CD4+ T cells starts with a source or production rate s and dead cells with rate α are reduced from the total population. It has a logistic growth with $rt(1 - \frac{T + T^*}{T_{\max}})$ where r is the proliferation rate. In infected CD4+ T cells it has an infection rate which is concentrated as K . Each infected CD4+ T cell is assumed to produce N virus particles during its life time, including any of its daughter cells. On finding the reproductive number R_0 , one can determine if the disease becomes endemic in a population or not. If $R_0 < 1$, the disease vanishes, and if $R_0 > 1$, the disease spreads and goes to the endemic level.

2.2 Parameter Specification

If one wishes to use a mathematical model to make predictions about a particular individual or population, estimation of model parameters from data is crucial. The parameter we used for model (2.1) was directly taken from [21] and [1].

Table 1. Parameters used for model (2.1).

Parameter Description	Parameter symbol	Parameter value
CD4+ T cell source rate	s	0.1 $mm^{-3}{}_{day}{}^{-1}$
Uninfected CD4+ T cell turn-over rate	α	0.02 day^{-1}
Infected CD4+ T cell turn-over rate	β	0.3 day^{-1}
Virus turn-over rate	γ	2.4 day^{-1}
Drug efficacy	ε	0.5
CD4+ T cell infection rate	K	0.0027 $mm^{-3}{}_{day}{}^{-1}$

3. Positivity of the solutions

Lemma 3.1[16] Let $T(0) > 0,\ T^*(0) \geq 0,\ V(0) \geq 0 \in \Omega$, then the solutions $T(t)$, $T^*(t)$ and $V(t)$ of the normalized model system of equation (3.1) are positive.

Proof: We have $\frac{dT}{dt} \geq s - \alpha T \Rightarrow \frac{dT}{dt} + \alpha T \geq s$

On simplifying

$T \geq \frac{s}{\alpha} + (T - \frac{s}{\alpha})e^{-\alpha t}$ Hence $T > 0$ at $t = 0$ and also $t \to \infty$

Similarly we find T^* and V are positive.

$(T(t) > 0, T^*(t) \geq 0, V(t) \geq 0, \forall\, t \geq 0)$

3.2 Disease free equilibrium

Since we are dealing with disease free equilibrium, hence we use $T^* = V = 0$ as it is assumed to be that, there is no infection. Thus the above system reduces to $\Rightarrow T_0 = \frac{T_{\max}}{2r}[(r-\alpha) + \sqrt{(r-\alpha)^2 + \frac{4sr}{T_{\max}}}]$

Thus the disease free equilibrium is $W_0 = (T_0, 0, 0)$

Let $R_0 = \frac{KNT_0}{\gamma}$ be the reproduction number given as [17]. It represents the average number of secondary infection caused by a single infected T cell in an entirely susceptible T cell population, throughout its period. We proceed into next steps.

Proposition 1. [21]

If $R_0 \leq 1$, the infection free equilibrium is w_0 is globally asymptotically stable in $(T(t) > 0, T^*(t) \geq 0, V(t) \geq 0, \forall\, t \geq 0)$. If $R_0 \geq 1$ then w_0 is unstable.

Epidemiologically, proposition 1 above implies that HIV/AIDS can be eliminated from the community when $R_0 < 1$ if the initial size of the sub population of the model are in the basin of attraction of the disease free equilibrium w_0. That means if $R_0 < 1$, then on average, an infected individual produce less than one new infected individual over the course of infectious period and the infection cannot grow.

3.3 Stability of the infection free equilibrium point w_0

Now to determine the local stability of w_0, the following variation matrix is computed corresponding to equilibrium point w_0 .Consider the model (2.1), Let $x = \frac{dT}{dt}, y = \frac{dT^*}{dt}, z = \frac{dV}{dt}$ then Jacobian of the system (2.1) at w_0 is

$$J(\mathrm{W}_0) = \begin{bmatrix} -\alpha + r(1 - \frac{T_0}{T_{\max}}) - \frac{rT_0}{T_{\max}} & -\frac{rT_0}{T_{\max}} & -KT_0 \\ 0 & -\beta & KT_0 \\ 0 & N\beta & -\gamma \end{bmatrix}$$

Since $W_0 = (T_0, 0, 0)$. An eigenvalue of $J(\mathrm{W}_0)$ is $-\alpha + r(1 - \frac{T_0}{T_{\max}}) - \frac{rT_0}{T_{\max}} = -\frac{s}{T_0} - \frac{rT_0}{T_{\max}} < 0$

From the first equation of (2.1). The other two eigenvalues have negative real parts if and only if $\beta\gamma - N\beta KT_0 > 0$, i.e., $R_0 < 1$. If $R_0 = 1$, one eigenvalue is 0 and it is simple. If $R_0 > 1$, w_0 has a positive eigenvalue. w_0 is thus unstable with a two-dimensional stable manifold and a one-dimensional unstable manifold. We arrive at the following local stability result for w_0 .

4. Numerical Results

We have already discussed about the infection free equilibrium and have found the locally asymptotically stability of it. Now we consider the stability of chronically infected equilibrium W^*. When $R_0 > 1$ the chronic-infection equilibrium W^* may only be stable for r small or large. Our numerical solutions consistently show the existence of periodic solutions when W^* is unstable. For the numerical result we use the parametric values used in Table 1 taken

from [21] and [1] but with the variation of r. More generally $s = 0.1\ mm^{-3}day^{-1}$, $\alpha = 0.02\ day^{-1}$, $\beta = 0.3\ day^{-1}$, $\gamma = 2.4\ day^{-1}$, $K = 0.0027\ mm^{-3}day^{-1}$, $T_{\max} = 1500\ mm^{-3}$, $N = 10$. Here we have shown local stability of both the healthy CD4+ T cells and HIV virus at r=0.005 [Figure 1.], letter we observed that, at the value of $r = 0.05$ and $r = 3$ W^* [Figure 2 and Figure 4] is globally stable whereas at $r = 0.8$, W^* is unstable and a periodic solution exists.

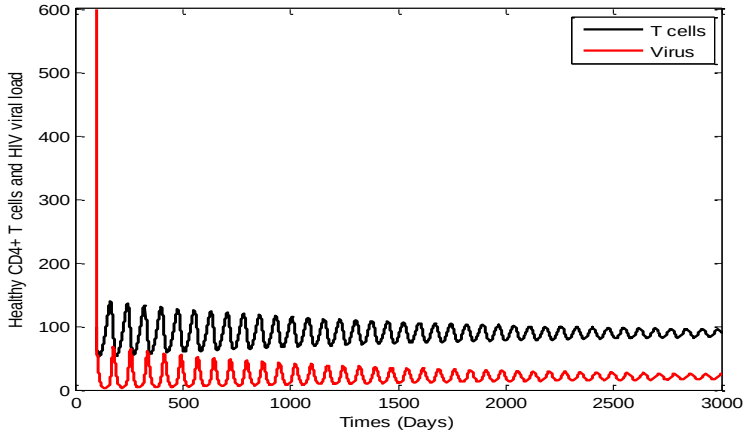

Figure 1. CD4+ T cells and HIV viral Load stability at r=0.05

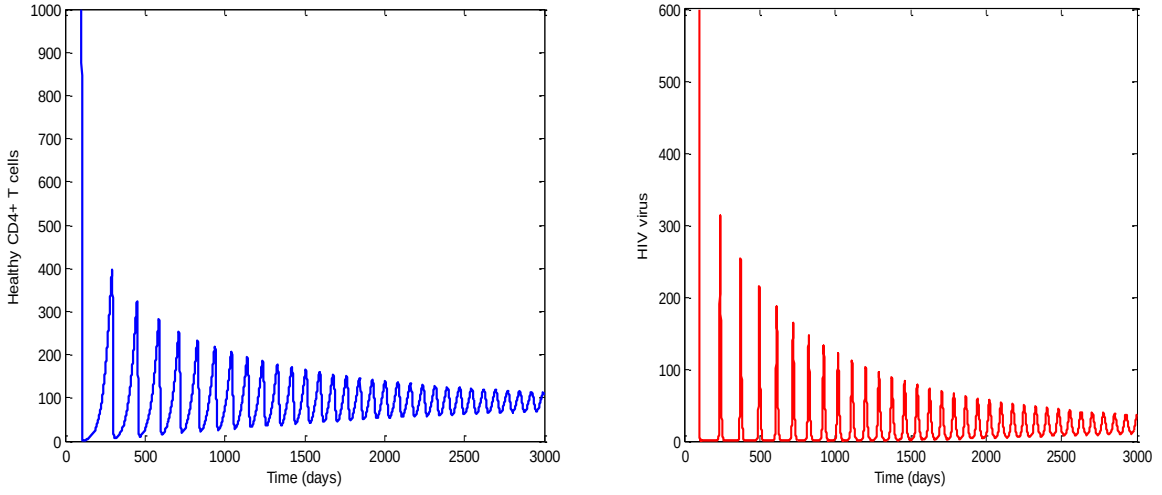

Figure 2. Using the parameter values of table 1 W is globally stable when r=0.05*

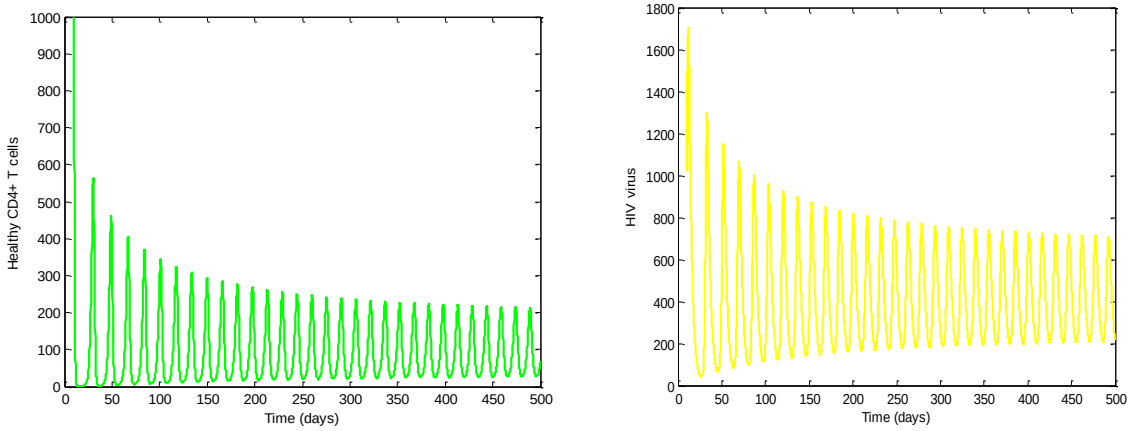

Figure 3. When r=0.8 a periodic solution is observed

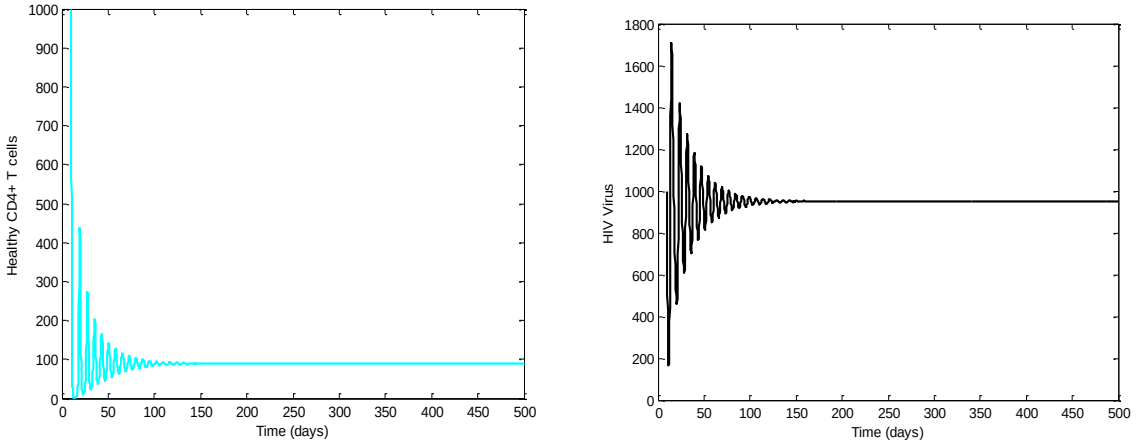

Figure 4. When r=3 W is globally stable*

For the stable and unstable solution of W^* corresponding with the values of r we have used the polynomial $F(\rho) = A\rho^3 + B\rho^2 + C\rho + D$ used in [21]. Where $A = 5.24\times10^6, B = 7.5\times10^4, C = -110, D = 0.6\times10^{-2}$ and whose three roots are $\rho_1 = 0.000062302, \rho_2 = 0.0012745$ and $\rho_3 = -0.0157105$. We observe W^* is unstable within the range of r between 0.093453 and 1.9118. From Figure 4 we observe viral load 600 mm^{-3} persists when $r = 3$ while it is below 100 mm^{-3} when $r = 0.05$. When $r = 3$ the initial oscillation disappear after 200 days whereas when $r = 0.05$ the damped oscillation are clearly visible after 2000 days. We also note that the values of R_0 in these three cases are related.

5. Conclusion

HIV has been considered as the most threatening issue over more than 30 years. The HIV pandemic disease is highly related to humans CD4+ T cells. We started our model with the logistic growth term $rT(1-\frac{T+T^*}{T_{\max}})$ as detailed in [21] which is assumed to be the growth of logistic healthy T cells, where T^* indicated as infected CD4+ T cells. The growth of the healthy T cells are decreased by the infection HIV. We also added a probability term ε with the infected

T cells. Models with these two different growth terms have the same basic reproduction number $R_0 = \frac{KNT_0}{\gamma}$, where T_0 is considered as equilibrium of CD4+ T cells in the absence of HIV infection. At disease free equilibrium point the model is assumed to stable and letter we conclude the stable and unstable condition of the chronic infected equilibrium points. With the proliferation term r and reproduction number we find the solution of it. We have used MATLAB to find the numerical solution at different equilibrium points and have observed the curve in periodic and damped oscillation. The global stability of W^* is established in [15] for HIV models with simplified logistic growth. The analysis in [15] relies in an essential way on the fact that the model is competitive. Models (2.1), with a complete logistic term, is no longer competitive.

Acknowledgements

The author would like to thank Mathematics Discipline of Khulna University, Bangladesh for all sorts of logistic supports while preparing this manuscript. The author would also like to thank the reviewers for the careful reading of this manuscript and their fruitful comments and suggestions which help to incorporate further modifications and developments of this manuscript.

References

[1] B.M. Adams, H.T. Banks, M.Davidiana, Hee-Dae Kwon, H.T. Tran, S.N.Wynne, E.S. Rosenberg, HIV dynamics: Modeling, data analysis, and optimaltreatment protocols 2004.
[2] H. T. Banks, D. M. Bortz, A parameter sensitivity methodology in the context of HIV delay equation models. Center for Research in Scientific Computation Box 8205, North Carolina State University Raleigh, NC 27695-8205, 2002
[3] M. H. A. Biswas, *Necessary Conditions for Optimal Control Problems with State Constraints: Theory and Applications*, PhD Thesis,Department of Electrical and Computer Engineering, Faculty of Engineering, University of Porto, Portugal, 2013.
[4] M. H. A. Biswas, AIDS epidemic worldwide and the millennium development strategies: A light for lives. *HIV and AIDS Review*, 11(4): 87-94 (2012).
[5] M. H. A. Biswas, Paiva LT, de PinhoMdR. A SEIR Model for Control of Infectious Diseases with Constraints. Mathematical Biosciences and Engineering, 11(4): 761-84 (2014).
[6]] M. H. A. Biswas, On the Evolution of AIDS/HIV Treatment: An Optimal Control Approach. *Current HIV Research,* 12(1), (2014), 1—12.
[7] M. H. A. Biswas, On the Immunotherapy of HIV Infections via Optimal Control with Constraint. Proceedings of the 18th International Mathematics Conference 2013, March 20—22, (2014), 51—54.
[8] M. H. A. Biswas, Optimal Chemotherapeutic Strategy for HIV Infections-State Constrained Case, Proceedings of the 1st PhD Students Conference in Electrical and Computer Engineering, Department of Electrical and Computer Engineering, Faculty of Engineering, University of Porto, Portugal on 28-29 June, 2012.
[9] M. H. A. Biswas, Optimal Control of Nipah Virus (NiV) Infections: A Bangladesh Scenario. *Journal of Pure and Applied Mathematics: Advances and Applications*, 12(1): 77—104, 2014.
[10] M. H. A. Biswas, Model and Control Strategy of the Deadly Nipah Virus (NiV) Infections in Bangladesh. Research & Reviews in BioSciences, 6(12), pp. 370—377, 2012.
[11] D.S.Callaway, A.S.Perelson, HIV-1 infection and low steady state viral loads, Bull.Math.Biol.64 (2001) 29–64.
[12] CM Durand, Blankson JN, Siliciano RF. Developing strategies for HIV-1 eradication. Trends in Immunology 2012; 33(11): 554-62.
[13] D Kirschner, Webb GF. Immunotherapy of HIV-1 Infection.Journal of Biological Systems, 6 (1): 71-83 (1998).
[14] MMO Labeodan, Stochastic Analysis of AIDS Epidemiology. Ph D Thesis, Faculty of Natural and Agricultural Sciences, University of Pretoria, Pretoria, (2009).
[15] P. D. Leenheer, H.L. Smith, Virus dynamics: a global analysis, SIAM J. Appl. Math. 63 (2003) 1313.
[16] R Nura. Modelingand optimal control strategy for HIV/AIDS disease in the presence of infective immigrantsand non-linear incidence 2013.
[17] A.S. Perelson, D.E. Kirschner, R. de Boer, Dynamics of HIV infection of CD4+ T cells, Math. Biosci. 114 (1993) 81.
[18] A.S.Perelson, P.W.Nelson, Mathematical analysis of HIV-1 dynamics in vivo, SIAM Rev.41 (1999) 3-44.
[19] Y. Roy, R.C. Host-pathogen interface: Ultrastructure of Salmonella virulence. Proc. XXIV Ann. conf. Electron Microscopy and allied fields Vol. CB-KS (2001).
[20] RP Walensky, Paltiel AD, Losina E, *et al*. The survival benefits of AIDS treatment in the United States. J Infect Dis. 2006; 194 (1):11-19.
[21] L. Wang, Michael Y. Li, Mathematical analysis of the global dynamics of a model for HIV infection of CD4+ T cells, Mathematical Bioscience 200 (2006), 44-57.

6th BSME International Conference on Thermal Engineering (ICTE 2014)

Study of Different types of Vegetable Oils as fuel sources and their performance analysis

Anup Saha[a], Ekramul Haque Ehite[a], Tanvir Hassan[a], M.M. Alam[b]1

[a]*Bangladesh University of Engineering and Technology, Dhaka-1000, Bangladesh*
[b] *Professor, Dept. of Mechanical Engineering,Bangladesh University of Engineering and Technology, Dhaka-1000, Bangladesh*

Abstract

In this research, Vegetable oils derived from Sesame Seed and Rice Bran are used and experimented upon. Using Kerosene as the solvent in varying proportions (30%, 50%, 70% by volume) with the pure vegetables oils, different blends of Sesame and Rice Bran Oils were produced. The important characteristic properties were found by experimentation, and compared with those of Straight Run Diesel. Subsequently, Straight Run Diesel, vegetable oils and their blends were used to run a diesel engine one-by-one and the performance analysis was done. From the comparative performance analysis, it was found that Rice Bran oil shows better performance as a fuel than Sesame with regards to power production and specific fuel consumption.

(ICTE 2014).

Keywords: Sesame Oil; Rice bran Oil; Density; Viscosity; Heating Value; Carbon Residue; Property Test.

1. Introduction

The global energy requirement is increasing in an exponential rate, leading to increased reliance on fossil fuels like coal, gasoline, crude oil etc., especially for the transport sector. Declining crude oil reserve, global warming, air pollution etc. however, is shifting the interest from petrochemical fuels towards alternative fuels, e.g. vegetable oils.

P D Dunn and Wasan Jompakdee [1] provided statistical information regarding vegetable oil production, its demand cost analysis in Northern Thailand. Yagnima et al [2] worked with a single cylinder, direct injection, four-stroke, air cooled diesel engine applying four blends (20%, 40%, 60%, 80% by volume) of soyabean oil with kerosene as well as rapeseed oil with kerosene. The result shows that a blend of 20% vegetable oil with 80% kerosene by volume fairly improves the thermal efficiency of the test engine under high load. According to Bhattacharya and Reddy [3],

* Corresponding Author. Tel.: +08801731940509;
E-mail address: anupme787@gmail.com

in short term tests, vegetable oil's higher viscosity and lower volatility is the main concern of its poor performance. In long term test, rapid cocking of injector nozzle and other parts, e.g. piston heads, intake valves and exhaust valves, gumming up of the piston ring, higher lubricating oil contamination have been detected. Bari & Roy [4] carried out the experiment using kerosene blends with 50% RBO by volume running a 2 cylinder, 4 stroke, direct injection diesel engine at variable load conditions but at constant speed of 1500 rpm. Performance test results showed a slight decrease in rated power of the engine but an increase in thermal efficiency & Bsfc.The first known use of vegetable oil as fuel in a diesel engine was a demonstration of an engine built by the Otto Company and designed to burn mineral oil, which was run on pure peanut oil at the 1900 World's Fair [5]. Haq carried out short-term tests burning blends of sesame oil containing 50% kerosene and 50% sesame in diesel engine. The viscosity of this blend was comparable to that of diesel, and the engine performance with this blends also become close to that of diesel [6]. Morshed employed preheating technique to the crude sesame oil and also to the 80% sesame blended with 20% diesel fuel oil and their effects was investigated on a direct injection, 4 stroke, 3 cylinder diesel engine. The performance parameters of the blend preheated at 100°C become very close to that of diesel fuel [7].

Nomenclature

Bmep	Brake mean effective pressure
Bsfc	Brake Specific fuel consumption
K	Kerosene
S	Sesame
RBO	Rice Bran Oil

2. Fuel Property Test

The following fuel samples have been tested:

- 100% Diesel
- 100% Sesame
- 100% Rice Bran
- 30% Sesame + 70% Kerosene
- 50% Sesame + 50% Kerosene
- 70% Sesame + 30% Kerosene
- 30% Rice Bran + 70% Kerosene
- 50% Rice Bran + 50% Kerosene
- 70% Rice Bran + 30% Kerosene

2.1 Density

Fig.1(a) shows variation of density for different fuel blends. Density decreases with increasing temperature regardless of fuel tested. RBO and its blends shows higher density than Sesame oil and its blends. However density of S30 and R30 blends is close to diesel at all tested temperatures.

2.2 Viscosity

ASTM D445 method has been applied to measure the viscosity, shown in Fig. 1(b). Sesame's viscosity is about 8 times higher than that of diesel fuel and Rice Bran is about 9 times higher in the room temperature. Pre-heating the blends to 100 ° C would cause to achieve comparable viscosity as that of diesel fuel at room temperature.

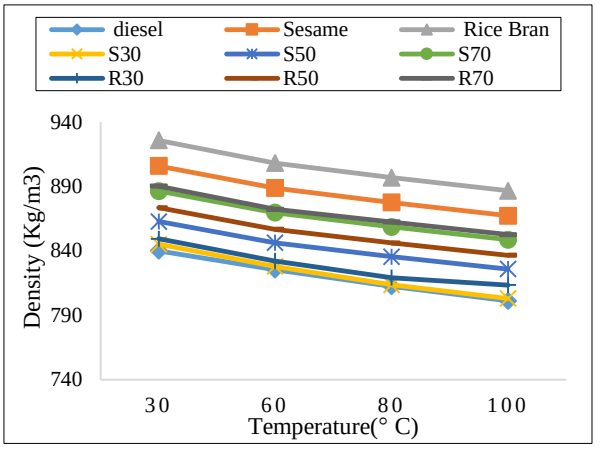

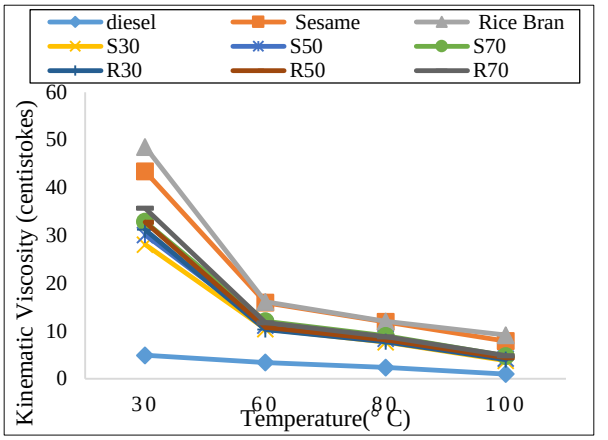

(a) (b)

Fig. 1. (a)Density variation of different fuels ; (b) Variation of viscosity

2.3 Heating Value

From figure 2 it is observed that, diesel fuel has heating value about 41.4 MJ/Kg. Compared to Diesel, Pure Sesame and Rice Bran have lower heating values. But as the proportion of kerosene increases, Heating values also rise. Among the blends, the R30 gives better result.

2.4 Carbon Residue

Conradson Carbon Residue (CCR) method is used to determine the carbon residue in fuels. From fig. 3(a) it is found that carbon residue for the vegetable oils is higher than fossil diesel. As vegetable oils contain higher amount of Free Fatty Acid (FFA), so their carbon residue is higher than that of petro-diesel.

2.5 Flash Point and Fire Point

Standard testing method ASTM D90 has been applied to detect flash point and fire point. Fig. 3(b) illustrates that flash point and the fire point for the vegetable oils is much higher than fossil diesel. At lower temperature, not enough vegetable oil fuel evaporates to form a combustible mixture. A higher flash point and fire point results in reduced fire hazard and increased fuel transportability for the vegetable oil .

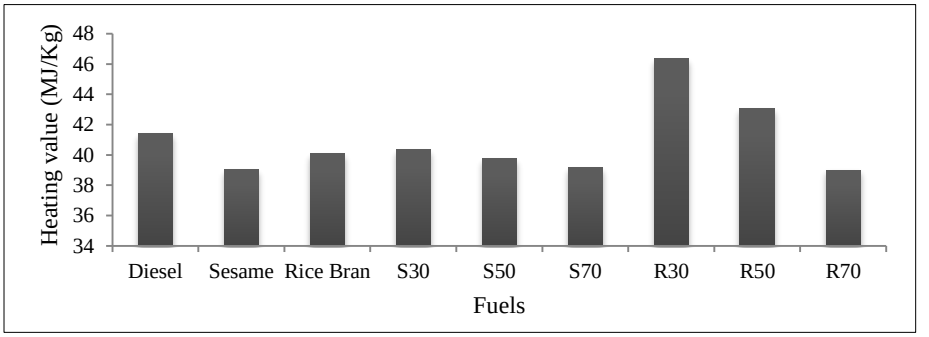

Fig. 2. Heating values of different fuels

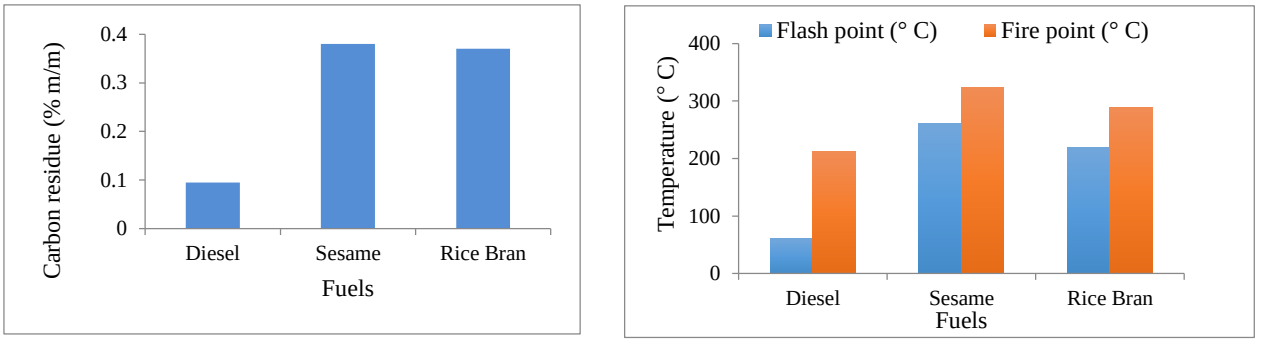

(a) (b)

Fig. 3. (a) Carbon Residue Percentage; (b) Flash point and fire point

3. Engine Performance Analysis

Performance tests have been performed on a single cylinder, four stroke diesel engine. The engine was maintained at rated rpm of 2200 rpm. Load was varied from 50% of rated load (3.6 kg) to 110% of rated load (around 8 kg). A hydraulic brake dynamometer directly coupled with the engine was used to load the engine. Load was varied by changing the water flow rate. Fuel supply system was modified, so that fuels could be supplied through a graduated burette. Fuel consumption rate was recorded by observing the time using a stop watch for every 30 ml of fuel. Speed was measured by digital tachometer and exhaust, lube oil and fuel inlet temperature was measured by using K-type thermocouple. Preheating was done manually using gas burner. Major engine specifications is shown in table 1.

Table 1.Major Engine Specifications

Brand Name	CHANGTUO
Model & Engine No	S1100A2 & 50393884
Manufacturer	CHANGCHAI CO. LTD
Type	Horizontal, Single Cylinder, four stroke, water cooled
Combustion Chamber	Swirl combustion chamber type
Rated Output & rpm	16 hp & 2200 rpm
Cylinder Bore & Piston stroke	100 mm & 115 mm
Net weight	160 kg

3.1 Brake Specific Fuel Consumption (Bsfc)

Variations of Bsfc with Bhp is shown in fig. 4. As load increases, Bsfc falls down and after reaching a minimum value, it rises again with load. The load corresponding to minimum Bsfc is particularly important since maximum thermal efficiency is attributed to this load. Sesame & Rice bran oil and blends rich with vegetable oils exhibits higher Bsfc than diesel. However, blends with 30% Rice bran, 50% Rice Bran and 30% Sesame exhibit lower Bsfc than diesel at any loading . Among them, blend 30% Rice Bran oil results in lowest Bsfc than any other blends.

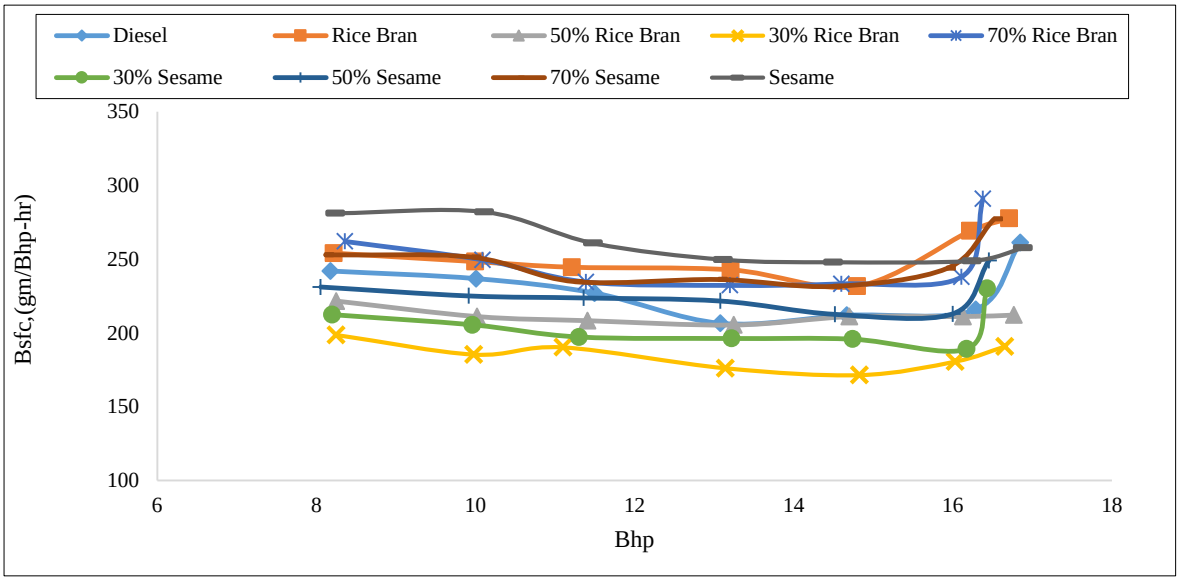

Fig. 4: Brake Specific Fuel Consumption

3.2 Exhaust Gas Temperature

Fig 5 represents variation of exhaust gas temperature with Bhp. Although there was not very significant variations in exhaust temperature, it is observed that 30% S, 30%RBO, 50% RBO blends have lower exhaust gas temperature than diesel oil, so possibility of lower NO_x formation. Except 50%S, other fuels have exhaust temperature higher than diesel.

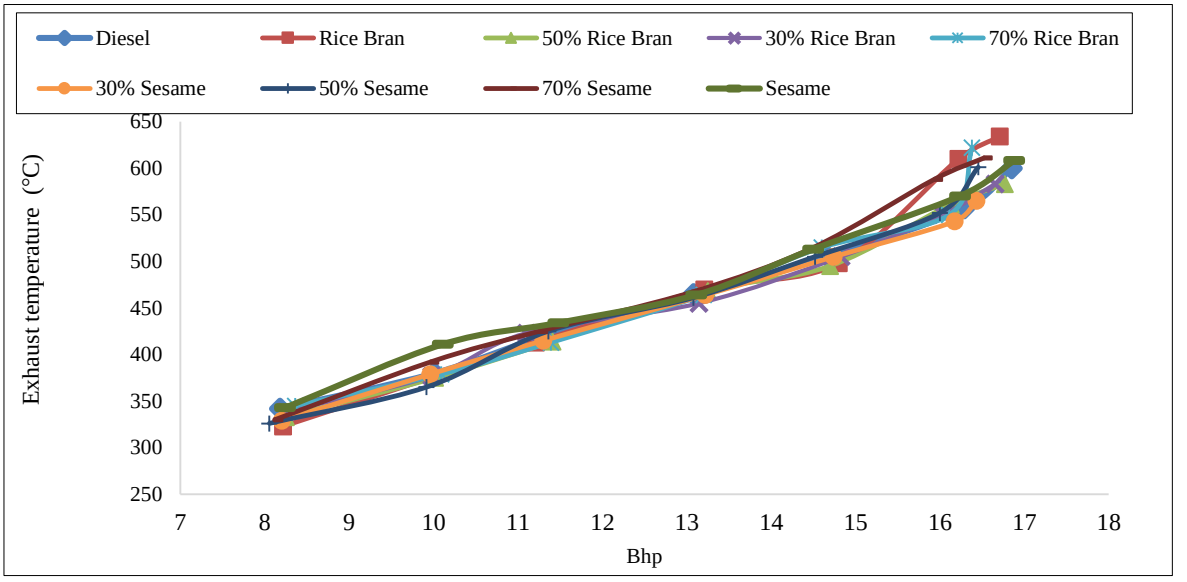

Fig. 5: Exhaust gas temperature

4. Cost Analysis

Cost analysis is very important for comparing the performance of different fuels. For introducing the preheating system for pure RBO and Sesame oil, it does not require much of initial investment. Only need a new fuel tank and oonew piping system. Heating energy can be used from the exhaust gas and for that an extra heat recovery system may be introduced, but it will not cost significantly, specially for a stationary engine. Table 2 shows the costs associated with various fuel samples.

Table 2. Cost of fuels:

Fuel Sample	Cost
Diesel	68
Sesame (S)	190
Rice Bran Oil (RBO)	148
Kerosene(k)	75
30% S + 70%k	109.5
50% S + 50%k	132.5
70% S + 30%k	155.5
30% RBO + 70%k	96.9
50% RBO+ 50%k	111.5
70% RBO+ 30%k	126.1

5. Conclusion:

Although from cost analysis, it may seem quite extravagant to use vegetable oils instead of Diesel. But since fossil fuel resources are declining rapidly, these alternative fuels might be a viable option in the near future. Property test results show that properties of the tested samples are comparable to diesel at higher temperature. So prior to supply into the engine, they must be preheated due to the higher viscosity and density of the vegetable oils at room temperature. Performance of the tested engine is somewhat better for Rice bran oil than Sesame. So this study concludes that Rice Bran Oil and Sesame oil can be used in the diesel engine with good efficiency.

References

[1] P.D. Dunn, W. Jompakdee, The use of vegetable oils as a diesel fuel substitute in Thailand , Proceeding of the Fourth International Conference on Small-Engines and their Fuels, Chiang Mai, Thailand, 21-24 September, 1993.

[2] F. Yaginama, S. Moriya, N. Isshiki, Study of Small high speed diesel engine with multi-fuels (blended fuels of Kerosene-vegetable oil), Proceeding of the Fourth International Conference on Small-Engines and their Fuels, Chiang Mai, Thailand, 21-24 September, 1993.

[3] Bhattacharyya, S., and C. S. Reddy. "Vegetable Oils as Fuels for Internal Combustion Engines: A Review." Journal of Agricultural Engineering Research ,57, (1994): 157.

[4] S. Bari , M.M. Roy , Prospect of Rice Bran Oil as an Alternative to Diesel fuel, Small- Engines, their Fuels and the Environment, Fifth International Conference, University of Reading , U.K., 5-7 April ,1995.

[5] Knothe, Gehard, Historical Perspectives on vegetable oil-based diesel Fuels, Inform 12(11):1103-1107; Retrieved 2009-06-24.

[6] M.Z Haq, Study of the Properties of Vegetable Oil as An Alternative To Diesel Fuel, M.Sc. Thesis, Department of Mechanical Engineering, Bangladesh University of Engineering and Technology, 1995.

[7] A. M. Morshed, Sesame Oil as an Alternative Fuel for Diesel Engines in Bangladesh, M.Sc. Thesis, Department of Mechanical Engineering, Bangladesh University of Engineering and Technology, 2008.

6th BSME International Conference on Thermal Engineering (ICTE 2014)

Analysis of effect of absorptive materials on performance of an acoustic board

Farhan Arafin[a], Erfanul Alam [b], M Ashiqur Rahman[a,b] *

[a]*70/a 2nd lane , Kalabagan, Dhaka-1211 , Bangladesh*
[b]*Room -318 , Ahsanullah Hall BUET, Dhaka-1415 , Bangladesh*
b

Abstract

Noise control and its principle play an important role in creating an acoustically pleasing environment. Acoustic boards are solid obstructions built between noise sources that are designed to be "line of sight" interruptions between the noise source and the receiver. This paper deals with a practical approach to design, develop and test an acoustic board where sound transmission loss is measured experimentally and compare with empirical value. Absorptive material plays a vital role in the performance of an acoustic board. The variation in performance characteristics, i.e. noise reduction capability of the acoustic board with three different absorptive materials is measured experimentally and the results have been compared to study of effect. The frequency of the transmitted sound ranged from 100 Hz to 3000 Hz. Transmission loss is increased because of the use of the absorptive material. At different frequencies an increase of 6 dB in transmission loss at different frequencies has been seen while using glass wool as absorptive material, whereas for foam it was found to be 4 dB.

* Corresponding author. Tel.: +8801737145986.
E-mail address: farhan.arafin.60@gmail.com

1877-7058 © 2015 The Authors. Published by Elsevier Ltd.
Peer-review under responsibility of organizing committee of the 6th BSME International Conference on Thermal Engineering (ICTE 2014).

Peer-review under responsibility of organizing committee of the 6th BSMEInternational Conference on Thermal Engineering (ICTE 2014).

*Keywords:*Transmission loss, Sound, Sound level, Acoustic board

Nomenclature

f Frequency, Hz
c Speed of sound, m./sec^2
N Fresnel number
ρ Density, kg/m^3
L characteristic length, m
T Temperature, K
τ Absorption coefficient

1. Introduction

An acoustic board (also called a sound wall, sound berm, sound barrier, or acoustical barrier) is an exterior structure designed to protect inhabitants of sensitive land use areas from noise pollution. There are two mechanism for noise control. Active noise control and passive noise control. Acoustic board is used for the passive control of noise. Acoustic boards (sometimes referred to as "noise barrier" or "sound walls") are intended to mitigate the effects of highway noise on activities near the highway. They do this primarily by blocking the direct path that sound must travel between the source of sound on the highway and the receiver exposed to the sound. Klingner and McNerney [1] reviewed the design process for highway acoustic boards, and presented a wide range of highway acoustic boards design satisfactorily. The information given in his report is intended to help Texas Department of Transportation designers produce highway acoustic boards that are effective from the viewpoints of acoustics, environment, traffic safety and structure. An introduction on synthetic materials for absorption was reviewed by Rahman and Raja [2]. They summarized on organic materials considerations for acoustic absorber in currently. Finally, they offered a review on research of using barrier and screens.

2. Theory of Acoustic board

Basically, acoustic boards reduce the sound level reaching receivers by blocking the straight-line path from the source to the receiver. While the perceived noise does not disappear, it is significantly reduced. According to Klingner and McNerney, by blocking the straight-line path even slightly, the noise barrier attenuates (reduces) the sound level at the receiver by about 5 dB. This attenuation is roughly equivalent to reducing the source noise by a factor of three (one-third the traffic). Making the barrier even higher, so that the sound is forced to travel along a longer path, usually produces an additional attenuation of at least 3 dB. The combined effect (a noise attenuation of 8 dB) is roughly equivalent to reducing the traffic by a factor of 6.factor of 6.

2.1 Hand Calculations of Transmission Loss

Insertion loss can be estimated by using the model proposed by Kurze and Anderson [3]. It is the result of compiling data of many researchers onto a single plot and developing a curve fit for a point source.

$$TL = 5dB + 20\log\left(\frac{\sqrt{2\pi N})}{\tanh\sqrt{2\pi N}}\right) dB \quad \text{up to } N = 12.5 \qquad 1(a)$$

$$TL = 20\ dB \qquad N > 12.5 \qquad 1(b)$$

N is defined as the Fresnel number, a nondimensional measure of how much farther the sound must travel as a result of the barrier. It is calculated with the following equation:

$$N = \frac{(a+b-l)}{c} f \tag{2}$$

"l" is the original length of the direct path from source to receiver, "*a"* and "*b"* are the lengths of the two straight-line segments comprising the path as modified by the acoustic board, "*f" is* the sound frequency in Hz, "*c" is* the speed of sound propagation in air (approximately 335 m/sec)

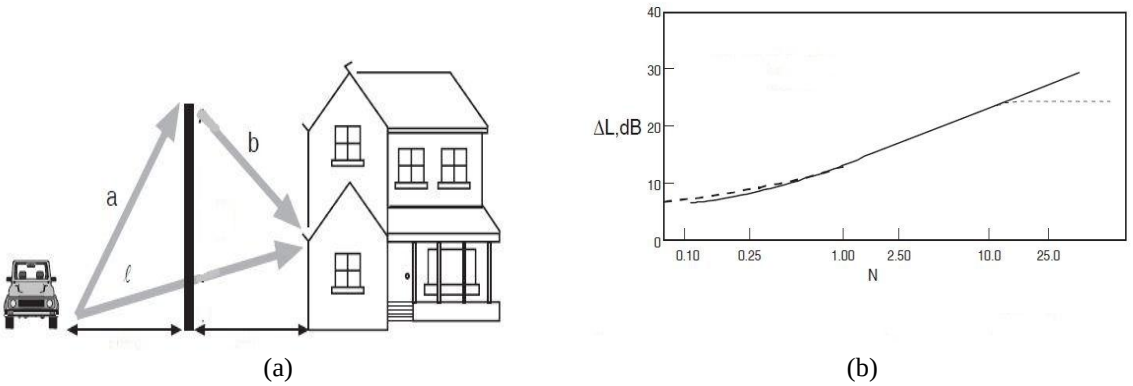

Fig.1. (a) Illustration of lengthened sound path due to acoustic board.; (b) Insertion loss versus Fresnel number for experimental and empirical data (solid line) according to Kurze and Anderson (1971)

3. Experimental Set-up

Figure 2(a) describes the setup of our experiment. We have used plywood to reduce the transmission of sound waves by restricting the amount that pass along and through the panel, sound reduction plywood is effective at a range of frequencies, while reducing the amount of weight needed to achieve these reductions, and also offering excellent strength/load carrying capacities. We have used perforated sheet in the front of the acoustic board. Perforated materials have many advantages of weight reduction; this is why perforated steel is preferred over other acoustic noise reduction material. As absorptive material glass wool and foam are used.

Setup particulars are as follows:

Height: 1.2192 m., Width: 1.2192 m., Thickness: 80.1 mm,

Total weight of the acoustic board – 53 kg, plywood thickness – 17.78 mm each, absorptive material thickness- 43 mm, surface area = 1.486 m^2, Surface density – 35.66 kg/m^2, base level of sound: 52 dB, temperature: 30^o C, measuring time span for each reading: 5 sec, position of board from sound source: 1 m

(a)

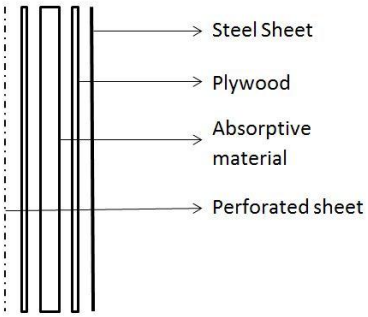

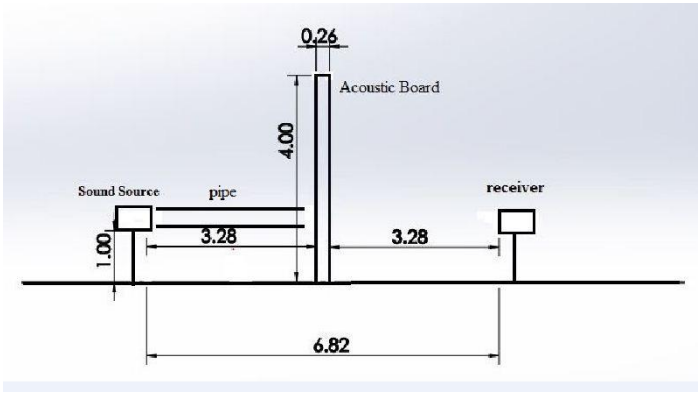

(b) (c)

Fig.2.(a) Acoustic Board used for the experiment; (b) Different layers of Acoustic Board; (b) schematic diagram of experimental setup

4. Results and Discussion

Figure 3 represents the transmission loss at different frequency when no absorptive material is used. Maximum transmission loss found in this process is 14 dB at 2800 Hz frequency. At this frequency the experimental transmission loss is closest to the empirical value. Minimum difference between the empirical transmission loss and the experimental one is 6.72 dB at 2800 Hz frequency.

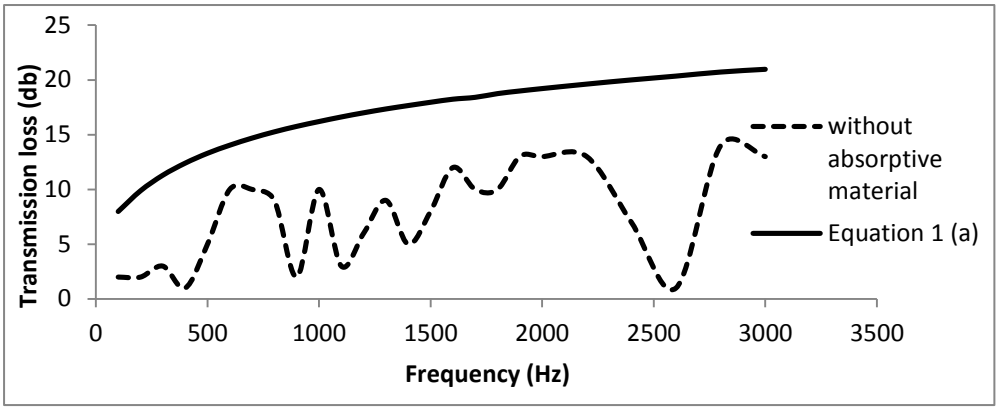

Fig.3. Transmission loss vs frequency (without absorptive material)

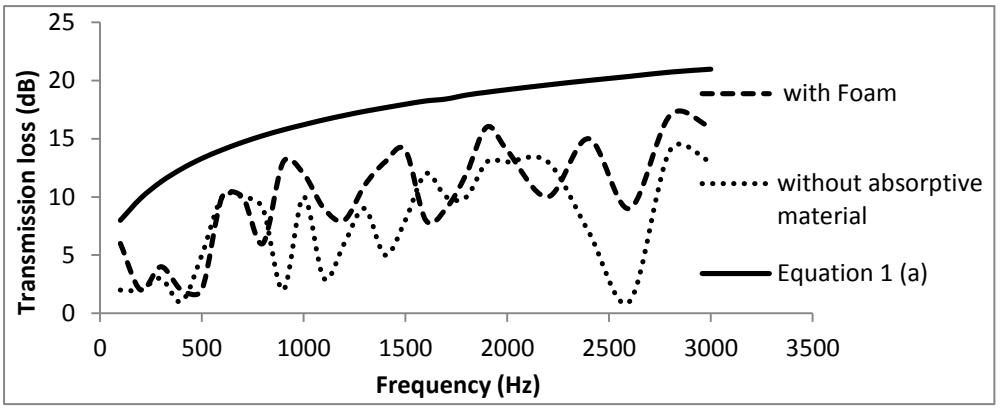

Fig.4: Transmission loss vs Frequency (foam as absorptive material)

Using foam as the absorptive material the result is shown in figure 4. It is seen that transmission loss increased a little. Maximum transmission loss found in this process is 17 dB at 2800 Hz frequency. At this frequency the experimental transmission loss is closest to the empirical value. Minimum difference between the empirical transmission loss and the experimental one is 1.98 dB at 100 Hz frequency.

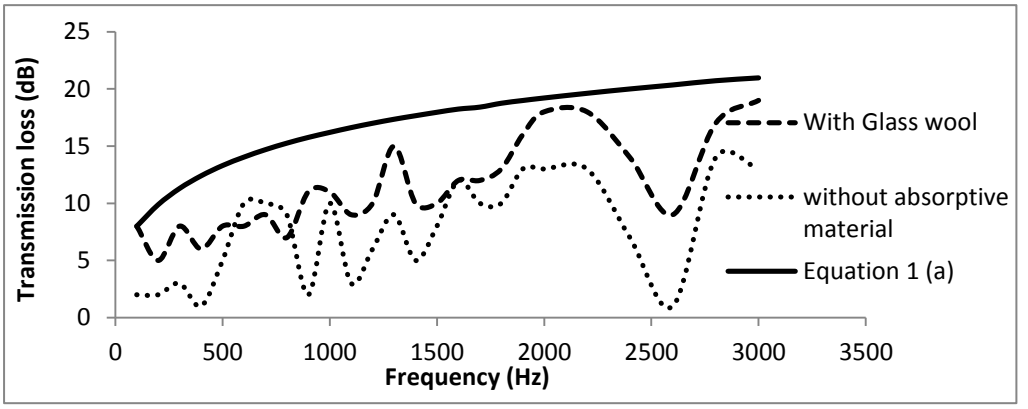

Fig.5. Transmission loss vs frequency (glass wool as absorptive material)

Figure 5 represents the transmission loss at different frequencies when glass wool is used as the absorptive material. There is a further increase in transmission loss because of using glass wool. The frequency where Minimum difference between the empirical transmission loss and the experimental one occurs shifted to left. It is now 1.21 dB at 2000 Hz frequency. Maximum transmission loss found in this process is 19 dB at 3000 Hz frequency. Comparison of transmission loss between the two absorptive materials is shown in the figure 6. It is seen that using glass wool as absorptive material increases the transmission loss. In 100-600 Hz range acoustic board with glass wool as absorptive material shows great noise attenuation. Again for frequency greater than 1800 Hz acoustic board gives the best performance. From figure 6 at 1 kHz acoustic board with foam as absorptive material gives the best performance. Maximum transmission loss in this frequency is 12 dB for foam. At 1kHz minimum difference between the empirical transmission loss and experimental transmission loss 4.2 dB.

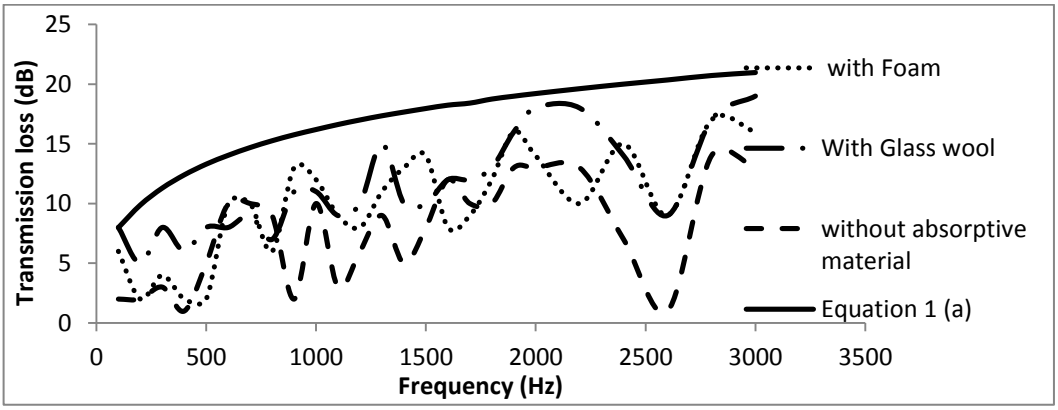

Fig.6. Transmission loss vs frequency (comparison between absorptive materials)

5. Conclusion

This experiment to examine the contribution of absorptive materials to noise attenuation. The performance of acoustic board is examined for two different absorptive materials. We can conclude our experiment by these outcomes, Absorptive materials improve the performance of acoustic board Acoustic board with glass wool as absorptive material have better transmission loss compared to board with foam as absorptive material. At different frequencies an increase of 6 dB (figure 6) in transmission loss is seen using glass wool as absorptive material, whereas for foam it is found to be 4 dB. Transmission loss at 1 kHz frequency for different absorptive materials are given below:

Table 1. STL at 1 kHz frequency for different absorptive materials

	Frequency	STL (dB)
Without absorptive material		10
With foam	1 kHz	12
With glass wool		11

References

[1] Klingner, R. E. and McNerney, M. T. (2002): "Design Guide for Highway Acoustic boards". – Research Report 0-1471-4.
[2] Rahman, L. A. and Raja, R. I. (2012): "Attenuation of Noise by Using Absorption Materials and Barriers". – International Journal of Engineering and Technology Volume 2 No. 7.
[3] Kurze, U. J. and Anderson, G. A. (1971): "Sound Attenuation by Barriers". – *Applied Acoustics* 4, pp.35-53.

6th BSME International Conference on Thermal Engineering (ICTE 2014)

Improved pyrolysis technology by using an opaque reactor preheated by solar collector

Md. Abdur Rahim[a], Muhammad Mahbubul Alam[b], Mohammad Rofiqul Islam[a], Md. Mehedi Hasan[a], Gobinda Mridha[a]

[a]*Rajshahi University of Engineering and Technology, Rajshahi-6204, Bangladesh*
[b]*Bangladesh University of Engineering and Technology,Dhaka-1000, Bangladesh*

Abstract

As energy crisis is going on in the world, so the attention of the scientists & engineers are turns to find out the alternative energy sources. Obviously energy source is limited, but try of mankind is unlimited & it is swimmingly. Looking for new things is the passion of mankind as well as scientists. According to this phenomena thermo chemical conversion processes such as gasification & pyrolysis have given a new foot print in the energy source. Performance & emission characteristics of pyrolytic oil are good, almost near to diesel. To obtain pyrolytic oil, we use scrap tires. In experimental work fixed bed reactor is used where solar energy is used for primary heating and charcoal is used for making desired heating condition. Bio mass is used because it is a replacement of fossil fuel & good energy source. As solar energy is used here, amount of charcoal is decreased. Our main objective is to use solar energy to decrease amount of charcoal as well as cost. Electricity may be used for heating the reactor but it is not efficient. In experiment double condenser (ice & water) is used to condense the gas. It is observed that it is possible to use tire pyrolysis oil in various sectors as an alternative fuel at present and future. In this manner it is found that 200 gm oil can be extracted from 500 gm scrap tube whose calorific value is about 3 MJ/kg. Again pyrolysis process does not give any bad effect to the environment i.e. this process is environment friendly. The produced tar is easily decomposed with soil so there is no problem. The only fact that a smell is produced which is reasonable.

Keywords: pyrolysis, bio mass, renewable energy, calorific value, alternative fuel;

Main text

The word “pyrolysis” comes from the Greek word “pyro” which means "fire" and “lysis” which means" separating". Pyrolysis is generally described as the thermal decomposition of the organic wastes in the absence of oxygen at temperature about 450° C. The products obtained from pyrolysis are - distillate oil, carbon char & hydrocarbon gas & other non condensable gases. The products obtained from pyrolysis are - distillate oil, carbon char & hydrocarbon gas & other non condensable gases. For pyrolysis process high amount of heat is the prime requirement. This high amount of heat cannot be obtained without firing in the reactor. Renewable solar energy can be used here for primary heating what we have done in our experiment but the obstacle is that we

could not combindly use solar energy & heat energy for firing. By only solar energy the pyrolysis process cannot be continued because tremendous amount of heat cannot be obtained by only solar heating from the perspective of Bangladesh.

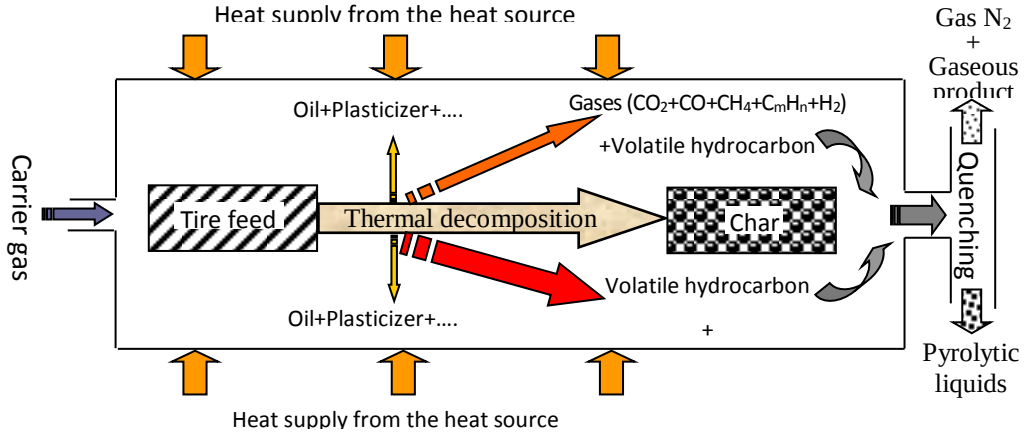

Fig. 1. Flow diagram of tire pyrolysis process

Nomenclature

HCV	higher calorific value
C	carbon
H	hydrogen
N	nitrogen
CH	hydrocarbon
Wt%	percentage of weight
O	oxygen
%	percentage

1. Solar Energy in Bangladesh

Solar Energy is a great source for solving energy crisis in Bangladesh. Bangladesh is situated between 20.30 and 26.38 degrees north latitude and 88.04 and 92.44 degrees east which is an ideal location for solar energy utilization. At this position the amount of hours of sunlight each day throughout a year is shown in the following graph in the Fig. 2. The highest and the lowest intensity of direct radiation in W/m² (Watts per square meter) are also shown in the following figure.

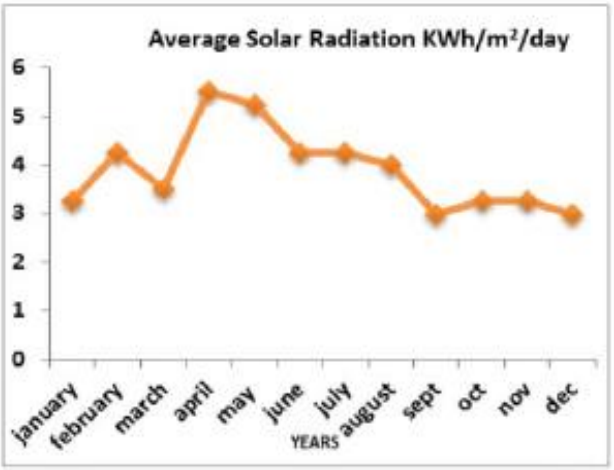

Fig. 2. Monthly average solar radiation profile in Bangladesh

2. Selection of feed material:

Every year huge amount of tires are produced from different types of vehicle. We have studied the approximate & elemental composition of it. Used tires price is also less & it is available, that's why we choose it. Proximate & elemental analysis of tires & tubes are given in the table below.

Table 1. An example of a table.

Proximate analysis (wt %)		Elemental analysis (wt %)	
Moisture	0.82	Carbon (C)	80.30
Volatile	62.70	Hydrogen (H)	7.18
Fixed carbon	32.31	Nitrogen (N)	0.50
Ash	4.17	Oxygen (O)	8.33
H.C.V (MJ/kg)	33.30	Others	3.69

3. Experimental setup & procedure:




Fig. 3. (a) Solar pre-heating by parabolic collector; (b) Experimental setup arrangement; (c) Feed material, reactor bed, burned charcoal & solid char (from the left)

Pyrolysis experiment is not so an easy work. The working process is quite hard. If solar system is added then it will become harder. At first the raw material which is used in this experiment was collected & having a good wash the materials were dried properly because the materials were collected from the used thrown materials. When it was completely dried, then the materials cut into small pieces (0.5 square inch). We took 500 gm as feed material and it was taken in the reactor. Then the reactor was put on the parabolic solar collector and it was heated about 50 minutes. The primary temperature of that day was 30℃ and after heating the reactor the inside temperature became 90℃. In the mean time our properly dried charcoal put in the bed in which firing takes place. The heated reactor then transferred quickly to the bed. For starting fire we have used negligible amount of paper & a little amount of kerosene (about 25-30 gm) which is negligible for much production. For pyrolysis system interior space of the reactor should inert i.e. interior space must be oxygen free. For making O_2 free we have used N_2 gas. After 15 sec interval N_2 gas was supplied for 15 sec. For burning charcoal air was supplied by the compressor from our laboratory. Blower can also be used for supplying air. Our reactor was sealed properly by gasket so that air cannot enter the reactor. By this time ice was collected & it was broken into small pieces. This is for ice condensing. Before we mentioned that we have used double condenser. Another is water condenser. By piping system counter flow heat exchanger was made. Both condensers are attested. When high amount of heat was obtained then from the reactor gases pass away through the exhaust port into the water condenser & then ice condenser. For condenser construction we have used copper pipe because of good conducting of heat. In the ice condenser copper pipe is in spiral shape so that conducting area can large in small length. As conducting area is large that's why more gases became condensed. At last we obtained 200gm oil from 500gm feed material. For thermal decomposition of 500gm feed material it required 4.5 kg of charcoal when solar energy is absent but when solar energy is present charcoal required 4 kg i.e. 0.5 kg charcoal is save. For this time required for solar heating 50 minutes & charcoal burning time 45 minutes. The inlet & exit temperature difference of water condenser is 5°C. After the experiment the amount of solid char obtained is 250gm. The Higher Calorific Value (HCV) of pyrolytic oil is 33.30 MJ/kg.

Reaction: The reaction takes place in pyrolysis system is given below-

$$C_aH_bO_c + \text{Heat} \longrightarrow H_2O + CO_2 + H_2 + CO + CH_4 + C_2H_6 + CH_2O + \ldots\ldots\ldots\ldots + \text{Tar(liquid oil)} + \text{Char} \quad (1)$$

4. Result & Discussion:

Many works have done on solar energy in the world. But here we have used solar energy combined with charcoal in pyrolysis system. Fig. 4. (a) we can understand easily the heating condition of the reactor with respect to the temperature. From the beginning we can see that temperature rise is more in starting time but in the ending time temperature rise is less. This means that it reaches in optimum condition. Heating condition also depends on solar intensity. If solar intensity is high then more high temperature will be obtained. If the sky is cloudy then efficiency will be fallen down, because it is totally depends on solar energy.

From Fig. 4. (b) we can see that by increasing time obtained oil is increases but when feed material is almost finish it suddenly fall down. Our system is not a continuous process; if continuous then it may be constant straight line after obtaining optimum level. From our experiment obtained oil & required charcoal (with & without solar energy) is represented by Fig. 4. (c). From both experiment for 500gm tire we got 200gm oil. Our experiment was prototype, as half kg charcoal is save in our experiment it means that 5 taka is save. But when it is in large scale then it will hope that it will beneficial.

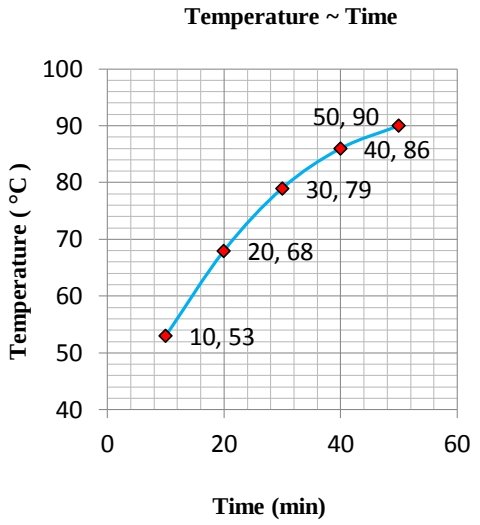

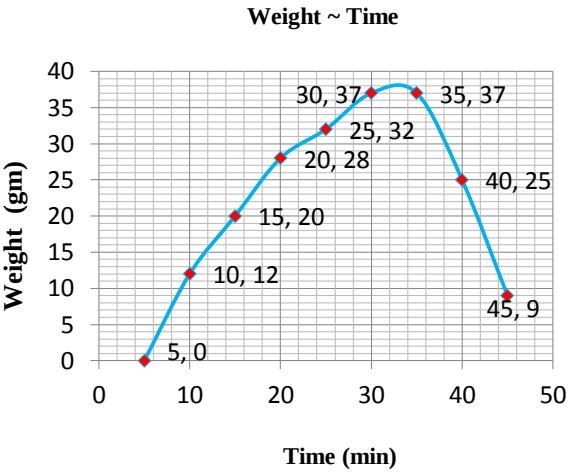

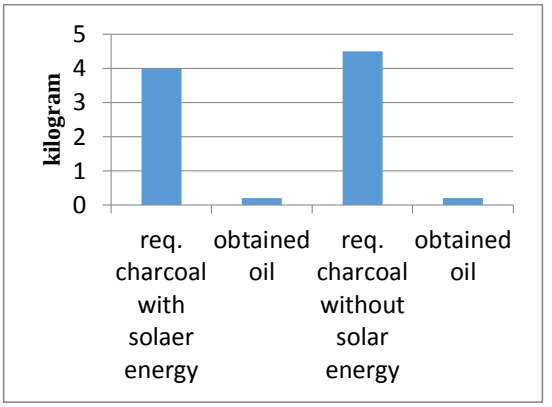

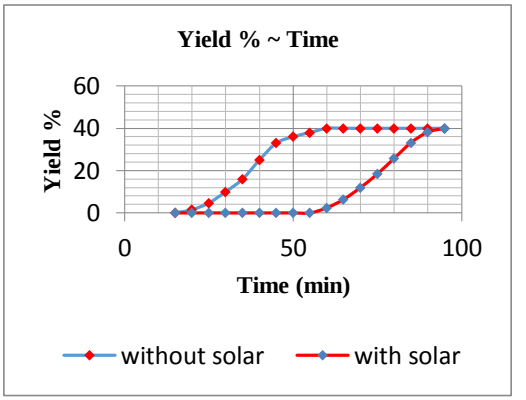

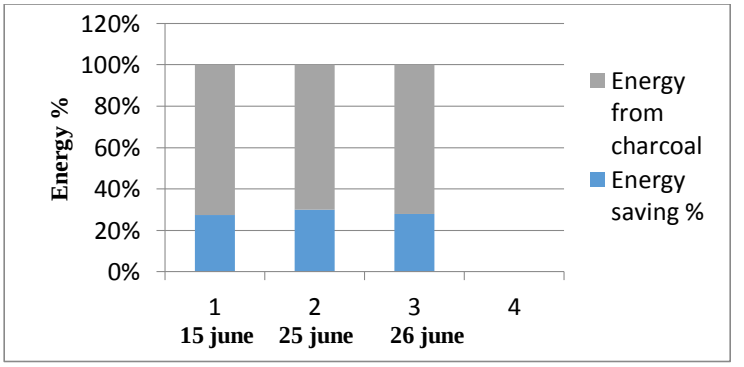

Fig. 4. (a) This curve shows the temperature variation according to time (b) It represents product output with respect to time (c) This shows that charcoal save by using solar energy for same amount of oil (d)These curve show yield % variation during time for using solar energy & without solar energy (e) Energy saving vs Date curve

From Fig. 4. (d) it can be seen that the experiment performed without solar energy required less time than performed with solar energy. From the beginning to 15 minutes the yield percent remains zero because during this time the feed material is preheated and reached the minimum pyrolysis temperature. Then the yield percent start increasing to 40% at the time of 60 minutes. On the other hand, the experiment performed with solar energy the yield % remains zero up to 55 minutes. Then gradually increases and reached to 40% within total time of 95 minutes.

From Fig. 4. (e) it can be seen that the percentage of saving energy is different in different date. The cause of variation of saving energy is that the weather is different in different date result a variation in the value of solar intensity .It has been also seen that the maximum energy saving is 30% at 25th June in 20014.So, in winter the energy saving must be less than energy saving in summer.

5. Conclusion:

Pyrolysis is the most effective process of converting the valuable liquid oils from various solid wastes like tire waste, organic wastes, plastic etc. For waste tires, pyrolysis is more suitable due to its low emission rate. The emission from the combustion of tires is lower than the combustion of solid coal. The pyrolytic liquids are more suitable as fuel than solid tires. By the proper filtration & purification of pyrolytic oil it may be the great source of good alternative fuel.

6th BSME International Conference on Thermal Engineering (ICTE 2014)

Design, construction and performance evaluation of a single plane balancing machine

Rifat Mahmud*[a], Abu Jafar Rasel[a], M. Ashiqur Rahman[b]

[a] *Graduate students, Mechanical Engineering, Bangladesh University of Engineering and Technology, Dhaka 1000, Bangladesh*

[b] *Professor, Department of Mechanical Engineering, Bangladesh University of Engineering and Technology, Dhaka 1000, Bangladesh*

Abstract

This paper focuses on the design, fabrication and performance evaluation of a single plane balancing machine. Here, the unbalanced force of the rotor is transmitted to the vibrating deflector via a support and the amount of deflection is converted to corresponding change in electric voltage by using a proximity sensor. The shaft position is measured with the help of a light sensor. All the data these two transducers gather are presented to the computer simultaneously to plot two graphs showing the binary values of the corresponding sensors vs. time. Comparing these graphs, the phase angle of the unbalanced force is determined. Further, the binary values of the proximity sensor is converted to corresponding displacement values. Using them for three known unbalanced masses, displacement vs. unbalanced mass graph is plotted. The amount of unknown unbalanced mass for a measured displacement can be found from this graph.

Keywords: dynamic balancing machine; vibrating deflector; proximity sensor; light sensor; binary values; phase angle; single plane rotor.

1. Introduction

Rotating machineries are commonly used in almost all mechanical systems. Vibration caused by mass imbalance is a common problem in such machineries. The current trend of rotating equipment towards higher power density clearly leads to higher operational speeds which cause much greater centrifugal imbalance forces [1].

Excessive vibration in rotating machinery can cause unacceptable noise and substantially reduce the life of bearings. Cyclic forces due to the out-of-balance are transmitted from bearings to a vibratory beam at points of

* Corresponding author. Tel.: +8801917517169.
E-mail address: 08rifat@gmail.com

application corresponding to the distance between bearings [2]. This unbalanced force is changed continuously with change in speed of the rotor and changing the dynamic behavior of the whole system continuously [3].

There are two types of unbalance, single plane (static unbalance) and multi-plane (dynamic unbalance). If the unit being balanced is very short in length in relation to its diameter, single-plane balancing will normally be acceptable. Traditional single plane balancing involves placing the unit on low friction bearings and allowing it to rotate and "settle" with the "heaviest" point falling to the bottom. Material is then removed from this point. This process is then repeated until no obvious "heavy" point seems to exist. Advancing this one stage further, the unit can be mounted on a purposefully built "Balancing Machine" that detects the "heavy" point electrically while it is being rotated. This increases the sensitivity and accuracy of the balance.

Single plane balancing machine is not a new concept. Martinson developed a balancing machine as early as 1870 [3]. On this machine the 'heavy spot' was marked by hand. At low speeds (sub-critical) the 'heavy' spot would coincide with the 'high' spot of the whirl according to Jeffcott's analysis [4]. Early balancers such as Weaver [5] realized that the balance weights and imbalances act as forces to the system. Weaver was aware that the forces at the bearing locations for a rigid rotor changed with the magnitude and phase of the imbalance weights.

Rathbone [6] used astrobo-vibroscope to study the vibration of a large rotor. Ribary [7] presented a graphical construction that balanced using only the amplitude taken from an initial run and three trial weight runs. Somervaille [8] considerably simplified the graphical construction of Ribary. Somervaille's construction is also known as the four circle method of balancing that is still in use today.

The literature review of balancing machine reveals that most of the earlier researchers focused on force transducers to find out the amount of unbalanced mass present in the test rotor. On the contrary, the distinct feature of the machine designed and constructed by the authors is that it uses only the displacement transducers to plot the reference curve from which the location and amount of unknown unbalanced mass are determined.

In the present paper the authors' main intense is to design a single plane balancing machine that can detect the position and amount of unbalance for a thin disk with electrical means, to construct it and to do some experimental study with it.

The rest of the paper is structured as follows. Section 2 presents the concept of the proposed machine with schemas and flowcharts. Section 3 shows the design and fabrication of the machine. Section 4 comprises of the experimental results obtained by using the fabricated machine. And lastly section 5 concludes the paper drawing the main directions for future work.

2. Concept of the proposed single plane balancing machine

Before starting the motor, the setup at a glance -

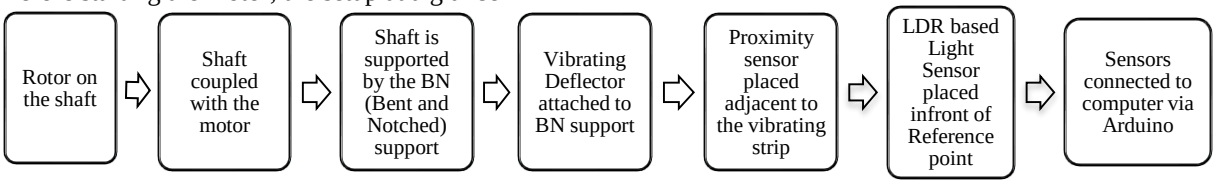

When rotor with unbalanced mass is attached to the machine and the motor is switched on -

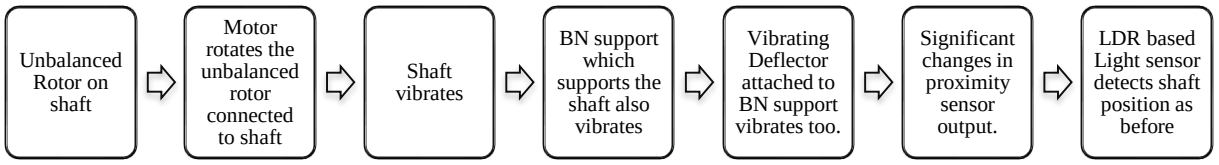

When proper balancing is done, to check whether actually the rotor is properly balanced or not

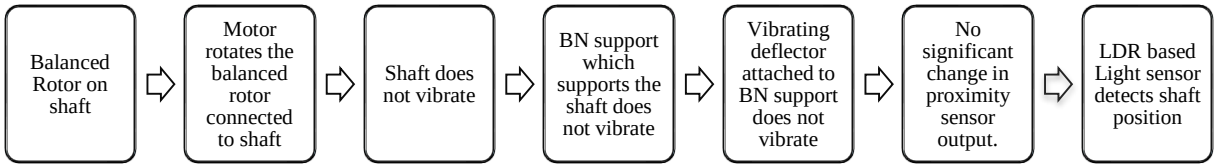

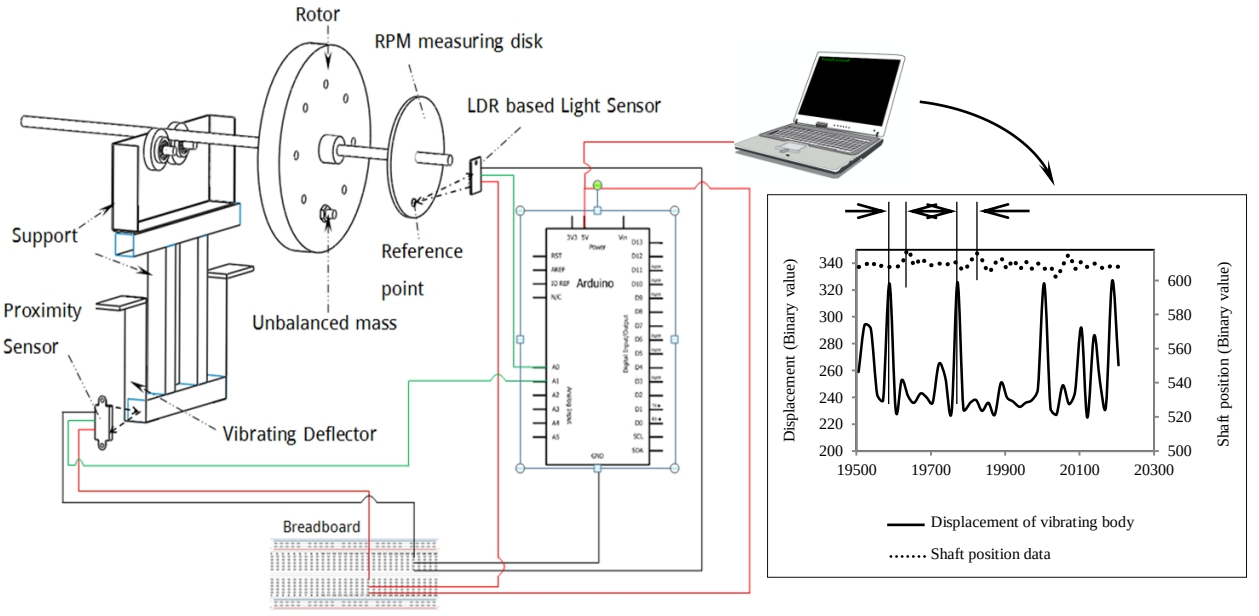

Fig. 1. Schematic diagram showing the basic working process with single plane unbalanced rotor.

3. Design and fabrication of the machine

Different parts of the setup were designed and assembled with SolidWorks 2012 software. The overall dimension of the setup is 125 cm × 60 cm × 55 cm which is the length, width and height respectively.

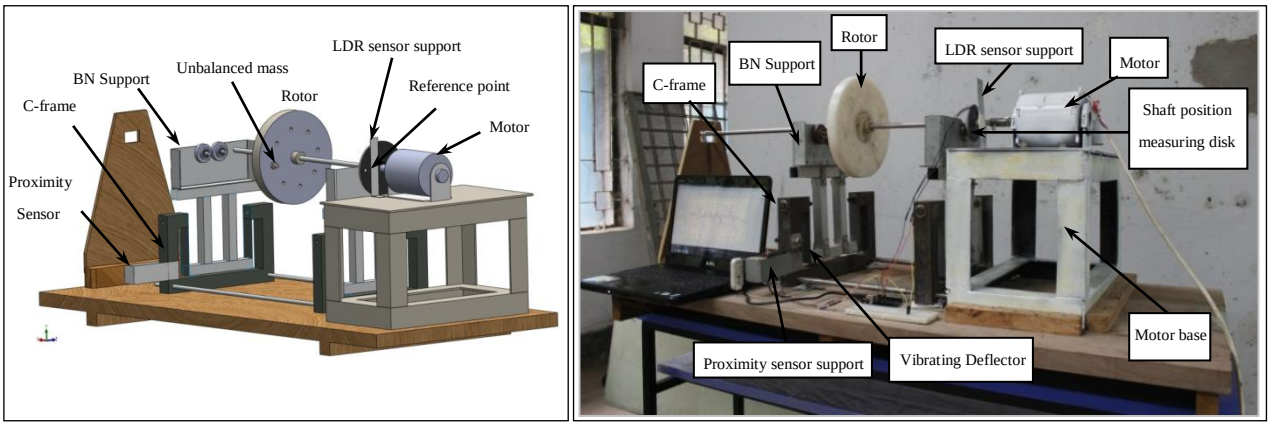

(a) (b)

Fig. 2. (a) Full design of the setup; (b) Fabricated balancing machine.

3.1. Mechanical parts design

Major mechanical parts of the machine include:

3.1.1. C-frame, BN support (Bent and Notched) and deflector attachment

The C-frame holds the vibrating deflector strips. There are 2 such frames casted from Cast Iron. To have a good surface finish, after casting they were machined in a shaper machine. The BN support provides support for the bearing bushings and transmits the resultant unbalanced force to the deflector strip. It is made of sheet metal after

properly being bent and notched. The upper part of the deflector attachment carries the BN support and the lower part is screwed to the vibrating deflector. The deflector attachment is made of 1"×1" square aluminium box channel.

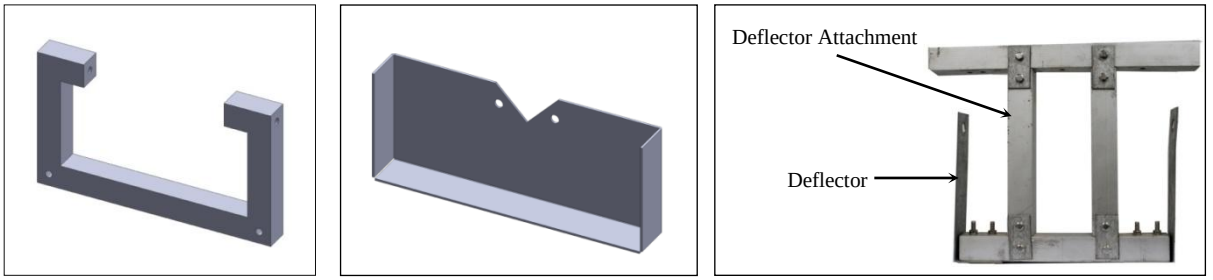

(a) (b) (c)

Fig. 3. (a) C-frame; (b) BN support; (c) Deflector attachment with vibrating deflector.

3.1.2. Rotor, shaft position measuring disk and sensor supports

Both the rotor and shaft position measuring disk material is Nylon. The radial holes on the rotor were drilled symmetrically by indexing in a vertical milling machine. Shaft position measuring disk carries the reference point that reflects light back to the LDR sensor. Rest of the disk is black that absorbs the incident light. It is used to generate shaft positioning curve. Proximity sensor support carries the proximity sensor to the predetermined distance (204 mm). It is made of sheet metal and bolted to the C-frame.

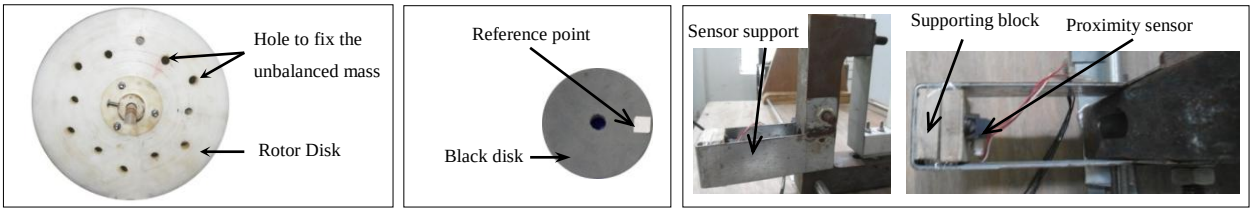

(a) (b) (c)

Fig. 4. (a) Single plane rotor; (b) Shaft position measuring disk; (c) Sensor support.

3.2. Electrical design

The primary transducers, proximity sensor and Light sensor, sense and digitalize the analog readings obtained from the vibrating deflector and shaft position measuring disk respectively. The digital data is sent to the computer via an Arduino board where they are monitored and captured to show the final output in graphical form.

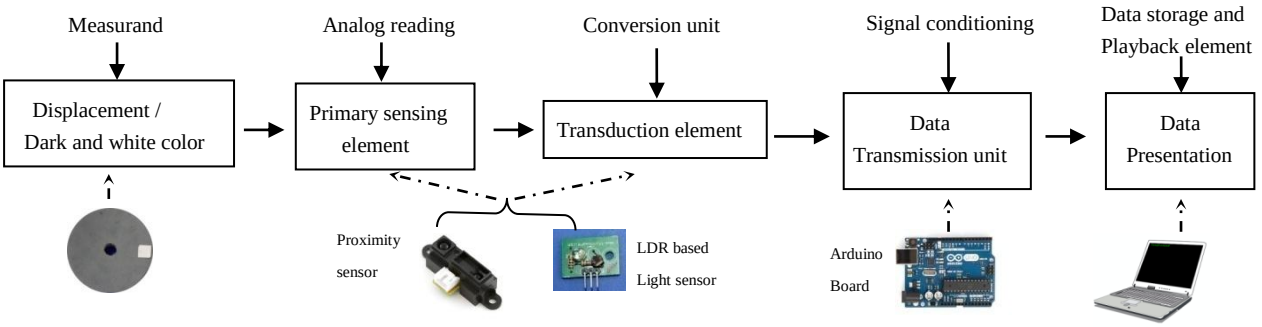

Fig. 5. The electrical setup at a glance.

3.2.1. Primary sensing and transduction element

3.2.1.1 Proximity sensor and Light sensor (LDR based)

A proximity sensor is able to detect the presence of nearby objects without any physical contact. It emits beam of electromagnetic radiation and looks for changes in the return signal and correspondingly change the voltage output.

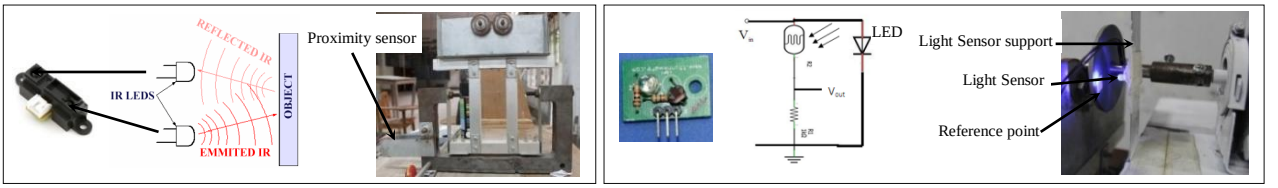

(a) (b)

Fig. 6. Sensor, its operating principle and location in the machine (a) Proximity sensor; (b) Light sensor.

A LDR based light sensor is a light-controlled variable resistor. Its resistance decreases with increasing incident light intensity. When LED light is reflected back by the dark colored shaft position measuring disk, voltage output is low and when by the reflexive material, voltage output is high. Details of the two sensors can be found in [9].

3.2.2. Data transmission

3.2.2.1. Arduino and serial communication

Arduino is an open-source physical computing platform based on a simple microcontroller board and a development environment for writing program for the board. The program used for Arduino in this setup can be found in [9]. Data transmission from Arduino to computer is done by serial communication. Arduino sends the data bits one by one or serially in the form of Highs (1) and Lows (0). The built-in analog-to-digital converter circuit reads the changing voltage input and converts it to an analogous number between 0 and 1023 (binary voltage value).

3.2.3. Data presentation

3.2.3.1. Monitoring the sensor output voltage and capturing the monitored data

Arduino software has a built-in monitor (serial monitor) which facilitates monitoring the sensor output voltage. It only shows the values but do not capture them. To capture the data special software named "Coolterm" is required. "Coolterm" captures and saves data in a text file which can be exported to excel to plot graphs.

4. Performance evaluation

4.1. Determination of vibration amplitude, amount of unbalanced mass and phase angle

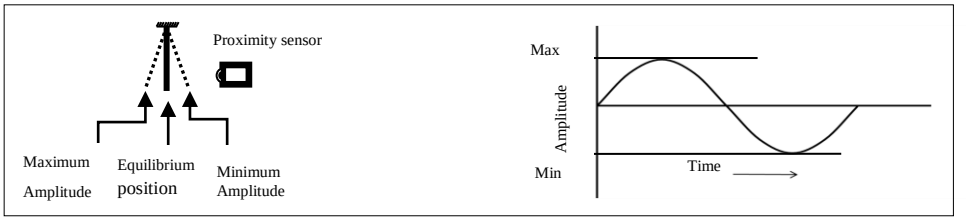

Fig.7. Deflection of the vibrating deflector.

- Due to the addition of unbalanced mass, the deflector strip vibrates and generates a binary value (sensor output voltage value) that is converted to distance by the formula taken from catalog of the proximity sensor,

$$\text{Distance (mm) from the sensor} = 12343.85 \times (\text{sensor output voltage value})^{-1.15} \quad (1)$$

The graph showing distance vs. binary voltage value gives the maximum and minimum distance of the vibrating deflector from the proximity sensor's position. These data gives the amplitude of vibration,

$$\text{Amplitude of vibration or Deflection from equilibrium position} = \frac{\text{Maximum distance} - \text{Minimum distance}}{2} \quad (2)$$

- The deflector strip can be approximated as a spring i.e. the deflection vs. unbalanced mass is a straight line. Adding 3 known masses in the standard rotor (having no residual unbalance) and measuring the deflection, the reference graph is plotted. For a measured deflection, this graph yields the amount of unbalance for a test rotor.

- $$\text{Phase angle, } \varphi = 2\pi \times \frac{AB}{CD}, \quad (3)$$

Where, AB = Distance between displacement peak value and adjacent shaft peak value (binary voltage value).
CD = Distance between consecutive two peaks of the displacement (binary voltage value).

The value of AB and CD are determined using CAD software (AutoCAD 2012) from the consolidated graph of the displacement and shaft position binary voltage value (sensor output voltage value) vs. time.

4.2. Experimental study

4.2.1. Proximity sensor calibration and rotating disk without unbalanced mass

From the calibration graph of fig. 8 (a), it is seen that voltage output from the proximity sensor fluctuates harshly if the object is less than 150 mm from the sensor. That is why the proximity sensor is placed 204 mm far from the vibrating deflector strip.

From fig. 8 (b), it is observed that there is no significant peak in the displacement curve (the tiny peaks are for electric noise in the proximity sensor) which indicates that the deflector is steady when the rotor runs without unbalanced mass. It also clarifies the absence of residual unbalance in the rotor which ensures its use as a standard rotor for determining the reference graph of deflection vs. unbalanced mass.

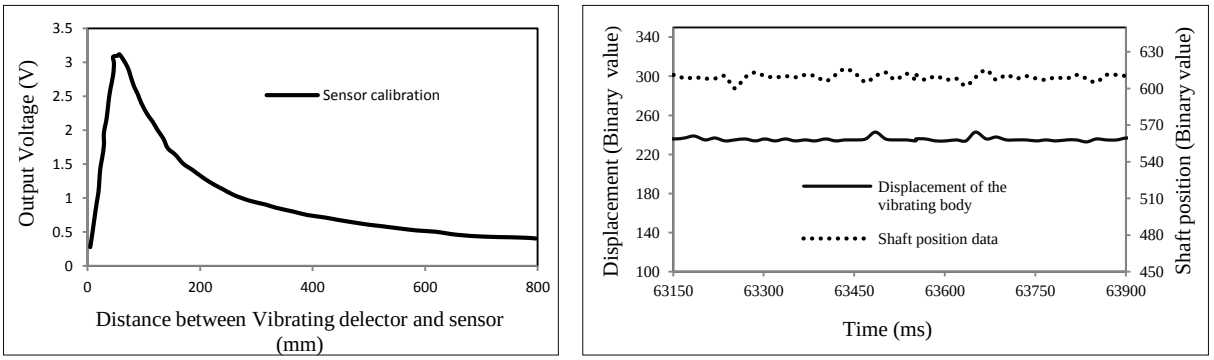

Fig. 8. (a) Proximity senor voltage output vs. displacement (b) The output of two sensors when the disk rotates without unbalanced mass.

4.2.2. Rotating disk with unbalanced mass of 20 gm.

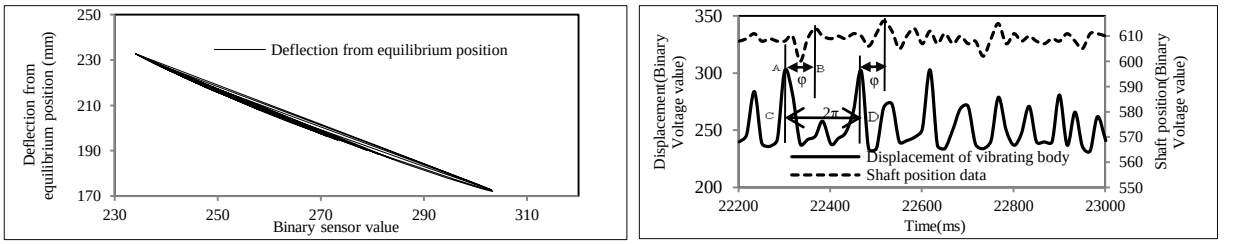

(a) (b)

Fig. 9. With unbalanced mass 20 gm. (a) Binary value converted to displacement (mm); (b) Graph plotted from the output of two sensors.

From fig. 9 (a), maximum distance = 235 mm and minimum distance = 173 mm. Using equation (2),

$$\text{Amplitude of vibration or Deflection from equilibrium position} = \frac{235-173}{2}\ \text{mm} = 31\ \text{mm}$$

From the fig. 9 (b), $\frac{AB}{CD} = \frac{2.65}{6.46} = 0.41$; Using equation (3), Phase angle, $\varphi = 360^0 \times 0.41 = 147.6^0$ (CCW)

4.2.3. Rotating disk with unbalanced mass of 60 gm.

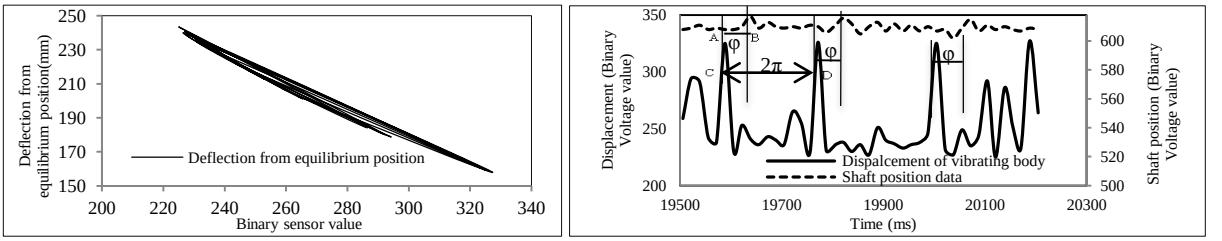

(a) (b)

Fig. 10. With unbalanced mass 60 gm. (a) Binary value converted to displacement; (b) Graph plotted from the output of two sensors.

From fig. 10 (a), maximum distance = 242 mm and minimum distance = 158 mm. Using equation (2),

$$\text{Amplitude of vibration or Deflection from equilibrium position} = \frac{242-158}{2}\ \text{mm} = 42\ \text{mm}$$

From the fig. 10 (b), $\frac{AB}{CD} = \frac{2.65}{6.90} = 0.39$; Using equation (3), Phase angle, $\varphi = 360^0 \times 0.39 = 140.4^0$ (CCW)

4.2.4. Rotating disk with unbalanced mass of 80 gm.

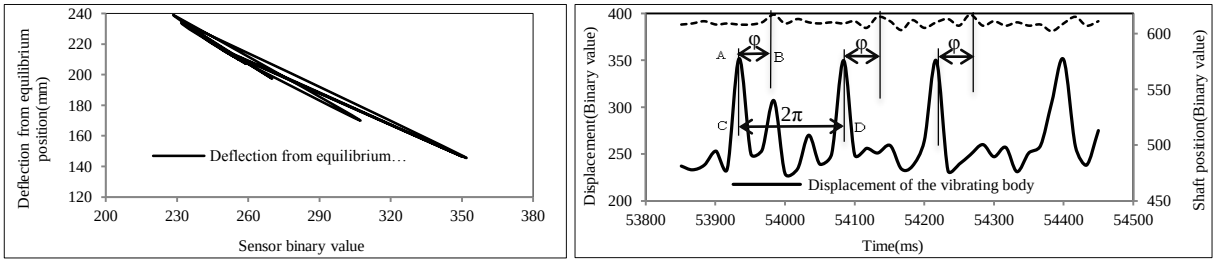

(a) (B)

Fig. 11. With unbalanced mass 80 gm. (a) Binary value converted to displacement; (b) Graph plotted from the output of two sensors.

From fig. 11 (a), maximum distance = 238 mm and minimum distance = 142 mm. Using equation (2),

$$\text{Amplitude of vibration or Deflection from equilibrium position} = \frac{238-142}{2}\ \text{mm} = 48\ \text{mm}$$

From the fig. 11 (b), $\frac{AB}{CD} = \frac{2.65}{6.6} = 0.40$; Using equation (3), Phase angle, $\varphi = 360^0 \times 0.40 = 144.4^0$ (CCW)

4.3. The reference curve to determine the amount of unbalanced mass

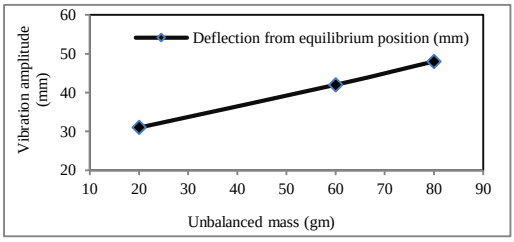

Fig. 12. Relation between unbalanced mass and vibration amplitude.

Fig. 12 shows the reference curve for determining the amount of unbalanced mass as explained in article 4.1 which is plotted using the experimental data. As expected, it is a straight line.

4.4 Result and Discussion

Table 1. Summary of the results.

Unbalanced mass (gm.)	Measured Phase angle in degree (CCW)	Actual Phase angle in degree (CCW)	% Error	Deflection (mm)
20	147.6	145	1.79	31
60	140.4	145	3.17	42
80	144.4	145	0.413	48

The low value of percentage error shown in table 1 implies that the results are pretty accurate. From the graph of fig. 9 (b), 10 (b) and 11 (b), it is seen that for every two peaks of the displacement value there is a peak for shaft value. The other minor peaks in the graphs are for unavoidable electrical noise which is common to every sensor.

5. Conclusion

This paper presents a new approach for measuring unbalanced mass of a thin rotor with a designed and fabricated single plane balancing machine. If a rotor is unbalanced, there will be a peak in the vibration amplitude and this peak will dominate its frequency spectrum. This peak value, along with the reference peak value of shaft position is combined here to find the location and amount of unbalanced mass by using two sensors. It is expected that with further modifications and developments, this machine can be used as a multiple plane dynamic balancing machine.

References

[1] Zhou, S. and Shi, J., Active Balancing and Vibration Control of Rotating Machinery. *The Shock and Vibration Digest*, 2001. 33(4), p.361.

[2] Reutlinger, W.D., *Dynamic Balancing Machine*, 1973. U.S. Pat. 3,902,373.

[3] Yadav, H.K., Upadhyay, S.H. and Harsha, S.P., Study of effect of unbalanced forces for high speed rotor. *Procedia Engineering*, 2013. 64, pp.593–602.

[4] Jeffcott, H.H., The lateral vibration of loaded shafts in the neighbourhood of a whirling speed – the effect of want of balance. *Philos. Mag.*, 1919. pp. 304–314. [online] Available at: <http://www.tandfonline.com/doi/abs/10.1080/14786440308635889?journalCode=tphm17#.U53SqHDxJhg>

[5] Weaver, S.H., Balancing of rotors in factory and at installation. *General Electric Review*, 1928. 31(10), p.542.

[6] Rathbone, T.C., Turbine vibration and balancing. *Trans. American Society of Mechanical Engineers*, 1929. 51(1), pp.267–284.

[7] Ribary, F., The balancing of masses in rotating bodies. *Brown Boveri Review*, 1936. 23(1), pp.186–192.

[8] Somervaille, I.J., Balancing a rotating disc, simple graphical construction. *Engineering*, 1954. 57(5), p.241.

[9] Mahmud, R. and Rasel, A.J., Design, fabrication and performance evaluation of a dynamic balancing machine, B. Sc. Thesis, Department of Mechanical Engineering, Bangladesh University of Engineering and Technology, Dhaka, 2014.